SPONTANEOUS SIMPLE AND FRACTAL SPATIAL PATTERN FORMATION IN NONLINEAR OPTICAL CAVITIES

Christopher BOSTOCK

School of Computing, Science and Engineering
College of Science and Technology
University of Salford, Salford, UK

Submitted in Partial Fulfilment of the Requirements of the Degree of Doctor of Philosophy, May 2015

Contents

List of Figures

Acknowledgments

I would like to start by expressing my utmost thanks to my supervisor Dr. James Christian for the support he has given me throughout my undergraduate and masters degrees, but more significantly the support which I have received throughout my PhD research. James has provided me with the confidence to present work at numerous conferences, which I will always be thankful for. He has also painstakingly gone though the content of this thesis and I cannot express my gratitude enough for this. Without James' encouragement, support, and advice this thesis would not of been possible.

I also want to thank the Physics department as a whole for making my time at Salford fun, enjoyable, and rewarding. Additionally, my thanks also goes out to my fellow peers, Emily McCoy and Helen Christie, for motivating me to venture outside of my comfort zone.

Finally, a special thanks to my family (Mum, Dad, Michael, and Louise) for their constant encouragement and support.

Abstract

The seminal work published by Alan Turing in 1952 provides the framework for our understanding of spontaneous pattern emergence in Nature. He proposed that when a reaction-diffusion system's uniform states become sufficiently stressed, arbitrarily-small disturbances combined with inherent feedback processes can lead to spontaneous self-organization into finite-amplitude patterns with a single dominant scalelength. In this thesis, Turing's universal mechanism is applied to a range of distinct nonlinear optical cavities. Of principal interest is a Fabry-Pérot (FP) resonator, which comprises a thin slice of diffusive Kerr-type material placed between two partially reflecting mirrors and pumped by an external plane wave. This model is a non-trivial generalization of the single-feedback mirror system, with the inclusion of the second mirror facilitating a disproportionate increase in complexity: here, the interplay between diffraction, counterpropagation and diffusive nonlinearity must be supplemented by more involved boundary conditions accommodating periodic pumping, mirror losses, interferomic mistuning, and time delays.

The presented research analyzes the thin-slice FP cavity mathematically and computationally, subject to plane wave pumping. Linear stability techniques are deployed to obtain the threshold spatial instability spectrum predicting the emergence of static patterns, and which exhibits a discrete-island type of structure. Simulations then consider the full dynamics of the system, testing theoretical analyses in the cases of instantaneous and diffusive medium responses. The emergence of both simple (single-scale) and fractal (multi-scale) spatial patterns is demonstrated, and specialist software used to assist with quantifying their dimension characteristics in terms of system parameters.

The first steps are also taken towards understanding the role played by nonparaxiality when

considering spatial fractal pattern formation in dispersive systems with a finite light-medium interaction length. The classic Schrödinger-type governing equations for bulk ring cavities are reformulated as Helmholtz-type problems, capturing a family of higher-order nonlinear effects that describe wavelength-scale spatial structure in the circulating field.

Chapter 1

Spontaneous optical patterns

The origin of our understanding of spontaneous pattern formation lies with the seminal work of Alan Turing in the early 1950s [1]. His original paper considered the chemical reactions of morphogens diffusing though a continuous ring of tissue. The uniform states of the system were perturbed slightly (for example, due to Brownian-motion fluctuations or effects from neighbouring structures), and a pattern subsequently developed in the concentrations of morphogen. Turing, thus, proposed a universal mechanism for describing the birth of simple patterns in reaction diffusion models. He predicted that when such a system is sufficiently stressed, arbitrarily-small disturbances to its uniform states (i.e., those solutions that are stationary in time and homogeneous in space) can lead to spontaneous self-organization into finite-amplitude patterns.

With simple pattern formation, the resulting structure tends to have a single dominant scalelength that is directly related to the most unstable spatial frequency in the system. Examples of simple patterns include hexagons, honeycombs, squares, stripes, rings, spirals, vortices, and single (or collections of) spots [2–9]. These patterns are familiar in everyday experience, appearing throughout Nature in activator-inhibitor chemical kinetics (animal coats, fish skins, shells), convective fluid flows (hydrodynamic vortices, Rayleigh-Bernard, Kelvin-Helmholtz, and Couette-Taylor instabilities), weather systems (tornadoes, hurricanes), and astrophysical phenomena (gravitational vortices, rotating spiral arms of galaxies) [5, 7, 10–14]. Pampaloni *et al.* have shown that is possible to observe patterns in two-dimensional crystals and quasicrystals [15].

1.1 Feedback and spontaneous symmetry-breaking

Feedback is a generic process whereby part of the output from a system is recombined with the input to regulate dynamical behaviour. There are two distinct types of feedback process: *positive* and *negative* [16]. The concept of positive feedback has been around since the 1920s, where it was used in regenerative circuits amplifying weak radio signals [17]. A simpler example can be found in audio systems, where a microphone registers part of an acoustic signal that is amplified by a speaker and subsequently re-registered by the microphone. A negative feedback system is where the output is used to reduce the input, which consequently reduces the output, and so on. Electronic amplifiers typically use this type of feedback to achieve stability and reduce distortion [16].

The general notion of "feedback" can be further categorized as being either *internal* or *external*. External feedback is when there is an interaction outside the system. An excellent example of this type of feedback in photonic contexts can be seen in later Chapters, and is typically associated with the partially-reflecting coupling mirror of an optical cavity. The role of such a mirror is to recycle part of the circulating cavity field while allowing it to combine with the laser field driving the system.

The particular systems considered in this thesis also exhibit internal feedback, which is linked to the nonlinear (dispersive and absorptive) properties of the host media (such as the Kerr effect). In Chapter 2, we investigate spontaneous pattern-forming properties though linear analysis of the single feedback-mirror (SFM) system [18, 19]. This elemental model comprises a single partially-reflecting mirror (providing external feedback) and a diffusive photoexcitation density in a thin slice of Kerr-type material that is driven by the total incoherent light intensity from forward- and backward-propagating waves (a source of internal feedback).

Another key concept is symmetry breaking, where vanishingly small-amplitude fluctuations to an otherwise uniform background field can cause the system to generate features which naturally stabilize competing processes [20]. These features may encourage the growth of further features or structures which, again, enhance the stability of the system. The particular mechanism causing the growth of ordered structures from background noise are commonly linked with the occurrence of phase transitions [20]. Spontaneous optical pattern formation

has been observed in several different systems with and without the consideration of external (e.g., mirror-type) feedback [21]. In the latter case, this occur when the field is travelling in a single direction, unidirectional. Pattern formation, in the latter case, is commonly referred to as modulation instability. It causes the breakdown of uniform states (plane waves) and is associated with the formation of localized states (such as solitons) [22].

It is also important to mention that spontaneous symmetry breaking is not strictly limited to optics. It is a universal phenomenon that appears in a vast range of areas including fluid dynamics, particle physics, biology, and economics [23–25].

1.2 Multi-Turing instability

Nature also provides us with a second class of pattern that is, in some sense, the opposite of a 'simple' one. Fractals are patterns that possess proportional levels of substructure spanning many decades of scale. Patterns with many such scales are often considered to by scale-free (i.e., having no natural scalelength). It is important to note that the *existence* of many different scales in a given pattern is not sufficient for it to merit the term *'fractal'*. Rather, the Fourier *amplitudes* associated with those scales (for example, in the power spectrum) must be comparable (and typically follow a power-law scaling rule) in order for the multi-scale characteristic to be truly meaningful.

A measure of the 'degree of complexity' in a fractal is provided by its dimension D. For a curve (or pattern) with topological dimension 1, one typically has $1 < D \leq 2$, where $D = 2$ is known as the area-filling limit (where the level of substructure is infinitely dense). There is no unique definition of D (in reality, there are many different, often interrelated, definitions). One cannot simply compare a fractal dimension of a pattern in one system directly to a fractal dimension in a completely unrelated system; the same definition has to be applied in measuring the dimension in both systems to obtain relevant comparison [26, 27]. It is also important that one applies an appropriate measure of D since some definitions are more practical and instructive than others. A short comparison of fractal dimension definitions can be seen later on (for physical fractals, one is often most concerned with self-affine measures for D, such as *power-spectrum*, *roughness-length*, *rescaled-range*, and *variogram* dimensions).

Fractals surround us every day: from ice crystals and snowflakes, to trees and clouds, to landscapes and coastlines. One can recognize complex dendritic patterns in electrical discharges such as lightning (so-called Lichtenberg figures) and in networks like river tributaries, plant root systems, and blood vessels in the human body. In reality, fundamental growth mechanisms in any system ultimately curtail the development of new structure (at either end of the scale range) beyond a limiting value. For example, in optics, diffraction can stop light patterns forming on sub-wavelength scales.

Turing considered models wherein the threshold instability spectrum comprises a single unique minimum (see Figure 1.1). However, there also exists a class of system whose threshold

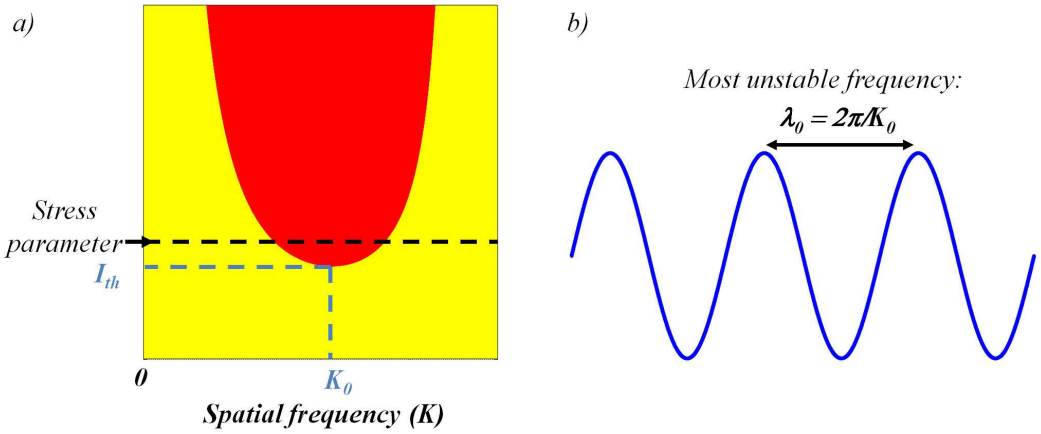

Figure 1.1: (a) A single Turing instability minimum, and (b) illustrating the relationship between pattern scalelength λ_0 and the most-unstable spatial frequency K_0.

instability spectrum comprises a discrete set many distinct but comparable minima (see Figure 1.2). When operating under highly stressed conditions (e.g., above several minima), it seems plausible that Turing's route to spontaneous *simple* patterns (spatial structure on a single dominant scalelength) will also provide a mechanism for generating spontaneous *fractal* patterns (spatial structure on many scales).

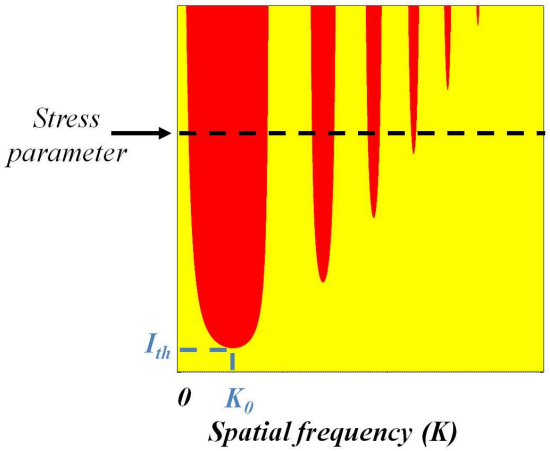

Figure 1.2: A multi-Turing threshold instability spectrum comprising many bands with comparable minima.

A note on mean-field theory

One of the earliest methods on analysing a nonlinear ring cavities was developed by Luigi Lugiato and René Lefever in the late 1980's [28]. Their technique involves making a set of assumptions about the mirror losses, and introduces longitudinal (spatial) averaging of the intracavity field to eliminate propagation effects. The result is a complex Ginzburg-Landau type of model (where wave equation and boundary condition are merged) for describing the time evolution of the transverse light distribution in the presence of diffraction, nonlinearity, and cavity effects (periodic pumping, losses, and interferometric mistuning). Mean-field models are analytically more tractable than the earlier 'lumped' models of McLaughlin, Moloney and Newell [29] (which typically use a nonlinear Schrödinger-type equation to describe the propagating intracavity field, and apply a lumped boundary condition at the start of each round-trip), and they have been heavily studied in the context of optical pattern formation and the growth of localized spatial structures [21, 30–36]. One key advantage of the Lugiato-Lefever approach is that the threshold condition predicting the onset of pattern formation is typically described by a quadratic equation. The Turing spectrum, then, has a single minimum (in Fourier space) whose position is determined by the strength of diffraction, the sign of the Kerr nonlinearity, and the interplay with (medium and interferometric) mistuning. Quantifying the behaviour of instabilities in mean-field models is much more straightforward than in their lumped counterparts, where the threshold condition is typically given by a complicated implicit (and transcendental) function.

There are two further salient points to note about mean-field theory. Firstly, it can give predictions that are qualitatively different from those of the corresponding lumped model (particularly in regimes involving the self-defocusing Kerr nonlinearity). Secondly, the existence of a single instability minimum in the Turing spectrum would appear to suggest that such models are not capable of supporting multi-scale (fractal) patterns (at least, not using the multiple-comparable-minima route).

1.3 Research novelty and thesis outline

The objective of the research presented in the following Chapters is to apply mathematical techniques (such as a linear stability analysis) to several different optical cavities with the intention of predicting, then simulating, spontaneous pattern emergence beyond the mean-field limit. Implicit in all this research is further testing the multiple-Turing-minima fractal-generating signature proposed by Huang *et al.* [37–39].

Novelty arises on several fronts. Firstly in Chapter 2, earlier analyses for the single feedback-mirror (SFM) system reviewed and a formal z-dependence in the amplitudes of the perturbation Fourier modes is introduced. Thereafter, the pattern-forming properties of the thin-slice nonlinear Fabry-Pérot (FP) cavity are investigated [34, 40, 41]. Physically, the FP cavity is closely related to the SFM model, but its additional boundary condition make for a much more subtle and complicated analysis. After briefly reviewing Ikeda-type instabilities [42–44], a detailed linear analysis of the plane-wave solutions is given. Extensive computations (with one and two transverse dimensions) simulate simple- and fractal-pattern emergence, and multi-scale behaviour is mapped-out (with the assistance of specialist software [45]) in terms of physical parameters for both instantaneous and diffusive nonlinearities.

In Chapter 3, we review and improve previous thin-slice linear analyses in dispersive ring-cavity geometries by introducing a similar type of propagation-dependence into the perturbative approach. The motivation behind such a generalization is to provide a mathematically more self-consistent description of any instabilities that are accessible through linearization methods. We also consider, for the first time, pattern formation in a bulk-medium ring cavity in the presence of Helmholtz diffraction. The inclusion of broadband diffraction effects is expected to yield corrections to the Turing instability spectrum at high spatial frequencies (precisely the regime in which paraxial optics no longer applies but where fractality tends to reside). A scalar nonlinear Helmholtz equation well-describes the propagation of light (even on the wavelength-scale) that is in a transverse-electric (TE) mode. For transverse-magnetic (TM) modes, we deploy instead a vectorized Helmholtz-type model derived from Maxwell's equations using an order-of-magnitude analysis [46].

Chapter 4 is concerned with the further development of understanding fractal formation

in bulk-medium geometries beyond mean-field theory. Here, the first steps are taken toward investigating pattern emergence in a slab of saturable-absorber material that completely fills a ring cavity. In particular, we consider the limit of weak absorption which should facilitate a simpler linear analysis than that of Brambilla, Columbo, and Magginpinto [47]. A multi-Turing threshold instability spectrum is indeed uncovered by a simplified analysis, but some physical inconsistencies are found to emerge from the analysis.

Conclusions about the thesis research outcomes and impact are drawn in Chapter 5, and some suggestions made for future avenues of exploration.

References

[1] A. M. Turing. The chemical basis of morphogenesis. *Philosophical Transactions of the Royal Society of London B*, 237(641):37–72, 1952.

[2] M. C. Cross and P. C. Hohenberg. Pattern formation outside of equilibrium. *Reviews of Modern Physics*, 65(3):851–1112, 1993.

[3] H. Meinhardt and H. Meinhardt. *Models of biological pattern formation.*, volume 6. London: Academic Press, 1982.

[4] A. Gierer and H. Meinhardt. A theory of biological pattern formation. *Kybernetik*, 12(1): 30–39, 1972.

[5] M. C. Cross and P. C. Hohenberg. Pattern formation outside of equilibrium. *Reviews of Modern Physics*, 65(3):851, 1993.

[6] J. E. Pearson. Complex patterns in a simple system. *Science*, 261(5118):189–192, 1993.

[7] J. D. Murray. How the leopard gets its spots. *Scientific American*, 258(3):80–87, 1988.

[8] Y. Xu, B. Zhu, and Y. Xu. A study on formation of regular honeycomb pattern in polysulfone film. *Polymer*, 46(3):713–717, 2005.

[9] R. D. Deegan. Pattern formation in drying drops. *Physical Review E*, 61(1):475, 2000.

[10] J. D. Murray. A pre-pattern formation mechanism for animal coat markings. *Journal of Theoretical Biology*, 88(1):161–199, 1981.

[11] K. J. Lee, W. D. McCormick, Q. Ouyang, and H. L. Swinney. Pattern formation by interacting chemical fronts. *Science*, 261(5118):192–194, 1993.

[12] T. R. Kline, W. F. Paxton, Y. Wang, D. Velegol, T. E. Mallouk, and A. Sen. Catalytic micropumps: Microscopic convective fluid flow and pattern formation. *Journal of the American Chemical Society*, 127(49):17150–17151, 2005.

[13] M. T. Chuang, P. C. Chiang, C. C. Chan, C. F. Wang, E. E. Chang, and C. T. Lee. The effects of synoptical weather pattern and complex terrain on the formation of aerosol events in the Greater Taipei area. *Science of the total environment*, 399(1):128–146, 2008.

[14] P. K. Maini, R. E. Baker, and C. Chuong. The Turing model comes of molecular age. *(Invited Perspective) Science*, 314(5804):1397–1398, 2006.

[15] E. Pampaloni, P. L. Ramazza, S. Residori, and F. T. Arecchi. Two-dimensional crystals and quasicrystals in nonlinear optics. *Physical Review Letters*, 74 (2):258–261, 1995.

[16] J. Daintith. *Oxford dictionary of physics*. Oxford University Press Oxford, 5th edition, 2005.

[17] D. A. Mindell. *Between human and machine: feedback, control, and computing before cybernetics.* JHU Press, 2002.

[18] W. J. Firth. Spatial instabilities in a Kerr medium with single feedback mirror. *Journal of Modern Optics*, 37:151–153, 1990.

[19] G. D'Alessandro and W. J. Firth. Hexagonal spatial patterns for a Kerr slice with a feedback mirror. *Physical Review A*, 41(1):537–548, 1992.

[20] S. M. Sears, M. Soljacic, D. N. Christodoulides, and M. Segev. Pattern formation via symmetry breaking in nonlinear weakly correlated systems. *Physical Review E*, 65(3; PART 2A):036620–036620, 2002.

[21] F. T. Arecchi, S. Boccaletti, and P. Ramazza. Pattern formation and competition in nonlinear optics. *Physics Reports*, 318(1):1–83, 1999.

[22] M. Soljacic, M. Segev, T. Coskun, D. N. Christodoulides, and A. Vishwanath. Modulation instability of incoherent beams in noninstantaneous nonlinear media. *Physical Review Letters*, 84(3):467, 2000.

[23] T. P. Cheng, L. F. Li, and T. P. Cheng. *Gauge theory of elementary particle physics.* Oxford: Clarendon press, 1984.

[24] R. Li and B Bowerman. Symmetry breaking in biology. *Cold Spring Harbor perspectives in biology*, 2(3):a003475, 2010.

[25] K. Matsuyama. Why are there rich and poor countries? symmetry-breaking in the world economy. *Journal of the Japanese and International Economies*, 10(4):419–439, 1996.

[26] H. Lauwerier. *Fractals: Images of chaos*. Penguin books, 1991.

[27] H. O. Peitgen, H. Jürgens, and D. Saupe. *Chaos and fractals: new frontiers of science*. Springer, 2004.

[28] L. A. Lugiato and R. Lefever. Spatial dissipative structures in passive optical systems. *Physical Review Letters*, 58(21):2209–2211, 1987.

[29] D. W. McLaughlin, J. V. Moloney, and A. C. Newell. New class of instabilities in passive optical cavities. *Physical Review Letters*, 54(7):681, 1985.

[30] M. Tlidi, P. Mandel, and R. Lefever. Localized structures and localized patterns in optical bistability. *Physical Review Letters*, 73(5):640, 1994.

[31] G. L. Oppo, M. Brambilla, and L. A. Lugiato. Formation and evolution of roll patterns in optical parametric oscillators. *Physical Review A*, 49(3):2028, 1994.

[32] N. B. Abraham and W. J. Firth. Overview of transverse effects in nonlinear-optical systems. *Journal of the Optical Society of America B*, 7(6):951–962, 1990.

[33] L. A. Lugiato, M. Brambilla, and A. Gatti. Optical pattern formation. *Advances in Atomic, Molecular, and Optical Physics*, 40:229–306, 1999.

[34] A. J. Scroggie, W. J. Firth, G. S. McDonald, M. Tlidi, R. Lefever, and L. A. Lugiato. Pattern formation in a passive Kerr cavity. *Chaos, Solitons & Fractals*, 4(8):1323–1354, 1994.

[35] L. A. Lugiato. Spatio-temporal structures. part I. *Physics reports*, 219(3):293–310, 1992.

[36] W. J. Firth and A. J. Scroggie. Spontaneous pattern formation in an absorptive system. *Europhysics Letters*, 26(7):521, 1994.

[37] J. G. Huang and G. S. McDonald. Spontaneous optical fractal pattern formation. *Physical Review Letters*, 94(17):174101, 2005.

[38] J. G. Huang. *Spontaneous optical fractals in linear & nonlinear systems.* Ph.D thesis, University of Salford, 2006.

[39] J. G. Huang, J. M. Christian, and G. S. McDonald. Spontaneous spatial fractal pattern formation in absorptive systems. *Journal of Nonlinear Optical Physics & Materials*, 21(02): art. no. 1250018, 2012.

[40] M. Möller, L. M. Hoffer, G. L. Lippi, T. Ackemann, A. Gahl, and W Lange. Fabry-Pérot and ring cavity configurations and transverse optical patterns. *Journal of Modern Optics*, 45(9):1913–1926, 1998.

[41] K. D. Stephen. *Optical coding via transverse patterns in nonlinear media.* PhD thesis, Strathclyde University, 1991.

[42] K Ikeda. Multiple-valued stationary state and its instability of the transmitted light by a ring cavity system. *Optics Communications*, 30(2):257–261, 1979.

[43] K. Ikeda, H. Daido, and O. Akimoto. Optical turbulence: chaotic behavior of transmitted light from a ring cavity. *Physical Review Letters*, 45(9):709, 1980.

[44] H. Nakatsuka, S. Asaka, H. Itoh, K. Ikeda, and M Matsuoka. Observation of bifurcation to chaos in an all-optical bistable system. *Physical Review Letters*, 50(2):109, 1983.

[45] BENOIT 1.3, TruSoft International Inc., www.trusoft-international.com.

[46] S. Chi and Q. Guo. Vector theory of self-focusing of an optical beam in Kerr media. *Optics Letters*, 20(15):1598–1600, 1995.

[47] M. Brambilla, L. Columbo, and T. Maggipinto. Three-dimensional self-organized patterns in the field profile of a ring cavity resonator. *Journal of Optics B: Quantum and Semiclassical Optics*, 6(5):S197, 2004.

Chapter 2

Nonlinear Fabry-Pérot cavity

The Kerr slice with a single feedback mirror (SFM) is perhaps the simplest nonlinear optical system to consider. Originally proposed by Firth [1], it comprises a thin slice of relaxing-diffusing Kerr-type material and a partially-reflecting feedback mirror placed some distance away in free space. Incident light illuminates the slice, traversing its near-negligible width in (effectively) zero time. Propagation through the medium results in only a phase modulation of the wave (diffraction may be neglected because the slice is thin). The phase-modulated wave then travels to the feedback mirror whereupon it is reflected back to the slice (that is, the forward wave is converted into a backward wave). In this free-space path, the light undergoes diffraction (which is usually treated within the paraxial approximation) and it is hence during this stage of each transit that amplitude modulations come into play. Upon reaching the slice, the forward and backward light waves drive the transverse diffusion of charge carriers inside the material.

Despite the simplicity of the SFM system, there are many different aspects to consider. One has to take into account the interplay between forward- and backward-propagating waves, diffraction, periodic pumping and losses (persistent re-injection of light into the slice, and energy escaping at the feedback mirror), and diffusion of the photoexcitation density that is driven by the light intensity (light-medium coupling). One also has three different timescales to consider: time for light to traverse the slice, the response time of the photoexcitation density, and the round-trip time of the light in the free-space path. This 'simple' system is, in reality, rather complicated and one can hence expect to find rich layers of complex spatiotemporal dynamics.

Spatial instabilities in the SFM system were first considered more than two decades ago. Firth's linear analysis [1] obtained the threshold condition as a function of spatial frequency, from which one can obtain the scalelength of emergent spatial structures. The instability spectrum for static patterns was found to comprise multiple bands whose existence can be directly attributed to the optical feedback provided by the mirror. The characteristics of these bands (e.g., their widths and the position of the minima) depend upon system parameters such as mirror reflectivity and the diffusion length. Subsequent numerical work by D'Alessandro and Firth [2] using plane-wave pumping demonstrated the emergence of static hexagonal arrays for both focusing and defocusing Kerr-type materials. Figure 2.1 indicates the most unstable wavelength, λ_0, in an emergent hexagonal pattern. Turbulence modes were also uncovered in some parameter regimes, though such modes cannot strictly be classified as 'static'. Weakly nonlinear analysis and computer-assisted algebra (which involves the solution of three coupled Ginzburg-Landau equations) subsequently predicted a leading-order approximation of pattern amplitude [3]. The effect of transverse boundary conditions was later discussed by Papoff *et al.* [4], who deployed group-theoretic analyses to quantify simulations with broad Gaussian pump beams (rather than plane waves). These patterns are reminiscent of those found experimentally by Grynberg, Maitre, and Petrossian [5].

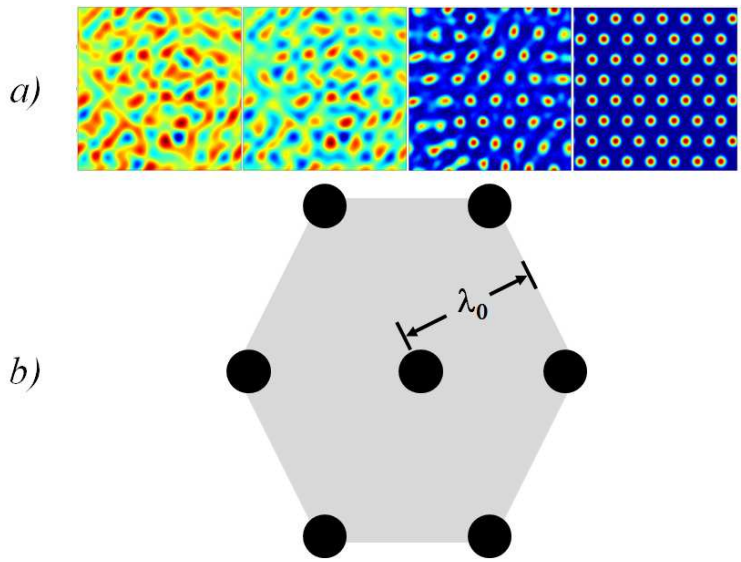

Figure 2.1: (a) Spontaneous hexagon formation in the SFM system. (b) The most unstable wavelength λ_0 determines the pattern size.

More sophisticated SFM-based configurations have considered a single slice with two feedback mirrors [6], and two slices with a single mirror [7]. In both cases, the qualitative features of the static instability threshold spectra are identical to those of Firth's SFM system [1].

The potential of simple systems for generating complex patterns was recognized 12 years later by Huang and McDonald [8]. They conjectured that *any* system whose Turing threshold spectrum comprises multiple minima may be capable of generating spontaneous fractal patterns. This signature of fractal-generating capacity was proposed to have independence with respect to: (i) the nature of the physical system (e.g., optical, fluidic, acoustic, etc.), and (ii) the details of the dominant feedback loops in the system (e.g., whether the nonlinearity is purely dispersive or purely absorptive). Extensive numerical investigations showed that the SFM system could indeed support spatial fractal patterns, and that the characteristics of the fractal (e.g., its dimension) depend upon system parameters. Subsequent analyses by Huang, Christian, and McDonald [9] tested the *system-independence* claim of the fractal-generating signature by considering slice materials in (dispersive and absorptive) optical ring cavities. In particular, they discovered the first evidence of spontaneous spatial fractal pattern formation in a purely-absorptive systems [10].

An intuitive generalization of the SFM system is that of the Fabry-Pérot (FP) cavity. The geometry of the FP cavity is identical to that of the SFM system, except that the input face of the slice is assumed to be partially reflecting. The nonlinear medium is then effectively sandwiched between two plane mirrors, so that the energy in the pump beam bounces back-and-forth periodically, passing through the slice each time. While the addition of a second mirror represents only a very small physical alteration to the system, the ensuing mathematical and computational complexity is disproportionately increased. It is perhaps for this reason that, to date, there exists relatively little published literature on nonlinear FP systems [11]. On the one hand, Margurger and Felber [12] have derived the input-output characteristics of an FP cavity completely filled with Kerr-type material (going well beyond the thin-slice approximation), while Firth [13] has considered a range of instability classes. Both analyses captured the cavity boundary condition but neglected diffraction. On the other hand, Moller *et al.* [14] considered a Kerr slice between two mirrors numerically and experimentally (incorporating transverse

effects), but provided no compelling theory.

To date, the fractal-generating capacity proposed by Huang and McDonald [8] has been verified in SFM and ring cavity [9, 10] geometries. The motivation behind the current programme of research is to develop a framework for predicting spatial instabilities in a nonlinear FP cavity, taking full account of both cavity and transverse (diffraction and diffusion) effects. This will be achieved using linearization techniques similar to those deployed by Firth [1] for the SFM. After determining the thresholds for both static (Turing) and oscillatory (Hopf) instabilities, theoretical predictions will be tested against full numerical computations.

Summary of parameters and variables

b	Complex perturbations for the backwards propagating field
B	Backwards propagating electric field
B_0	Uniform state of B
f	Complex perturbations for the forwards propagating field
F	Forward propagating electric field
F_0	Uniform state of F
F_{in}	Amplitude of the plane wave pump field
d	The distance between nonlinear slice, and the mirror
$\boldsymbol{K}$	Transverse spatial frequency
I_0	Initialized intensity
I_{th}	Intensity threshold
K_C	High frequency cut-off
K_0	Most unstable frequency
$2\pi/k_0$	Free-space wavelength of the pump light
n	Photoexcitation density
n_0	Uniform state of n
r_1^2	Intensity reflectivity of the slice mirror
r_2^2	Intensity reflectivity of the feedback mirror
t	Time co-ordinate
t_1^2	Intensity transmissivity
t_R	Transit time
z	Longitudinal space co-ordinate
δ	Linear interferometric mistuning
Δn	Real perturbation to the photoexcitation density
ε	Parameters of smallness
θ	Phase/propagation factor
λ	Complex Lyapunov exponent
Λ	Growth rate
τ	Relaxation time
χ	Nonlinearity of the Kerr medium
Ω	Temporal frequency
$\nabla_\perp^2$	Transverse Laplacian

2.1 Review of the single feedback-mirror

In this section, we review the SFM model (see figure 2.2). A linear stability analysis of its uniform solutions will be performed, and the formation of spontaneous patterns demonstrated through computer simulations.

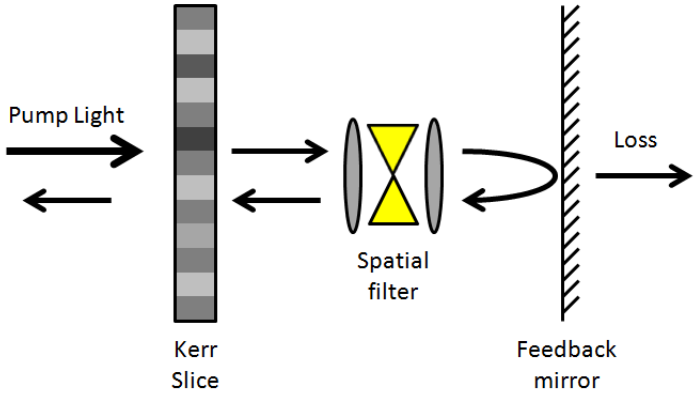

Figure 2.2: Schematic diagram of the classic single feedback-mirror system [1].

2.1.1 Model equations

Inside the slice, the coupled field-medium dynamics are governed by [1]

$$\frac{\partial F}{\partial z} = i\chi n F, \tag{2.1a}$$

$$\frac{\partial B}{\partial z} = -i\chi n B, \tag{2.1b}$$

$$-l_D^2 \nabla_\perp^2 n + \tau \frac{\partial n}{\partial t} + n = |F|^2 + |B|^2, \tag{2.1c}$$

where t denotes the time coordinate, z is the longitudinal space coordinate, and $\nabla_\perp^2$ is the transverse Laplacian. The forward- and backward-propagating electric field envelopes are denoted by F and B, respectively, and χ parametrizes the nonlinearity (positive for a focusing Kerr medium, negative for defocusing). The photoexcitation density n has a relaxation time τ and a diffusion length l_D (note that diffusion in the longitudinal direction can be neglected by assuming that the slice thickness L satisfies the inequality $L \ll l_D$). The slice limit also

allows one to neglect a detailed nonparaxial treatment of potential small-scale structure in electric fields within the medium (which would otherwise complicate analysis without necessarily providing any new qualitative predictions) [15].

Free-space propagation over a distance $2d$ (from the slice to the mirror and back again) in transit time t_R is handled by the boundary condition

$$B(\boldsymbol{x}, L, t) = r_2 \exp\left(i\frac{d}{k_0}\nabla_\perp^2\right) F(\boldsymbol{x}, L, t - t_R), \tag{2.2}$$

where r_2^2 is the intensity reflectivity of the feedback mirror, and $2\pi/k_0$ is the free-space wavelength of the pump light. The inherent assumption of beam paraxiality in Eq. (2.2) will be relaxed for computations, where Helmholtz diffraction will implemented instead.

The uniform states of the SFM system are those that are homogeneous in space ($\nabla_\perp^2 \to 0$, hence no transverse effects) and stationary in time ($\partial/\partial t \to 0$, hence no dynamical effects). Denoting the uniform states with a "0" index, it can be shown that:

$$F^0(z) = F_{in} \exp(i\chi n_0 z), \tag{2.3a}$$

$$B^0(z) = r_2 F_{in} \exp\left[i\chi n_0 \left(2L - z\right)\right], \tag{2.3b}$$

$$n_0 = (1 + r_2^2)|F_{in}|^2, \tag{2.3c}$$

where F_{in} is the (complex) amplitude of the plane wave pump field.

2.1.2 Linear stability analysis

We consider a small perturbation to uniform state (2.3) that may be written as:

$$F(\boldsymbol{x}, z, t) = F^0(z)\left[1 + f(\boldsymbol{x}, z, t)\right], \tag{2.4a}$$

$$B(\boldsymbol{x}, z, t) = B^0(z)\left[1 + b(\boldsymbol{x}, z, t)\right], \tag{2.4b}$$

$$n(\boldsymbol{x}, t) = n_0 + \Delta n(\boldsymbol{x}, t). \tag{2.4c}$$

Here, f and b are complex perturbations satisfying $|f| \ll O(1)$ and $|b| \ll O(1)$ (their complex character means both amplitude and phase of the electric fields are disturbed), while Δn is a real perturbation to the photoexcitation density that satisfies $|\Delta|n/n_0 \ll O(1)$. The dependence of f and b on the longitudinal coordinate represents a generalization of Firth's analysis [1], which assumes f and b to be independent of z. Substituting Eqs. (2.4a)−(2.4c) into Eq. (2.1c), then linearizing in the perturbations around the uniform state leads to the following equation for the perturbed field-medium dynamics:

$$\left(-l_D^2\nabla_\perp^2 + \tau\frac{\partial}{\partial t} + 1\right)\Delta n(\boldsymbol{x},t) = |F_{in}|^2[f(\boldsymbol{x},z,t) + f^*(\boldsymbol{x},z,t)] + r_2^2|F_{in}|^2[b(\boldsymbol{x},z,t) + b^*(\boldsymbol{x},z,t)]\,. \tag{2.5}$$

By substituting Eqs. (2.4a) and (2.4b) into Eqs. (2.1a) and (2.1b), respectively, and integrating one can retrieve the z-dependence of f and b as:

$$f(\boldsymbol{x},z,t) \;\; = f(\boldsymbol{x},0,t) + i\chi\Delta n(\boldsymbol{x},t)z, \tag{2.6a}$$

$$b(\boldsymbol{x},z,t) \;\; = b(\boldsymbol{x},0,t) - i\chi\Delta n(\boldsymbol{x},t)z, \tag{2.6b}$$

A key part of the analysis is how one relates the f and b source terms on the right-hand side of Eq. (2.5) to Δn. Substituting Eq. (2.4a) and (2.4b) into Eq. (2.2) yields:

$$b(\boldsymbol{x},L,t) \simeq \exp\left(i\frac{d}{k_0}\nabla_\perp^2\right) f(\boldsymbol{x},L,t-t_R). \tag{2.7}$$

Consider now the source terms in Eq.(2.5). By using the solutions for f and b, the following relation can be obtained:

$$f(\boldsymbol{x},z,t) + f^*(\boldsymbol{x},z,t) \;\; = \;\; f(\boldsymbol{x},0,t) + f^*(\boldsymbol{x},0,t), \tag{2.8a}$$

$$b(\boldsymbol{x},z,t) + b^*(\boldsymbol{x},z,t) \;\; = \;\; b(\boldsymbol{x},0,t) + b^*(\boldsymbol{x},0,t). \tag{2.8b}$$

Through combining Eqs. (2.6b), (2.6b) and (2.7) and by transforming to the Fourier (transverse spatial frequency) domain $\boldsymbol{K}$, whereby $\nabla_\perp^2 \to -K^2$ and transformed quantities are denoted by

tildes, it can be shown that:

$$\tilde{b}(\boldsymbol{K},0,t) = \exp(-i\theta)\left[\tilde{f}(\boldsymbol{K},0,t-t_R) + i\chi L\Delta\tilde{n}(\boldsymbol{K},t-t_R)\right] + i\chi L\Delta\tilde{n}(\boldsymbol{K},t), \tag{2.9}$$

where $\theta = K^2 d/k_0$. Now Eq. (2.5) can be simplified by eliminating $\tilde{b}$ to give:

$$\begin{aligned}\left(1 + l_D^2K^2 + \tau\frac{\partial}{\partial t}\right)\Delta\tilde{n}(\boldsymbol{K},t) &= |F_{in}|^2\left[\tilde{f}(\boldsymbol{K},0,t) + \tilde{f}^*(\boldsymbol{K},0,t)\right] \\ &+ r_2^2|F_{in}|^2\Big[\exp(-i\theta)\tilde{f}(\boldsymbol{K},0,t-t_R) + \exp(i\theta)\tilde{f}^*(\boldsymbol{K},0,t-t_R) \\ &+ 2\chi L\sin\theta\Delta\tilde{n}(\boldsymbol{K},t-t_R)\Big].\end{aligned} \tag{2.10}$$

Which may be simplified further:

$$\begin{aligned}\left(1 + l_D^2K^2 + \tau\frac{\partial}{\partial t}\right)\Delta\tilde{n}(\boldsymbol{K},t) &= |F_{in}|^2\left[\tilde{f}(\boldsymbol{K},0,t) + \tilde{f}^*(\boldsymbol{K},0,t)\right] \\ &+ 2r_2^2\chi L|F_{in}|^2\sin\theta\Delta\tilde{n}(\boldsymbol{K},t-t_R) \\ &+ r_2^2|F_{in}|^2\cos\theta\left[\tilde{f}(\boldsymbol{K},0,t-t_R) + \tilde{f}^*(\boldsymbol{K},0,t-t_R)\right] \\ &- ir_2^2|F_{in}|^2\sin\theta\left[\tilde{f}(\boldsymbol{K},0,t-t_R) + \tilde{f}^*(\boldsymbol{K},0,t-t_R)\right].\end{aligned} \tag{2.11}$$

The delay-differential equation derived by Firth [1] can be recovered by setting the perturbations at the input face of the slice to zero i.e., $\tilde{f}(\boldsymbol{K},0,t) = 0$. This, in turn, shows that $\Delta\tilde{n}$ satisfies:

$$\left(1 + l_D^2K^2 + \tau\frac{\partial}{\partial t}\right)\Delta\tilde{n}(\boldsymbol{K},t) = 2r_2^2\chi L|F_{in}|^2\sin\theta\Delta\tilde{n}(\boldsymbol{K},t-t_R). \tag{2.12}$$

By assuming time dependence of the form

$$\Delta\tilde{n}(\boldsymbol{K},t) = \eta\exp(\lambda t) + \eta^*\exp(\lambda^* t), \tag{2.13}$$

where $\lambda \equiv \Lambda - i\Omega$ is a complex Lyapunov exponent with (Turing) growth rate Λ and temporal

(Hopf) frequency Ω, it follows that

$$1 + l_D^2 K^2 + (\Lambda - i\Omega)\tau = 2r_2^2 \chi L |F_{in}|^2 \sin\theta \exp(-\Lambda t_R + i\Omega t_R). \tag{2.14}$$

Equation (2.14) can then be re-expressed in the more convenient form

$$\left[\left(1 + l_D^2 K^2 + \Lambda\tau\right)^2 + (\Omega\tau)^2\right]^{1/2} = 2r_2^2 \chi L |F_{in}|^2 \sin\theta \exp\left[-\Lambda\tau + i(\Omega t_R + \alpha)\right], \tag{2.15a}$$

$$\tan\alpha \equiv \frac{\Omega\tau}{1 + l_D^2 K^2 + \Lambda\tau}. \tag{2.15b}$$

Equations (2.15a) and (2.15b) can now be analyzed to find the thresholds for static (Turing) and oscillatory (Hopf) instabilities.

2.1.3 Static threshold curves

To obtain the threshold spectrum for static patterns one sets $\Omega = 0$ (to discard oscillatory solutions) and $\Lambda = 0$ [which itself is the boundary between growth ($\Lambda > 0$) and decay ($\Lambda < 0$)]. By denoting the plane wave pump intensity at threshold by $|F_{in}|^2 \rightarrow I_{th}$, it follows that the threshold condition is

$$\chi L I_{th} = \frac{1 + l_D^2 K^2}{2r_2^2 \sin\theta}. \tag{2.16}$$

Here, $\chi L I_{th}$ (which has units of nonlinear phase shift) plays the role of a stress parameter. In the absence of diffusion (i.e., $l_D = 0$), the threshold spectrum comprises a large number (in principle, a discrete infinity) of spatial-frequency bands that share a common minimum (see figure 2.3). With increasing K, the bands become narrower and more closely spaced. The picture changes qualitatively for finite diffusion (i.e., $l_D > 0$), whereby the effect of the $l_D^2 K^2$ factor in the numerator of Eq. (2.16) is to impose a quadratic envelope on the minima (in Fourier space). The separation between the bands also tends to increase (rather than decrease) with K.

The most unstable spatial frequency corresponds to the K with the lowest threshold. Denoting that frequency by K_0, the most unstable wavelength is defined to be $\lambda_0 \equiv 2\pi/K_0$ and it is

this quantity that determines the scalelength of the pattern that eventually grows to dominate the system.

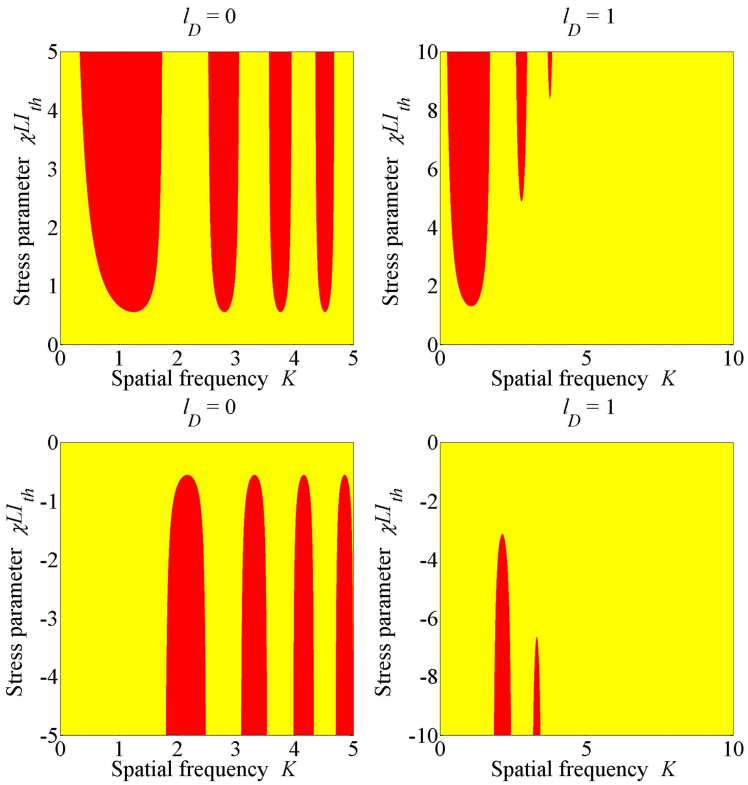

Figure 2.3: Static threshold curves for the SFM system with a (top panes) focusing ($\chi = +1$) and (bottom panes) defocusing ($\chi = -1$) Kerr nonlinearity, when $r_2^2 = 0.9$, $l_D = 0$, $d/k_0 = 1$, $\tau = 0$, $\delta = \pi/4$, and $L = 1$.

2.1.4 Concluding Remarks

Here, the single feedback mirror has been analysed analytically though the use of a stability analysis. Unlike the original work presented by Firth in the early 90's [1], the analysis implemented in this thesis has the additional novelty of a z-dependent perturbation. The resulting threshold spectrum remains unchanged, and gives identical result to those of Firth. This analysis indicates that the z-dependent perturbation is not necessarily required for the single feedback mirror system, however this produced a more well rounded result.

2.2 Nonlinear Fabry-Pérot cavity

Having established a working knowledge of the SFM system, similar linearization techniques will now be applied to the nonlinear FP cavity, a schematic diagram of the cavity can be seen in figure 2.4. However, there are some subtle differences in the analysis that will be detailed as we go along.

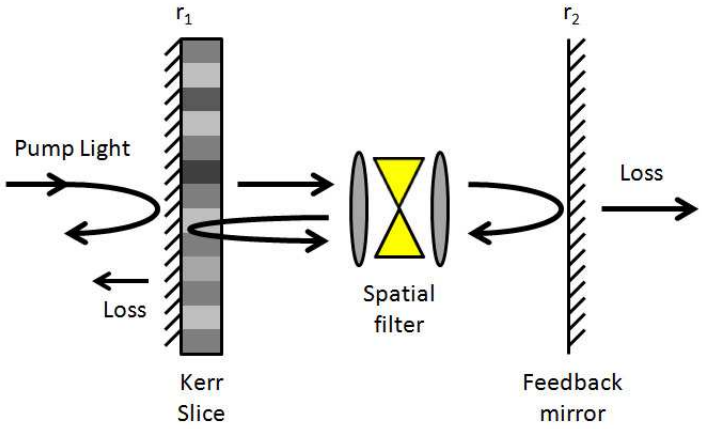

Figure 2.4: Schematic diagram of the Fabry-Pérot cavity.

2.2.1 Boundary conditions and uniform states

The FP cavity we will consider is described by model (2.1) [16]. A major difference introduced by the reflecting face of the slice is that SFM boundary condition − which acts solely on the backward field [c.f. Eq. (2.2)] − must be supplemented by an additional boundary condition on the forward field at the system input. Hence, for the FP cavity:

$$F(\boldsymbol{x},0,t) = t_1 F_{in} + r_1 \exp(i\delta) B(\boldsymbol{x},0,t), \tag{2.17a}$$

$$B(\boldsymbol{x},L,t) = r_2 \exp\left(i\frac{d}{k_0}\nabla_\perp^2\right) F(\boldsymbol{x},L,t-t_R), \tag{2.17b}$$

where r_1^2 and r_2^2 are the intensity reflectivities of the slice and feedback mirror, respectively, and $t_1^2 \equiv 1 - r_1^2$. The parameter δ represents a net linear interferometric mistuning. Now, the (total) source of forward fields driving the cavity comprises a fraction of the plane-wave pump

F_{in}, plus a fraction of the recycled backward field (reflected at $z = 0$).

The target is to analyze the stability of model (2.1) against pattern-forming instabilities, subject to boundary conditions (2.17a) and (2.17b). To this end, one must begin by finding the uniform states of the FP cavity, which are given by:

$$F^0(z) = \frac{t_1 F_{in}}{1 - r_1 r_2 \exp(i\Phi)} \exp(i\chi n_0 z), \tag{2.18a}$$

$$B^0(z) = r_2 \frac{t_1 F_{in}}{1 - r_1 r_2 \exp(i\Phi)} \exp\left[i\chi n_0 (2L - z)\right], \tag{2.18b}$$

$$n_0 = \frac{(1 + r_2^2) t_1^2 |F_{in}|^2}{1 + r_1^2 r_2^2 - 2 r_1 r_2 \cos\Phi}, \tag{2.18c}$$

where $\Phi \equiv \delta + 2\chi L n_0$ contains both linear (interferometric) and nonlinear (medium-induced) mistunings. This solution describes the expected multi-stable characteristic of an FP cavity. Furthermore, in the limit that $r_1^2 \to 0$, the SFM uniform states [c.f. solution (2.3)] are clearly recovered.

2.2.2 Linear stability analysis

We proceed in a similar way as with the SFM system, perturbing the stationary state of the cavity according to:

$$F(\boldsymbol{x}, z, t) = F^0(z)\left[1 + f(\boldsymbol{x}, z, t)\right], \tag{2.19a}$$

$$B(\boldsymbol{x}, z, t) = B^0(z)\left[1 + b(\boldsymbol{x}, z, t)\right], \tag{2.19b}$$

$$n(\boldsymbol{x}, t) = n_0 + \Delta n(\boldsymbol{x}, t). \tag{2.19c}$$

The forward and backward perturbations *must* contain explicit z dependence in order to accommodate the boundary condition on the forward field. Substitution of Eqs. (2.19a)−(2.19c)

into Eq. (2.1c) yields

$$\left(-l_D^2\nabla_\perp^2+\tau\frac{\partial}{\partial t}+1\right)\Delta n(\boldsymbol{x},t)=|F_0|^2[f(\boldsymbol{x},z,t)+f^*(\boldsymbol{x},z,t)] + r_2^2|F_0|^2[b(\boldsymbol{x},z,t)+b^*(\boldsymbol{x},z,t)]\,, \tag{2.20a}$$

$$|F_0|^2 \equiv \frac{t_1^2|F_{in}|^2}{1+r_1^2r_2^2-2r_1r_2\cos\Phi}. \tag{2.20b}$$

By substituting Eqs. (2.19a) and (2.19b) into Eqs. (2.1a) and (2.1b) and integrating, it can also be shown that the z-dependence of f and b is simply

$$f(\boldsymbol{x},z,t)=f(\boldsymbol{x},0,t)+i\chi\Delta n(\boldsymbol{x},t)z, \tag{2.20c}$$

$$b(\boldsymbol{x},z,t)=b(\boldsymbol{x},0,t)-i\chi\Delta n(\boldsymbol{x},t)z. \tag{2.20d}$$

Equations (2.20c) and (2.20d) show that the perturbation to the photoexcitation density is driven by the real quantities $f(\boldsymbol{x},0,t)+f^*(\boldsymbol{x},0,t)$ and $b(\boldsymbol{x},0,t)+b^*(\boldsymbol{x},0,t)$. Substituting solutions (2.19a) and (2.19b) into boundary conditions (2.17a) and (2.17b) yields the following relations:

$$f(\boldsymbol{x},0,t) = r_1r_2\exp(i\Phi)b(\boldsymbol{x},0,t), \tag{2.21a}$$

$$b(\boldsymbol{x},L,t) = \exp\left(\frac{d}{k_0}\nabla_\perp^2\right)f(\boldsymbol{x},L,t-t_R), \tag{2.21b}$$

respectively. The forward perturbation $f(\boldsymbol{x},0,t)$ can thus be eliminated using Eq. (2.21a), so that the right-hand side of Eq. (2.20a) becomes

$$|F_0|^2r_1r_2\left[\exp(i\Phi)b(\boldsymbol{x},0,t)+\exp(-i\Phi)b^*(\boldsymbol{x},0,t)\right]+|F_0|^2r_2^2\left[b(\boldsymbol{x},0,t)+b^*(\boldsymbol{x},0,t)\right]. \tag{2.22}$$

Then, using Eq. (2.20d), one can relate $b(\boldsymbol{x},0,t)$ to $\Delta n(\boldsymbol{x},t)$. Finally, after Fourier transfor-

mation, one is left with the following equation for the medium dynamics:

$$\left(1 + l_D^2 K^2 + \tau\frac{\partial}{\partial t}\right)\Delta\tilde{n}(\boldsymbol{K},t) = |F_0|^2(r_2^2 + r_1 r_2\cos\Phi)\left[\tilde{b}(\boldsymbol{K},L,t) + \tilde{b}^*(\boldsymbol{K},L,t)\right]$$
$$+ i|F_0|^2 r_1 r_2 \sin\Phi\left[\tilde{b}(\boldsymbol{K},L,t) - \tilde{b}^*(\boldsymbol{K},L,t)\right] \quad (2.23a)$$
$$- 2\chi L|F_0|^2 r_1 r_2\sin\Phi\Delta\tilde{n}(\boldsymbol{K},t).$$

Similarly, combining Eq. (2.21a) with Eq. (2.20c) and then Fourier transforming leads to:

$$\tilde{b}(\boldsymbol{K},L,t) = r_1 r_2\exp[i(\Phi-\theta)]\tilde{b}(\boldsymbol{K},L,t-t_R)$$
$$+ i\chi L\left\{r_1 r_2\exp[i(\Phi-\theta)] + \exp(-i\theta)\right\}\Delta\tilde{n}(\mathbf{K},t-t_R). \quad (2.23b)$$

The factor $\tilde{b}(\boldsymbol{K},L,t)$ on the right-hand side of Eq. (2.23a) thus plays the role of a time-retarded source term since it is directly related to physical quantities of the previous transit, namely $\tilde{b}(\boldsymbol{K},L,t-t_R)$ and $\tilde{n}(\boldsymbol{K},t-t_R)$. By assuming the perturbations have the following time dependence:

$$\Delta\tilde{n}(\boldsymbol{K},t) = \eta\exp(\lambda t) + \eta^*\exp(\lambda^* t), \quad (2.24a)$$

$$\tilde{b}(\boldsymbol{K},L,t) = \epsilon\exp(\lambda t) + \mu^*\exp(\lambda^* t), \quad (2.24b)$$

extensive algebraic manipulation leads to the following characteristic equation [16]

$$(\tau\lambda + C)\left[\exp(\lambda t_R) - D\right]\left[\exp(\lambda t_R) - D^*\right] = (A+iB)\left[\exp(\lambda t_R) - D^*\right]E$$
$$+ (A - iB)\left[\exp(\lambda t_R) - D\right]E^*, \quad (2.25a)$$

where

$$A \equiv |F_0|^2(r_2^2 + r_1 r_2 \cos\Phi), \tag{2.25b}$$

$$B \equiv |F_0|^2 r_1 r_2 \sin\Phi, \tag{2.25c}$$

$$C \equiv 1 + l_D^2 K^2 + 2\chi L B, \tag{2.25d}$$

$$D \equiv r_1 r_2 \exp[i(\Phi - \theta)], \tag{2.25e}$$

$$E \equiv i\chi L \left[D + \exp(-i\theta)\right]. \tag{2.25f}$$

The solution of Eq. (2.25a) determines the instabilities in the FP cavity.

2.2.3 Static threshold curves

By setting $\lambda = 0$ and assuming that, at threshold, $|F_0|^2 \equiv I_{th}$, it can be shown that the static threshold instability spectrum is given by

$$\chi L I_{th} = \frac{\left[1 + r_1^2 r_2^2 - 2r_1 r_2 \cos(\Phi - \theta)\right](1 + l_D^2 K^2)}{2(1 + r_1^2) r_2^2 \sin\theta - 2r_1 r_2 (1 + r_2^2)\left[\sin\Phi + \sin(\Phi - \theta)\right]}. \tag{2.26}$$

This result is a direct generalization of the threshold condition for the SFM system, and it reduces to Eq. (2.16) in the limit that $r_1 \to 0$. In the absence of diffusion ($l_D = 0$), the spatial frequency bands share a common (global) minimum which can be seen in figure 2.5. This type of behaviour is reminiscent of the SFM system. Similarly, in the presence of finite diffusion ($l_D > 0$) the global-minimum characteristic disappears and a degree of frequency discrimination is introduced (see figure 2.6).

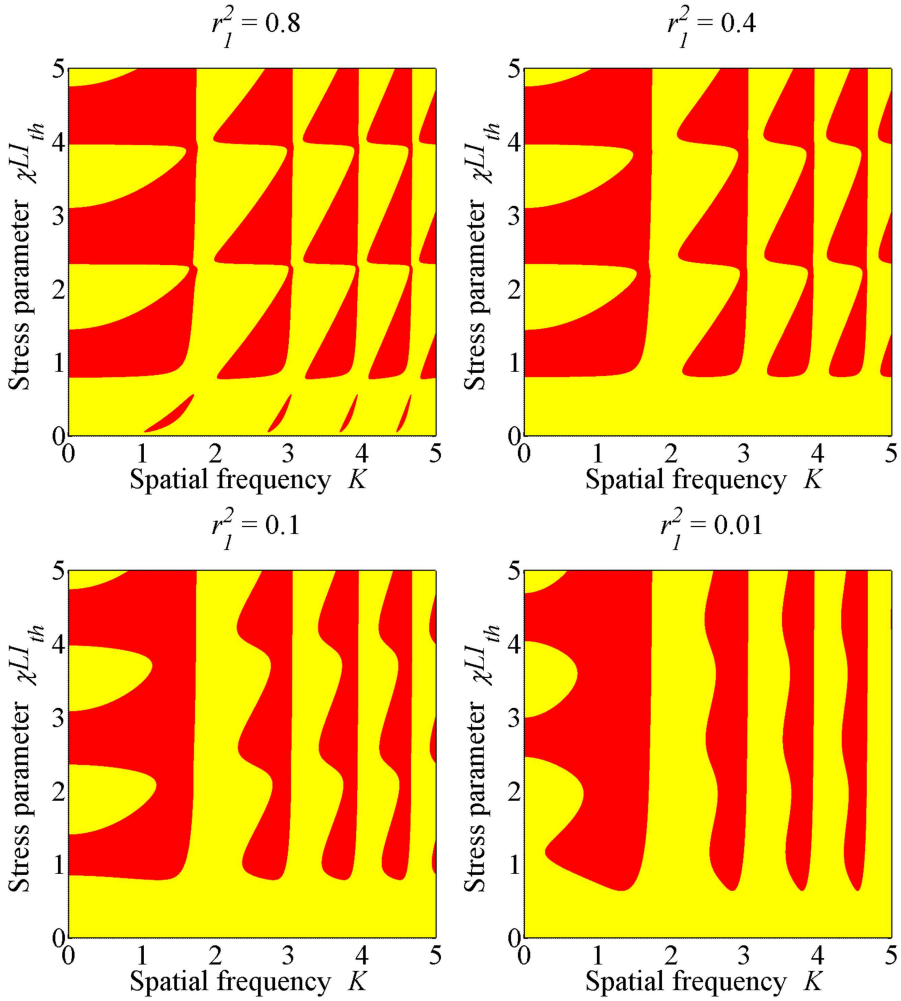

Figure 2.5: Static threshold instability curves for the FP cavity with no diffusion ($l_D = 0$) in a focusing medium ($\chi = +1$) when reflectivity coefficient r_1^2 is gradually increased, $r_2^2 = 0.9$, with a cavity mistuning of $\delta = \pi/4$, $d/k_0 = 1$, $\tau = 0$, and $L = 1$.

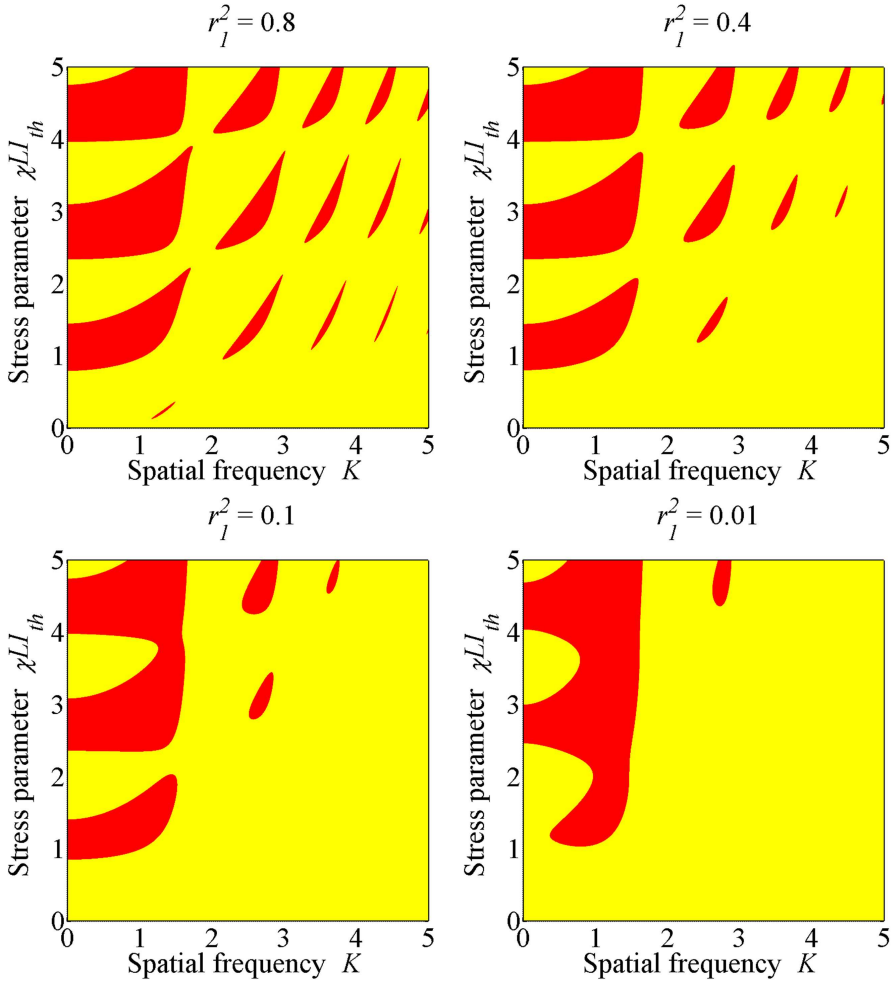

Figure 2.6: Static threshold instability curves for the FP cavity with finite diffusion ($l_D = 1$) in a focusing medium ($\chi = +1$) when reflectivity coefficient r_1^2 is gradually increased, $r_2^2 = 0.9$, with a cavity mistuning of $\delta = \pi/4$, $d/k_0 = 1$, $\tau = 0$, and $L = 1$.

A technique to check the consistency of the analysis, in part, is to obtain the values of the limit points within the stationary state and the $K = 0$ intersections with the χLI_{th}-axis from the threshold plot (see figure 2.7). These values should agree with one another after a scaling factor has been introduces. The regions where the first spectral band intersects the χLI_{th}-axis are associated with the negative-slope regions of the stationary solution, and one then expects to encounter Ikeda-type instabilities in these regions.

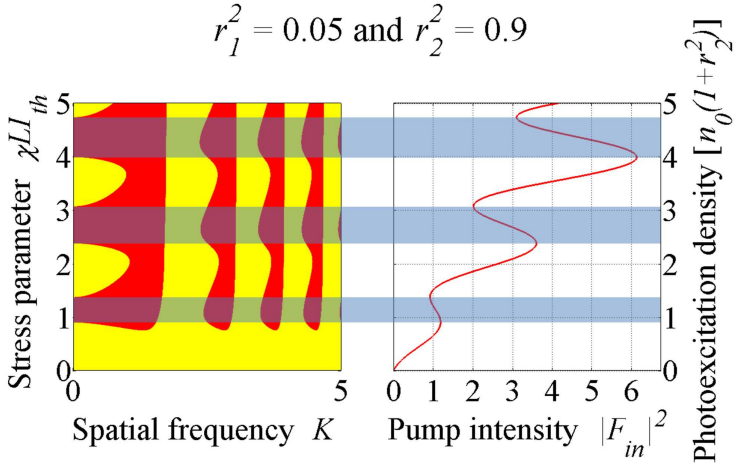

Figure 2.7: Static threshold curve compared to stationary state of the FP cavity where $r_1^2 = 0.05$ $r_2^2 = 0.9$ with a cavity mistuning of $\delta = \pi/4$, $l_d = 0$, $d/k_0 = 1$, $\tau = 0$, and $L = 1$.

2.2.4 Plane-wave dynamics

It is well documented that optical systems with bistability are capable of exhibiting chaotic behaviour [13, 17–20]. The FP cavity in particular has been found to embody such 'sensitive dependence on initial conditions' (where arbitrarily-small variations in the input of a system can have a dramatic impact on the long-term output). However, the thin-slice model (which may be regarded as a driven-damped nonlinear system) has not been anlayzed in the same context. In this section, the dynamical features of the plane-wave thin-slice FP cavity will be considered, and several tools deployed (time series, phase space portraits, bifurcation diagrams) to investigate the response of the system

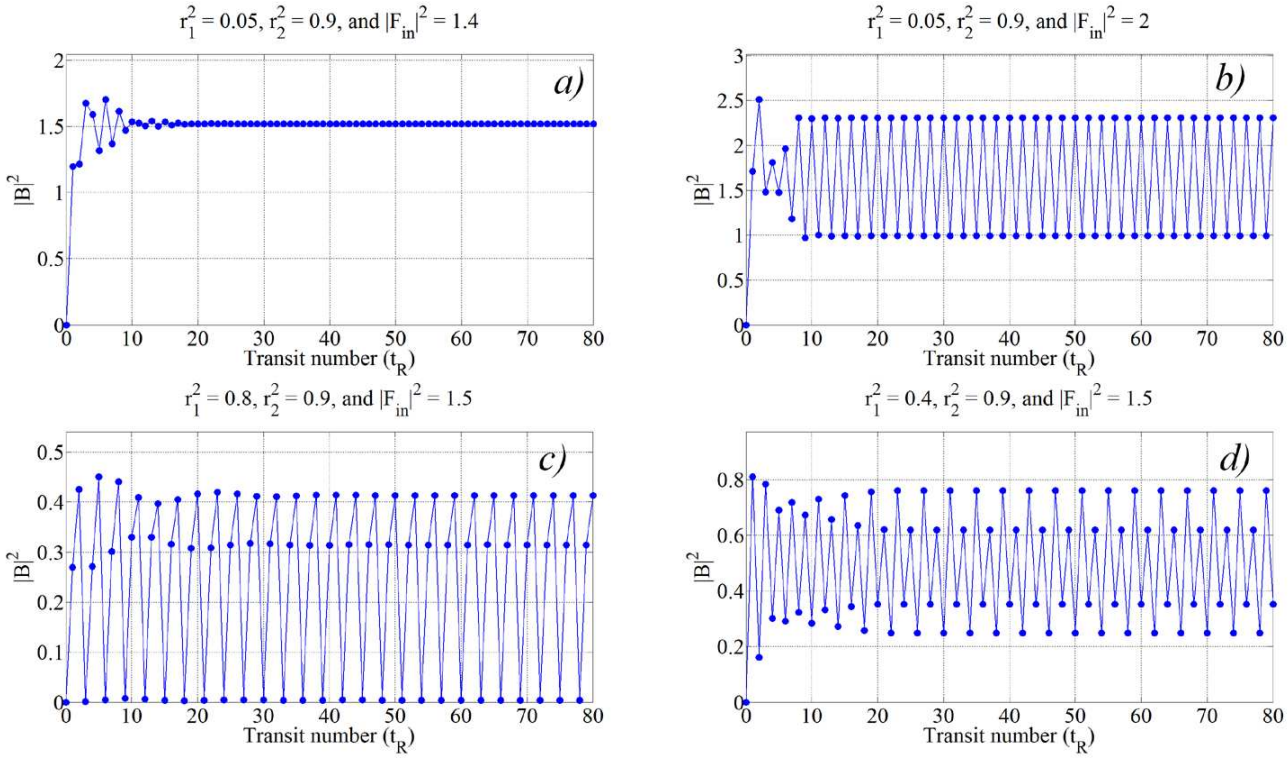

Figure 2.8: Time series plots of the Fabry-Pérot cavity. For *a*) $r_1^2 = 0.05$, $r_2^2 = 0.9$, $|F_{in}|^2 = 1.4$, for *b*) $r_1^2 = 0.05$, $r_2^2 = 0.9$, $|F_{in}|^2 = 2$, for *c*) $r_1^2 = 0.8$, $r_2^2 = 0.9$, $|F_{in}|^2 = 1.5$, and for *d*) $r_1^2 = 0.4$, $r_2^2 = 0.9$, $|F_{in}|^2 = 1.5$, where $\chi = +1$, $\delta = \pi/4$, $l_D = 0$, $\tau = 0$ and $L = 1$.

Firth has previously analysed the nonlinear FP system and discovered that Ikeda-type instabilities may occur within several different classes of cavity [13]. Figure 2.8 shows typical times series for the thin-slice model. The output typically undergoes short-lived transient

oscillations before tending toward and settling down onto an asymptotic periodic motion. We note, in passing, that the period-3 oscillation in figure 2.8(c) can be taken as a general signature that the system will be able to display chaotic behaviour in some parameter regimes [21].

Chaotic behaviour in the FP cavity is shown in Figure 2.9. To determine if the model is truly behaving chaotically, one might compare the time series from two simulations for identical parameters but where the initial conditions are slightly different. Figures 2.9(a) and 2.9(b) are certainly non-chaotic for weak slice feedback (as parametrized by r_1^2), and both trajectories reveal the same qualitative pattern in the long term (i.e., converging on a period-2 attractor). For stronger slice feedback, chaos is often found in the dynamics, for instance in Figs. 2.9(c) and 2.9(d). Figure 2.9 shows the behaviour of the cavity when starting from cold and using two pump intensities that differ by a small amount ε (in this case $\varepsilon = 10^{-4}$). The traces overlap for the first few transits before starting to diverge after around $t = 10t_R$. The long-term time series in those cases no longer resemble one another and the behaviour may thus be classified as "chaotic."

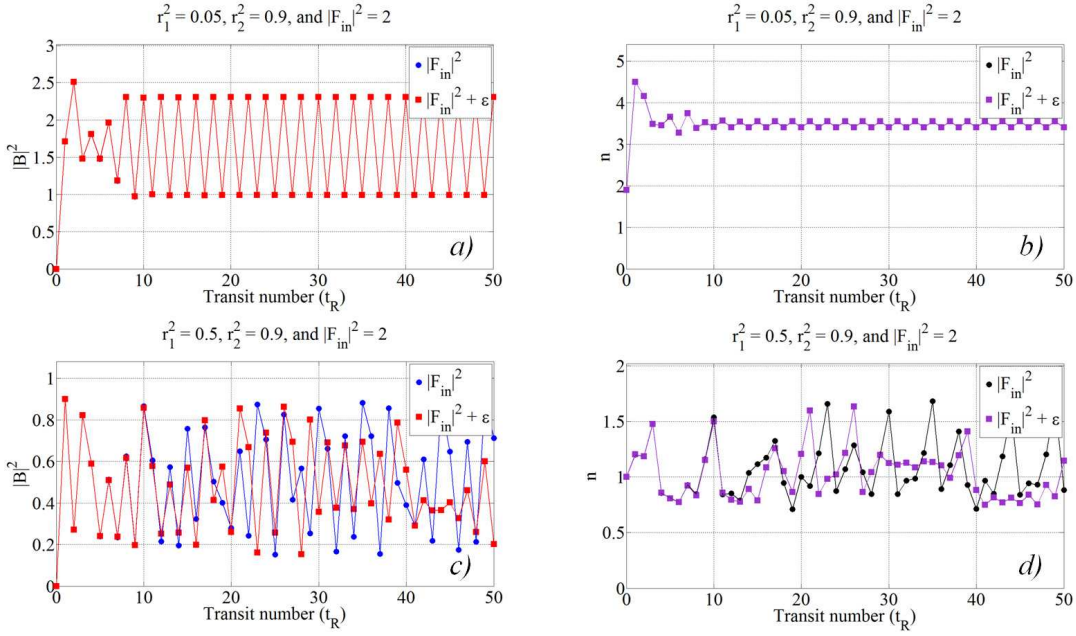

Figure 2.9: Comparing two time series plots in the Fabry-Pérot cavity with a input difference of $\varepsilon = 10^{-4}$, $r_2^2 = 0.9$, and $|F_{in}|^2 = 2$. Top row: $r_1^2 = 0.05$ and in the bottom row: $r_1^2 = 0.5$. Other parameters are: $\chi = +1$, $\delta = \pi/4$, $l_D = 0$, $\tau = 0$, and $L = 1$.

2.2.4.1 Phase Space

Phase space portraits provide a means of visualizing and classifying the long-term state of a system. Periodic trajectories in discrete models can be represented by a set of points in a phase space (e.g., period-1, period-2 and period-4 cycles are represented by 1, 2 and 4 'dots' in a plane, respectively). In contrast, chaotic trajectories may make sophisticated and exotic 'fractal dust' (see figure 2.10) patterns in phase space (suggesting an underlying order and regularity see figure 2.11), even though the time series may appear to be erratic. A more extensive set of phase-space portraits for the FP cavity is given in appendix E.

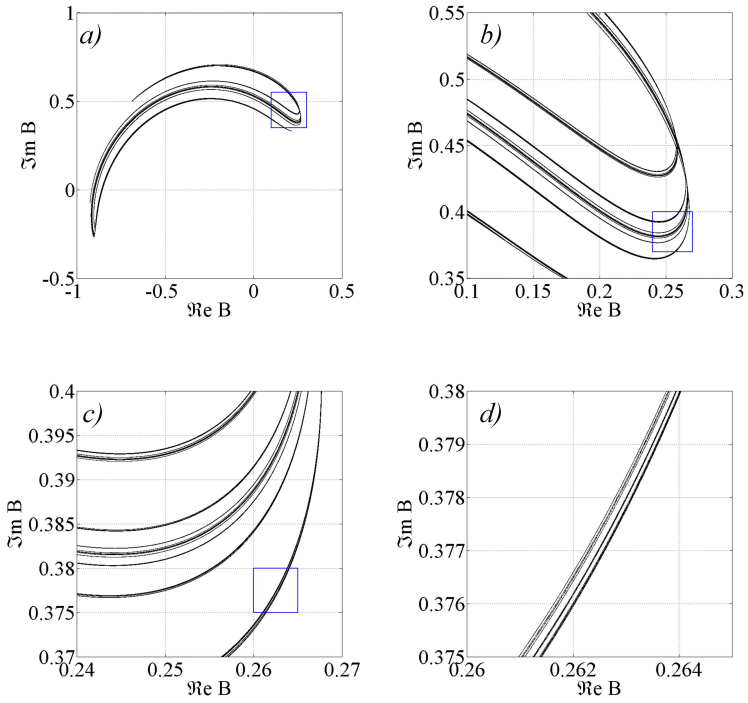

Figure 2.10: A phase space plot showing the fractal nature of the FP cavity when $r_1^2 = 0.5$, $r_2^2 = 0.9$, $|F_{in}|^2 = 2$, $\chi = +1$, $\delta = \pi/4$, $l_D = 0$, $\tau = 0$, and $L = 1$. This figure contains approximately 26 million points.

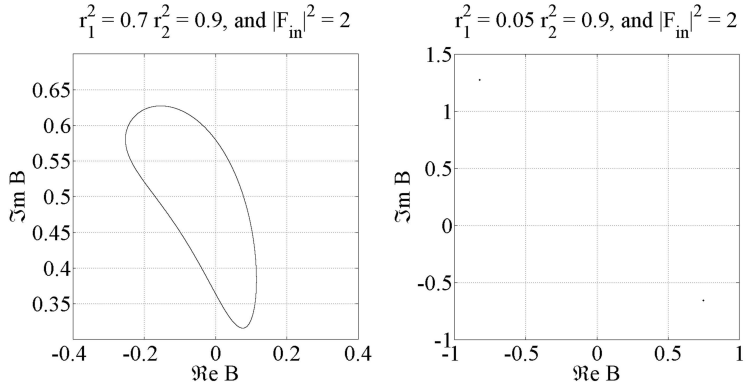

Figure 2.11: Phase space portraits of FP cavity showing alternative results other than fractal dust. Here r_1^2, r_2^2 and $|F_{in}|$ are defined above the relevant plots and $\chi = +1$, $\delta = \pi/4$, $l_D = 0$, $\tau = 0$, and $L = 1$.

2.2.4.2 Bifurcation

The global dynamics of the FP system are well captured by constructing a set of bifurcation diagrams with, for example, the pump intensity $|F_{in}|^2$ as the control parameter and the photoexcitation density n as the physical variable of interest. Figure 2.12 shows a typical bifurcation diagram for moderate slice feedback ($r_1^2 = 0.5$) and strong mirror feedback ($r_2^2 = 0.9$). Starting from 'cold' (an unexcited state with $F = B = n = 0$ at time-zero) and with $|F_{in}|^2 = 0$, the cavity tends to settle down onto period-1 oscillation until $|F_{in}|^2 \approx 1.43$, at which point we encounter the first period-doubling bifurcation [see Figure 2.12(a)]. Shortly after, there is a dramatic change in qualitative behaviour when the period-2 solution splits into many branches simultaneously [see figure 2.12(b)].

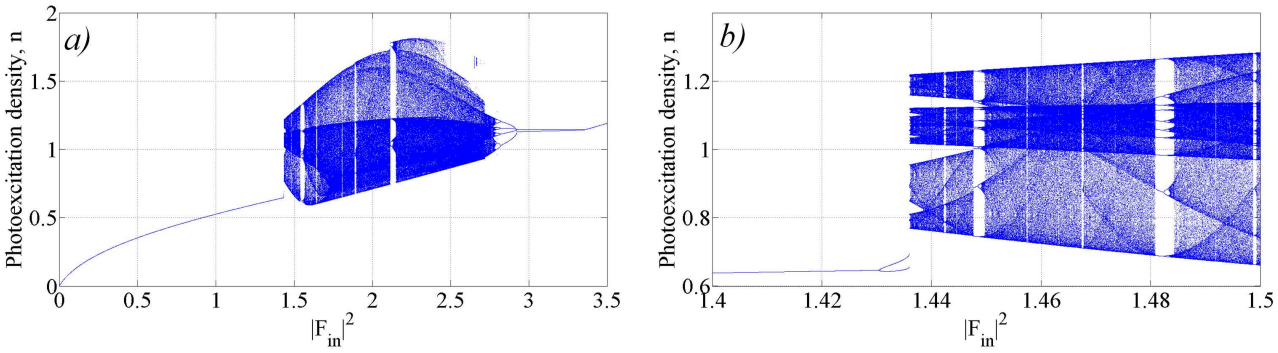

Figure 2.12: Bifurcation diagram of the FP cavity when $r_1^2 = 0.5$, $r_2^2 = 0.9$, $\chi = +1$, $\delta = \pi/4$, $l_D = 0$, $\tau = 0$, and $L = 1$. Pane *a*) shows the behaviour of the cavity as the pump intensity is increased from $0 < |F_{in}|^2 \leq 3.5$, while pane *b*) is a magnification of the system entering chaotic regime ($1.4 < |F_{in}|^2 \leq 1.5$).

Figure 2.12 may at first suggest that high intensities (e.g., $|F_{in}^2| \geq 3$) can be associated with the cavity having a long-term behaviour that is non-chaotic. Such a conclusion is not supported by a wider set of simulation results. Appendix E contains an extensive selection of bifurcation diagrams from across a range of parameter space, wherein it can be seen that higher intensities are not necessarily associated with the predicted stationary-state solution (i.e., Ikeda-type instabilities remain prevalent at high intensities [22]).

A modified approach to constructing a more subtle type of bifurcation diagram is to initialize the cavity on one of the branches of the stationary solution (see Figure 2.13), and then track the long-term state of the system (in this approach, the system has a different initial condition for each value of pump intensity $|F_{in}|^2$). States lying on branches that have a positive slope are expected to be stable [22, 23] while those on negative-slope branches are unstable.

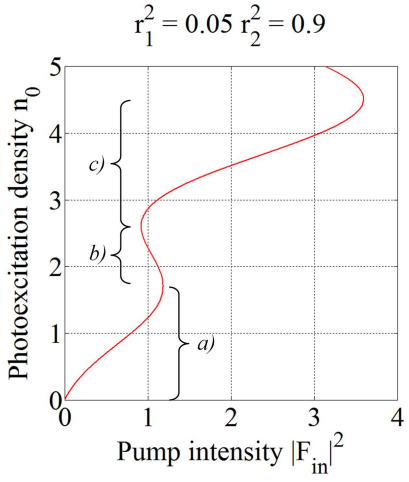

Figure 2.13: A diagram indicating the different branches of the stationary state.

For moderate slice feedback (e.g., $r_1^2 = 0.5$), the cavity tends to remain on the lower branch if it is initialized on that branch [see Fig. 2.14(a)].

As mentioned in Sec. 2.2.3, the negative-slope regions of the stationary-state curve coincide with the $K = 0$ intersections of the Turing threshold plot. Initializing the cavity on the middle branch does not necessarily suggest that there will be an immediately-apparent Ikeda-type instability present, and such longer-term stability can be seen in figure 2.14 *b*). However, in the case of this parameter regime and when initializing on the middle branch [see Fig. 2.14(b)], a preliminary inspection suggests that the system will naturally converge on a period-3 attractor. Closer inspection reveals that the perceived "period-3 oscillation" is nothing of the kind; numerical investigations show that it is, in reality, a very finely-spaced sequence of period-1 and period-2 attractors [c.f., Fig. 2.15(a)] which, when viewed at sufficiently high resolution, gives the impression of a period-3 pattern. Initialization on the upper branch can result in a similar phenomenon as one approaches a period-doubling bifurcation cascade [see figures 2.14(c) and 2.15(b)].

It should be noted that for a given value of $|F_{in}|^2$ there can be multiple values of n_0 that satisfy the stationary-state solution. Here, we have selected particular values of n_0 and then calculated the corresponding $|F_{in}|^2$ values so the cavity can be initialized more readily on any particular branch of the stationary-state curve (since each n_0 is associated with a *unique* $|F_{in}^2|$). For example, defining n_0 to be in the range $0 < n_0 < 1.7$ ensures the cavity will be on the lower

branch (see figure 2.13 *a*)).

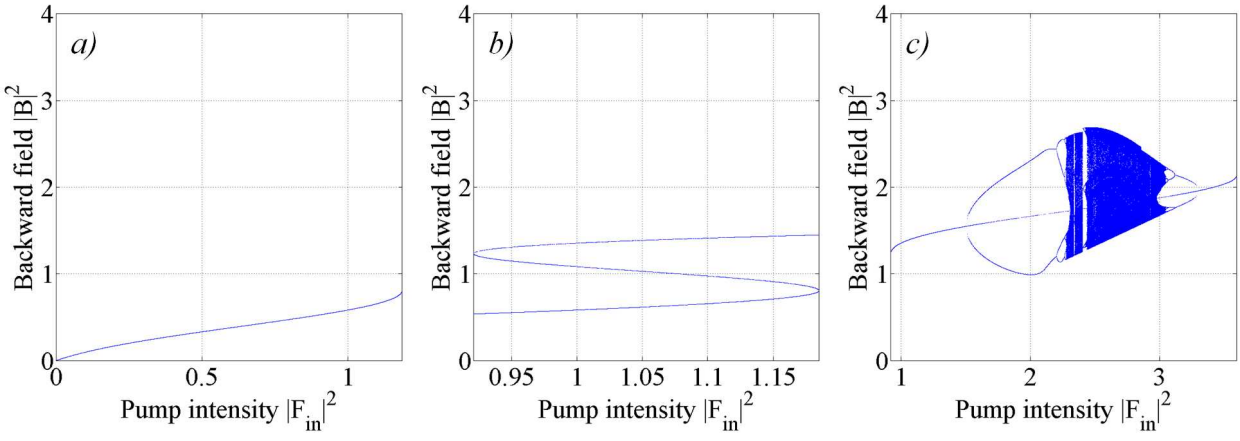

Figure 2.14: Bifurcation diagrams of the FP cavity when initialized on the stationary state curve for $r_1^2 = 0.05$, $r_2^2 = 0.9$, $\delta = \pi/4$, $l_D = 0$, $\tau = 0$, $\chi = +1$, and $L = 1$. Plot a) has been initialized with the values of n_0 to lie within $0 < n_0 < 1.7$,. Plot b) has been initialized with the values of n_0 to lie within $1.7 < n_0 < 2.6$. Plot c) has been initialized with the values of n_0 to lie within $2.6 < n_0 < 4.5$.

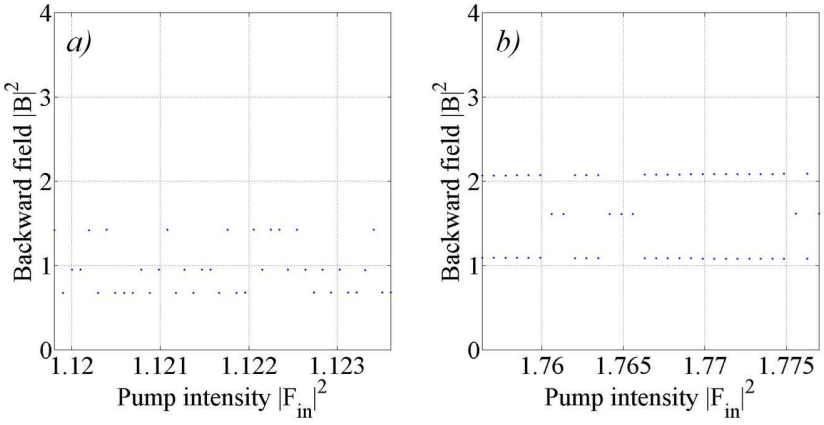

Figure 2.15: A low resolution bifurcation diagram showing the unique properties of the FP cavity when $r_1^2 = 0.05$, $r_2^2 = 0.9$, $\delta = \pi/4$, $l_D = 0$, $\tau = 0$, $\chi = +1$, and $L = 1$. Here plot a) has been initialized with the values of n_0 to lie within $2.00 < n_0 < 2.01$ (middle branch), and plot b) has been initialized with the values of n_0 to lie within $3.4 < n_0 < 3.41$ (upper branch).

2.2.4.3 Critical slowing

Critical slowing is a phenomenon associated with the response time of a nonlinear system that is being driven close to one of its critical points. It is an effect whereby the switching time (i.e., the time to make the transition between stable branches) diverges algebraically [24]. Two such points in the FP cavity are the up-switching and down-switching points, as indicated in figure 2.16. The characteristic "S" shape of the stationary state curve is indicative of bistablity – there exists a band of input intensities where the cavity may have two stable outputs for a given input (recall that the middle branch is always unstable – any attempt to excite states on this branch will usually result in a jump to either the upper or lower branch). The bistability of the FP cavity is well-documented [23, 25–32], and we do not discuss it further here.

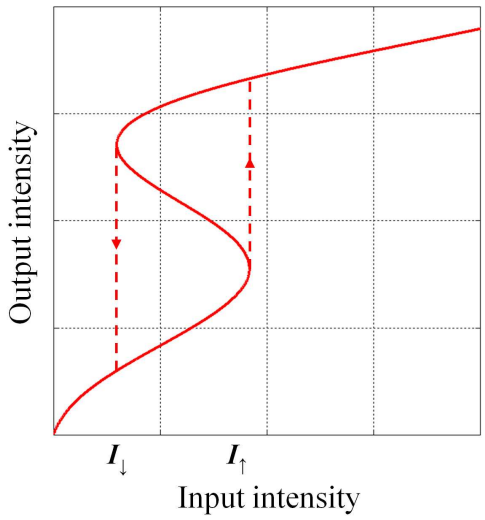

Figure 2.16: A diagram indicating the location of the switching points within the stationary state.

Critical slowing occurs when the pump intensity is close to a switching point ($I_\uparrow$ or $I_\downarrow$). For example, as $|F_{in}|^2 \rightarrow I_\uparrow$, the time take for the system to settle down onto the upper branch tends to increase dramatically for small changes in $|F_{in}|^2$. The divergence in the response time for a system with weak slice feedback is shown in figure 2.17.

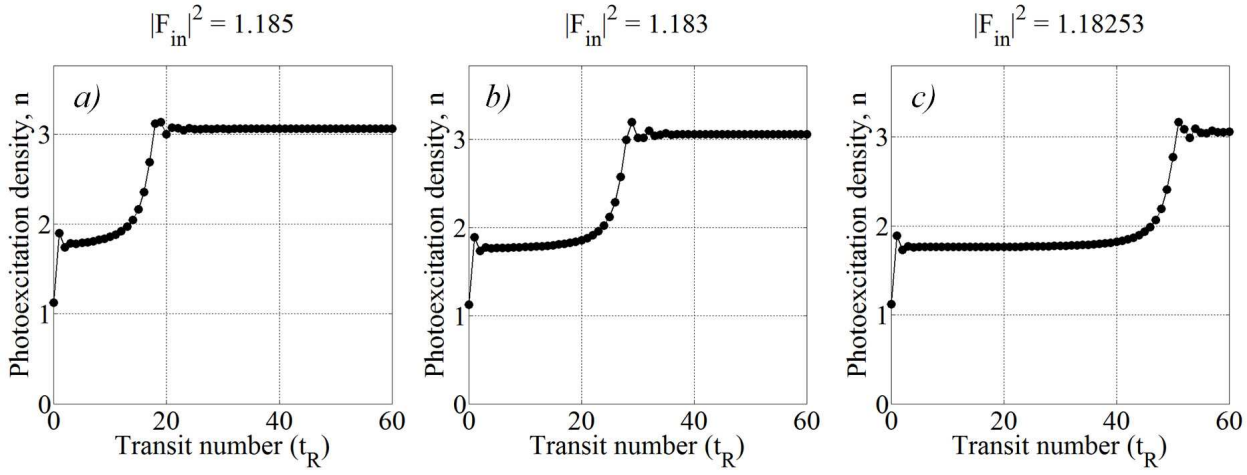

Figure 2.17: Response time of the FP cavity when $r_1^2 = 0.05$, $r_2^2 = 0.9$, $\delta = \pi/4$, $\chi = +1$, $l_D = 0$, $\tau = 0$, $L = 1$, and the corresponding values of $|F_{in}|^2$ are defined above the relevant plots.

2.2.5 Helmholtz diffraction and spatial filtering

Diffraction (an amplitude modulation in real space) is equivalent to a phase shift in Fourier space. With this in mind, boundary condition (2.17b) can be written as

$$\tilde{B}(\mathbf{K}, L, t) = r_2 \exp\left[-i\theta(K^2)\right] \tilde{F}(\mathbf{K}, L, t - t_R), \tag{2.27a}$$

$$\theta(K^2) = \frac{d}{k_0} K^2. \tag{2.27b}$$

The simulations of Huang and McDonald [8] placed a spatial filtering element in the free-space path which allowed control of the highest spatial frequency K_C that can propagate in the system. Such filtering can be implementing computationally by assuming Helmholtz (rather than paraxial) diffraction [33], whereby

$$\theta(K^2) = \left(\frac{2d}{k_0}\right) \frac{K^2}{1 + \sqrt{1 - K^2/K_C^2}}. \tag{2.28}$$

The use of the Helmholtz diffraction operator allows for a more accurate handling of high spatial frequencies. Here, K_C plays the role of a high-frequency cut-off so that portions of the spectrum with $K > K_C$ are attenuated. When $K_C = k_0$ and $K/k_0 \ll O(1)$, recovers the paraxial phase factor of Eq. (2.27b).

It is crucial that the numerical grid be configured correctly, so that simulated results are reasonable, accurate, and unambiguous. To that end, we define the real-space and Fourier domains such that k_0 is less than half the maximum K on the grid. This prevents the occurrence of ghosting, where undersampling high spatial frequencies masquerade as low frequencies and corrupt the integrity of the numerical solution.

2.2.6 Pattern formation with one transverse dimension

The numerical analyses of the FP system within this section are presented in the limit of a local [i.e., instantaneous ($\tau = 0$) and non-diffusing ($l_D = 0$)] Kerr-type response. The selection of results illustrates simple static pattern formation process with a single transverse dimension ($\nabla_\perp^2 \to \partial^2/\partial x^2$), and details are given about the general computational approach.

The transverse domain x is configured so that it can accommodate an integer number of most-unstable-wavelengths. This choice allows the most unstable spatial frequency to grow without 'feeling' the effect of transverse periodic boundaries (see figure 2.18). Helmholtz diffraction in the free-space path is implemented using fast Fourier transforms (FFTs) as described in Sec. 2.2.5. To illustrate simple pattern formation, the cut-off frequency K_C is set so that only those waves within the first instability band are free to propagate in the system (waves with $K > K_C$ are attenuated). The perturbed uniform state (2.19) is then initialized with a small level of (Gaussian-filtered) complex noise, and the following algorithm is implemented in a MATLAB code:

1. Initialize a uniform state of the system (plus a small level of noise).
2. Calculate the forward field at the output face of the slice (a phase modulation).
3. Calculate the backward field at the output face of the slice (FFT/IFFT pair).
4. Recalculate the photoexcitation density.
5. Apply the boundary condition.
6. Repeat steps 2-5 until the number of required transits has been reached.

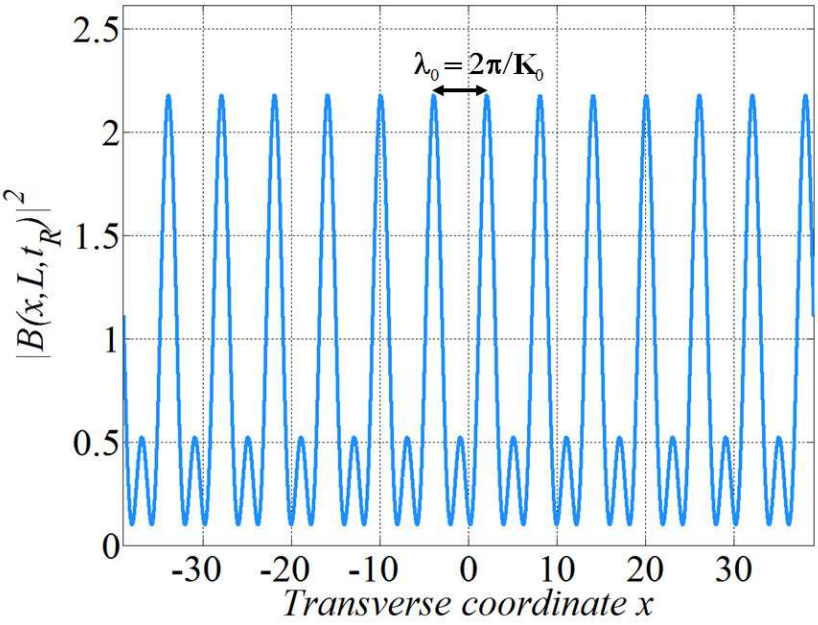

Figure 2.18: The time-asymptotic ($t = 512t_R$) static pattern that emerges in the FP system where $r_1^2 = 0.01$, $r_2^2 = 0.9$, $I_0 = 0.773$, $K_0 = 1.3146$, $K_C = 1.715$, $l_D = 0$, $\tau = 0$, $\chi L = +1$, $\delta = \pi/4$, and $d/k_0 = 1$.

During the early stages of the pattern formation process, all the spatial frequencies in the system (which are present due to the addition of noise) compete with each other through nonlinear interactions. However, the most unstable frequency K_0 eventually dominates since it has the lowest threshold and, hence, the highest growth rate. The system thus exhibits *winner takes all* dynamics (see figure 2.18), whereby a single spatial frequency takes over the pattern (though weaker harmonics are also present). Note that noise is added merely to accelerate pattern emergence in regimes where instability already exists. Without noise, patterns would still appear (with finite numerical accuracy providing the symmetry-breaking perturbation) but only after maybe hundreds of thousands of transits.

An example is shown in figure 2.19, where the system has been initialized at threshold. After approximately $100t_R$, a finite-amplitude pattern starts growing spontaneously on top of the noisy plane wave solution. The pattern is classified as 'static' because, once established, it does not change in time. More simulations are shown in figure 2.21, going progressively further above threshold.

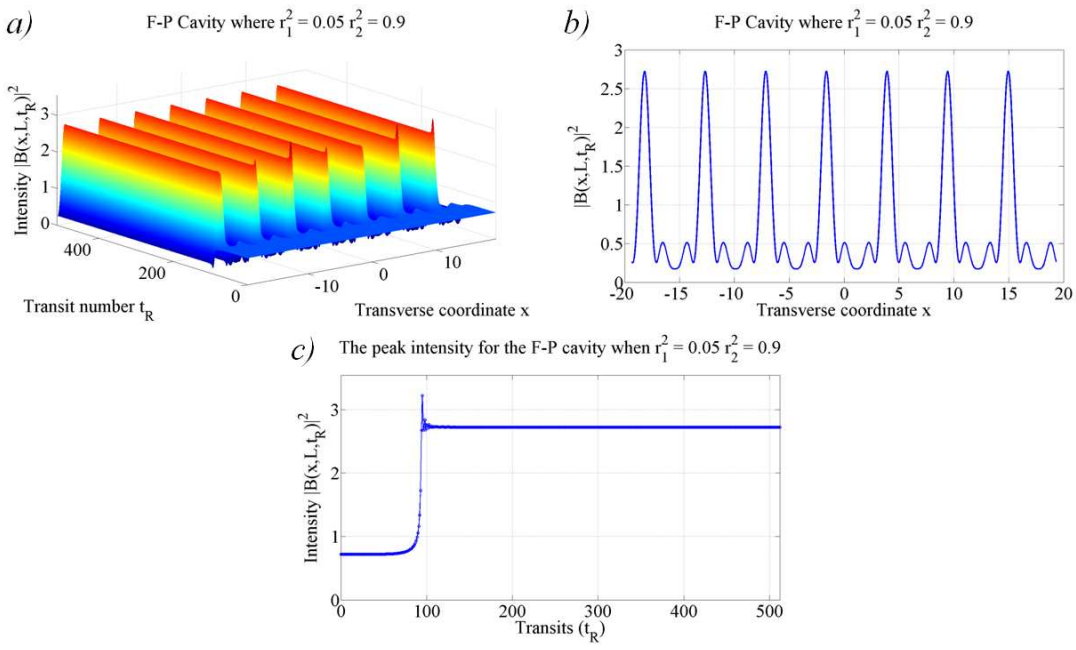

Figure 2.19: Spontaneous static pattern formation in the FP cavity driven at threshold: (a) evolution of the transverse intensity pattern, (b) the output field of the simulation, and (c) the evolution of the peak intensity. Parameters are $r_1^2 = 0.05$, $r_2^2 = 0.9$, $I_0 = 0.9057$, $K_0 = 1.2875$, $K_C = 1.663$, $l_D = 0$, $\tau = 0$, $\chi L = +1$, $\delta = \pi/4$, and $d/k_0 = 1$.

It should be noted that the value of r_1^2 was chosen to be much less than unity as a result of inspecting the threshold curves. The base of the first instability band becomes flatter as r_1^2 increases. However, when $r_1^2 \ll 1$ the band contains a well-defined minimum making it possible to find a meaningful value for K_0. Additionally, when r_2^2 is also varied, one can find parameters where an island develops within the threshold. From this island, values for K_0, and I_{th} can be obtained that accommodate for pattern formation parameters regimes other than $r_1^2 \ll 1$, an example of this can be seen in figure 2.20.

Figure 2.21 demonstrates the effect of increasing the intensity of the pump field. As the field is increased, the cavity becomes more stressed. The static patterns produced from the FP cavity in figure 2.21 are qualitatively similar to those produced in the SFM system [34]. However, at higher pump intensity (e.g. 50% above threshold) the patterns in the FP cavity can potentially break down creating a non-periodic structure.

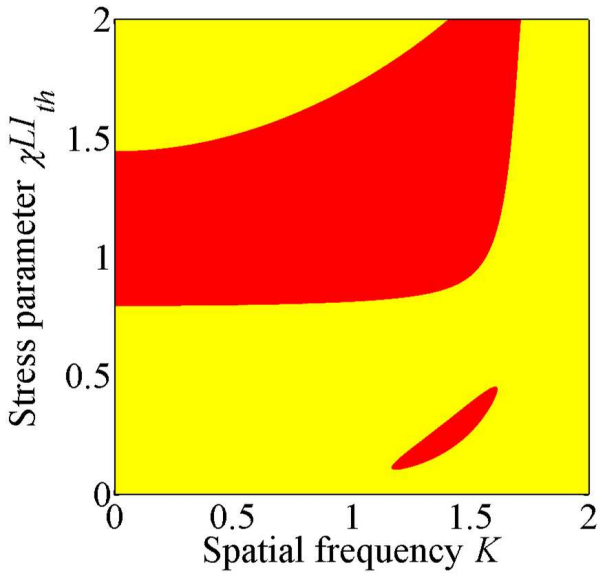

Figure 2.20: Threshold spectrum indicating the presence of a island when $r_1^2 = 0.6$,$r_2^2 = 0.9$, $\delta = \pi/4$, $l_d = 0$, $d/k_0 = 1$, $\tau = 0$, and $L = 1$.

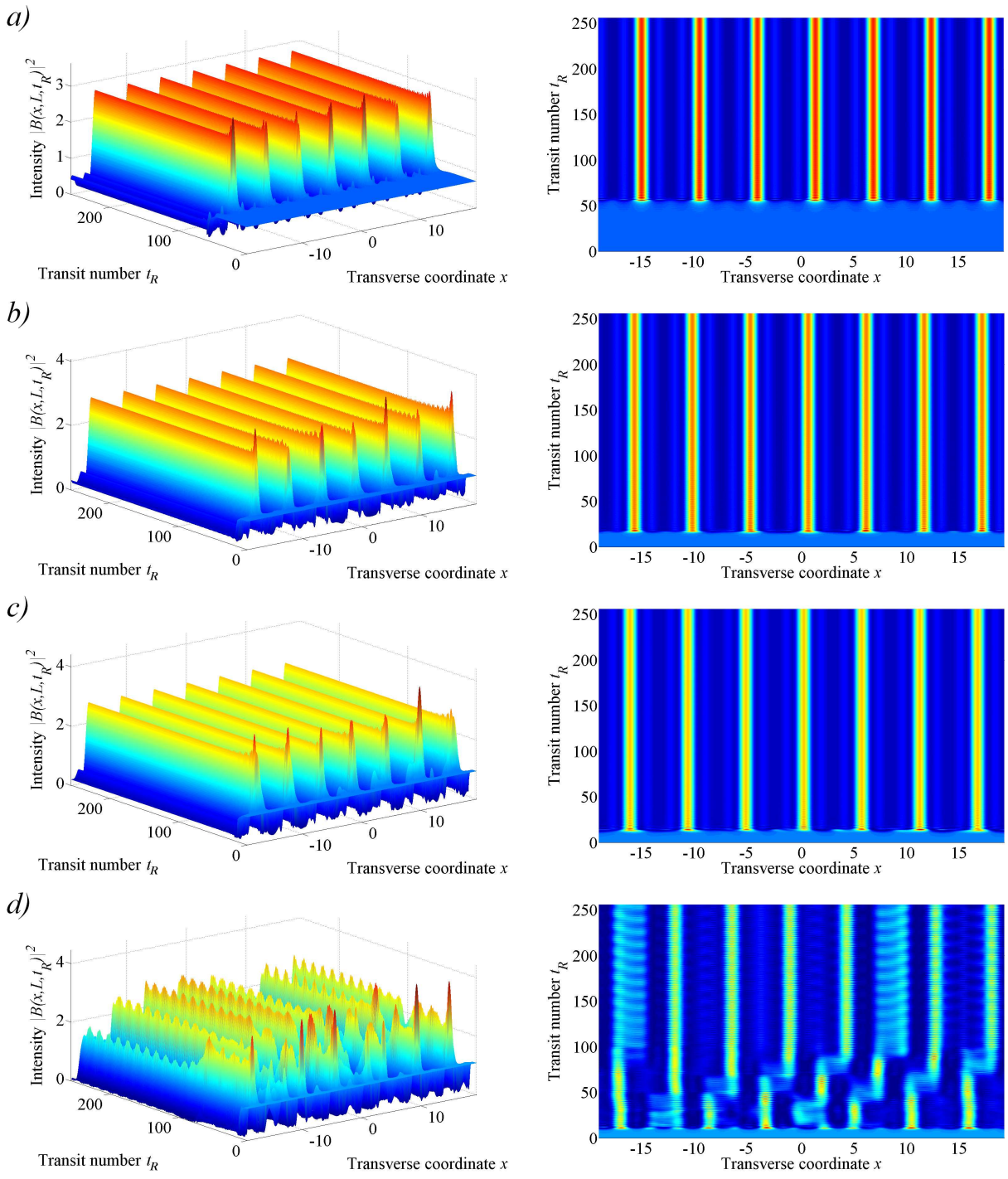

Figure 2.21: Spontaneous static pattern formation in the FP cavity when operating at *a)* 10%,*b)* 30%, *c)* 40%, and *d)* 50% above threshold. Parameters are $r_1^2 = 0.05$, and $r_2^2 = 0.9$., $K_0 = 1.2875$, $K_C = 1.663$, $l_D = 0$, $\tau = 0$, $\chi L = +1$, $\delta = \pi/4$, $d/k_0 = 1$, and the intensity threshold is $I_{th} = 0.75476$.

Fractal patterns in one transverse dimension

Simulations have also been preformed to observe the transition from a simple pattern to a *fractal*. This is achieved by simulating a filtered cavity until a simple pattern has been formed, then adjusting the filter to allow more spatial frequencies to circulate. The resulting simulations can be seen in figure 2.22. Figure 2.22 *a)* shows the pattern generated by the cavity using the same technique in the previous simulations. However, figure 2.22 *b)* shows the first transit after the filter is adjusted. The system is starting to generate a more complex pattern while the following transit produces an even more complex pattern. It should be noted that the power spectrum, in this thesis, has been defined to be the Fourier transform of the intensity of B.

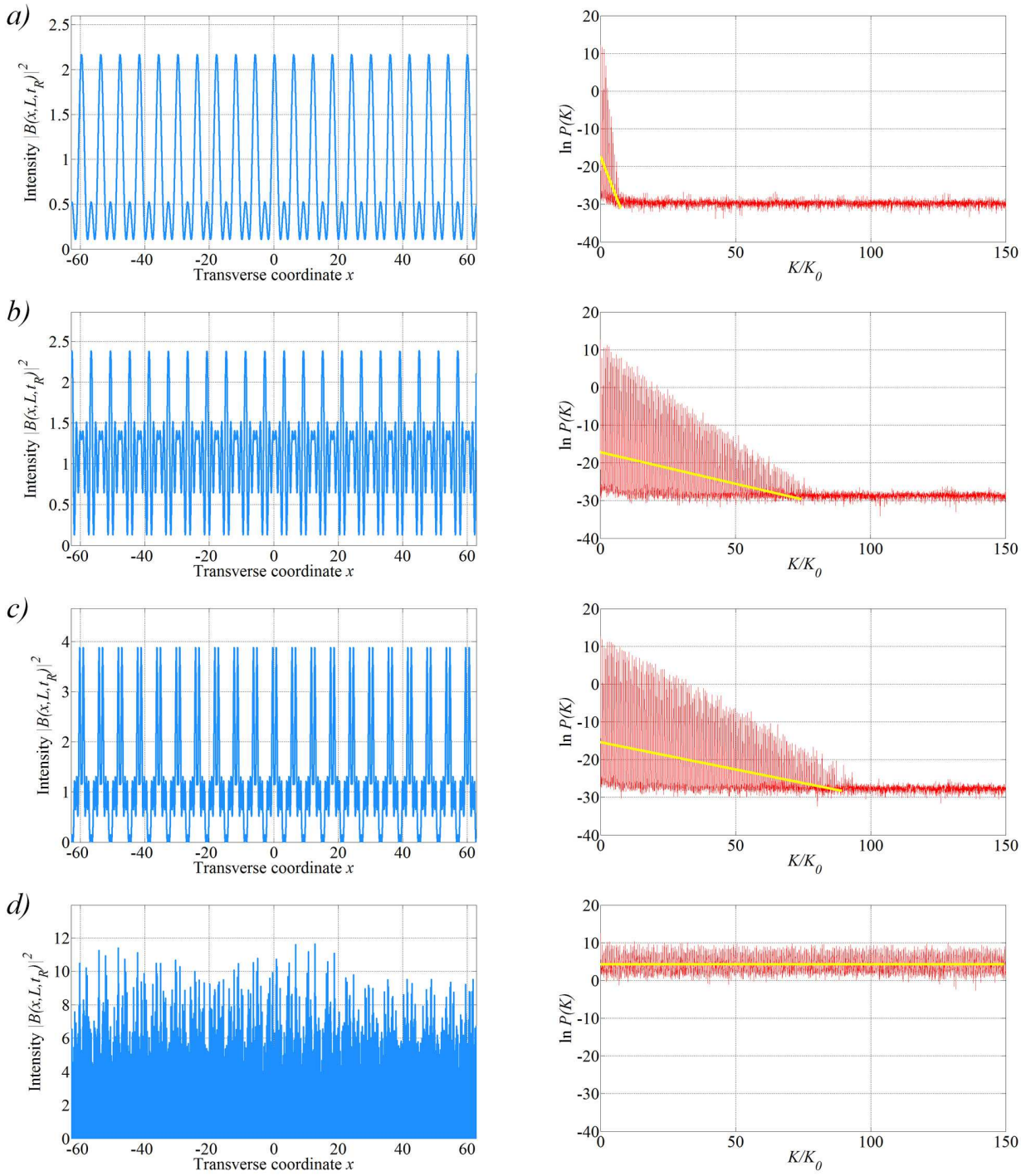

Figure 2.22: The pattern formation,and power spectrum of of the FP cavity. Parameters are $r_1^2 = 0.05$, $r_2^2 = 0.9$, $I_0 = 0.898$, $K_0 = 1.2875$, $K_C = 1.663$, $l_D = 0$, $\tau = 0$, $\chi L = +1$, $\delta = \pi/4$, $d/k_0 = 1$, and *a)* $512t_R$ (filtered), *b)* $513t_R$ (unfiltered), *c)* $514t_R$ (unfiltered), and *d)* $522t_R$ (unfiltered).

The following results deploy the roughness-length method to estimate the fractal dimension of the backwards intensity. The system parameters are $r_1^2 = 0.05$, $r_2^2 = 0.9$, $I_{th} = 0.89809$, $K_0 = 1.2875$ and $K_C = 1.663$ while the numerical grid contains 2^{18} (262144) points in the x domain (accommodating 64 most-unstable wavelengths). The plots shown in figure 2.23 correspond to the patterns in figure 2.22. Furthermore, figure 2.23 *a)* is the result from the established simple pattern which has an estimated fractal dimension of $D_{RL} = 0.381$. The following figures *b*), *c*), and *d*) show the progression of the first stages of the transition from a simple pattern to a fractal. The dimension for these transits are $D_{RL} = 0.777$, $D_{RL} = 0.994$, and $D_{RL} = 1.311$ respectively. A consequence of implementing algorithms to estimate fractal dimension can lead to predictions outside of the accepted range i.e. $1 < D \leqslant 2$. To accommodate this, when D has been found to be less that one is it appropriate to set $D = 1$. Similarly when D has been estimated to be greater than two, we set $D = 2$.

Figure 2.23 shows the results from roughness-length calculation for the initial stages of the transition towards a fractal pattern. The distinct features of these figures are identified by two regions a positive gradient and a plateau. With increasing number of transits the plateau steadily becomes the more dominate feature within the plot. Figure 2.24 displays the result from the roughness-length method with an estimated fractal dimension of $D_{RL} = 1.988$.

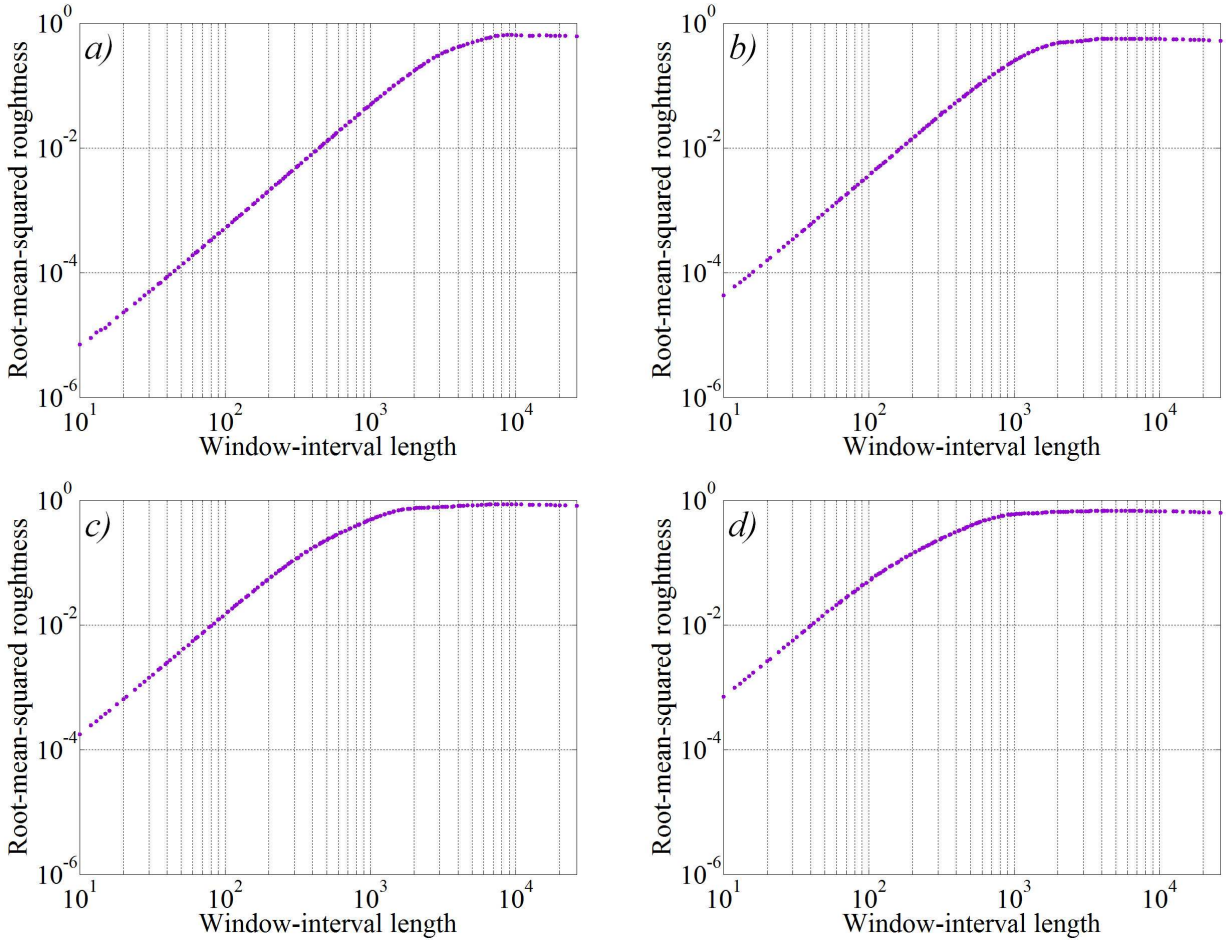

Figure 2.23: Roughness length plots for the FP cavity. Parameters are $r_1^2 = 0.05$, $r_2^2 = 0.9$, $I_0 = 0.898$, $K_0 = 1.2875$, $K_C = 1.663$, $l_D = 0$, $\tau = 0$, $\chi L = +1$, $\delta = \pi/4$, and $d/k_0 = 1$. Here, *a*) established pattern (filtered), *b*) $+1t_R$ (unfiltered), *c*) $+2t_R$ (unfiltered), and *c*) $+3t_R$ (unfiltered).

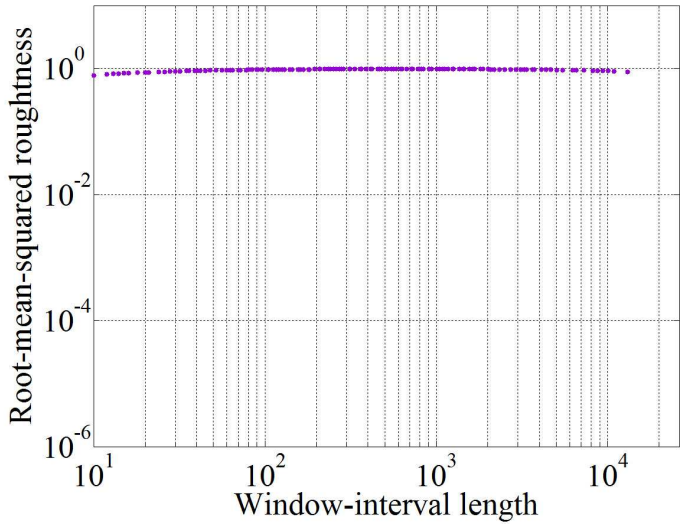

Figure 2.24: Roughness-length plot for the system after an additional 18 unfiltered transits. Parameters are $r_1^2 = 0.05$, $r_2^2 = 0.9$, $I_0 = 0.898$, $K_0 = 1.2875$, $K_C = 1.663$, $l_D = 0$, $\tau = 0$, $\chi L = +1$, $\delta = \pi/4$, and $d/k_0 = 1$.

Moreover, there are additional method available to calculate the estimated fractal dimension of the cavity [35]. The subsequent figure details each of the methods available with the calculated fractal dimension against the transit for each of these methods. Here $t_R = 0$ is defining the established simple pattern formation with the parameter described above.

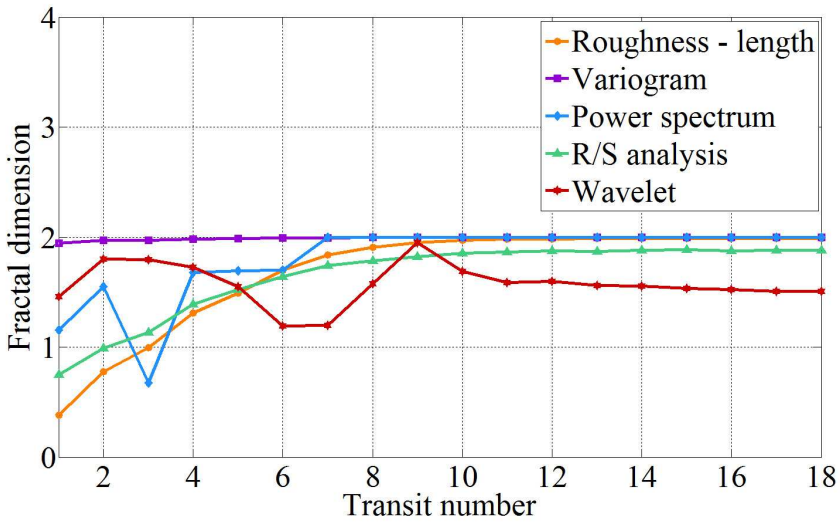

Figure 2.25: Fractal dimension of the cavity with progressing transits. Parameters are $r_1^2 = 0.05$, $r_2^2 = 0.9$, $I_0 = 0.8981$, $K_0 = 1.2875$, $K_C = 1.663$, $l_D = 0$, $\tau = 0$, $\chi L = +1$, $\delta = \pi/4$, and $d/k_0 = 1$. With 2^{18} points in the x-domain.

From the brief analysis of the different algorithms available to estimate the fractal dimension, the roughness-length method appears to be the most reliable for this type of system. Additionally, roughness-length has the smoothest curve, in figure 2.25, transitioning from a nonfractal pattern to a fractal pattern.

2.2.6.1 Pattern formation in a defocusing medium

Attention is now turned to the self-defocusing nonlinearity ($\chi L = -1$) with a range of Turing threshold spectra shown in figure 2.26

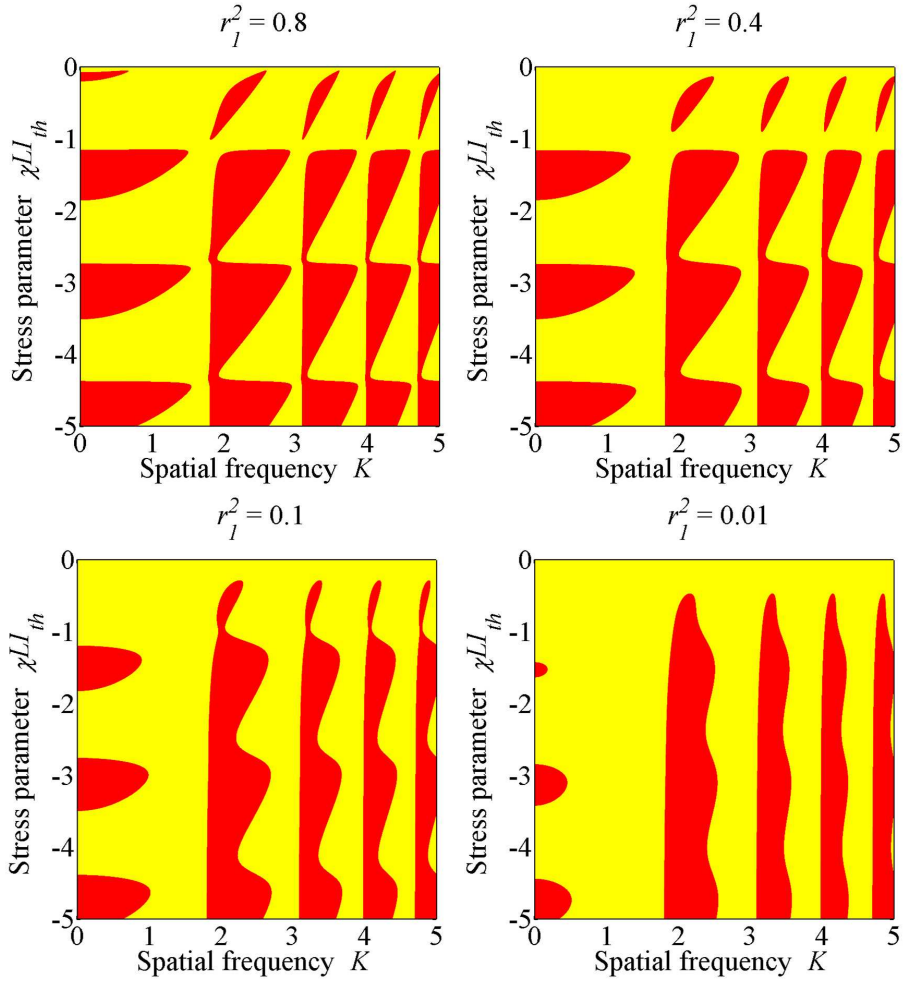

Figure 2.26: Static threshold instability curves for the FP cavity with no diffusion ($l_D = 0$) in a defocusing medium ($\chi = -1$) when reflectivity coefficient r_1^2 is gradually increased, $r_2^2 = 0.9$, with a cavity mistuning of $\delta = \pi/4$, $l_d = 0$, $d/k_0 = 1$, $\tau = 0$, and $L = 1$.

Figure 2.27 shows the transition from simple pattern to fractal with a defocusing medium alongside the corresponding roughness-length calculations from BENOIT. Comparing with the focusing medium, there are two clear differences. Firstly, the transition towards a fractal is much slower. Figure 2.25 reveals that $D_{RL} \simeq 2$ is reached within around 12 transits after the filter is adjusted, while the defocusing system reaches the same level of fractality after around 175 transits (more akin to the dynamics of the SFM model). The slower transition from simple

pattern to fractal could be a consequence of using a lower pump intensity (we note, in passing, that the only fair way to establish which nonlinearity accommodates *faster* fractal formation is to compare simulations for the two cases when operating at the same fraction above threshold). The relevant parameters (I_0, K_0, and K_C) where obtained from appropriate threshold plots calculated from Eq. 2.26. Furthermore, the defocusing FP cavity generates area-filling patterns that are qualitatively identical to those in both the SFM [8] and ring cavity geometries [9, 10, 34].

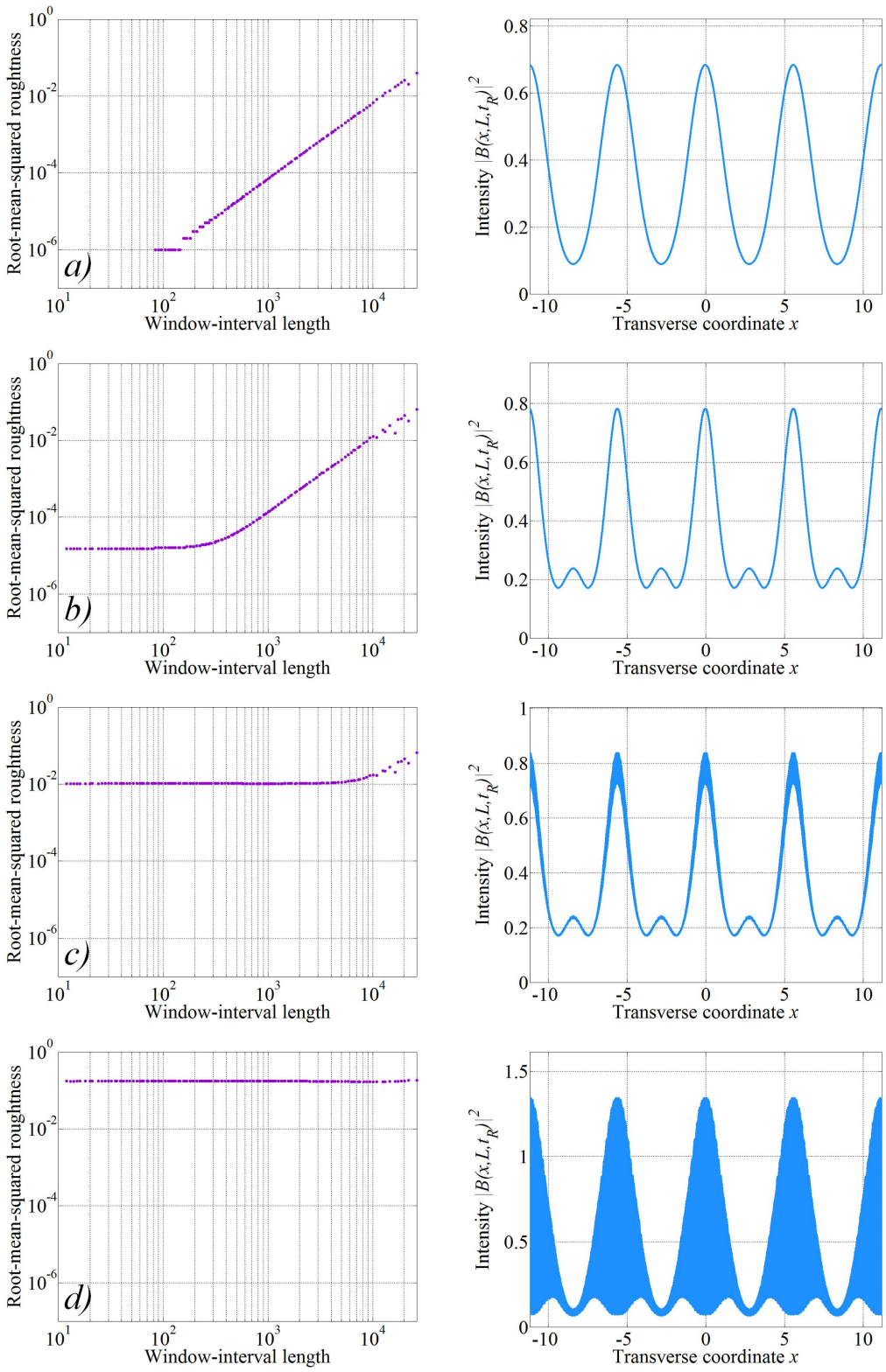

Figure 2.27: Transition from simple pattern to fractal dimension in the FP cavity with a defocusing medium where *a*) initialized pattern (filtered), *b*) $+140t_R$ (unfiltered), *c*) $+170t_R$ (unfiltered), and *d*) $200t_R$ (unfiltered). Parameters are $r_1^2 = 0.1$, $r_2^2 = 0.9$, $I_0 = 0.45$, $K_0 = 2.25$, $K_C = 1.5$, $l_D = 0$, $\tau = 0$, $\chi L = -1$, $\delta = \pi/4$, and $d/k_0 = 1$.

Figure 2.28 shows the progression of the calculated roughness-length dimension (obtained from BENOIT [35]) in the defocusing FP cavity as a function of transit number. It can be seen that even an instantaneous nonlinearity can exhibit a somewhat sluggish response in the sense of growth at high-K. For instance, approximately 125 transits are required for small-scale structures to begin developing appreciably, and a further 75 transits in order to reach a dimension of $D_{RL} \simeq 2$. The small-scale region refers to the estimated dimension associated with the initial slope of the log-log spectrum, whereas the large-scale relates to the estimated dimension of the plateau produced at the larger window-interval lengths.

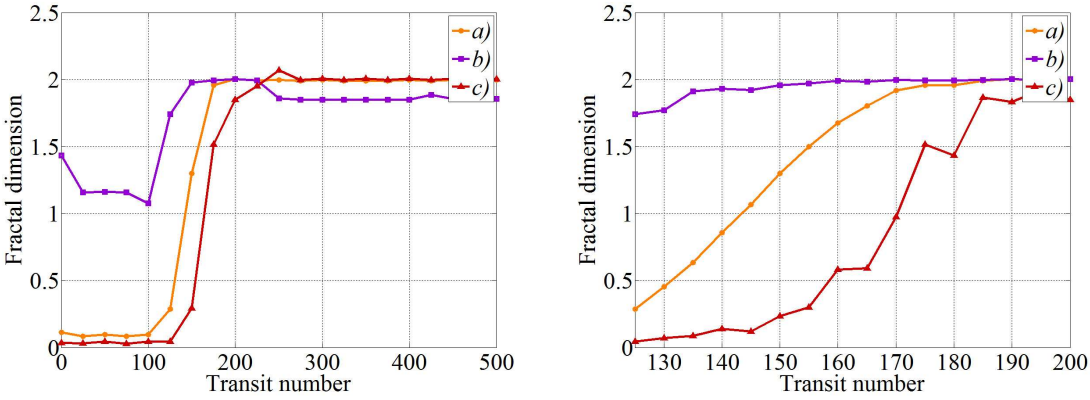

Figure 2.28: Fractal dimension with progressing transits for a defocusing medium, with curves presented for: a) entire data set, b) small-scale region, and c) large-scale region. Parameters are $r_1^2 = 0.1$, $r_2^2 = 0.1$, $I_0 = 0.45$, $K_0 = 2.25$, $K_C = 1.5$, $l_D = 0$, $\tau = 0$, $\chi L = -1$, $\delta = \pi/4$, and $d/k_0 = 1$

The plot on the left-hand side of 2.28 shows an overview of the transition toward a fractal, while the plot on the right-hand shows a higher resolution sampling in the range where the pattern starts to become gradually more complex. It can be seen that there are stages during the transition where the small-scale region has an estimated dimension of $D_{RL} = 2$ and the large-scale region where $D_{RL} < 1$. Such results hint at the inherent complexity of the fractal-formation process and also reveal potential limitations on the applicability of dimension measures [36].

2.2.6.2 Fractal pattern formation with finite diffusion

To fully understand the fractal-generating nature of the FP cavity, further numerical analysis of the cavity is implemented to observe pattern formation in the presence of finite diffusion ($l_D \neq 0$). Simulating the cavity under these conditions increases the complexity of the numerical integration, and calculating the photoexcitation density n has changed from the simple definition of $n = |F|^2+|B|^2$ to the partial differential equation given by Eq. 2.1c.

A finite-difference algorithm has been implemented to compute photoexcitation density n. This chosen algorithm is an explicit scheme; other approaches such as the Crank-Nicolson method are implicit and will give more accurate results. However, the drawback with implementing Crank-Nicolson is that additional methods (such as a tridiagonal matrix algorithm or a Gauss-Seidel iteration technique) must be deployed to solve the resulting matrix problem [37]. The advantage of finite-difference is that it drastically reduces computation time, allowing for a larger number of points in the transverse domain. For simulations with a single transverse coordinate x, a grid with 2^{17} $(134,072)$ points was used.

It is now instructive to consider how the effect of finite diffusion can influence the long-term characteristics of the pattern (in the absence of spatial filtering). The power spectrum provides a convenient presentation of complexity in Fourier space, with a typical example shown in figure 2.29 comparing the spectra for four values of l_d after a fixed time $t = 2048t_R$. As the levels of diffusion increases, the power spectrum acquires a more negative average gradient. This trend is associated with the diffusion process quenching fractality (i.e., the growth of high spatial frequencies) [8–10].

General trends of behaviour in the diffusive FP cavity are shown in figure 2.30 for fixed l_D. The power spectrum of the simple pattern starts off with a steep negative gradient over a small range of K/K_0, with $\ln P(K) \sim -30$ representing the computational noise floor. As time increases, nonlinear processes (such as spatial harmonic generation and four-wave mixing) leads to a growth in Fourier amplitudes at higher K/K_0. After a sufficiently long time, the cavity reaches a dynamic equilibrium state: the linear trend in the power spectrum remains fixed while the real-space pattern continues to evolve and develop. This type of behaviour is qualitatively identical to that discovered in other simple systems [8–10].

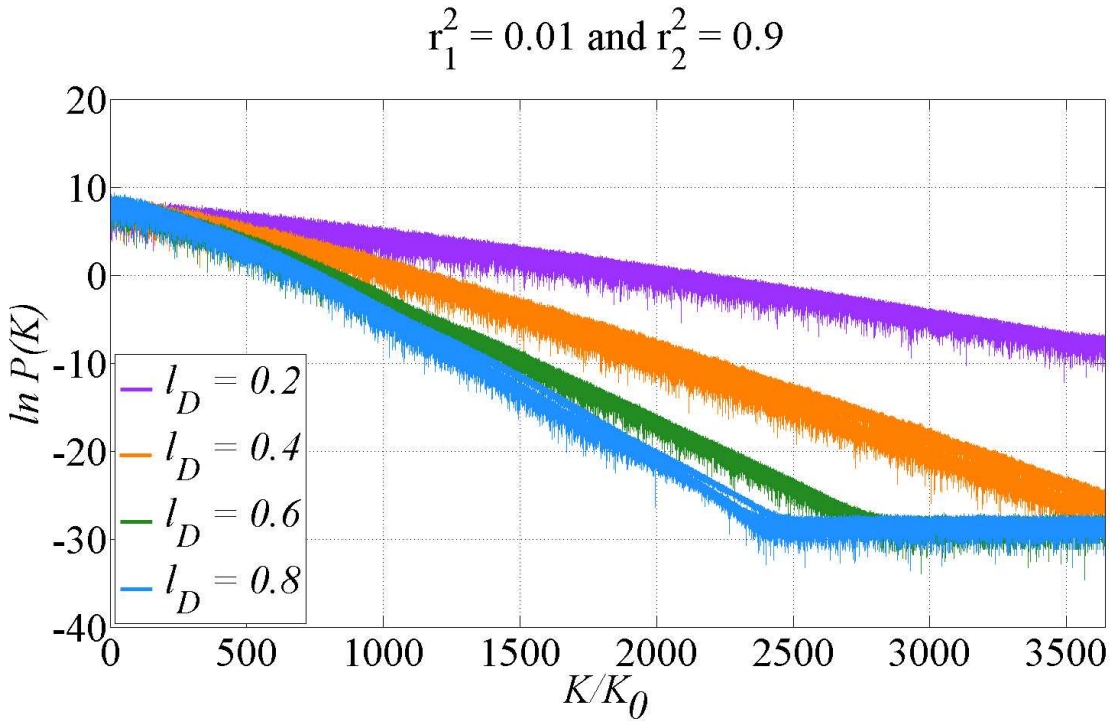

Figure 2.29: Variation in the power spectrum with diffusion length where $t_R = 2048$, $r_1^2 = 0.01$, $r_2^2 = 0.9$, $I_0 = 0.9057$, $K_0 = 1.2875$, $K_C = 1.663$, $\tau = 1$, $\chi L = +1$, $\delta = \pi/4$, and $d/k_0 = 1$.

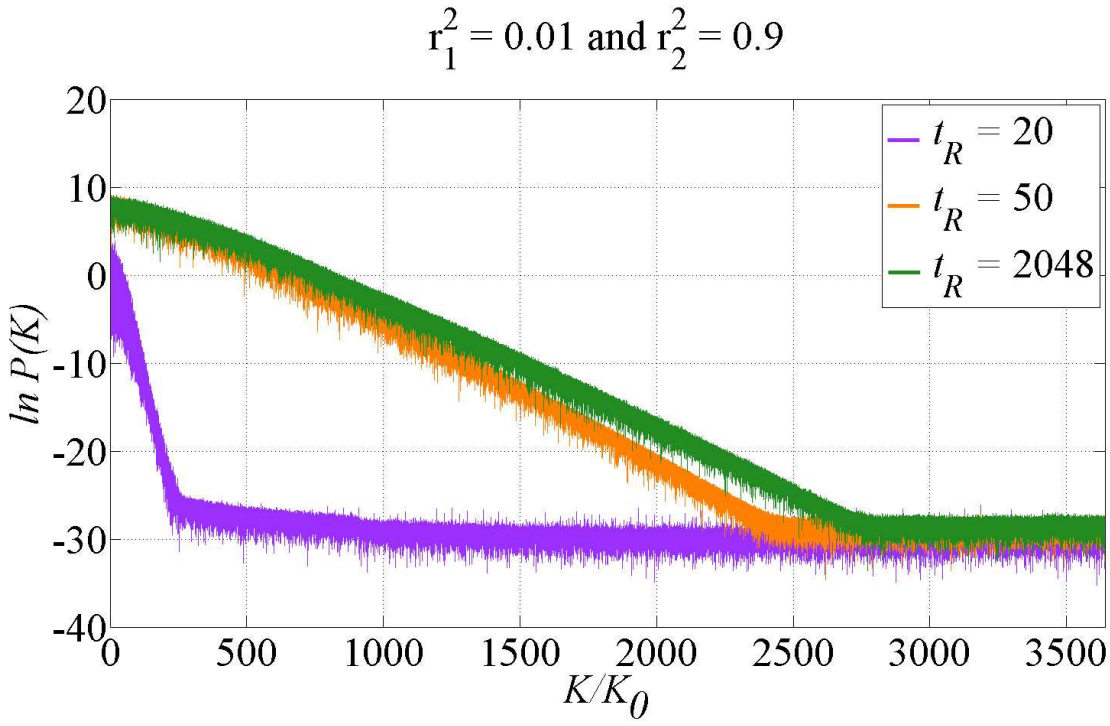

Figure 2.30: Comparison of power spectrum at different points in time, where $l_D = 0.6$ $r_1^2 = 0.01$, $r_2^2 = 0.9$, $r_2^2 = 0.9$, $I_0 = 0.9057$, $K_0 = 1.2875$, $K_C = 1.663$, $\tau = 1$, $\chi L = +1$, $\delta = \pi/4$, and $d/k_0 = 1$.

From inspection of figures 2.29 and 2.30, it appears that the average trend of the power spectrum can be well-described by the relationship:

$$\ln P(K) = bK + c, \tag{2.29}$$

where the gradient $b = d(\ln P)/dK$ is negative, and c is the intercept. It follows that b and c are numerical "fit" parameters that will depends in some way upon system details. The parameter of principal interest is b, since gradients in the power spectrum can be directly related to a fractal dimension [38]. The linear rule embodied by Eq. 2.29 appears in other systems [8–10], where b is determined by an interplay between, for example, mirror reflectivity, pump intensity, and diffusion length.

Figure 2.31 shows how the gradient b depends upon diffusion length. A larger l_D leads to an increasingly negative b, but in contrast to the SFM system [34], the relationship is *not* linear.

The influence of the intracavity intensity I_0 on b is shown in figure 2.32; this dependence is, however, qualitatively similar to the SFM system [34].

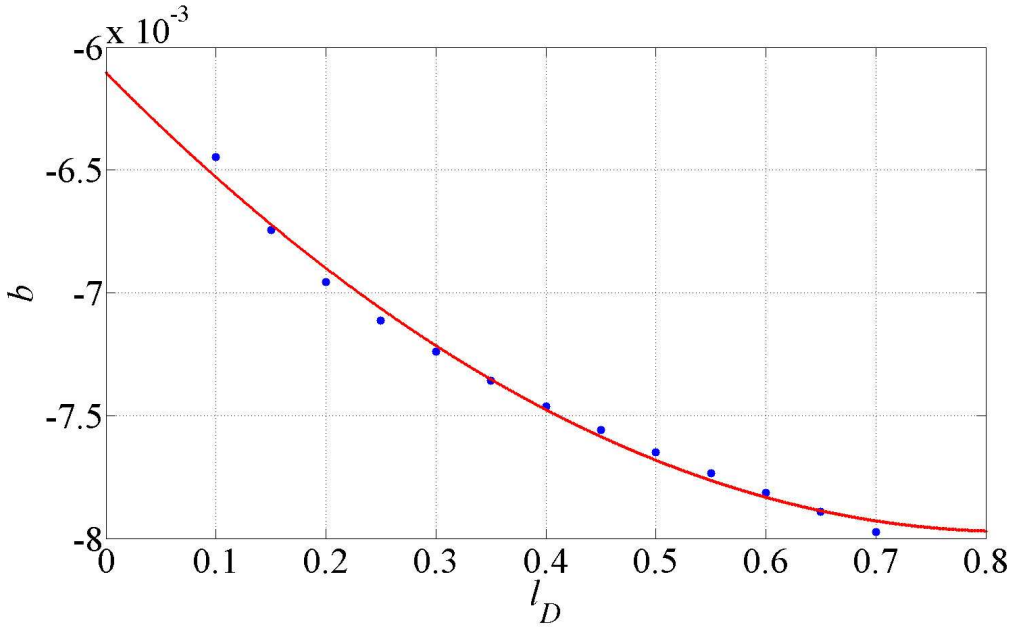

Figure 2.31: Variation of the b with increasing values of l_D, where $r_1^2 = 0.1$, $r_2^2 = 0.9$, $I_0 = 3I_{th}$, $I_{th} = 0.79433$, $K_0 = 1.1776$, $K_C = 1.663$, $\tau = 1$, $\chi L = +1$, $\delta = \pi/4$, and $d/k_0 = 1$.

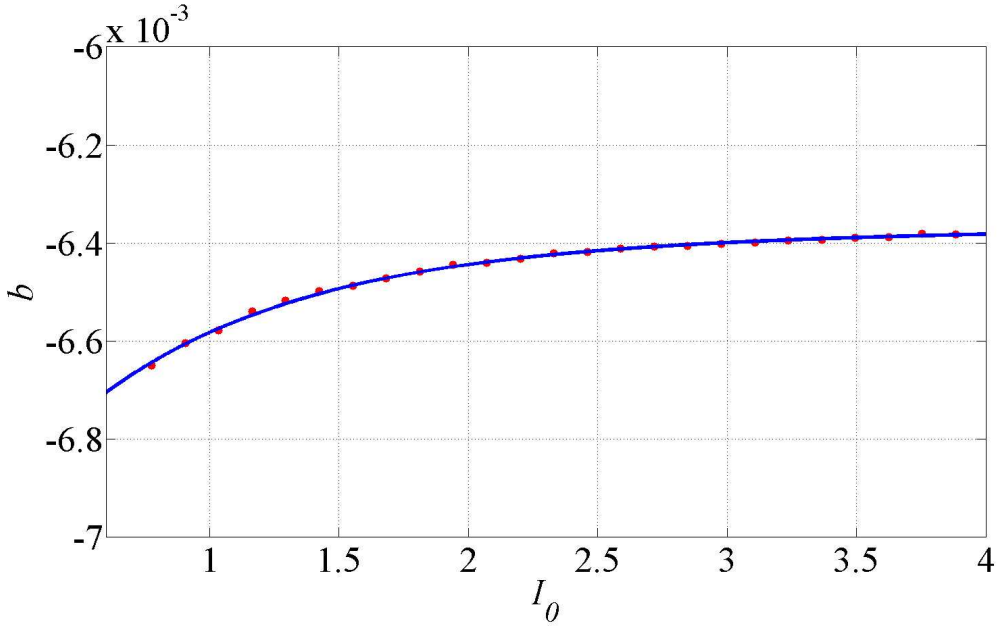

Figure 2.32: Variation of the b with increasing values of I_0, where $r_1^2 = 0.1$, $r_2^2 = 0.9$, $l_D = 0.1$, $K_0 = 1.1776$, $K_C = 1.663$, $\tau = 1$, $\chi L = +1$, $\delta = \pi/4$, and $d/k_0 = 1$.

2.2.7 Pattern formation with two transverse dimensions

After simulating the FP cavity with a single transverse dimension, it is now desirable to extend those considerations to regimes involving two dimensions. The numerical integration procedure remains effectively the same as before, but the resolution is necessarily lower (we consider computations on a 512×512 grid).

Simple pattern emergence (in this case, a hexagon) is illustrated in figure 2.33 for a low level of feedback from the slice ($r_1^2 = 5\%$). The uniform solution is initialized above threshold, and a small level of background noise added to seed any instability. Other examples of pattern formation (such as squares and stripes) are shown in figure 2.34 for an increased level of slice feedback (e.g. $r_1^2 \geqslant 10\%$). It is worth noting that the pattern formation in parts *a*) and *b*) are not static and, instead, they display a $2t_R$-type oscillation. However, figure 2.34 is unable to demonstrate this oscillation as the maximum intensity for both states share the same value, and the patterns are simple shifted in space. Furthermore, this result suggests that for sufficiently high slice feedback there may exist Hopf modes with a lower threshold than the Turning modes. Firth has touched on this subject in the absence of transverse effects [13]. The Hopf modes for the thin-slice FP cavity are obtainable by analysing the stability condition for the plane wave solutions (the only currently known exact analytical solutions to the model equations). Such an investigation will be performed at a later date, and we do not consider oscillatory patterns further.

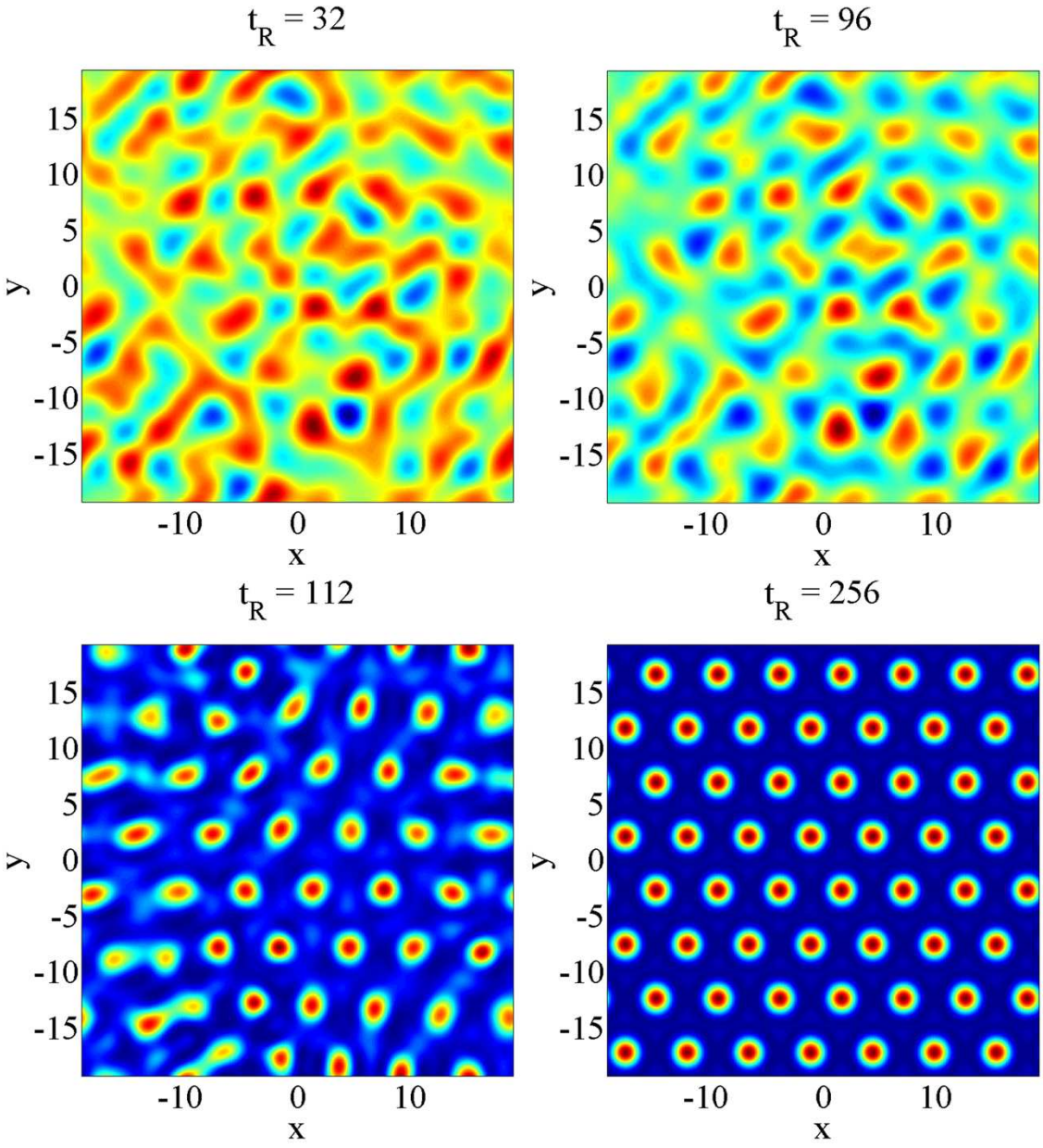

Figure 2.33: 2D pattern formation in the FP cavity resulting in a hexagonal pattern formation, with the parameters $r_1^2 = 0.05$, $r_2^2 = 0.9$, $K_0 = 1.3$, $l_D = 0$, $K_0 = 1.1776$, $K_C = 1.8$, $\tau = 1$, $\chi L = +1$, $\delta = \pi/4$, and $d/k_0 = 1$.

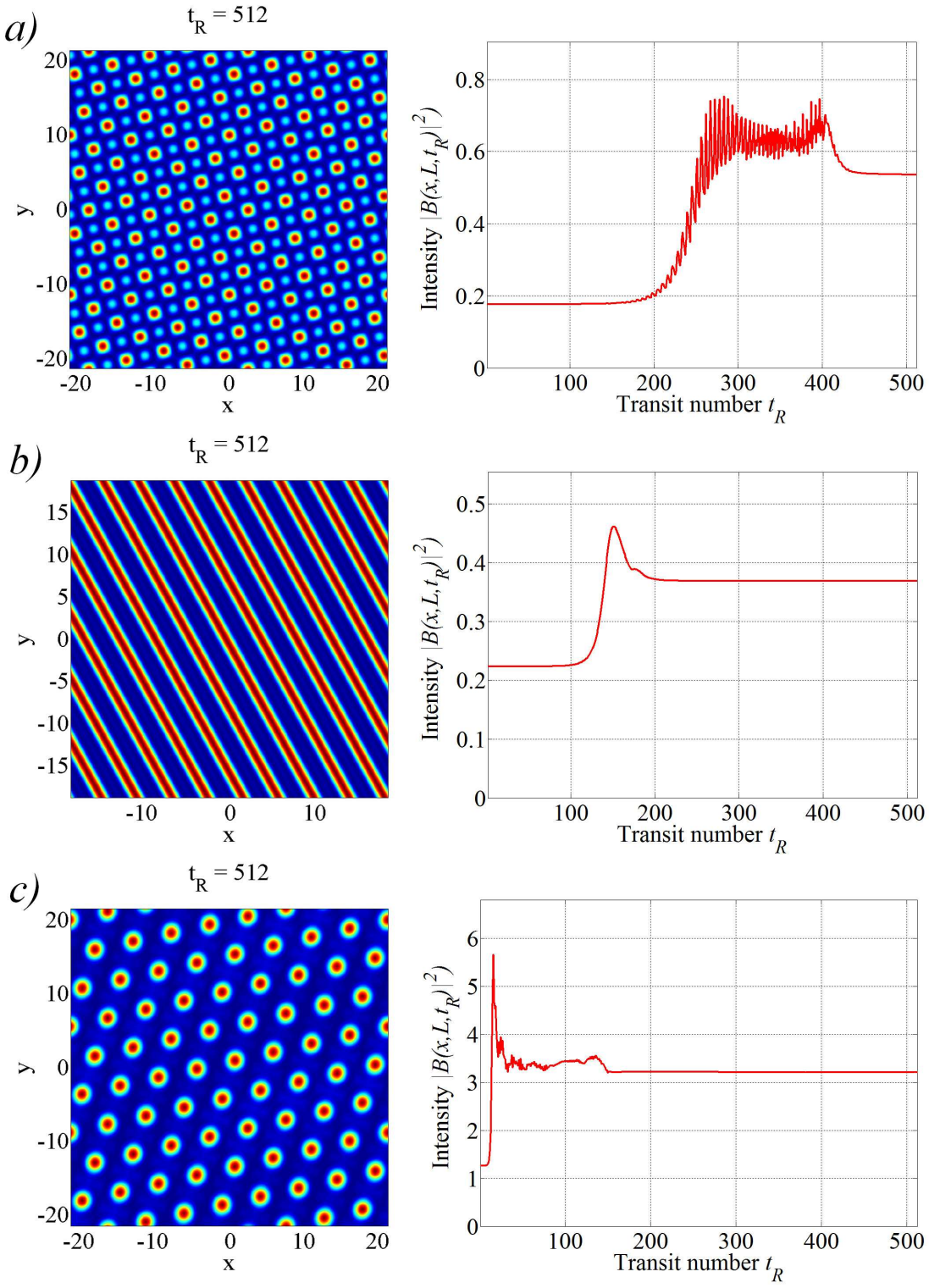

Figure 2.34: 2D pattern formation in the FP cavity resulting in alternative pattern formation, where $r_2^2 = 0.7$, $l_D = 0$, $\tau = 1$, $\chi L = +1$, $\delta = \pi/4$, $d/k_0 = 1$ *a*) $r_1^2 = 0.7$, $I_{th} = 0.25$, $K_0 = 1.175$, $K_C = 2.1$, for *b*) $r_1^2 = 0.5$, $I_{th} = 0.32$, $K_0 = 1.33$, $K_C = 2.1$ and for *c*) $r_1^2 = 0.1$, $I_{th} = 1.81$, $K_0 = 1.162$, $K_C = 2.3$. Here, intensity B refers to the peak intensity of the backwards field.

Two-dimensional patterns in a defocusing medium

The FP cavity with a defocusing medium with two transverse dimensions can also generate simple static patterns such as stripes (figure 2.35) and squares (figure 2.36). Most-unstable spatial frequencies and threshold intensities are obtained from the Turning spectrum (figure 2.26).

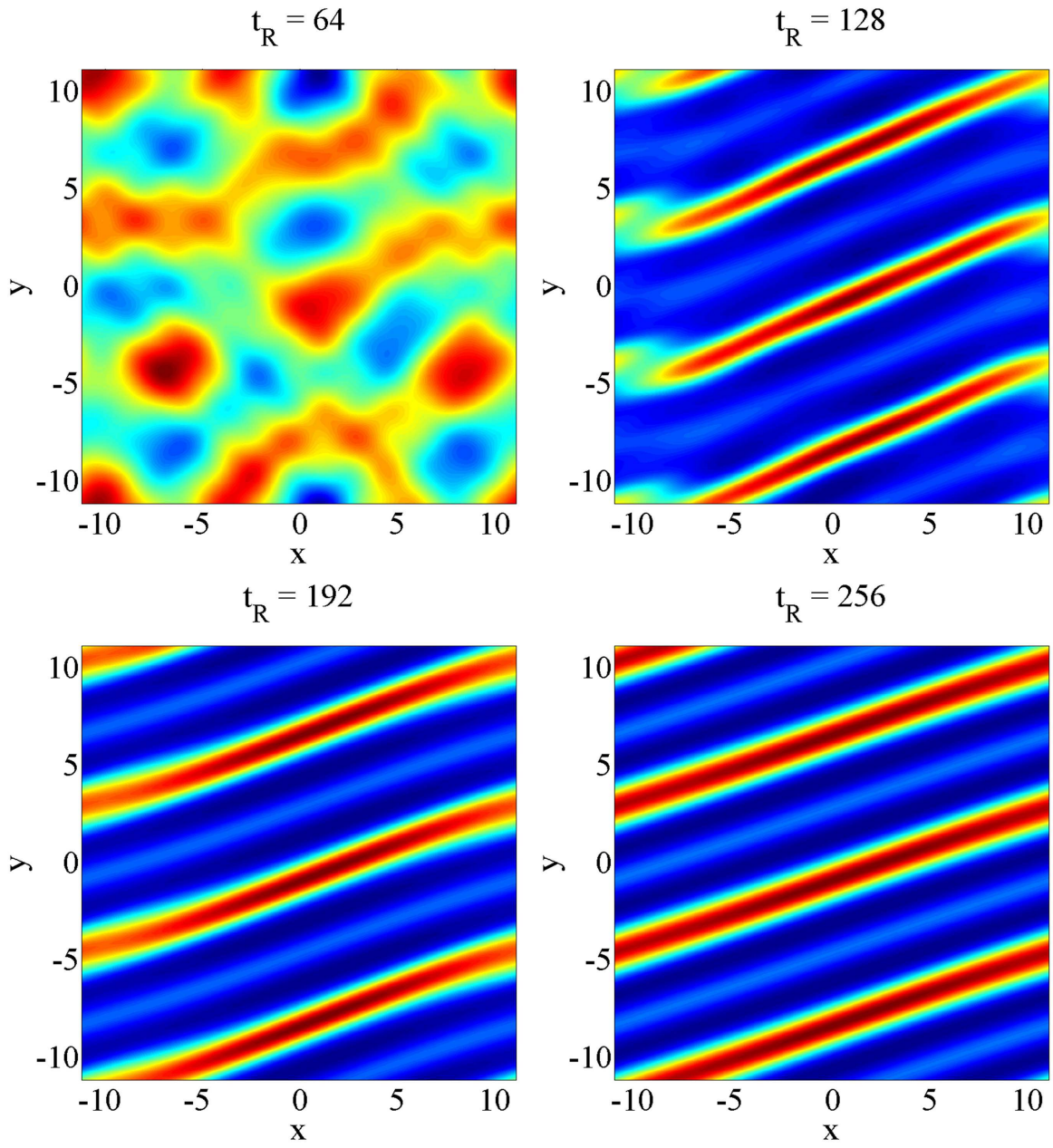

Figure 2.35: Two-dimensional patterns in a defocusing medium where $r_1^2 = 0.8$, $r_2^2 = 0.1$,, $I_0 = 0.978$, $l_D = 0$, $K_0 = 2.2438$, $K_C = 2.8$, $\tau = 1$, $\chi L = -1$, $\delta = \pi/4$, and $d/k_0 = 1$.

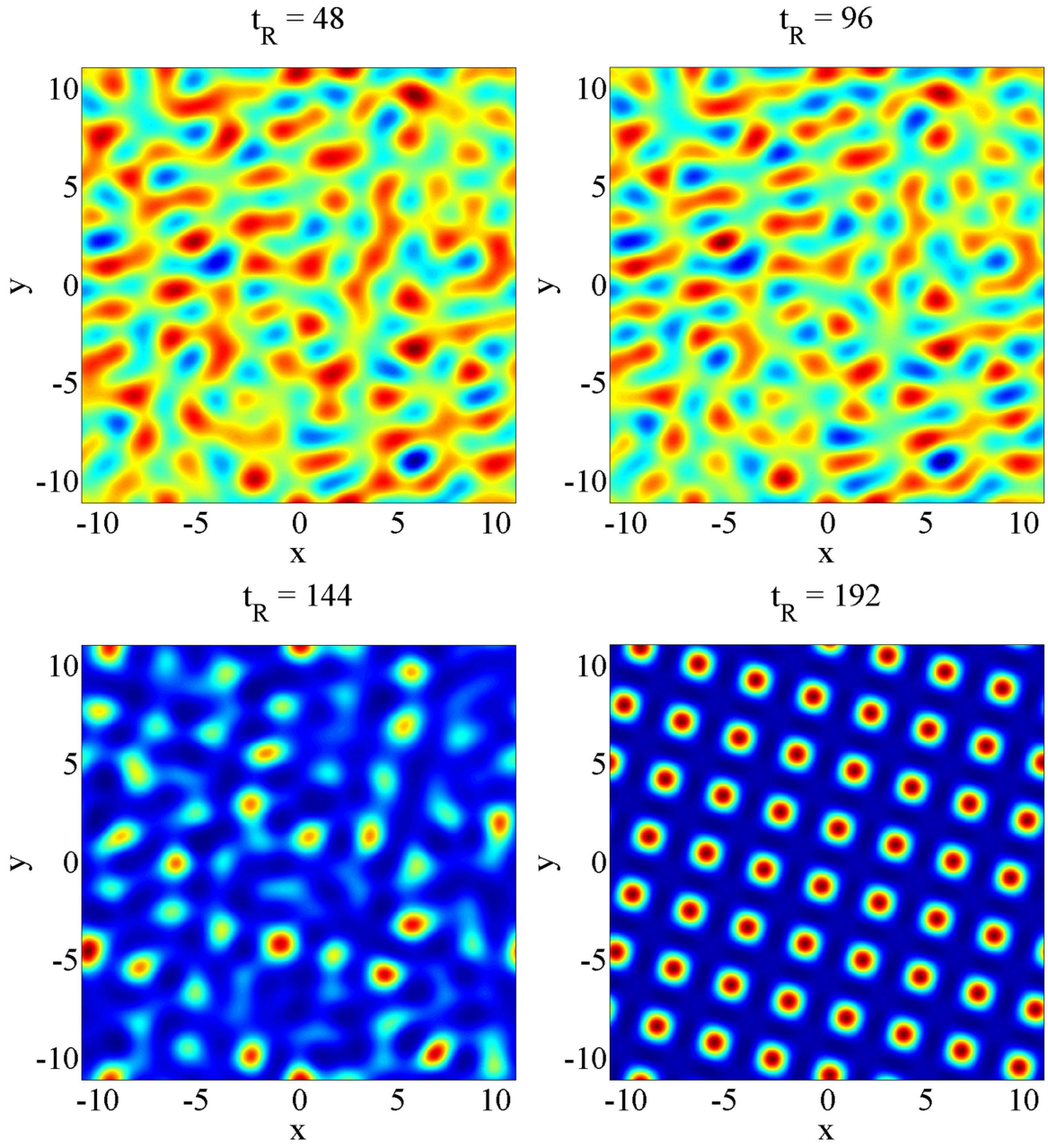

Figure 2.36: Two-dimensional patterns in a defocusing medium where $r_1^2 = 0.1$, $r_2^2 = 0.9$,, $I_0 = 0.3473$, $l_D = 0$, $K_0 = 2.26$, $K_C = 3.5$, $\tau = 1$, $\chi L = -1$, $\delta = \pi/4$, and $d/k_0 = 1$.

Two-dimensional fractal pattern formation

We now consider the transition from simple pattern towards a fractal in the case of a focusing medium with two transverse dimensions. Simulations begin with the hexagon structure shown in figure 2.33 *d*) at time $t = 256t_R$. The filter is adjusted (by setting $K_c = k_0$), and the pattern allowed to evolve with spatial frequencies $0 \leqslant K \leqslant k_0$ contributing to the dynamics. With each transit, the pattern is more complex, with an increasing level of small-scale structures developing though intrinsic nonlinear dynamics.

A similar process occurs for the defocusing medium, with the transition toward fractality shown in figure 2.38. There, the initial simple pattern is given in figure 2.36 *d*) with the filter adjusted at $t = 512t_R$.

It should be noted that the transition towards fractality shown in figures 2.37 and 2.38 is incomplete. In principle, these patterns would evolve into volume-filling stuctures where dimension is 3. However, finite computational resources severely limit the k_0 value that can be used in simulations with two transverse dimensions. Hence, the solutions shown can ever achieve their volume-filling character because the spatial bandwidth is artificially curtailed. We note, however, that the fundamental process by which higher spatial frequencies are generated exactly mimics the simpler 1D patterns (where much larger k_0 values may be used).

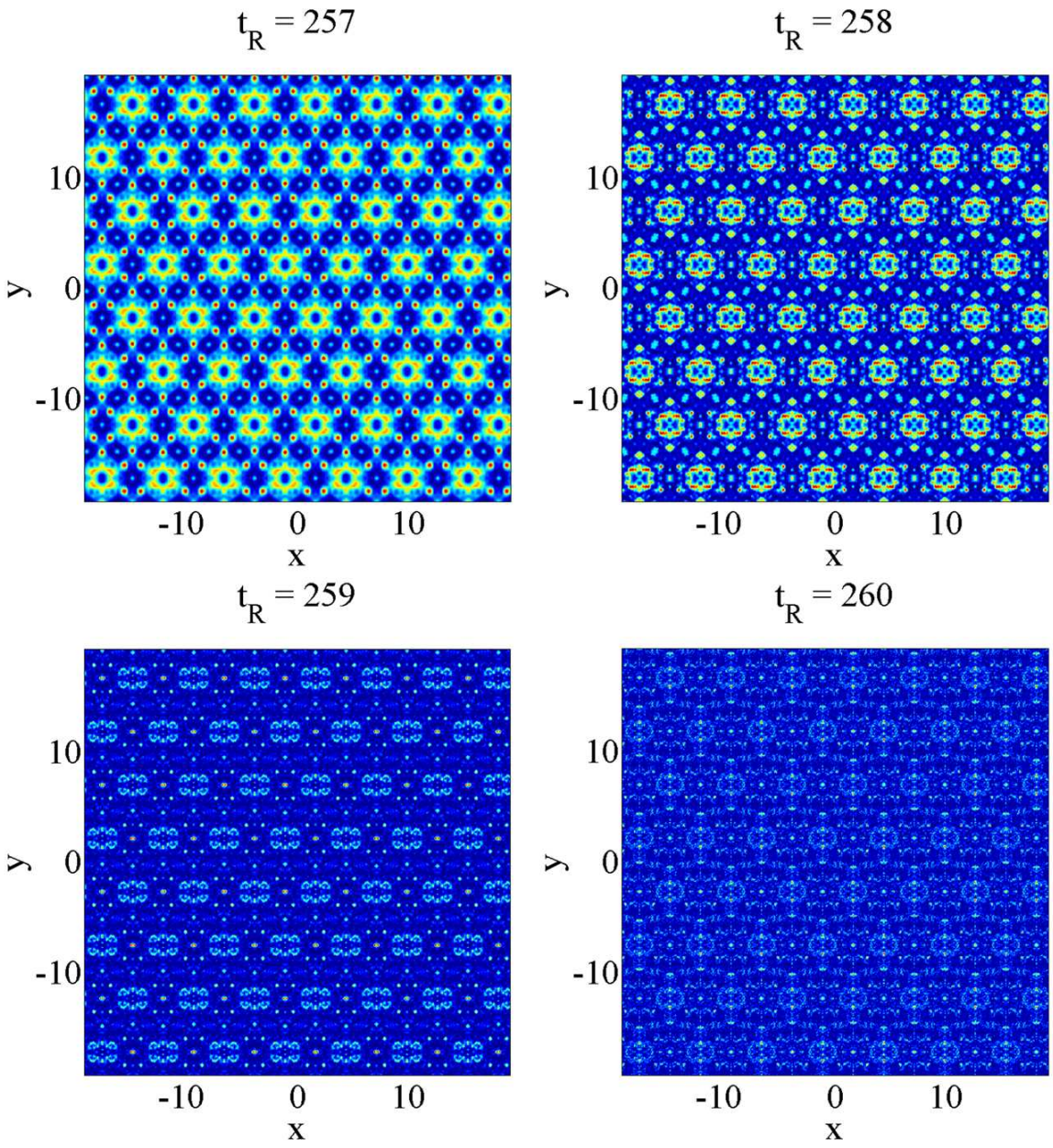

Figure 2.37: 2D fractal formation in the FP cavity where the filter has been removed after the 256th transit, with the parameters $r_1^2 = 0.8$, $r_2^2 = 0.1$,, $I_0 = 0.978$, $l_D = 0$, $K_0 = 2.2438$, $\tau = 1$, $\chi L = 1$, $\delta = \pi/4$, and $d/k_0 = 1$.

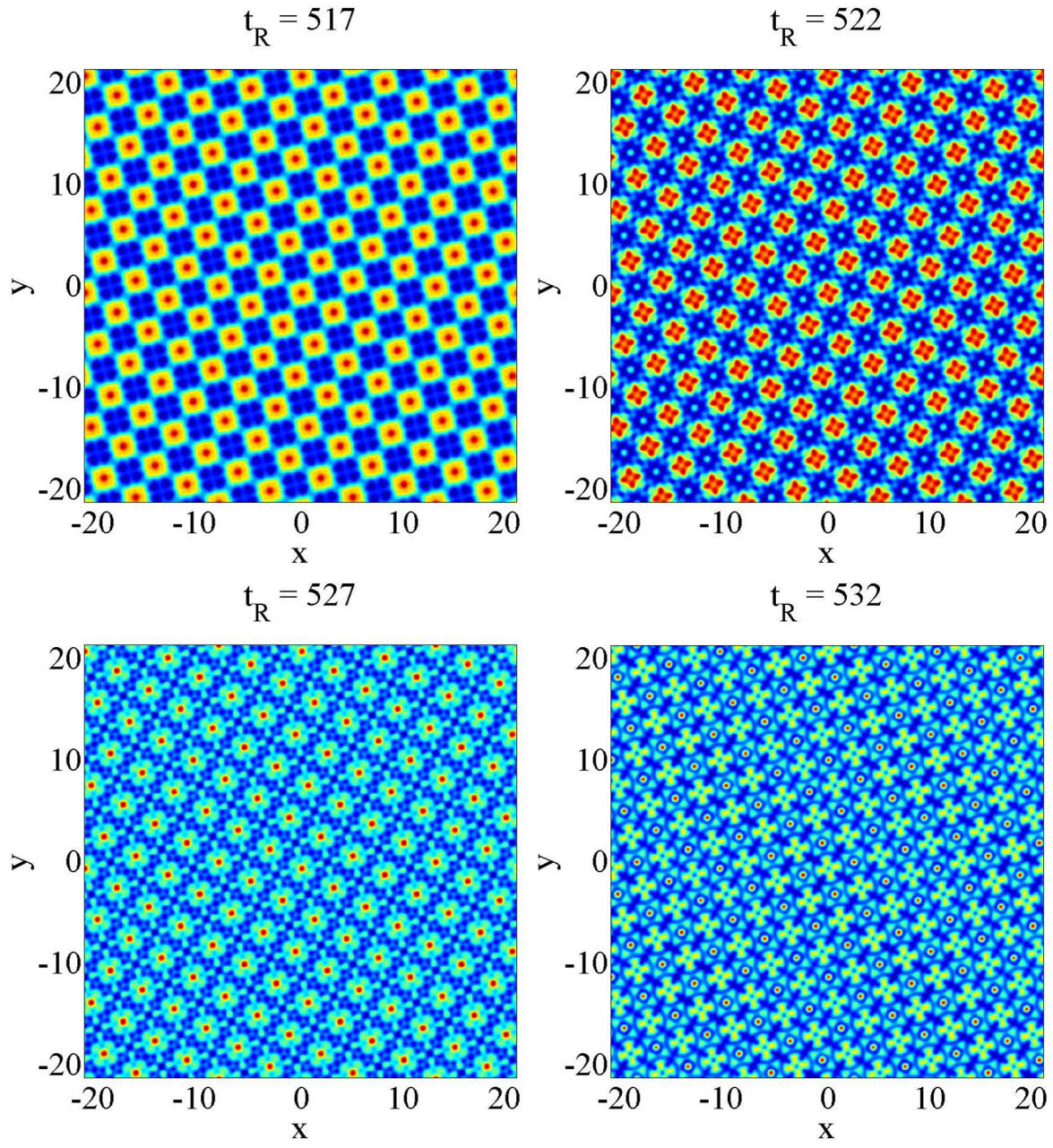

Figure 2.38: 2D fractal formation in the FP cavity where the filter has been removed after the 256th transit, with the parameters $r_1^2 = 0.1$, $r_2^2 = 0.9$,, $I_0 = 0.3473$, $l_D = 0$, $K_0 = 2.26$, $\tau = 1$, $\chi L = 1$, $\delta = \pi/4$, and $d/k_0 = 1$.

For clarification figures 2.39 *a*), *b*), *c*) and *d*) are the resulting threshold plots for the parameters used in figures 2.35, 2.36, 2.37, and 2.38, respectively. In the defocusing case (figures 2.39 *a*), and *b*)) the K_0 value is obtained from the tip of the uppermost left island and the K_C value is selected to be after the edge of the spectral band below this island. In the case of figure 2.39 *c*), the K_0 value is obtained from the minimum located at the bottom of the first band and the K_C value is chosen to allow all of the frequencies of the band to circulate around the cavity. The K_0, and K_C values in figure 2.39 *d*) are selected in the same manner as figure 2.39 *c*), but the K_0 now has to allow for the formation of an island below the first spectral band. In this case, K_0 is selected to be the tip of this island.

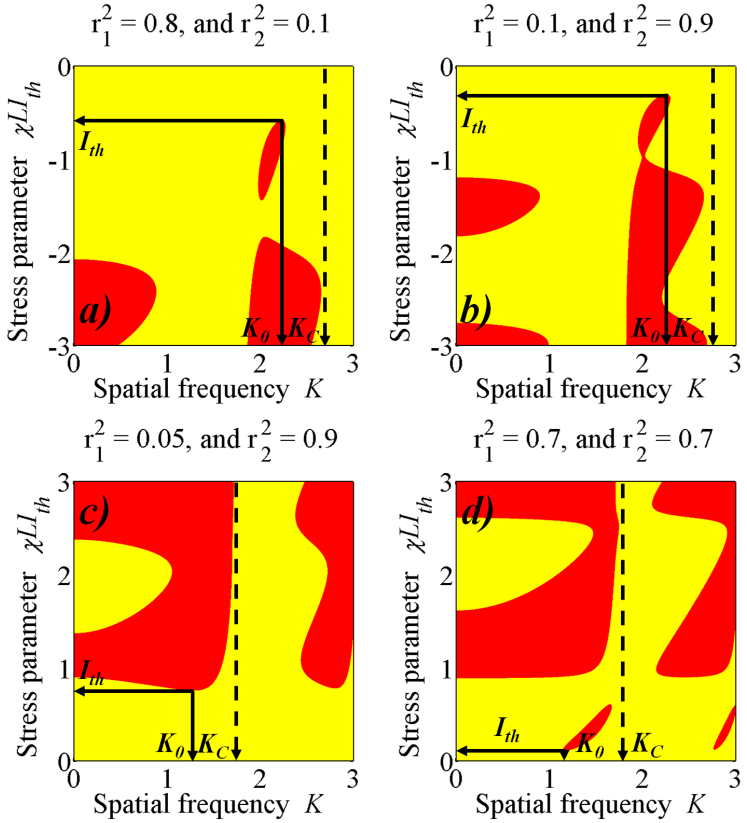

Figure 2.39: Threshold plots for the FP cavity where *a*) and *b*) have $\chi L = -1$ (defocusing medium), whereas *c*) and *d*) have $\chi L = -1$ (focusing medium). Parameters are $l_D = 0$, $\tau = 1$, $\delta = \pi/4$, and $d/k_0 = 1$.

2.3 Conclusion

The research undertaken in this chapter considers the spontaneous pattern formation in slice-based nonlinear optical models, namely the SFM system and the FP cavity. By deploying generalizations of the techniques developed by Firth *et al.* [1, 11], it has been possible to derive the threshold condition for static patterns in a nonlinear FP cavity. In addition to, threshold condition for the SFM system has been re-derived with the added novelty of z-dependent perturbations in the fields F and B.

It is essential to obtain, and quantify, the most-unstable spatial frequency before preforming any numerical calculations, since the computational grid must be configured based on predictions from the linear analysis. Detailed simulations have confirmed that spontaneous pattern formation is not only possible in the FP cavity, but that both single and multi-scale spatial structures may exist. This novel result has been found by analysing real space patterns using specialize software [35] to estimate various fractal dimensions. Key results show that the FP cavity comprising instantaneous Kerr medium can support patterns with fractal dimension 2, which denotes area-filling. The outcome of this analysis only strengthens the mechanism proposed by Huang *el at.*.

A computationally-intensive task was to allow for finite diffusion (i.e., non-zero of τ and l_D). Such considerations were accommodated by implementing a finite-difference scheme to solve the diffusion equation for the photoexcitation density. The benefit this approach over, say, the Crank-Nicolson method is that larger transverse domains may be used without an unacceptable increase in computational time.

Extensive simulation work has been uncovered key characteristics in both the simple and fractal patterns that the FP cavity can generate. Of particular interest is the linear relationship underpinning the power spectrum, $P(K)$, of the fractal states, where $\ln P(K) \sim bK$. The dependence of the numerical fit parameter b on both the diffusion length and intracavity intensity has mapped out, and a comparison made with the SFM system. Similarities and difference have been uncovered.

References

[1] W. J. Firth. Spatial instabilities in a Kerr medium with single feedback mirror. *Journal of Modern Optics*, 37:151–153, 1990.

[2] G. D'Alessandro and W. J. Firth. Spontaneous hexagon formation in a nonlinear optical medium with feedback mirror. *Physical Review Letters*, 66(2):2597–2600, 1991.

[3] G. D'Alessandro and W. J. Firth. Hexagonal spatial patterns for a Kerr slice with a feedback mirror. *Physical Review A*, 41(1):537–548, 1992.

[4] F. Papoff, G. D'Alessandro, G. L. Oppo, and W. J. Firth. Local and global effects of boundaries on optical-pattern formation in Kerr media. *Physical Review A*, 48(1):635–641, 1993.

[5] G. Grynberg, A. Maitre, and A. Petrossian. Flowerlike patterns generated by a laser beam transmitted through a rubidium cell with single feedback mirror. *Physical Review Letters*, 72(15):2379–2382, 1994.

[6] M. A. Vorontsov and A. Y. Karpov. Kerr slice-based nonlinear interferometer with two-dimensional feedback: control of roll and hexagon formation. *Optics Letters*, 20(24):2466–2468, 1995.

[7] E. V. Degtiarev and V. Wataghin. Stability analysis of a two-component nonlinear optical system with 2-D feedback. *Optics Communications*, 124:309–312, 1996.

[8] J. G. Huang and G. S. McDonald. Spontaneous optical fractal pattern formation. *Physical Review Letters*, 94(17):174101, 2005.

[9] J. G. Huang, J. M. Christian, C. Bostock, and G. S McDonald. Spontaneous spatial optical fractals in ring cavities. *Manuscript in preparation*, 2015.

[10] J. G. Huang, J. M. Christian, and G. S. McDonald. Spontaneous spatial fractal pattern formation in absorptive systems. *Journal of Nonlinear Optical Physics & Materials*, 21(02): art. no. 1250018, 2012.

[11] *Spontaneous spatial structures in simple systems and defocusing media*, Proceedings on Nonlinear Dynamics in Optical Systems 7, Afton, Oklahoma, June 4–8 1990. Optical Society of America.

[12] J. H. Marburger and F. S. Felber. Theory of a lossless nonlinear Fabry-Pérot interferometer. *Physical Review A*, 17 (1):335–342, 1978.

[13] W. J. Firth. Stability of nonlinear Fabry-Pérot resonators. *Optics Communications*, 39(5): 343–346, 1981.

[14] M. Möller, L. M. Hoffer, G. L. Lippi, T. Ackemann, A. Gahl, and W. Lange. Fabry-Pérot and ring cavity configurations and transverse optical patterns. *Journal of Modern Optics*, 45(9):1913–1926, 1989.

[15] S. Chi and Q. Guo. Vector theory of self-focusing of an optical beam in Kerr media. *Optics Letters*, 20(15):1598–1600, 1995.

[16] K. D. Stephen. *Optical coding via transverse patterns in nonlinear media.* PhD thesis, Strathclyde University, 1991.

[17] T. Takizawa, Y. Liu, and J. Ohtsubo. Chaos in a feedback Fabry-Pérot interferometer. *IEEE Journal of Quantum Electronics*, 30(2):334–338, 1994.

[18] R. G. Harrison, W. J. Firth, and I. A. Al-Saidi. Observation of bifurcation to chaos in an all-optical Fabry-Pérot resonator. *Physical Review Letters*, 53:258–261, 1984.

[19] J. M. Aguirregabiria and L. L. Bel. Delay-induced instability in a pendular fabry-pérot cavity. *Physical Review A*, 36(8):3768, 1987.

[20] K Ikeda and M Mizuno. Modeling of nonlinear Fabry-Pérot resonators by difference-differential equations. *IEEE Journal of Quantum Electronics*, 21(9):1429–1434, 1985.

[21] T. Y. Li and J. A. Yorke. Period three implies chaos. *American Mathematical Monthly*, pages 985–992, 1975.

[22] K Ikeda. Multiple-valued stationary state and its instability of the transmitted light by a ring cavity system. *Optics Communications*, 30(2):257–261, 1979.

[23] P. Mandel. *Theoretical problems in cavity nonlinear optics*, volume 21. Cambridge University Press, 2005.

[24] G. S. McDonald and W. J. Firth. Switching dynamics of spatial solitary wave pixels. *Journal of the Optical Society of America B*, 10(6):1081–1089, 1993.

[25] H. Gibbs. *Optical bistability: controlling light with light*. Elsevier, 1985.

[26] D Miller. Refractive Fabry-Pérot bistability with linear absorption: theory of operation and cavity optimization. *IEEE Journal of Quantum Electronics*, 17 (3):306–311, 1981.

[27] S. D. Gupta and G. S. Agarwal. Dispersive bistability in coupled nonlinear Fabry-Pérot resonators. *Journal of the Optical Society of America B*, 4(5):691–695, 1987.

[28] A. S. Patrascu, C. Nath, M. Le Berre, E. Ressayre, and A. Tallet. Optical bistability and self-oscillation of a nonlinear Fabry-Pérot interferometer filled with a nematic-liquid-crystal film. *Optics Letters*, 8(1):39–41, 1983.

[29] A. S. Patrascu, C. Nath, M. Le Berre, E. Ressayre, and A. Tallet. Multi-conical instability in the passive ring cavity: linear analysis. *Optics Communications*, 91(5):433–443, 1992.

[30] H. A. Al-Attar, H. A. MacKenzie, and W. J. Firth. Critical slowing-down phenomena in an InSb optically bistable etalon. *Journal of the Optical Society of America B*, 3(9): 1157–1163, 1986.

[31] H. Nakatsuka, S. Asaka, H. Itoh, K. Ikeda, and M Matsuoka. Observation of bifurcation to chaos in an all-optical bistable system. *Physical Review Letters*, 50(2):109, 1983.

[32] H. M. Gibbs, F. A. Hopf, D. L. Kaplan, and R. L. Shoemaker. Observation of chaos in optical bistability. *Physical Review Letters*, 46(7):474, 1981.

[33] M. D. Feit and J. A. Fleck Jr. Beam nonparaxiality, filament formation, and beam breakup in the self-focusing of optical beams. *Journal of the Optical Society of America B*, 5(3): 633–640, 1988.

[34] J. G. Huang. *Spontaneous optical fractals in linear & nonlinear systems.* Ph.D thesis, University of Salford, 2006.

[35] BENOIT 1.3, TruSoft International Inc., www.trusoft-international.com.

[36] M. Berry, C. Storm, and W. Van Saarloos. Theory of unstable laser modes: edge waves and fractality. *Optics Communications*, 197(4):393–402, 2001.

[37] W. Press, S. Teukolsky, W. Vetterling, and B Flannery. *Numerical recipes in Fortran 77.* Cambridge University Press, 1986.

[38] J. Courtial, J. Leach, and M. J. Padgett. Image processing: Fractals in pixellated video feedback. *Nature*, 414(6866):864–864, 2001.

Chapter 3

Dispersive ring cavity

To further test the proposed universal fractal-generating mechanism, it is necessary to consider light in bulk systems [1] (i.e., where there is a finite light-medium interaction length). A simple candidate system that has suggested itself in the past (by virtue of its multi-minimum Turing threshold spectrum) is that of two counterpropagating-beams in a slab of Kerr material [2]. Despite its experimental simplicity, the counterpropagating-beams problem is fraught with near-overwhelming mathematical and computational complexity. Extensive analysis from 2010 concluded that the numerical algorithm of Geddes *et al.* [3] used to integrate the governing equations could not be trusted to handle high spatial frequencies correctly. Finding conclusive evidence of a fractal-generating capacity in that model was, thus, not possible. An alternative candidate system is a ring cavity filled with nonlinear (e.g., Kerr-type) material, as investigated by McLaughlin, Moloney, and Newell [4].

This chapter considers multi-Turing instabilities of dispersive nonlinear ring cavities. Huang *et al.* [5] proposed a general mechanism for fractal formation which is independent of the context of the nonlinearity. The first section in this chapter covers a review of the dispersive ring cavity with the added novelty of longitudinally-dependent perturbations. The motivation of this reworked analysis is to provide a more mathematically self-consistent description of the threshold condition for static patterns (which itself remains unchanged). Earlier research by McLaughlin *et al.* [4] derived the threshold condition for a ring cavity containing a slab of Kerr material with propagation within the paraxial regime. A consequence of adopting the paraxial wave-optics approach is that high spatial frequencies (i.e., precisely those spectral components

that are so vital for establishing the multi-scale nature of a pattern) are not adequately described. Here, we take the first steps toward understanding pattern formation in slab geometry with a generic dispersive nonlinearity. The light-medium interaction length is then finite, and the full generality of the Helmholtz diffraction operator is retained to provide a more complete description of broadband spatial spectra.

Summary of parameters and variables

A_n	Electric field envelope
a	Transverse scale parameter
c	Speed of light in a vacuum
d	Free-space path length
f	Complex perturbations for the forwards propagating field
F_n	Forward propagating electric field
F_0	Uniform state of F
F_{in}	Amplitude of the plane wave pump field
I_{th}	Intensity threshold
k	Wave number
$2\pi/k_0$	Free-space wavelength of the pump light
$\boldsymbol{K}$	Transverse spatial frequency
K_C	High frequency cut-off
K_0	Most unstable frequency
k_ζ	Dispersion relation
L	Length of the cavity
l_D	Diffusion length
n	Photoexcitation density
n_0	linear refractive index
$N(\lvert F_n\rvert^2)$	Generic nonlinearity function
r_1^2	Intensity reflectivity of the slice mirror
t	Time co-ordinate
t_1^2	Intensity transmissivity
t_R	Transit time
z	Longitudinal space co-ordinate
γ	Defined to be 2κ
δ	Linear interferometric mistuning
Δn	Real perturbation to the photoexcitation density
ζ	Longitudinal space co-ordinate (scaled)
θ	Phase/propagation factor
κ	Variable defined to be $1/(2kL)$
λ	Complex Lyapunov exponent
Λ	Growth rate
σ	Defined to be $L/(ka^2)$
τ	Relaxation time
ξ	Transverse space co-ordinate (scaled)
Φ	Total (linear and nonlinear) mistuning
χ	Nonlinearity of the Kerr medium
ω	Frequency
Ω	Temporal frequency
$\nabla_\perp^2$	Transverse Laplacian

3.1 Review of the thin-slice geometry

A schematic diagram of the thin-slice ring cavity is shown in figure 3.1. The system comprises a four-mirror ring configuration with a free-space path length of d, a slice with near-negligible thickness L, and a coupling mirror with intensity reflectivity r_1^2.

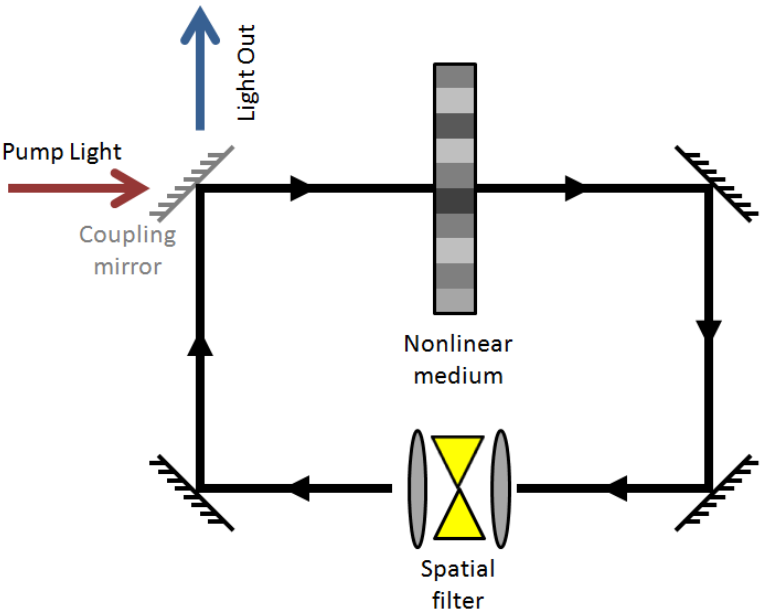

Figure 3.1: Schematic diagram of a nonlinear ring cavity.

The coupled field-medium dynamics are described by:

$$\frac{\partial F}{\partial z} = i\chi n F, \tag{3.1a}$$

$$-l_D^2 \nabla_\perp^2 n + \tau \frac{\partial n}{\partial t} + n = |F|^2, \tag{3.1b}$$

where F is the electric field, t denotes time, z is the longitudinal space coordinate, and $\nabla_\perp^2$ is the transverse Laplacian. The structure of this uni-directional system mimics that of the bi-directional SFM and FP geometries (in fact, it can be recovered from those models by setting $B = 0$, so that there is no backward-propagating field). The boundary condition describing the

intra-cavity field at the coupling mirror is given by

$$F(\boldsymbol{x},0,t) = t_1 F_{in} + r_1 \exp(i\delta) \exp\left(i\frac{d}{2k_0}\nabla_\perp^2\right) F(\boldsymbol{x},L,t-t_R), \tag{3.2}$$

which is reminiscent of the corresponding condition in the FP model. The parameter $t_1^2 \equiv 1-r_1^2$ is the intensity transmissivity and δ is the interferometric mistuning. The stationary state solution of the cavity (obtained by neglecting transverse effects) can be shown to be

$$F^0(z) = \frac{t_1 F_{in}}{1 - r_2 \exp(i\Phi)} \exp(i\chi n_0 z), \tag{3.3a}$$

$$n_0 \equiv |F^0(z)|^2 = \frac{t_1^2 |F_{in}|^2}{1 + r_1^2 - 2r_1 \cos\Phi}, \tag{3.3b}$$

where $\Phi \equiv \delta + \chi L n_0$ is the total (linear and nonlinear) mistuning.

3.1.1 Linear stability analysis

A linear stability analysis can be deployed to obtain the criteria for predicting the onset of pattern-forming instabilities in the ring cavity. To that end, we look for perturbed solutions of the form

$$F(\boldsymbol{x},z,t) = F^0(z)\left[1 + f(\boldsymbol{x},z,t)\right], \tag{3.4a}$$

$$n(\boldsymbol{x},t) = n_0 + \Delta n(\boldsymbol{x},t). \tag{3.4b}$$

When these solutions are substituted into Eq. (3.1b) and stationary state Eq. (3.3) is eliminated, the following linearized master equation can be obtained:

$$\left(-l_D^2\nabla_\perp^2 + \tau\frac{\partial}{\partial t} + 1\right)\Delta n(\boldsymbol{x},t) = |F_0|^2[f(\boldsymbol{x},0,t) + f^*(\boldsymbol{x},0,t)], \tag{3.5a}$$

where

$$|F_0|^2 = n_0. \tag{3.5b}$$

A further substitution of solution Eq. (3.4a) into boundary condition Eq. (3.2) also yields

$$f(\boldsymbol{x},0,t) = r_1 \exp(i\Phi) \exp\left(i\frac{d}{2k_0}\nabla_\perp^2\right) f(\boldsymbol{x},L,t-t_R), \tag{3.6}$$

while integration of Eq. (3.1a) uncovers a simple z-dependence for the perturbation f:

$$f(\boldsymbol{x},z,t) = f(\boldsymbol{x},0,t) + i\chi\Delta n(\boldsymbol{x},t)z. \tag{3.7}$$

By taking the Fourier transform of Eqs. (3.5) and (3.6), one arrives at

$$\left(l_D^2K^2 + \tau\frac{\partial}{\partial t} + 1\right)\Delta\tilde{n}(\boldsymbol{K},t) = |F_0|^2\left[\tilde{f}(\boldsymbol{K},0,t) + \tilde{f}^*(\boldsymbol{K},0,t)\right], \tag{3.8a}$$

$$\tilde{f}(\boldsymbol{K},0,t) = r_1 \exp[i(\Phi-\theta)][\tilde{f}(\boldsymbol{K},0,t-t_R) + i\chi L\Delta\tilde{n}(\boldsymbol{K},t-t_R)], \tag{3.8b}$$

where $\theta \equiv K^2d/2k_0$. By assuming time dependence of the form

$$\begin{aligned}\tilde{f}(\boldsymbol{K},0,t) &= \epsilon\exp(\lambda t) + \mu^*\exp(\lambda^* t),\\ \tilde{n}(\boldsymbol{K},t) &= \eta\exp(\lambda t) + \eta^*\exp(\lambda^* t),\end{aligned} \tag{3.9}$$

and substituting this ansatz pair into Eq. (3.8a), one can relate the ϵ and μ to η according to

$$\epsilon = \frac{E}{\exp(\lambda t_R) - D}\eta, \tag{3.10a}$$

$$\mu = \frac{E^*}{\exp(\lambda t_R) - D^*}\eta, \tag{3.10b}$$

where:

$$D \equiv r_1\exp[i(\Phi-\theta)], \tag{3.11a}$$

$$E \equiv i\chi LD. \tag{3.11b}$$

The characteristic equation for dispersive ring cavity with a z-dependent perturbation can be

obtained by substituting the ansatz pair, and additionally the above equations into Eq. (3.8a).

$$[\exp(\lambda t_R) - D]\,[\exp(\lambda t_R) - D^*]\left(1 + l_D^2 K^2 + \lambda\tau\right) = |F_0|^2\{[\exp(\lambda t_R) - D^*]\,E\}$$

$$+ |F_0|^2\{[\exp(\lambda^* t_R) - D]\,E^*\}\,. \qquad (3.12)$$

3.1.2 Static threshold curves

The threshold spectrum for static patterns can be obtained from Eq. (3.12) by setting $\lambda = 0$ and defining $|F_0|^2 \equiv I_{th}$. One then obtains:

$$\chi L I_{th} = -\frac{(1 + l_D^2 K^2)[1 + r_1^2 - 2r_1\cos(\Phi - \theta)]}{2r_1\sin(\Phi - \theta)}, \qquad (3.13)$$

where $\chi L I_{th}$ again measures nonlinear phase shift. The most unstable frequency, K_0, is taken to be K at lowest threshold point and the most-unstable wavelength is defined to be $\lambda_0 \equiv 2\pi/K_0$. Furthermore, the resulting Turing spectra obtained from threshold condition 3.13 remained unchanged from the original work by Huang *et al.* [6] (see figures 3.2 and 3.3).

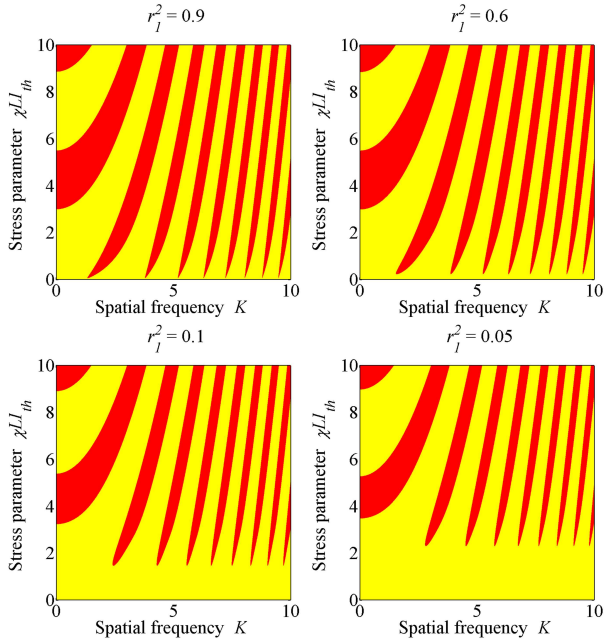

Figure 3.2: Static threshold curves of the dispersive ring cavity with zero diffusion, where $l_D = 0$, $\tau = 0$, $\delta = \pi/4$, $L = 1$, $d/k0 = 1$, $\chi = +1$, and the r_1^2 values are above the corresponding plots.

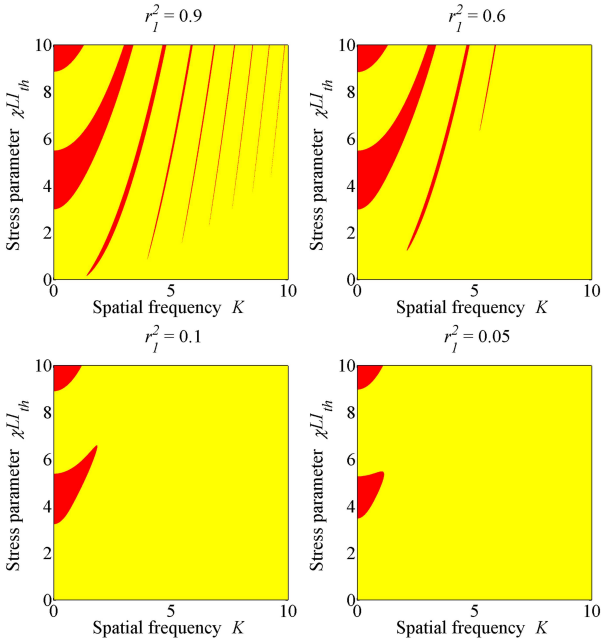

Figure 3.3: Static threshold curves of the dispersive ring cavity with finite diffusion, where $l_D = 1$, $\tau = 0$, $\delta = \pi/4$, $L = 1$, $d/k0 = 1$, $\chi = +1$, and the r_1^2 values are above the corresponding plots.

3.1.3 Concluding remarks

The reworked calculation for the thin-slice ring cavity provides a mathematically more self-consistent description of the linear analysis, but yields the same threshold spectrum remains unchanged [6, 7] when introducing z-dependence into the field perturbation.

3.2 Dispersive bulk ring cavity

We now consider a ring cavity containing a slab of medium with a local (instantaneous) generic nonlinearity function (see figure 3.4). Such a model may capture, for instance, Kerr- or saturable-type materials [4]. A defining feature of the highly idealized thin-slice geometry is that diffraction may be neglected inside the medium – propagation through the slice results solely in a phase modulation of the transmitted light.

The objective now is to begin modelling bulk systems where the light-medium interaction length is finite so that diffraction can no longer be neglected. To accommodate such physical considerations, we adopt an approach that is similar in spirit to that of McLaughlin, Moloney, and Newell [4]. The intra-cavity field during the n-th transit is found by integrating a formal wave equation, and the solution is then subjected to a discrete boundary condition that lumps together (at the cavity input) periodic pumping, coupling-mirror losses, and interferometric mistuning. Novelty in our analysis arises by replacing the nonlinear-Schrödinger equation [4] with its more general nonlinear-Helmholtz counterpart [8]. In this way, we naturally avoid placing paraxial constraints on the spatial spectrum of the circulating beam and are able to well-describe small-scale optical structure in the electric field. At the outset, one expects new quantitative predictions of the Helmholtz model to become important in high-K and high-stress regimes (where corrections to paraxial theory are expected to be non-negligible) [9, 10].

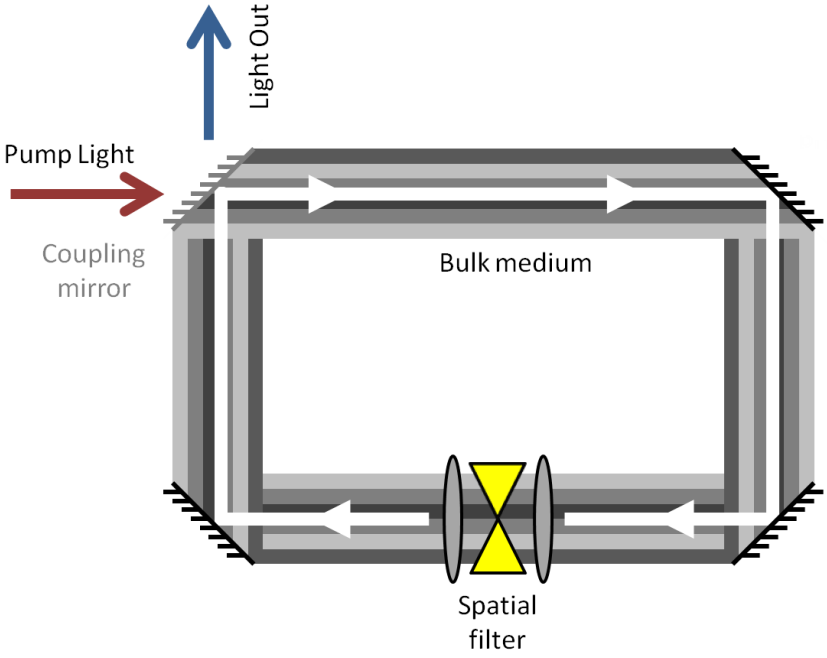

Figure 3.4: Schematic diagram of the bulk ring cavity.

3.2.1 Model equations

The nonlinear Helmholtz equation [9, 10] is now supplemented with a boundary condition to give the following:

$$\frac{\partial^2 A_n}{\partial z^2} + i2k\frac{\partial A_n}{\partial z} + \nabla_\perp^2 F_n + \frac{\omega^2}{c^2} 2n_0 n_2 |A_n|^2 A_n = 0, \tag{3.14a}$$

$$A_{n+1}(\boldsymbol{x}, 0) = t_1 A_{in} + r_1 \exp(i\delta) A_n(\boldsymbol{x}, L), \tag{3.14b}$$

where A_n is the electric field envelope, $\nabla_\perp^2$ is the transverse Laplacian, $k^2 \equiv n_0^2\omega^2/c^2$, n_0 is the linear refractive index at frequency ω and c is the vacuum speed of light. The cavity is driven by an external plane wave pump field with (generally complex) amplitude A_{in}, the intensity reflectivity and transmissivity coefficients of the coupling mirror (denoted by r_1^2 and t_1^2, respectively) are related by $r_1^2 + t_1^2 = 1$, and δ is the interferometric mistuning. It is convenient to normalize model (3.14) according to $\zeta \equiv z/L$ and $\xi = x/a$, where a is a transverse scale

parameter. After normalization, the governing equation and boundary become

$$\kappa\frac{\partial^2 F_n}{\partial\zeta^2} + i\frac{\partial F_n}{\partial\zeta} + \frac{\sigma}{2}\nabla_\perp^2 F_n + \chi LN(|F_n|^2)F_n = 0, \tag{3.15a}$$

$$F_{n+1}(\boldsymbol{\xi}, 0) = t_1 F_{in} + r_1 \exp(i\delta) F_n(\boldsymbol{\xi}, 1), \tag{3.15b}$$

respectively, where $\kappa = 1/(2kL)$, $\sigma = L/(ka^2)$, and χ flags the sign of the nonlinearity coefficient n_2. Note that we have introduced a generic nonlinearity function $N(|F_n|^2)$. For a Kerr type of nonlinearity, one has that $N(|F_n|^2) \equiv \pm|F_n|^2$; equally, one may introduce other functional forms (e.g., to include a quintic contribution [11, 12] or saturation effects [6, 7, 13, 14]).

Stationary solutions

To identify the stationary solutions, we neglect transverse effects (by setting $\nabla_\perp^2 \to 0$) and seek plane waves of Eq. (3.15a) that have the form $F_n \to F^0(\zeta) \equiv F_0 \exp(ik_\zeta \zeta)$, where k_ζ is the propagation constant and the (complex) amplitude F_0 will eventually be determined from boundary condition (3.15b). Substituting the trial solution for F_n into Eq. (3.15a) yields the quadratic dispersion relation

$$\kappa k_\zeta^2 + k_\zeta - \chi LN(|F_0|^2) = 0, \tag{3.16}$$

which has two solution branches:

$$k_\zeta = \frac{1}{2\kappa}\left[-1 \pm \sqrt{1 + 4\kappa\chi LN(|F_0|^2)}\right]. \tag{3.17}$$

Here, the $\pm$ sign describes waves travelling in the forward $(+)$ and backward $(-)$ longitudinal direction. Since the ring cavity under consideration is uni-directional, we discard backward solutions and select only the positive root of Eq. (3.17). The (forward) stationary states of Eq. (3.15a) are then given by

$$F^0(\zeta) = F_0 \exp\left[i\sqrt{1 + 4\kappa\chi LN(|F_0|^2)}\frac{\zeta}{2\kappa}\right] \exp\left(-i\frac{\zeta}{2\kappa}\right), \tag{3.18a}$$

where

$$F_0 = \frac{t_1 F_{in}}{1 - r_1 \exp(i\Phi)} \tag{3.18b}$$

and $\Phi = \delta + [\sqrt{1 + 4\kappa\chi LN(|F_0|^2)} - 1]/2\kappa$. The stationary states of the paraxial ring cavity model [i.e., $F^0(\zeta) \approx F_0 \exp[i\chi LN(|F_0|^2)z]$ and $\Phi \approx \delta + \chi LN(|F_0|^2)$] can be recovered in the simultaneous double limit $\kappa \ll O(1)$ and $\kappa\chi LN(|F_0|^2) \ll O(1)$. Stationary state characteristics of Helmholtz and paraxial nonlinear ring cavities are shown in figure 3.5. In particular, we note from figure 3.5 that Helmholtz corrections start becoming important in higher-intensity regimes.

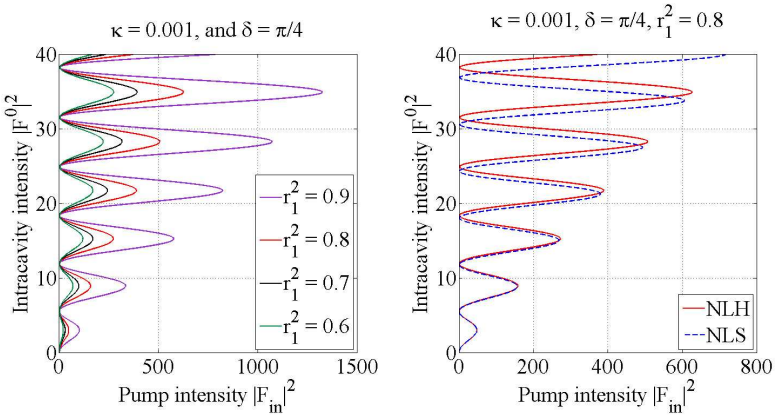

Figure 3.5: The stationary state solution for dispersive bulk ring cavity cavity. The diagram on the left-hand side is the resulting solution when varying values of r_1^2. The pane on the right-hand side illustrates the difference between paraxial (NLS) and Helmholtz (NLH) stationary states, and confirms that the dominant correction in the $K = 0$ solution occurs at higher intensity. Where $l_D = 1$, $\tau = 0$, $\delta = \pi/4$, $L = 1$, $d/k0 = 1$, and $\chi = +1$.

3.2.2 Linear stability analysis

We now use linearization techniques to predict the threshold instability spectrum for static patterns in the Helmholtz ring cavity model [c.f. Eqs. (3.14a) and (3.14b)], following the method established by McLaughlin *et al.* [4]. One begins by assuming a solution of the form

$$F_n(\boldsymbol{\xi},\zeta) = F_0\left[1+\eta f_n(\boldsymbol{\xi},\zeta)\right]\exp\left[i\sqrt{1+4\kappa\chi LN(|F_0|^2)}\frac{\zeta}{2\kappa}\right]\exp\left(-i\frac{\zeta}{2\kappa}\right), \tag{3.19}$$

where $f_n(\boldsymbol{\xi},\zeta)$ is a complex function describing a phase and amplitude modulation and η is a small parameter satisfying $|\eta| \ll O(1)$. In the linear approximation, the intensity I_n is given approximately by $I_n \equiv |F_n|^2 \approx |F^0|^2(1+f_n+f_n^*) = I^0 + \delta I_n$, where $I^0 \equiv |F^0|^2$ and $\delta I_n \equiv I^0(f_n+f_n^*)$. One can now Taylor-expand the generic nonlinearity function $N(I_n)$ around I^0 according to

$$N(I^0+\delta I_n) = N(I^0) + \left(\frac{dN}{dI}\right)_{I=I^0}\delta I_n + \frac{1}{2!}\left(\frac{d^2N}{dI^2}\right)_{I=I^0}(\delta I_n)^2 + ... \tag{3.20}$$

Substituting perturbed solution (3.19) into Eq. (3.15a), linearizing in f_n and cancelling the stationary state [using Eq. (3.16)], it can be shown that

$$\kappa\frac{\partial^2 f_n}{\partial\zeta^2} + i\sqrt{1+4\kappa\chi LN(|F_0|^2)}\frac{\partial f_n}{\partial\zeta} + \frac{\sigma}{2}\nabla_\perp^2 f_n(\boldsymbol{\xi},\zeta)$$

$$+ \chi LN'(|F_0|^2)|F_0|^2[f_n(\boldsymbol{\xi},\zeta) + f_n^*(\boldsymbol{\xi},\zeta)] = 0, \tag{3.21}$$

where $N'(|F_0|^2) \equiv (dN/dI)_{I=I^0}$. Substituting solution (3.19) into boundary condition (3.15b) then yields additional information about the properties of f_n:

$$f_{n+1}(\boldsymbol{\xi},0) = r_1\exp(i\Phi)f_n(\boldsymbol{\xi},1). \tag{3.22}$$

To proceed with the analysis, we consider f_n to be a single Fourier mode with spatial frequency $\boldsymbol{K}$ and complex wavenumber β (whose real and imaginary parts correspond to the propagation

constant and growth rate of f_n, respectively):

$$\begin{aligned} f_n(\xi,\zeta) &= \exp(i\beta\zeta)\left[a_n\exp(i\boldsymbol{K}\cdot\boldsymbol{\xi})+b_n\exp(-i\boldsymbol{K}\cdot\boldsymbol{\xi})\right] \\ &\quad+\exp(-i\beta\zeta)\left[c_n\exp(i\boldsymbol{K}\cdot\boldsymbol{\xi})+d_n\exp(-i\boldsymbol{K}\cdot\boldsymbol{\xi})\right], \end{aligned} \tag{3.23}$$

and where a_n, b_n, c_n, and d_n are complex constants to be determined. Substituting ansatz (3.23) into Eq. (3.21) leads to four auxiliary algebraic equations:

$$-\chi LN'(|F_0|^2)|F_0|^2 d_n^* = \left(-\kappa\beta^2-\epsilon\beta-\frac{\sigma K^2}{2}+\chi LN'(|F^0|^2)|F_0|^2\right)a_n, \tag{3.24a}$$

$$-\chi LN'(|F_0|^2)|F_0|^2 c_n^* = \left(-\kappa\beta^2-\epsilon\beta-\frac{\sigma K^2}{2}+\chi LN'(|F_0|^2)|F_0|^2\right)b_n, \tag{3.24b}$$

$$-\chi LN'(|F_0|^2)|F_0|^2 b_n^* = \left(-\kappa\beta^2+\epsilon\beta-\frac{\sigma K^2}{2}+\chi LN'(|F_0|^2)|F_0|^2\right)c_n, \tag{3.24c}$$

$$-\chi LN'(|F_0|^2)|F_0|^2 a_n^* = \left(-\kappa\beta^2+\epsilon\beta-\frac{\sigma K^2}{2}+\chi LN'(|F_0|^2)|F_0|^2\right)d_n. \tag{3.24d}$$

The parameter β can be obtained by combining Eqs. (3.24a) and (3.24d), in which case

$$(\chi LN'(|F_0|^2)|F_0|^2)^2 = (\alpha+\epsilon\beta)(\alpha-\epsilon\beta), \tag{3.25}$$

where $\alpha \equiv -\kappa\beta^2-\sigma K^2/2+\chi LN'(|F_0|^2)|F_0|^2$. Expanding the right-hand side of Eq. 3.25 leads to a quartic equation for β, namely

$$0 = \kappa^2\beta^4-\left[1+6\kappa\chi LN'(|F_0|^2)|F_0|^2-2\kappa\left(\frac{\sigma K^2}{2}\right)\right]\beta^2+\left(\frac{\sigma K^2}{2}\right)\left[\left(\frac{\sigma K^2}{2}\right)-2\chi LN'(|F_0|^2)|F_0|^2\right]. \tag{3.26}$$

It is interesting to note that Eq. (3.26) describes (thresholdless) modulational instabilities in the scalar nonlinear Helmholtz equation in the absence of cavity feedback [15]. Following Ref. [15], Eq. (3.26) can be simplified to a quadratic (in β^2) by setting $S \equiv \beta^2$:

$$\kappa^2 S^2 - BS + C = 0, \tag{3.27a}$$

where

$$B \equiv 1 + 6\kappa\chi LN'(|F_0|^2)|F_0|^2 - 2\kappa\left(\frac{\sigma K^2}{2}\right) \tag{3.27b}$$

and

$$C \equiv \left(\frac{\sigma K^2}{2}\right)\left[\left(\frac{\sigma K^2}{2}\right) - 2\chi LN'(|F_0|^2)|F_0|^2\right]. \tag{3.27c}$$

Substituting ansatz (3.23) into boundary condition (3.22) yields the following relationships:

$$a_{n+1} + c_{n+1} = r_1 \exp(i\Phi)\left[\exp(i\beta L)a_n + \exp(-i\beta L)c_n\right], \tag{3.28a}$$

$$b_{n+1} + d_{n+1} = r_1 \exp(i\Phi)\left[\exp(i\beta L)b_n + \exp(-i\beta L)d_n\right]. \tag{3.28b}$$

The constants b_n and d_n can now be eliminated [using Eqs. (3.24b) and (3.24c), respectively] from Eq. (3.28b) so that

$$\frac{c^*_{n+1}}{\alpha - \epsilon\beta} + \frac{a^*_{n+1}}{\alpha + \epsilon\beta} = r_1 \exp(i\Phi)\left[\exp(i\beta L)\frac{c^*_n}{\alpha - \epsilon\beta} + \exp(-i\beta L)\frac{a^*_n}{\alpha + \epsilon\beta}\right]. \tag{3.29}$$

which can then be back-substituted into Eq. (3.28a) to give the following relations:

$$a_{n+1} = r_1 \exp(i\beta L)\left(\cos\Phi + iY\sin\Phi\right)a_n + i(1+Y)r_1 \sin\Phi \exp(-i\beta L)c_n, \tag{3.30a}$$

$$c_{n+1} = r_1 \exp(-i\beta L)\left(\cos\Phi - iY\sin\Phi\right)c_n + i(1-Y)r_1 \sin\Phi \exp(i\beta L)a_n, \tag{3.30b}$$

where $Y \equiv \alpha/\epsilon\beta$. From here a 2×2 matrix problem can be formulated:

$$\begin{pmatrix} a_{n+1} \\ c_{n+1} \end{pmatrix} = \mathbf{M} \cdot \begin{pmatrix} a_n \\ c_n \end{pmatrix}, \tag{3.31a}$$

where

$$\mathbf{M} \equiv \begin{bmatrix} r_1 \exp(i\beta L)\left(\cos\Phi + iY\sin\Phi\right) & i(1+Y)r_1 \sin\Phi \exp(-i\beta L) \\ i(1-Y)r_1 \sin\Phi \exp(i\beta L) & r_1 \exp(-i\beta L)\left(\cos\Phi - iY\sin\Phi\right) \end{bmatrix}. \tag{3.31b}$$

The eigenvalues λ of $\mathbf{M}$ can be obtained by solving the characteristic equation $det(\mathbf{M} - \lambda\mathbf{1}) = 0$,

or

$$\begin{vmatrix} M_{11} - \lambda & M_{12} \\ M_{21} & M_{22} - \lambda \end{vmatrix} = 0 \tag{3.32}$$

which is equivalent to the quadratic equation $\lambda^2 - \lambda \mathrm{Tr}\mathbf{M} + \det \mathbf{M} = 0$ [where $\mathrm{Tr}\mathbf{M} = 2r_1 b$, $\det \mathbf{M} = r_1^2$, and $b \equiv \cos\Phi\cos(i\beta L) - Y\sin\Phi\sin(\beta L)$]. The matrix problem then becomes $\lambda^2 - 2r_1 b\lambda + r_1^2 = 0$ so that the threshold condition is met when $\lambda = 1$ (in which case, b is assumed to reach its threshold value $b \to b_{th}$). Since $1 - 2r_1 b_{th} + r_1^2 = 0$, it follows that

$$b_{th} = \frac{1}{2}\left(r_1 + \frac{1}{r_1}\right). \tag{3.33}$$

3.2.2.1 Static threshold curves

The threshold condition for the bulk ring cavity with a Kerr-type host medium is the following:

$$\cos\Phi_{th}\cos(\beta_{th}L) - Y_{th}\sin\Phi_{th}\sin(\beta_{th}L) = \frac{1}{2}\left(r_1 + \frac{1}{r_1}\right). \tag{3.34}$$

Equation (3.34) is analogous to the result found in the classic analysis of McLaughlin *et al.* [4], but with alternative (nonparaxial-type) expressions for Y_{th} and β_{th}. Plots of threshold instability spectra for a focusing (defocusing) Kerr nonlinearity are shown in figure 3.6 [figure 3.7]. We also point out that the instability at $K = 0$ maps directly onto the unstable middle branches of the stationary state curve, as expected [see figure 3.8].

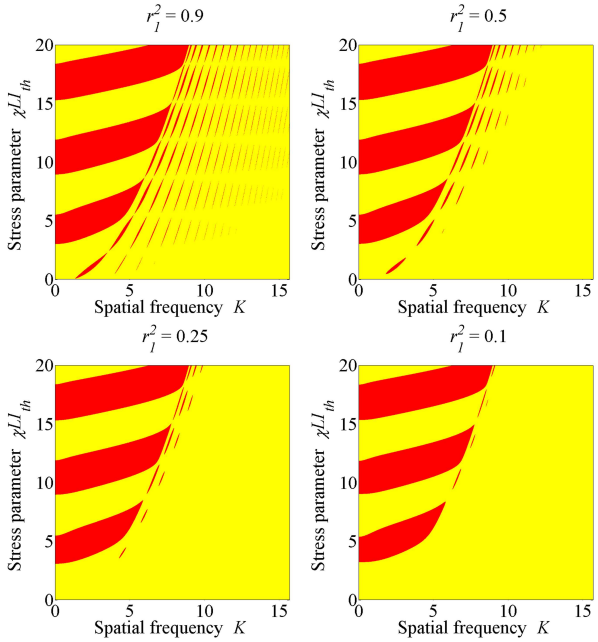

Figure 3.6: Static threshold curves of the bulk ring cavity in a defocusing medium where $\kappa = 0.001$, $\sigma = 0$, $\delta = \pi/4$, $L = 1$, $d/k0 = 1$, and $\chi = +1$.

Here, χIL plays the same role as before (the stress parameter) and it still has units of (paraxial) nonlinear phase shift. In the case of the self-focusing (self-defocusing) medium, χ is assigned the value of $+1$ (-1).

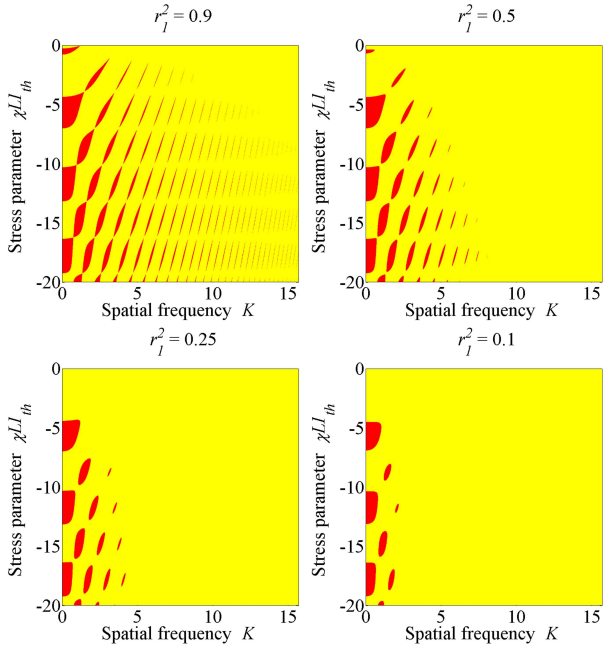

Figure 3.7: Static threshold curves of the bulk ring cavity in a defocusing medium where $\kappa = 0.001$, $\sigma = 0$, $\delta = \pi/4$, $L = 1$, $d/k0 = 1$, and $\chi = -1$.

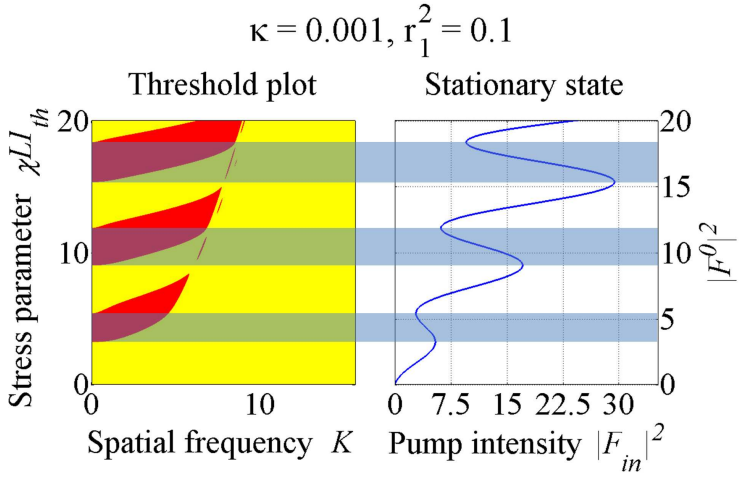

Figure 3.8: Static threshold curves compared to the switching points within the stationary state where $\kappa = 0.001$, $r_1^2 = 0.9$, $\sigma = 0$, $\delta = \pi/4$, $L = 1$, $d/k0 = 1$, and $\chi = +1$.

An alternative way to visualize how the two cavity models (nonlinear Helmholtz and nonlinear Schrödinger) differ from one another is by comparing the differences between two threshold plots for similar system parameters (see figure 3.9). The bands indicate where the two results

disagree. At low-K (large pattern scales) and small κ (long cavities), there tends to be more of an agreement between the models (since the paraxial and Helmholtz diffraction operators are convergent in those regimes).

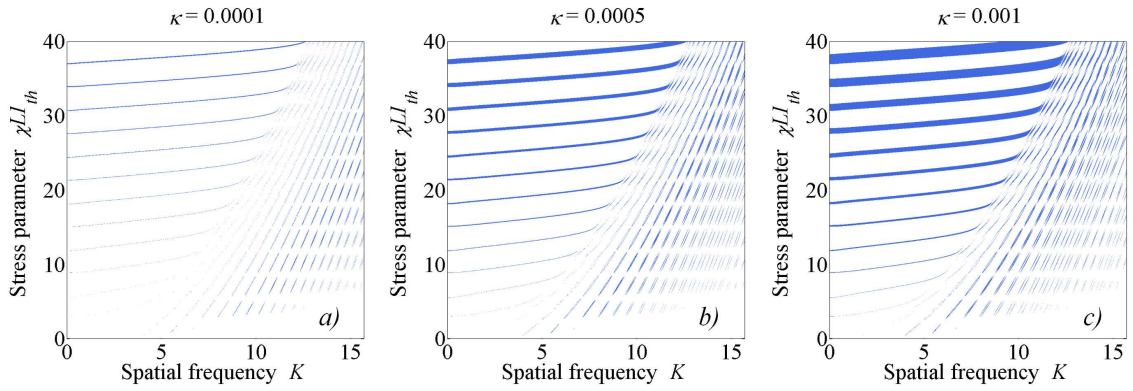

Figure 3.9: NLH and NLS threshold variations, the blue element of the figure indicates the differences in the resulting threshold plots between the two models, when $r_2^2 = 0.9$, $\sigma = 0$, $\delta = \pi/4$, $L = 1$, $d/k0 = 1$, and $\chi = +1$.

3.2.3 Simulations

The preliminary simulation of the Helmholtz bulk ring cavity with one and two transverse dimensions is discussed in this section. In contrast to numerics in the previous section, simulating a ring cavity with a bulk medium in the absence of the slowly-varying envelope approximation (SVEA) is much more involved than in thin-slice systems. Here, numerical methods such as Feit-Fleck [8] and difference-differential [8, 16] are implemented to calculate the field during each transit. The transverse x domain has been configured to accommodate predefined number of integer number of most-unstable-wavelengths. Again, this allows the most unstable spatial frequencies to grow in the cavity freely (i.e., without "*feeling*" the transverse periodic boundaries). Computationally there are several steps to the numerical calculation:

1. Initialization of a stationary state of the system (Eq. 3.3) plus a small level of filtered noise.

2. Implementation of the Feit-Fleck method to estimate the field at the first longitudinal step.

3. Deployment of the difference-differential method up until the boundary condition.

4. Application of the boundary condition.

5. Implementation of the Feit-Fleck method to generate the second step after the boundary condition.

6. Deployment of the difference-differential method up until the boundary condition.

7. Repeating steps 2–6 over the desired number of transits.

The algorithms implemented throughout simulation of the bulk ring cavity included the Feit-Fleck and difference-differential methods. The Feit-Fleck method consists of splitting the evolution operator into separate stages, sandwiching a nonlinear step between two linear half-steps [the latter being computed using Fast Fourier transforms (FFTs)]. This symmetrized algorithm results in a more accurate numerical solution. The difference-differential method

deploys centred finite-difference approximations to replace the longitudinal derivatives ($\partial/\partial\zeta$ and $\partial^2/\partial\zeta^2$), and the transverse diffraction operator ($\partial^2/\partial\xi^2$) is computed usings FFTs [16].

The difference-differential method is generally a very accurate and robust numerical scheme [16]. In recent years higher-order numerical methods have also been developed to solve the nonlninear Helmholtz equation in layered media which could be potentially used to reduce the error even further [17, 18].

A low level of noise is initially added to the system to accelerate the pattern-forming process. The reason for filtering the noise is to accommodate (as closely as possible) the periodic boundary conditions required by FFTs. Filtering is achieved by multiplying a white noise profile by a Gaussian function in Fourier space. Attenuating the highest frequencies produces coloured noise which is then implemented in the simulation. We note that patterns would still emerge *without* this random component to the initial solution (with finite numerical accuracy providing symmetry-breaking perturbations), but many tens (or hundreds) of thousands of transits may be required. Pattern formation in the bulk ring cavity is qualitatively similar to that in the FP problem, with allowed spatial frequencies competing for growth. Eventually, however, the most-unstable frequency K_0 will dominate since it has the lowest threshold and therefore the highest growth rate.

Simple pattern formation

Pattern formation within the Helmholtz bulk ring cavity model is qualitatively identical to that in other systems (see Chapter 2). A strong quantitative difference is the number of transits required in order for static patterns to emerge: from a few hundred in thin-slice system to several thousand in the bulk model. Typical simple pattern formation with one transverse dimension (1D) and a focusing Kerr nonlinearity is shown in figure 3.10, where the cavity is initialized at 25% above threshold. The corresponding simulation in 2D (where all cavity parameters retain their previous values from the 1D calculation) is shown in figure 3.11. The static structure that emerges is more complicated than a simple hexagon pattern. It involves two interlocked hexagons patterns, one of which involves circular filaments and the other elliptical filaments.

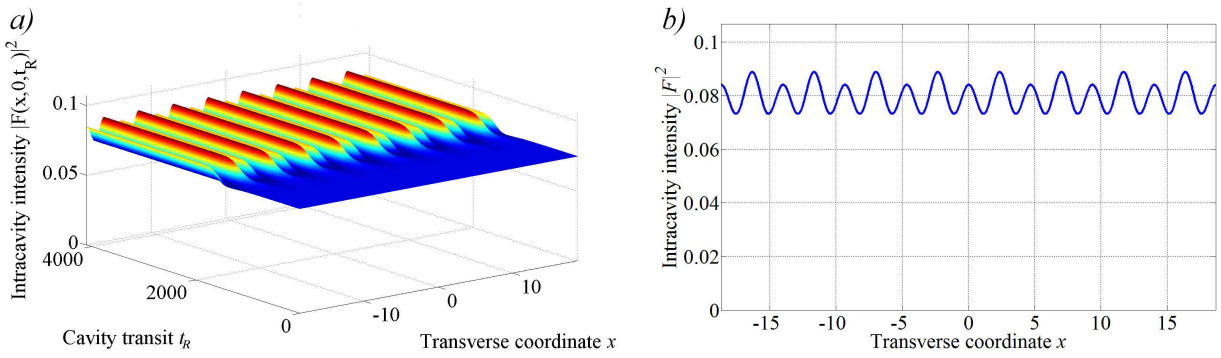

Figure 3.10: 1D pattern formation within the Helmholtz bulk ring cavity with a focusing Kerr nonlinearity when $r_1^2 = 0.9$, $I_0 = 0.072$, $K_0 = 1.347$, $K_C = 3.5$, $\sigma = 0$, $\delta = \pi/4$, $L = 1$, $d/k0 = 1$, and $\chi = +1$.

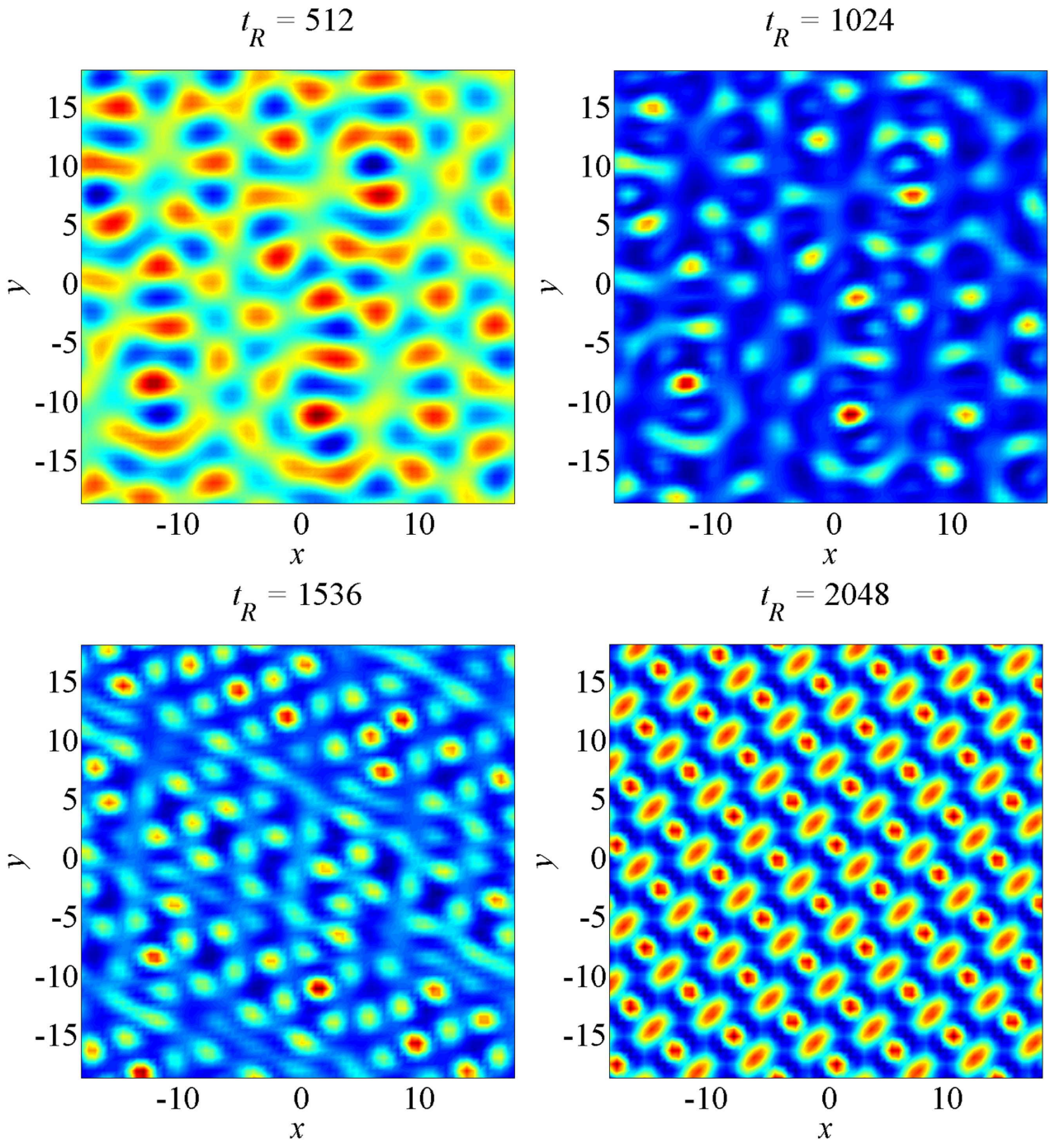

Figure 3.11: 2D pattern formation within the Helmholtz bulk ring cavity with a focusing Kerr nonlinearity where $r_1^2 = 0.9$, $I_0 = 0.072$, $K_0 = 1.347$, $K_C = 3.5$, $\sigma = 0$, $\delta = \pi/4$, $L = 1$, $d/k0 = 1$, and $\chi = +1$.

Fractal pattern formation

Intensive simulations of system 3.15 have demonstrated that simple patterns do not undergo a transition to fractal patterns when the spatial filter is adjusted. One explanation for this surprising result may lies with the threshold itself. When attempting to initialize a scenario where the cavity is expected to show a transition from simple to a fractal patterns, one must adjust the filter so that the circulating field has unhindered access to its full (physically-meaningful) bandwidth. In addition to allowing more spatial frequencies to propagate (and thereby participate in wave-mixing processes), one is also required to be above the intensity threshold. In the case of the bulk cavity, one has to operate above the intensity minimum of the *second* spectral band, as shown in figure 3.12 (otherwise the system is operating without any additional Turing instabilities once the filter is removed). In the case of the bulk cavity, observing the transition to fractality means initializing at $\approx 700\%$ above the threshold associated with the first minimum. In such regimes, numerical instabilities appear to take over the system.

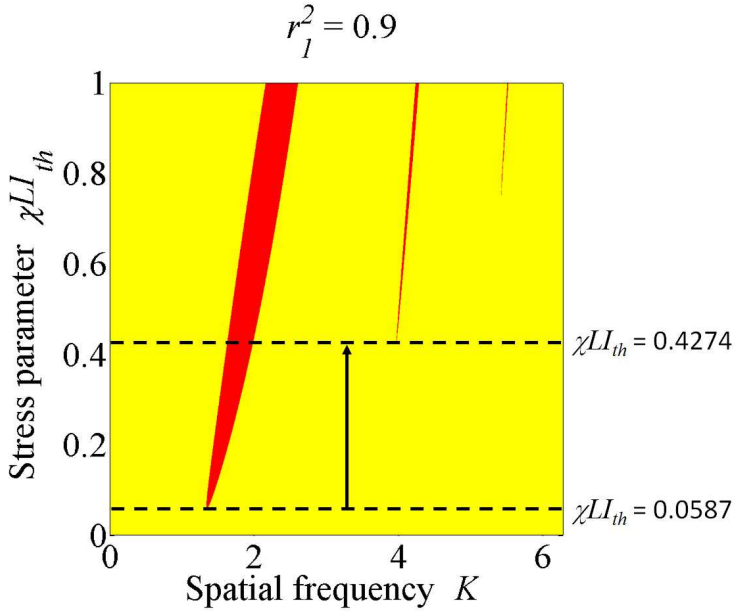

Figure 3.12: Threshold condition of the bulk ring cavity showing the intensity difference of the first two spectral bands where $r_2^2 = 0.9$, $\sigma = 0$, $\delta = \pi/4$, $L = 1$, $d/k0 = 1$, and $\chi = +1$.

The subsequent simulations demonstrate how higher intensities can rapidly develop into instability. In figure 3.13, the cavity was initialized at approximately half of the intensity

threshold of the second spectral band. The field was in the process of localizing preferentially into a simple (regular) pattern of filaments up until approximately 250 transits, after which point the solution becomes highly erratic. As the initialization intensity is increased, the growth rate of the numerical instability increases still further (as shown in figure 3.14, initialized at just above the second minimum). In such regimes (i.e., so far above threshold), the cavity does not even produce a simple pattern (so the transition to fractality is not really meaningful). It should be noted that alternatives to the Helmholtz filter were also used (for instance, top-hat and super-Gaussian forms [19]).

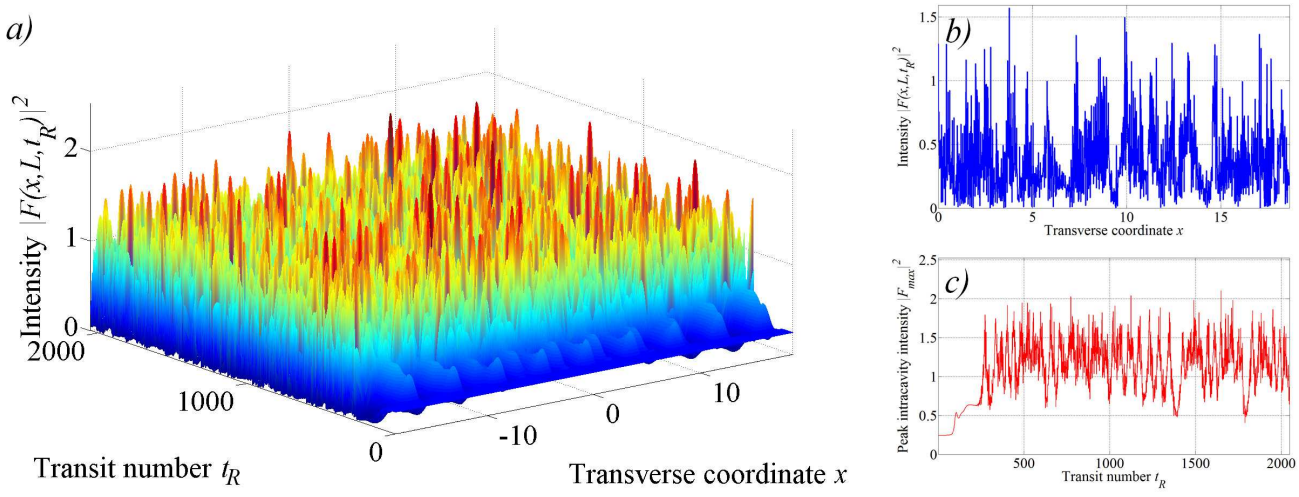

Figure 3.13: A 1D simulation for the Helmholtz bulk ring cavity with a focusing Kerr nonlinearity, where $r_1^2 = 0.9$, $I_0 = 0.24$, $K_0 = 1.347$, $K_C = 3.5$, $\sigma = 0$, $\delta = \pi/4$, $L = 1$, $d/k0 = 1$, and $\chi = +1$. Here, b) is the resulting field profile at the end of the simulation, and c) is the peak intensity of the field at each transit.

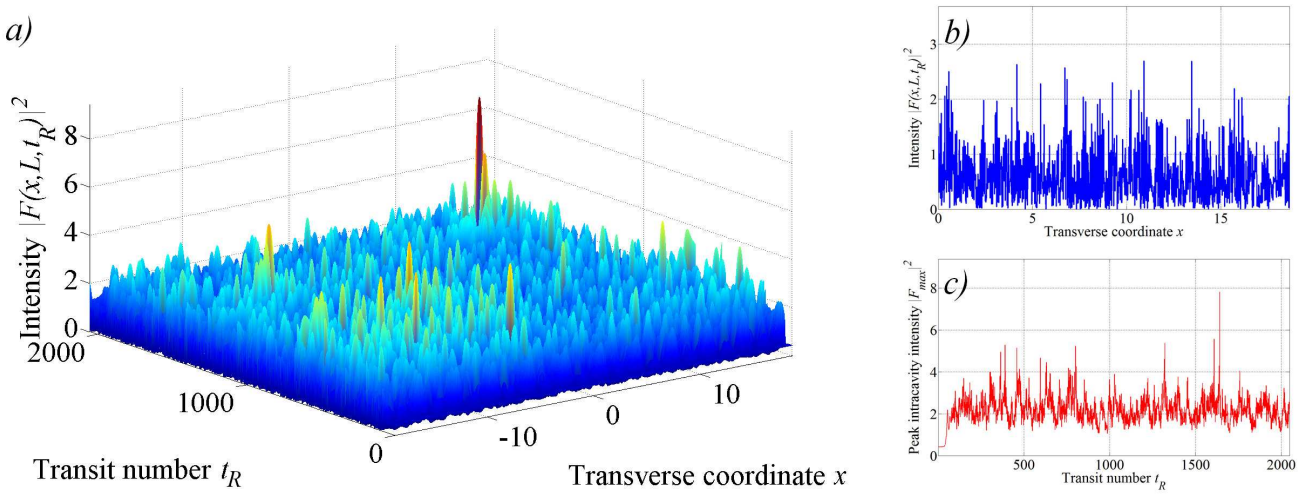

Figure 3.14: A 1D simulation for the Helmholtz bulk ring cavity with a focusing Kerr nonlinearity, where $r_1^2 = 0.9$, $I_0 = 0.42$, $K_0 = 1.347$, $K_C = 3.5$, $\sigma = 0$, $\delta = \pi/4$, $L = 1$, $d/k0 = 1$, and $\chi = +1$. Here, b) is the resulting field profile at the end of the simulation, and c) is the peak intensity of the field at each transit.

The absence of simple pattern emergence and the unexpected appearance of the numerical instability may be due to the limitations of the "lumped" model. In the classic approach, the cavity boundary condition is applied once per transit (at the start of each round trip). One possibility that might help explain the instability in the Helmholtz bulk ring cavity is that 'time' cannot be so easily eliminated by taking the continuous-wave limit when one: (i) goes beyond the slowly-varying envelope approximation, and (ii) operates at higher intensities. It would be interesting, then, to model the cavity and pattern-formation processes using a full finite difference time domain (FDTD) approach.

3.3 Ultranarrow-beam modelling

Following the analysis of the bulk ring cavity beyond the SVEA, an obvious extension is to investigate a more complete Helmholtz-type system where a set of leading-order ultranarrow-beam corrections are retained within the model equations. These leading order corrections, considered by Chi and Guo [20], are obtained from an order-of-magnitude analysis of vector nonlinear Maxwell equations. They are derived from the accommodation of additional terms originating in the nonlinear polarization $\mathbf{P}_{NL}$ and the divergence term $\nabla(\nabla\cdot\mathbf{P}_{NL})$. The aim of considering this model is to predict how ultranarrow-beam terms modify the Turing threshold spectrum, and to determine if the modifications to the spectrum will allow for fractal formation.

3.3.1 Model equations

The model equation for the ultranarrow-beam ring cavity is [20]

$$\frac{\partial^2 A_n}{\partial z^2} + i2k\frac{\partial A_n}{\partial z} + \nabla_\perp^2 A_n + \frac{\omega^2}{c^2}2n_0 n_2 |A_n|^2 A_n$$

$$+ 2\frac{n_2}{n_0}\left[\frac{\partial^2}{\partial x^2}(|A_n|^2 A_n) + \frac{2}{3}\left|\frac{\partial A_n}{\partial x}\right|^2 A_n - \frac{1}{3}\left(\frac{\partial A_n}{\partial x}\right)^2 A_n^*\right] = 0, \tag{3.35}$$

where all the symbols retain their earlier definitions. By using the same normalization as for the pure-Helmholtz model [c.f., Eq. (3.15a)], one can arrive at the following dimensionless governing equation:

$$\kappa\frac{\partial^2 F_n}{\partial \zeta^2} + i\frac{\partial F_n}{\partial \zeta} + \frac{\sigma}{2}\nabla_\perp^2 F_n + \chi L|F_n|^2 F_n$$

$$+ \gamma\chi L\left[\frac{\partial^2}{\partial \xi^2}(|F_n|^2 F_n) + \frac{2}{3}\left|\frac{\partial F_n}{\partial \xi}\right|^2 F_n - \frac{1}{3}\left(\frac{\partial F_n}{\partial \xi}\right)^2 F_n^*\right] = 0, \tag{3.36a}$$

$$F_{n+1}(\boldsymbol{\xi}, 0) = t_1 F_{in} + r_1 \exp(i\delta) F_n(\boldsymbol{\xi}, 1), \tag{3.36b}$$

where, numerically, $\gamma \equiv 2\kappa$ but we retain a separate symbol in order to be able to distinguish contributions from the Helmholtz term (i.e., $\kappa\partial^2 F_n/\partial\zeta^2$) and the ultranarrow-beam terms.

The plane waves of Eq. 3.36a are identical to the those of the Helmholtz model [c.f., Eqs. 3.15a] (since the three ultranarrow-beam terms always sum to zero for such solutions). The perturbed solution is now defined to be

$$F(\boldsymbol{\xi},\zeta) = F_0[1+\eta f_n(\boldsymbol{\xi},\zeta)]\exp\left[i\sqrt{1+4\kappa\chi L|F_0|^2}\frac{\zeta}{2\kappa}\right]\exp\left(-i\frac{\zeta}{2\kappa}\right), \tag{3.37}$$

where the perturbation $f_n(\boldsymbol{\xi})$ is a complex function with order-unity magnitude that describes the phase and amplitude modulation and η is a small parameter satisfying $\eta \ll O(1)$. Following the prescription in the pure-Helmholtz analysis, the linearized master equation can be obtained by substituting perturbed solution (3.37) into Eq. (3.36a), keeping terms up to f_n and cancelling the plane wave component:

$$\kappa\frac{\partial^2 f_n}{\partial\zeta^2} + i\sqrt{1+4\kappa\chi LN(|F_0|^2)}\frac{\partial f_n}{\partial\zeta} + \frac{\sigma}{2}\nabla_\perp^2 f_n(\boldsymbol{\xi},\zeta)$$

$$+ \chi L|F_0|^2[f_n(\boldsymbol{\xi},\zeta) + f_n^*(\boldsymbol{\xi},\zeta)] + \gamma\chi L|F_0|^2\left(2\frac{\partial^2 f_n}{\partial\xi^2} + \frac{\partial^2 f_n^*}{\partial\xi^2}\right) = 0. \tag{3.38}$$

To proceed, f_n is treated as a single Fourier mode with spatial frequency $\boldsymbol{K}$ and complex wavenumber β. Substituting ansatz (3.22) into Eq. (3.28a) yields the following set of algebraic equations:

$$-\chi L|F_0|^2(1-K^2\gamma)d_n^* = \left[-\kappa\beta^2 - \epsilon\beta - \frac{\sigma K^2}{2} + \chi L|F_0|^2(1-2K^2\gamma)\right]a_n, \tag{3.39a}$$

$$-\chi L|F_0|^2(1-K^2\gamma)c_n^* = \left[-\kappa\beta^2 - \epsilon\beta - \frac{\sigma K^2}{2} + \chi L|F_0|^2(1-2K^2\gamma)\right]b_n, \tag{3.39b}$$

$$-\chi L|F_0|^2(1-K^2\gamma)b_n^* = \left[-\kappa\beta^2 + \epsilon\beta - \frac{\sigma K^2}{2} + \chi L|F_0|^2(1-2K^2\gamma)\right]c_n, \tag{3.39c}$$

$$-\chi L|F_0|^2(1-K^2\gamma)a_n^* = \left[-\kappa\beta^2 + \epsilon\beta - \frac{\sigma K^2}{2} + \chi L|F_0|^2(1-2K^2\gamma)\right]d_n. \tag{3.39d}$$

The propagation constant β can be obtained using the same technique as before, i.e., by substituting Eq. (3.39a) into Eq. (3.39d) to produce

$$\left[\chi L|F_0|^2(1-K^2\gamma)\right]^2 = (\alpha-\epsilon\beta)(\alpha+\epsilon\beta), \tag{3.40}$$

where

$$\alpha = -\kappa\beta^2 - \frac{\sigma K^2}{2} + \chi L|F_0|^2(1-2K^2\gamma). \tag{3.41}$$

Expanding Eq. 3.40 leads to a quartic equation for β, which can be simplified to a quadratic in β^2 by defining the relation $S \equiv \beta^2$:

$$0 = \kappa^2 S^2 - BS + C, \tag{3.42}$$

where

$$B \equiv 1 + 6\kappa\chi L|F_0|^2 - 2\kappa\left(\frac{\sigma K^2}{2} + 2K^2\gamma\chi L|F_0|^2\right), \tag{3.43a}$$

and,

$$C \equiv \left(\frac{\sigma K^2}{2}\right)\left[\left(\frac{\sigma K^2}{2}\right) - 2\chi L|F_0|^2(1-2K^2\gamma)\right] - 2K^2\gamma\left(\chi L|F_0|^2\right)^2\left(1-\frac{3}{2}K^2\gamma\right). \tag{3.43b}$$

The analysis from this point onward is unchanged from the pure-Helmholtz calculation of the previous section. As a result of this, the threshold condition for the ultranarrow-beam scenario is given by

$$\cos\Phi_{th}\cos(\beta_{th}L) - Y_{th}\sin\Phi_{th}\sin(\beta_{th}L) = \frac{1}{2}\left(r_1 + \frac{1}{r_1}\right), \tag{3.44}$$

While the analysis of this system produces a result with the same formal structure as Eq. (3.34), the parameters α, and β have different definitions resulting in two unique threshold conditions. In the limit that nonparaxial contributions can be neglected, we can easily recover the paraxial Turing spectrum (a physical and mathematical requirement).

3.3.2 Nonparaxial Turing instability spectrum

In considering the stability of plane waves of cavity system 3.36a, we have been able to derive an analytical expression for the Turing spectrum in the presence of both Helmholtz and ultranarrow-beam nonparaxiality. The spectra plotted in figure 3.15 demonstrates that in the long-wavelength (i.e., low-K) range and for low intensities (i.e., close to the first instability island), the predictions of McLaughlin *et al.* [4] hold true. That is, the scalelength of any emergent *simple* patterns (which are, by definition, dominated by a single spatial frequency) tend to be largely the same in both paraxial and nonparaxial regimes. Moreover, high spatial frequencies tend to be filtered out during the initial stages of pattern formation (where one is waiting for the emergence of a simple structure from the perturbed plane-wave solution).

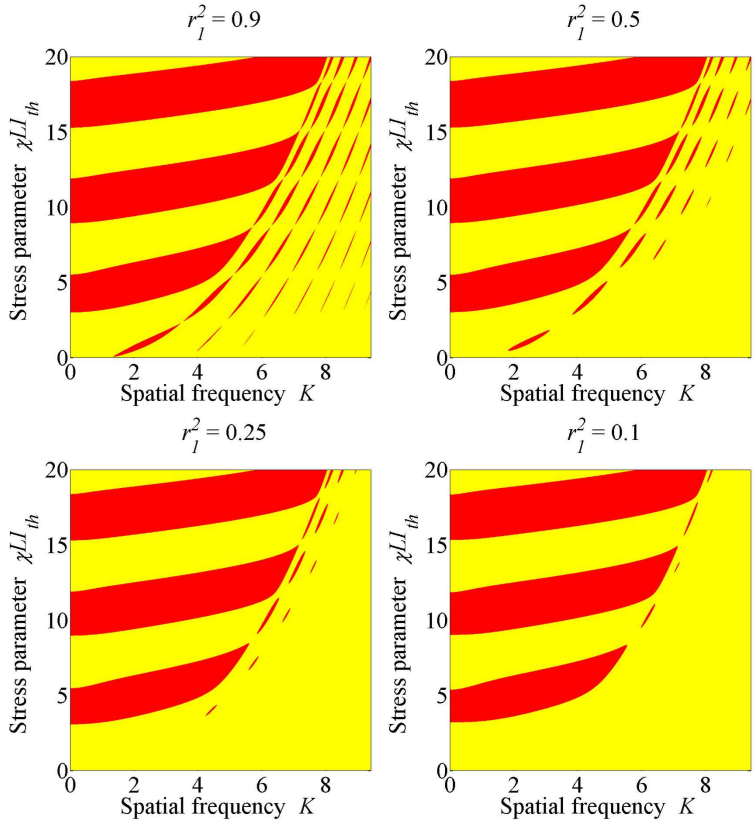

Figure 3.15: Static threshold instability curves of the ultranarrow-beam Helmholtz ring cavity in a focusing medium where $\kappa = 0.001$, $\sigma = 0$, $\delta = \pi/4$, $L = 1$, $d/k0 = 1$, and $\chi = +1$.

To compare how the purely-Helmholtz and ultranarrow-beam Turing threshold spectra differ from one another, figure 3.16 plots areas of disagreement between the two predictions. The

main differences appear at higher spatial frequencies and higher intensities.

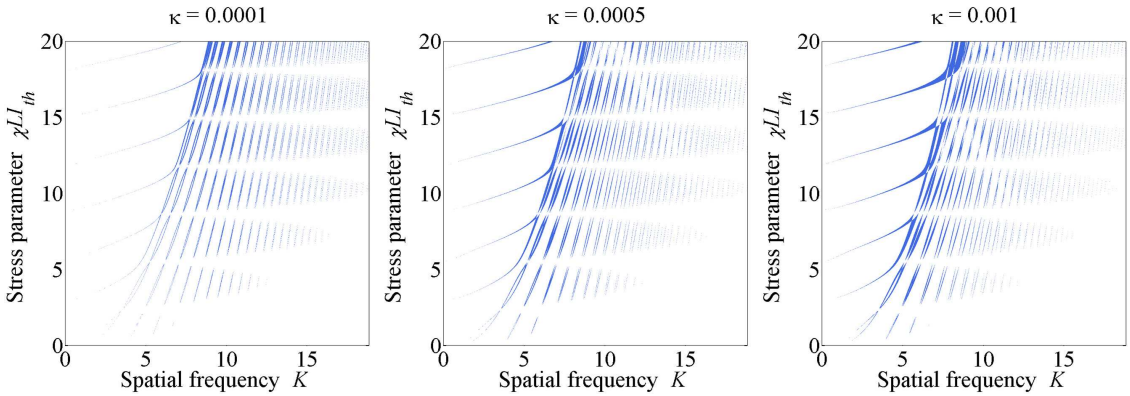

Figure 3.16: NLH and UNB threshold variations, the blue element of the figure indicates the differences in the resulting threshold plots between the two models, where $r_2^2 = 0.9$, $\sigma = 0$, $\delta = \pi/4$, $L = 1$, $d/k0 = 1$, and $\chi = +1$

3.4 Conclusion

In this Chapter, we have analyzed the threshold condition for (static) Turing patterns in a dispersive ring cavity when the host medium has a finite length. The representation of the instability spectrum differs from that of McLaughlin *et al.* [4], whose represented pattern formation in terms of a system parameter crossing a "gain = loss" line. The main step forward has been to consider a more complete description of diffraction in two distinct but related nonparaxial contexts.

Firstly, we have gone beyond the SVEA and proposed a scalar Helmholtz model for pattern formation. The analytical approach taken to finding the Turing spectrum has followed the traditional ansatz prescription and resulted in an expression for the threshold condition which is formally identical to that in paraxial theory (though with very different parameter definitions) [4]. The qualitative properties of the paraxial Turing spectrum remain, with the main quantitative corrections occurring (as expected) at high spatial frequencies and high intensities – precisely those regimes wherein one expects paraxial-based descriptions of small-scale spatial features to fail. While the long-wave characteristics of the pure-Helmholtz Turing spectrum do not tend to change significantly (compared with paraxial predictions [4]), some fairly extensive simulation work has demonstrated the existence of unanticipated numerical instabilities in higher-intensity regimes (where one would otherwise expect to find fractal patterns).

Secondly, we have started to develop models based on ultranarrow-beam arguments. These considerations are inherently vector in nature: in addition to the dominant transverse electric field component, a smaller longitudinal component is also required so that Maxwell's equations can be satisfied more rigorously. In the context of simple pattern formation, the most-unstable frequency (and its corresponding wavelength) are almost unchanged. However, we expect this family of (leading-order) correction terms to become important when describing wavelength-scale spatial structure in the circulating cavity field. It is notable that both pure-Helmholtz and ultranarrow-beam corrections to the Turing spectrum of paraxial theory are parametrized by a single number (that is, κ) and the largest corrections are found in those regimes where the assumptions of paraxial theory are bound to fail. Simulations to investigate the pattern-forming properties of the ultranarrow-beam Helmholtz cavity model have not yet been performed. It

is possible that the higher-order nonlinear-derivative terms in system (3.36) may help suppress the numerical instabilities encountered in the pure-Helmholtz regime.

References

[1] J. G. Huang and G. S. McDonald. Spontaneous optical fractal pattern formation. *Physical Review Letters*, 94(17):174101, 2005.

[2] W. J. Firth and C. Paré. Transverse modulational instabilities for counterpropagating beams in Kerr media. *Optics Letters*, 13(12):1096–1098, 1988.

[3] J. B. Geddes, R. A. Indik, J. V. Moloney, and W. J. Firth. Hexagons and squares in a passive nonlinear optical system. *Physical Review A*, 50(4):3471, 1994.

[4] D. W. McLaughlin, J. V. Moloney, and A. C. Newell. New class of instabilities in passive optical cavities. *Physical Review Letters*, 54(7):681, 1985.

[5] J. G. Huang, J. M. Christian, C. Bostock, and G. S McDonald. Spontaneous spatial optical fractals in ring cavities. *Manuscript in preparation*, 2015.

[6] J. G. Huang. *Spontaneous optical fractals in linear & nonlinear systems*. Ph.D thesis, University of Salford, 2006.

[7] J. G. Huang, J. M. Christian, and G. S. McDonald. Spontaneous spatial fractal pattern formation in absorptive systems. *Journal of Nonlinear Optical Physics & Materials*, 21(02): art. no. 1250018, 2012.

[8] M. D. Feit and J. A. Fleck Jr. Beam nonparaxiality, filament formation, and beam breakup in the self-focusing of optical beams. *Journal of the Optical Society of America B*, 5(3): 633–640, 1988.

[9] P. Chamorro-Posada, G. S. McDonald, and G. H. C. New. Non-paraxial solitons. *Journal of Modern Optics*, 45(6):1111–1121, 1988.

[10] P. Chamorro-Posada, G. S. McDonald, and G. H. C. New. Propagation properties of non-paraxial spatial solitons. *Journal of Modern Optics*, 47(11):1877–1886, 2000.

[11] J. M. Christian, G. S. McDonald, and P. Chamorro-Posada. Bistable Helmholtz solitons in cubic-quintic materials. *Physical Review A*, 76(3B):033833, 2007.

[12] K. I. Pushkarov, D. I. Pushkarov, and I. V. Tomov. Self-action of light beams in nonlinear media: soliton solutions. *Optical and Quantum Electronics*, 11(6):471–478, 1979.

[13] A. S. Patrascu, C. Nath, M. Le Berre, E. Ressayre, and A Tallet. Multi-conical instability in the passive ring cavity: linear analysis. *Optics Communications*, 91(5):433–443, 1992.

[14] M. Le Berre, A. S. Patrascu, E. Ressayre, and A. Tallet. Daisy patterns in the passive ring cavity with diffusion effects. *Optics Communications*, 123(4):810–824, 1996.

[15] J. M. Christian, G. S. McDonald, and P. Chamorro-Posada. Helmholtz bright and boundary solitons. *Journal of Physics A: Mathematical and Theoretical*, 40 (7):1545–1560, 2007.

[16] P. Chamorro-Posada, G. S. McDonald, and G. H. C. New. Non-paraxial beam propagation methods. *Optics Communications*, 192(1):1–12, 2001.

[17] G. Baruch, G. Fibich, and S. Tsynkov. High-order numerical method for the nonlinear Helmholtz equation with material discontinuities in one space dimension. *Journal of Computational Physics*, 227(1)(820–850), 2007.

[18] G. Baruch, G. Fibich, and S. Tsynkov. A high-order numerical method for the nonlinear Helmholtz equation in multidimensional layered media. *Journal of Computational Physics*, 228(10)(3789–3815), 2009.

[19] C. Bostock. Two-colour Helmholtz solitons with a defocusing Kerr nonlinearity. Master's thesis, University of Salford, 2011.

[20] S. Chi and Q. Guo. Vector theory of self-focusing of an optical beam in Kerr media. *Optics Letters*, 20(15):1598–1600, 1995.

Chapter 4

Absorptive ring cavity

Chapters 2 and 3 have considered the fractal-generating signature proposed by Huang and McDonald [1] in two very different configurations: the thin-slice FP cavity and the filled ring cavity. In both cases, the system nonlinearity was taken to be purely dispersive and of the Kerr type. In the interests of testing the multi-Turing signature more widely, it is necessary to extend these considerations to different classes of media.

In this Chapter, we consider a two-level Maxwell-Bloch saturable absorber. The model deployed is a simplified version of the full system analyzed by Patrascu *et al.* [2, 3], whereby the polarization material variable has been adiabatically eliminated. The population-difference variable has been retained, and to reduce the overall complexity of the linear analysis we focus on the thin-slice geometry. Diffusion is introduced phenomenologically [4], so that the ring cavity behaves like a two-component reaction-diffusion system (with a cavity boundary condition capturing longitudinal periodicity).

The analysis undertaken here generalizes that of Huang *et al.* [1, 5, 6], mainly by incorporating a longitudinal dependence to the perturbation Fourier amplitudes. In so-doing, one is able to develop a (physically and mathematically) more self-consistent description of the reduced system, and the Turing threshold condition is found to be identical to its earlier incarnation [5]. Attention will be paid mainly to purely-absorptive regimes, but a detuning parameter is included to accommodate dispersion. A subsequent analysis also takes the first steps toward understanding fractal pattern formation in slab (i.e., bulk) configurations, where the light-medium interaction length is finite and cannot be treated within the thin-slice approximation.

Summary of parameters and variables

d	Free-space path length
f	Complex perturbations for the forwards propagating field
F_0	Uniform State of F
F_n	Forward propagating electric field
F_{in}	Amplitude of the plane wave pump field
I_{th}	Intensity threshold
k	Wave number
$\boldsymbol{K}$	Transverse spatial frequency
K_C	High frequency cut-off
K_0	Most unstable frequency
k_ζ	Dispersion relation
$2\pi/k_0$	Free-space wavelength of the pump light
L	Length of the cavity
l_D	Diffusion length
r_1^2	Intensity reflectivity of the slice mirror
R_1^2	Lumped loss parameter
t	Time co-ordinate
t_R	Transit time
t_1^2	Intensity transmissivity
T_1	Relaxation time of ω
T_2	Dephasing time of the polarization
z	Longitudinal space co-ordinate
α_0	Absorption coefficient
β	Longitudinal wavevector
γ	Complex propagation constant
δ	Linear interferometric mistuning
Δ	Detuning parameter
θ	Phase/propagation factor
κ	is defined to equal $1/(2kL)$
λ	Complex Lyapunov exponent
Λ	Growth rate
σ	is defined to equal $L/(ka^2)$
Φ	Total (linear and nonlinear) mistuning
ω	Population difference
ω_0	Uniform state of ω
Ω	Temporal frequency
$\nabla_\perp^2$	Transverse Laplacian

4.1 Review of the thin-slice geometry

In this section, we undertake a comprehensive review of a ring cavity containing a thin slice of nonlinear material that, in addition to dispersion, also allows for absorption (see figure 4.1). A linear analysis of this system is expected to yield the threshold condition for predicting the onset of pattern-formation instabilities.

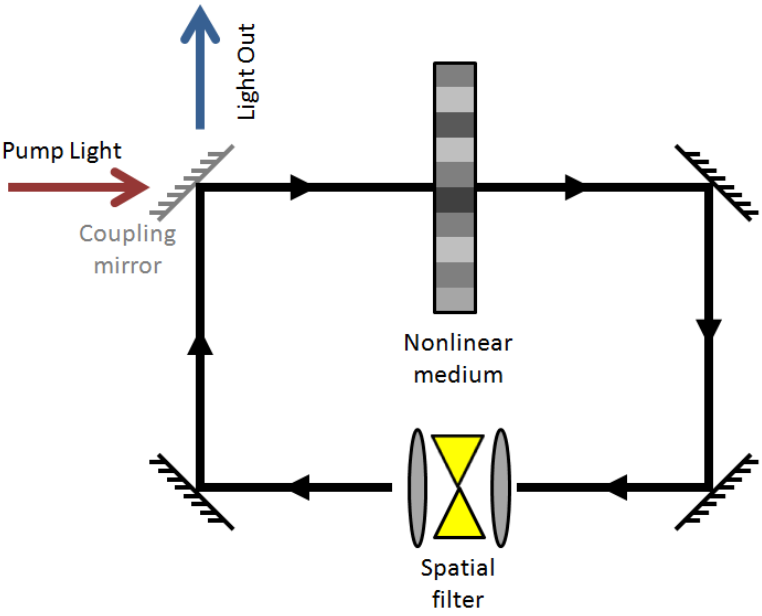

Figure 4.1: Schematic diagram of a nonlinear ring cavity.

Model equations

The coupled field-medium dynamics within the slice are governed by

$$\frac{\partial F}{\partial z} = \left(\frac{\alpha_0}{2}\right)\frac{Fw}{1+i\Delta}, \tag{4.1a}$$

$$T_1\frac{\partial w}{\partial t} - l_D^2\nabla_\perp^2 w + (1+w) = -\frac{T_1T_2}{1+\Delta^2}|F|^2 w, \tag{4.1b}$$

where F is the electric field envelope and w is the population difference, t denotes time, z is the longitudinal coordinate, and $\nabla_\perp^2$ is the transverse Laplacian. The relaxation time T_1 for w is assumed to be much longer than the dephasing time T_2 for the polarization so that

$T_2 \ll T_1$. Other parameters are the absorption coefficient α_0 and the detuning parameter Δ (which quantifies the difference between the pump and atomic-resonance frequencies). The Maxwell-Bloch model in Eqs. (4.1a) and (4.1b) may be either purely absorptive (where $\Delta = 0$) or perdominantly dispersive (where $|\Delta| \gg O(1)$).

The boundary condition for the absorptive cavity has the same formal structure as in the purely-dispersive case, namely

$$F(\boldsymbol{x}, 0, t) = t_1 F_{in} + r_1 \exp(i\delta) \exp\left(i \frac{d}{2k_0} \nabla_\perp^2\right) F(\boldsymbol{x}, L, t - t_R), \tag{4.2}$$

where r_1^2 and t_1^2 are the intensity reflectivity and transmissivity coefficients (related by $r_1^2 + t_1^2 = 1$), respectively, and δ is the interferometric mistuning parameter. In the limit of weak absorption, where w is assumed to be constant across the slice, Eqs. (4.1) and (4.2) have the following (approximate) stationary solution:

$$F^0(z) \simeq F_0 \exp(\gamma z), \quad w_0 \simeq -\frac{1 + \Delta^2}{1 + \Delta^2 + T_1 T_2 |F_0|^2}, \quad \text{and} \quad \gamma \equiv \left(\frac{\alpha_0 w_0}{2}\right) \frac{1}{1 + i\Delta}. \tag{4.3a}$$

Here, γ is a complex propagation constant describing the amplitude and phase modulation of the wave incident on the input face of the slice. As before, the complex amplitude F_0 is determined by boundary condition (4.2) to be

$$F_0 = \frac{t_1 F_{in}}{1 - R_1 \exp(i\Phi)}, \quad \text{or equivalently} \quad |F_0|^2 = \frac{t_1^2 |F_{in}|^2}{1 + R_1^2 - R_1 \cos(\Phi)}, \tag{4.3b}$$

where

$$R_1^2 \equiv r_1^2 \exp\left(-\frac{\alpha_0 L}{1 + \Delta^2 + T_1 T_2 |F_0|^2}\right) \tag{4.3c}$$

is a lumped loss parameter (with contributions from both the coupling mirror and medium absorption) and

$$\Phi \equiv \delta - \left(\frac{\alpha_0 L}{2}\right) \frac{\Delta}{1 + \Delta^2 + T_1 T_2 |F_0|^2} \tag{4.3d}$$

is the total mistuning. The stationary state solution can be seen in figure 4.2.

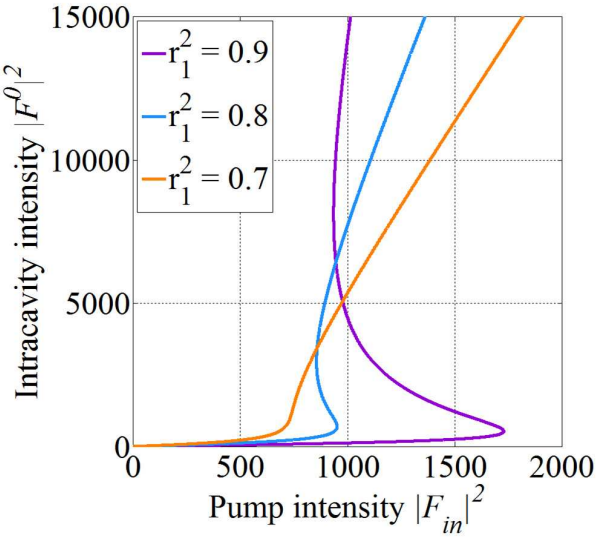

Figure 4.2: Stationary state of the absorptive bulk ring cavity where $\delta = 0$, $\Delta = 0$, $\alpha_0 L = 10$, $T_1 T_2 = 0.01$, $\sigma = 1$, and $d/k_0 = 1$.

4.1.1 Linear stability analysis

A linear stability analysis is now performed on system (4.1) to assess the susceptibility of its approximate stationary states to small-amplitude background fluctuations. The formal procedure closely follows that for the thin-slice dispersive ring cavity model. We perturb $F^0(z)$ and w_0 according to

$$F(\boldsymbol{x}, z, t) = F^0(z)[1 + f(\boldsymbol{x}, z, t)] \quad \text{and} \quad w(\boldsymbol{x}, t) = w_0 + \delta w(\boldsymbol{x}, t). \tag{4.4}$$

A master equation governing the dynamics of the medium excitation δw can be obtained by substituting Eq. (4.4) into Eq. (4.1), linearizing in f and δw, and cancelling the stationary solution given in Eq. (4.3). This procedure leads to:

$$\left(T_1 \frac{\partial}{\partial t} - l_D^2 \nabla_\perp^2 + 1\right) \delta w(\boldsymbol{x}, t) \simeq$$

$$-\frac{T_1 T_2}{1 + \Delta^2} |F_0|^2 \delta w(\boldsymbol{x}, t) + \frac{T_1 T_2 |F_0|^2}{1 + \Delta^2 |F_0|^2} [f(\boldsymbol{x}, z, t) + f^*(\boldsymbol{x}, z, t)]. \tag{4.5a}$$

One must also ensure that the assumed solution given in Eqs. (4.4a) and (4.4b) satisfies boundary condition (4.2). Hence, it follows that

$$f(\boldsymbol{x},z,t)=R_1\exp(i\Phi)\exp\left(i\frac{d}{2k_0}\nabla_\perp^2\right)\left[f(\boldsymbol{x},z,t-t_R)+\left(\frac{\alpha_0 L}{2}\right)\frac{\delta w(\boldsymbol{x},t-t_R)}{1+i\Delta}\right]. \tag{4.5b}$$

By taking the Fourier transform of Eqs. (4.5a) and (4.5b), one arrives at

$$\left(T_1\frac{\partial}{\partial t}+l_D^2\boldsymbol{K}^2+1\right)\delta\tilde{w}(\boldsymbol{K},t)\simeq$$

$$-\frac{T_1T_2}{1+\Delta^2}|F_0|^2\delta\tilde{w}(\boldsymbol{K},t)+\frac{T_1T_2|F_0|^2}{1+\Delta^2|F_0|^2}[\tilde{f}(\boldsymbol{K},z,t)+\tilde{f}^*(\boldsymbol{K},z,t)] \tag{4.6a}$$

and

$$\tilde{f}(\boldsymbol{K},0,t)=R_1\exp(i\Phi)\exp\left(-i\frac{K^2d}{2k_0}\right)\left[\tilde{f}(\boldsymbol{K},z,t-t_R)+\left(\frac{\alpha_0 L}{2}\right)\frac{\delta\tilde{w}(\boldsymbol{K},t-t_r)}{1+i\Delta}\right]. \tag{4.6b}$$

The time-dependent perturbation are assumed to be of the form

$$\tilde{f}(\boldsymbol{K},t)=\epsilon\exp(\lambda t)+\mu^*\exp(\lambda^* t)\quad\text{and}\quad\delta\tilde{w}(\boldsymbol{K},t)=\eta\exp(\lambda t)+\eta^*\exp(\lambda^* t). \tag{4.7a}$$

By substituting Eqs. (1.7a) and (1.7b) into Eq. (4.6b), is it possible to relate ϵ and μ to η through

$$\epsilon=\frac{E}{\exp(\lambda t_R)-D}\eta\quad\text{and}\quad\mu=\frac{E^*}{\exp(\lambda t_R)-D^*}\eta, \tag{4.7b}$$

where

$$D\equiv R_1\exp[i(\Phi-\theta)],\quad E\equiv\left(\frac{\alpha_0 L}{2}\right)\frac{D}{1+i\Delta},\quad\text{and}\quad\theta\equiv\frac{K^2d}{2k_0}. \tag{4.7c}$$

The following characteristic equation for the thin-slice absorptive cavity can now be obtained by substituting ansatz pair (4.7) into Eq. (4.6a):

$$[\exp(\lambda t_R)-D][\exp(\lambda t_R)-D^*](\lambda T_1+C)=AE[\exp(\lambda t_R)-D^*]$$

$$+AE^*[\exp(\lambda t_R)-D], \tag{4.8a}$$

$$\text{where} \quad A \equiv \frac{T_1 T_2 |F_0|^2}{1 + \Delta^2 + T_1 T_2 |F_0|^2} \quad \text{and} \quad C \equiv 1 + l_D^2 K^2 + \frac{T_1 T_2 |F_0|^2}{1 + \Delta^2}. \tag{4.8b}$$

By anticipating that the threshold condition $\lambda = 0$ is met at an intracavity intensity denoted by $|F_0|^2 \rightarrow I_{th}$, it can be shown that the spectrum for Turing (static) patterns is given by

$$1 + l_D^2 K^2 + \frac{T_1 T_2 I_{th}}{1 + \Delta^2} = \frac{T_1 T_2 I_{th}}{1 + \Delta^2 + T_1 T_2 I_{th}} \left(\frac{R_1 \alpha_0 L}{1 + \Delta^2} \right) \frac{\cos(\Phi - \theta) - R_1 + \Delta \sin(\Phi - \theta)}{1 + R_1^2 - 2R_1 \cos(\Phi - \theta)}. \tag{4.9}$$

4.1.2 Threshold curves

To plot the threshold spectrum for the absorptive ring cavity, one must solve Eq. (4.9) numerically. In the absence of diffusion (where one sets $l_D = 0$), the spectral bands presented in figure 4.3 (top row) all share a common minimum (a feature also present in the non-diffusing SFM system and FP cavity). With increasing K, the bands become more closely-spaced (another common feature). For a finite level of diffusion, threshold condition (4.9) imposes a quadratic envelope, $\sim l_D^2 K^2$, on the minima.

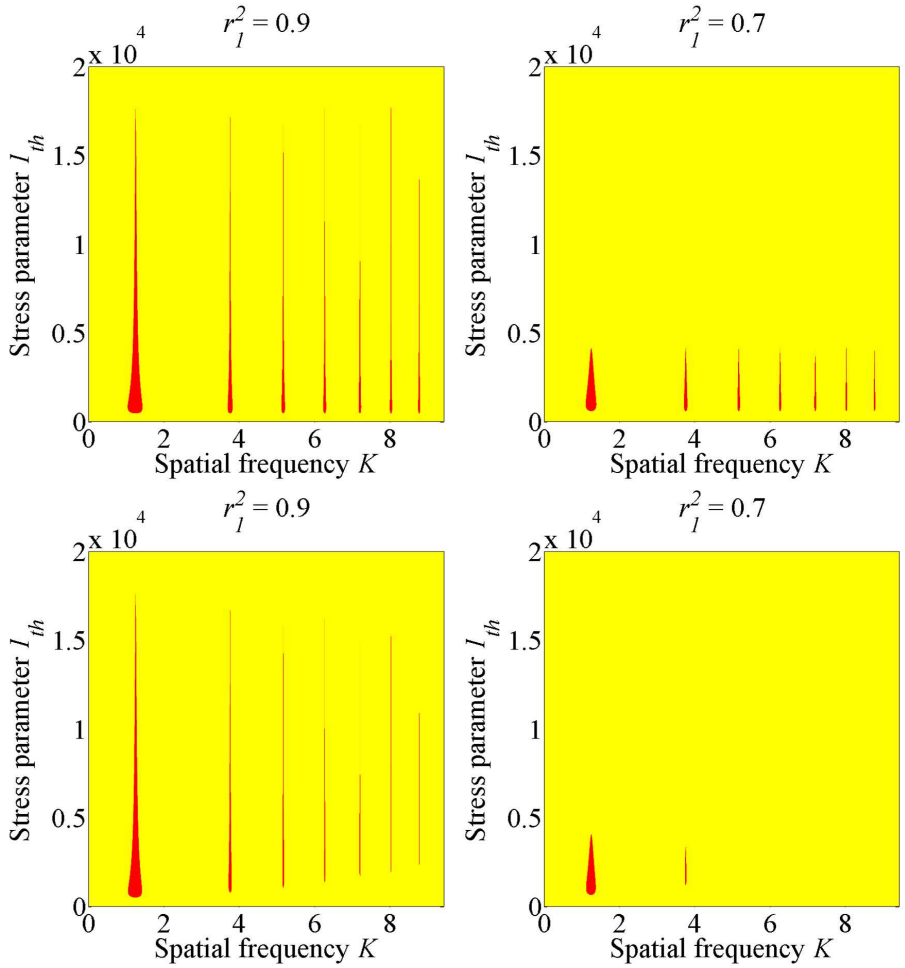

Figure 4.3: Static threshold instability curves for (top row) zero diffusion ($l_D = 0$) and (bottom row) finite diffusion ($l_D = 0.4$). Other parameters defined to be $\delta = 0.4$, $\Delta = 0$ (purely-absorptive medium), $d/2k_0 = 1$, $\sigma = 1$, $\alpha_0 L = 10$, and $T_1 T_2 = 0.01$.

4.1.3 Concluding remarks

We have re-analyzed the ring-cavity system when the host medium in in the form of a thin slice of Maxwell-Bloch-type saturable absorber [1, 6]. The novelty in this analysis lies in the introduction of z-dependence into the Fourier mode amplitudes that represent the perturbation. While the formal result remains unchanged (that is to say, the Turing spectrum and its predictions for spontaneous pattern emergence), the reworked analysis is more mathematically self-consistent.

4.2 Absorptive bulk ring cavity

We now turn our attention to configurations involving a ring cavity system, but where the medium has a finite length (and, according to the boundary condition, fills the resonator completely), a schematic diagram of the cavity can be seen in figure 4.4. A similar model has been considered by Brambilla, Columbo and Maggipinto [7], but their approach was somewhat involved. Here, we consider if a simplified analysis (akin to that used in dispersive cavities [8]) can make similar qualitative and quantitative predictions. In the same spirit as the analysis in Sec. 3.2.1, we introduce a generic nonlinearity function that describes both dispersion and absorption.

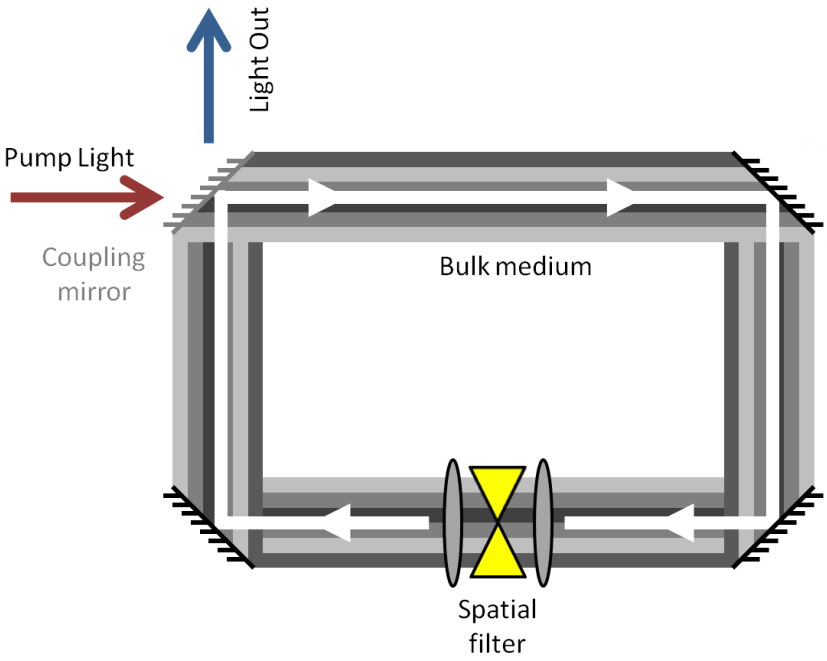

Figure 4.4: Schematic diagram of the bulk ring cavity.

4.2.1 Model equations

To proceed, we consider Eqs. (4.1a) and (4.1b) in a limiting case. The population difference w is assumed to be instantaneous by setting $T_1 \partial w/\partial t \to 0$ (facilitated, in part by assuming no spontaneous emission so that $T_1 = 0$). If, in combination, there is no diffusion of w, we can

neglect the transverse term $l_D^2\nabla_\perp^2 w$. Under those assumptions, Eq. (4.1b) yields

$$w = -\frac{1+\Delta^2}{1+\Delta^2+T_1T_2|F|^2}. \tag{4.10}$$

One may now substitute this expression for w into Eq. (4.1a). For a finite cavity length L, diffraction must occur continuously over each transit so that

$$i\frac{\partial F}{\partial z} + \frac{\sigma}{2}\nabla_\perp^2 F + i\left(\frac{\alpha_0 L}{2}\right)\frac{1-i\Delta}{1+\Delta^2+T_1T_2|F|^2}F = 0. \tag{4.11a}$$

Here, $0 \leq z \leq 1$ is the normalized longitudinal coordinate (measured along the cavity axis), and if distances in the transverse plane are measured in units of a (a transverse scalelength), then $\sigma = L/2k_0a^2$ is related to the Fresnel number of the circulating beam. All other model parameters retain their earlier definitions.

The boundary condition for the bulk system now has to be modified slightly, just as in Chapter 3. Since (paraxial) diffraction is accommodated in the wave equation [c.f., Eq. 4.1], it follows that the longitudinal boundary condition on F must read

$$F(\boldsymbol{x}, 0) = t_1F_{in} + r_1\exp(i\delta)F(\boldsymbol{x}, 1), \tag{4.11b}$$

where the parameters r_1, t_1, δ and F_{in} have the same meaning as before. It is relatively straightforward to show that the stationary states of the bulk absorptive cavity are identical to those of the corresponding thin-slice model [c.f., solution (4.3)].

4.2.2 Linear analysis

For the absorptive cavity, it is convenient to introduce a parametrization into the wave equation for F such that

$$i\frac{\partial F}{\partial z} + \frac{\sigma}{2}\nabla_\perp^2 F + g(I)F = 0, \quad \text{where} \quad g(I) \equiv i\left(\frac{\alpha_0 L}{2}\right)\frac{1-i\Delta}{1+\Delta^2+T_1T_2I}, \tag{4.12}$$

and $I \equiv |F|^2$. We now look for perturbed solutions of the form

$$F(\boldsymbol{x}, z) = F^0(z)[1 + f(\boldsymbol{x}, z)], \tag{4.13}$$

and where, in the linear approximation,

$$I = |F^0(z)|^2[1 + f(\boldsymbol{x}, z)]\,[1 + f^*(\boldsymbol{x}, z)] \simeq |F^0(z)|^2[1 + f(\boldsymbol{x}, z) + f^*(\boldsymbol{x}, z)] \equiv I^0 + \delta I, \tag{4.14}$$

with $I^0 \equiv |F^0(z)|^2$ and $\delta I \equiv I^0(f + f^*)$. One can now substitute the linearized result $I \simeq I^0 + \delta I$ into $g(I)$, Taylor-expanding that function around I^0 according to

$$g(I^0 + \delta I) = g(I^0) + \left(\frac{dg}{dI}\right)_{I=I^0} \delta I + \frac{1}{2!}\left(\frac{d^2g}{dI^2}\right)_{I=I^0} (\delta I)^2 + ... \tag{4.15}$$

Keeping terms only up to first order in δI, substitution into Eq. (4.12) and cancellation of the stationary state leads to a linearized master equation for f:

$$i\frac{\partial}{\partial z} f(\boldsymbol{x}, z) + \frac{\sigma}{2}\nabla_\perp^2 f(\boldsymbol{x}, z) + G\left(|F_0|^2\right)[f(\boldsymbol{x}, z) + f^*(\boldsymbol{x}, z)] \simeq 0, \tag{4.16a}$$

where

$$G\left(|F_0|^2\right) \equiv |F_0|^2\left(\frac{dg}{dI}\right)_{I=|F_0|^2} = -i\left(\frac{\alpha_0 L}{2}\right)\frac{(1 - i\Delta)\,T_1T_2|F_0|^2}{\left(1 + \Delta^2 + T_1T_2|F_0|^2\right)^2}. \tag{4.16b}$$

Substitution of perturbed solution (4.13) into boundary condition (1.11b) yields

$$f(\boldsymbol{x}, 0) = R_1 \exp(i\Phi) f(\boldsymbol{x}, 1), \tag{4.16c}$$

which has exactly the same structure as the corresponding results for the bulk dispersive cavity, and where R_1 and Φ retain their definitions from the (thin-slice) stationary state solution [c.f. Eqs. (4.3c) and (4.3d)].

We now seek solutions to the perturbed system using an ansatz of the form

$$f(\boldsymbol{x}, z) = \epsilon(z) \exp(i\boldsymbol{K} \cdot \boldsymbol{x}) + \mu^*(z) \exp(-i\boldsymbol{K} \cdot \boldsymbol{x}). \tag{4.17}$$

Substituting this trial solution into Eq. (4.16a), it is possible to construct a 2×2 matrix problem describing the evolution (in z) of the Fourier mode complex amplitudes $\epsilon(z)$ and $\mu(z)$:

$$\frac{d}{dz}\begin{pmatrix}\epsilon\\ \mu\end{pmatrix} = i\mathbf{M}\cdot\begin{pmatrix}\epsilon\\ \mu\end{pmatrix}, \tag{4.18a}$$

where

$$\mathbf{M} = \begin{bmatrix} G(|F_0|^2) - \frac{1}{2}\sigma K^2 & G(|F_0|^2) \\ -G^*(|F_0|^2) & -\left(G^*(|F_0|^2) - \frac{1}{2}\sigma K^2\right)\end{bmatrix}. \tag{4.18b}$$

A formal integration of matrix equation (4.18a) over a single transit around the cavity provides the vector solution

$$\mathbf{A}(1) \equiv \exp(i\mathbf{M})\cdot\mathbf{A}(0) \equiv \mathbf{E}\cdot\mathbf{A}(0), \tag{4.19}$$

where $\mathbf{A} \equiv (\epsilon \quad \mu)^{\mathrm{T}}$ and T denotes the transpose. Exponentiating the matrix $i\mathbf{M}$ using the standard 2×2 formula (see endnote located at the end of the chapter) gives the following entries for $\mathbf{E} \equiv \exp(i\mathbf{M})$:

$$\begin{aligned}
E_{11} &= \exp\left\{-\Im\mathrm{m}\left[G(|F_0|)^2\right]\right\}\left[\cosh\left(\frac{D}{2}\right) + i\frac{2}{D}\left\{\Re\mathrm{e}\left[G(|F_0|)^2 - \theta\right]\right\}\sinh\left(\frac{D}{2}\right)\right],\\
E_{12} &= \exp\left\{-\Im\mathrm{m}\left[G(|F_0|)^2\right]\right\} i\frac{2G(|F_0|^2)}{d}\sinh\left(\frac{D}{2}\right),\\
E_{21} &= -\exp\left\{-\Im\mathrm{m}\left[G(|F_0|)^2\right]\right\} i\frac{2G^*(|F_0|^2)}{d}\sinh\left(\frac{D}{2}\right),\\
E_{22} &= \exp\left\{-\Im\mathrm{m}\left[G(|F_0|)^2\right]\right\}\left[\cosh\left(\frac{D}{2}\right) - i\frac{2}{D}\left\{\Re\mathrm{e}\left[G(|F_0|)^2 - \theta\right]\right\}\sinh\left(\frac{D}{2}\right)\right],\\
D &= 2\sqrt{\theta\left\{2\Re\mathrm{e}\left[G(|F_0|^2 - \theta\right]\right\} + \Im\mathrm{m}^2\left[G(|F_0|^2)\right]}.
\end{aligned} \tag{4.20}$$

Also, substituting Fourier mode (4.17) into boundary condition (4.16c) yields

$$\mathbf{A}(0) = R_1\begin{bmatrix}\exp(i\Phi) & 0\\ 0 & \exp(-i\Phi)\end{bmatrix}\mathbf{A}(L) \tag{4.21}$$

After combining Eq. (4.21) with Eq. (4.19), we obtain

$$\begin{bmatrix} 1 - R_1 \exp(i\Phi) E_{11} & -R_1 \exp(i\Phi) E_{12} \\ -R_1 \exp(i\Phi) E_{21} & 1 - R_1 \exp(i\Phi) E_{22} \end{bmatrix} \begin{bmatrix} \epsilon(1) \\ \mu(1) \end{bmatrix} = \begin{bmatrix} 0 \\ 0 \end{bmatrix}, \tag{4.22}$$

where non-trivial solutions demand that the 2×2 system matrix above must have a vanishing determinant. Since $\det(\mathbf{E}) \equiv E_{11}E_{22} - E_{12}E_{21} = +1$, it follows that at threshold (where $|F_0|^2 \rightarrow I_{th}$), the Turing instability spectrum is given by

$$E_{11} \exp(i\Phi_{th}) + E_{22} \exp(-i\Phi_{th}) = 2 \left[\cos\Phi_{th} \cos(\beta_{th} L) - \frac{\Re\mathrm{e}[G(I_{th})] - \theta}{\beta_{th} L} \sin\Phi_{th} \sin(\beta_{th} L) \right], \tag{4.23a}$$

where

$$E_{11} = \cos(\beta_{th} L) + i \frac{\Re\mathrm{e}[G(I_{th})] - \theta}{\beta_{th} L} \sin(\beta_{th} L), \tag{4.23b}$$

$$E_{12} = i \frac{G(I_{th})}{\beta_{th} L} \sin(\beta_{th} L), \tag{4.23c}$$

$$E_{21} = -i \frac{G^*(I_{th})}{\beta_{th} L} \sin(\beta_{th} L), \tag{4.23d}$$

$$E_{22} = \cos(\beta_{th} L) - i \frac{\Re\mathrm{e}[G(I_{th})] - \theta}{\beta_{th} L} \sin(\beta_{th} L), \tag{4.23e}$$

and

$$i\beta_{th} L \equiv \sqrt{\theta \left\{ 2\Re\mathrm{e}\left[G(I_{th}) - \theta \right] \right\} + \Im\mathrm{m}^2\left[G(I_{th}) \right]}. \tag{4.23f}$$

These results also coincide with that of the dispersive ring cavity when the imaginary part of the nonlinearity is set to zero, $\Im m(G) \rightarrow 0$.

4.2.3 Threshold curves

Typical threshold instability spectra are shown in figure 4.5. They reveal some characteristics that are qualitatively similar to those of the thin-slice system (compare with figure 4.3), namely the instability bands having a "tear" shape and the existence of a global minimum.

More detailed considerations have brought to light a discrepancy in the analysis. In particularly, one can show graphically that the Ikeda-type instability in the $K = 0$ (associated with negative slopes in the stationary state input/output curve) is absence from the Turing spectrum, which can be seen in figure 4.6. At present, the origin of the inconsistency is unknown.

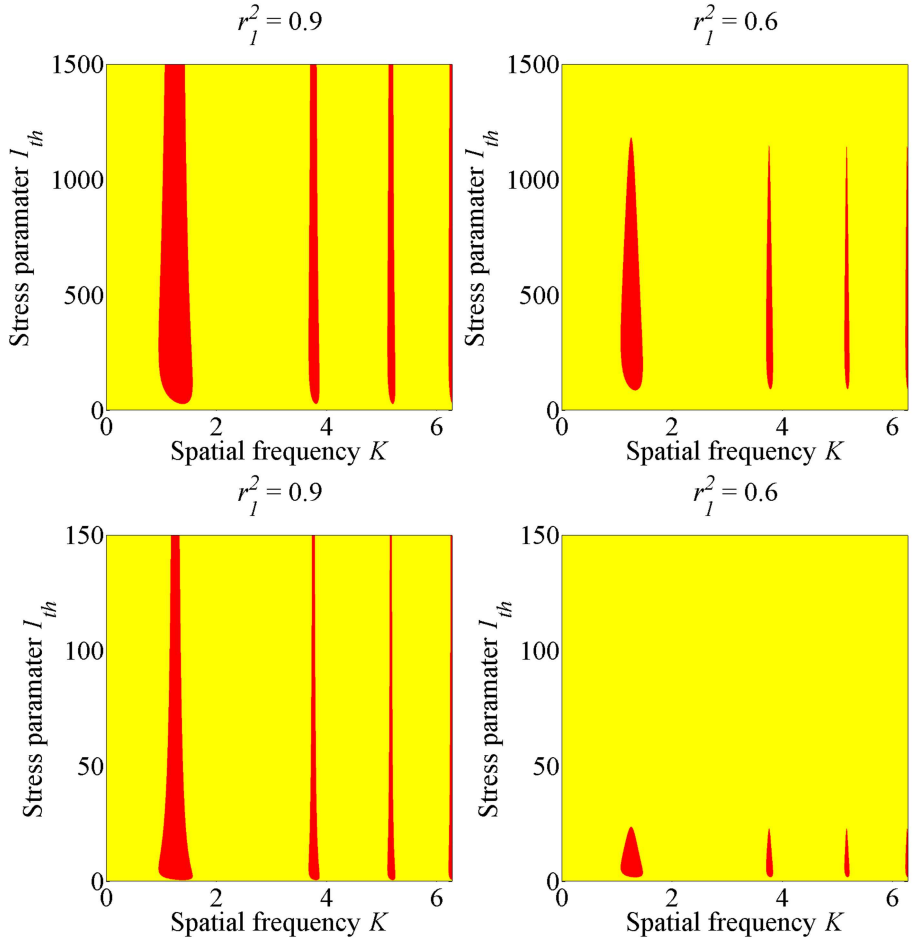

Figure 4.5: Static threshold instability curves for a ring cavity with a absorptive host medium, where $\delta = \pi/4$, $\Delta = 0$, $\sigma = 1$, $\alpha_0 l = 1$, and $d/k_0 = 1$ where top row $T_1 T_2 = 0.01$, and the bottom row $T_1 T_2 = 0.5$.

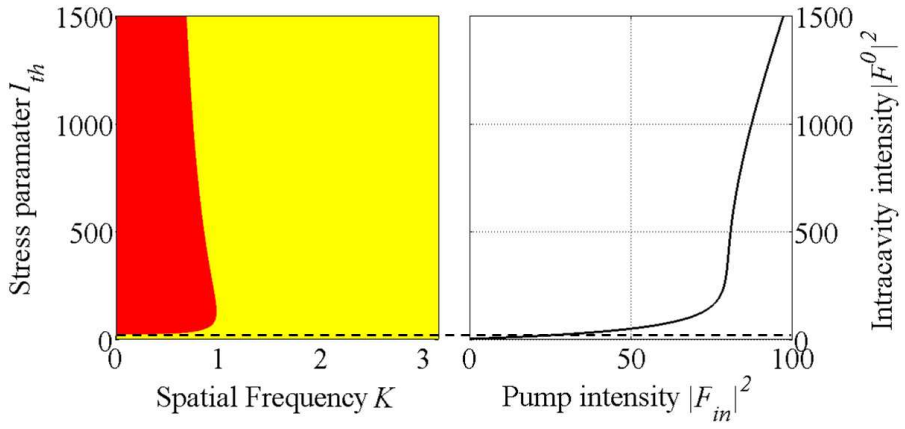

Figure 4.6: The stationary state next to the corresponding threshold plot, where $r_1^2 = 0.9$, $\delta = 0$, $\alpha_0 L = 1$, $\Delta = 0$, $d/k_0 = 1$, $T_1 T_2 = 0.01$, and $\sigma = 1$.

4.2.4 Simulations

Extensive simulations with system 4.1 have, to date, uncovered no evidence of pattern formation. This is a somewhat surprising result, since the existence of spatial structures in absorptive cavities is well-known [5, 6, 9, 10]. One potential explanation for the absence of pattern formation is that all the simulations have been performed on the basis of the linear analysis in Sec. 4.2.2. Since that analysis is incomplete (i.e., does not accurately reduct $K = 0$ Ikeda-type instabilities), it is not, in retrospect, too surprising that it fails at finite-K also. Even initializing the stationary state at 10 (see figure 4.7) and 100 (see figure 4.8) times the predicted threshold value does not lead to meaningful (finite amplitude) pattern emergence.

It is tempting, but difficult, to compare these results to those obtained by Patrascu *et al.* for the full Maxwell-Bloch model. While we are concerned primarily with the case of a purely-absorptive system (where $\Delta = 0$), they consider regimes are are strongly dispersive (where $|\Delta| \gg 1$).

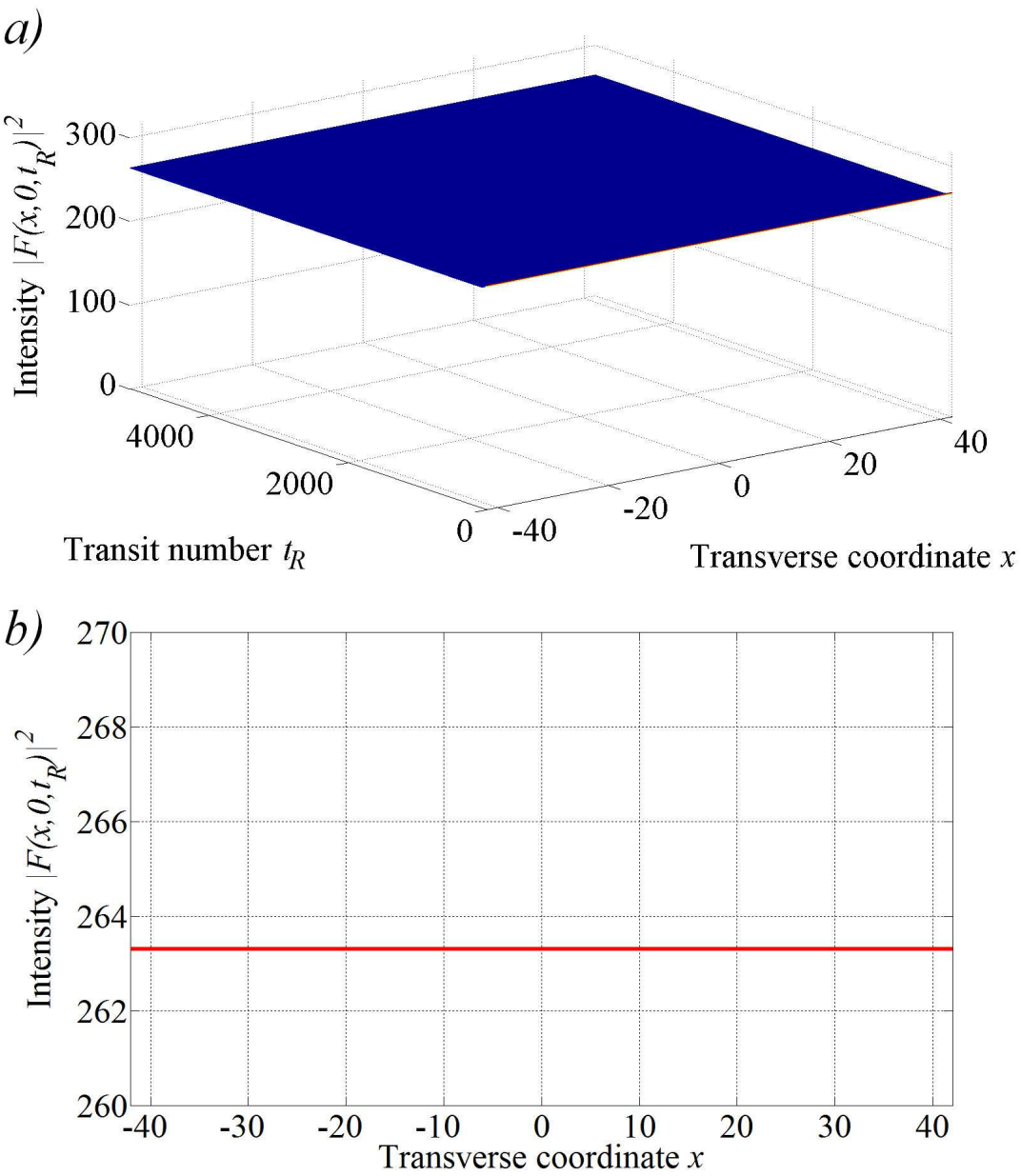

Figure 4.7: Simulations of the absorptive bulk ring cavity where $r_1^2 = 0.9$, $I_0 = 26.784 \times 10$, $K_0 = 0.5988$, $K_C = 0.9$, $T_1T_2 = 0.1$, $\delta = \pi/4$, $\alpha_0 L = 1$, $\Delta = 0$, and $d/k_0 = 1$.

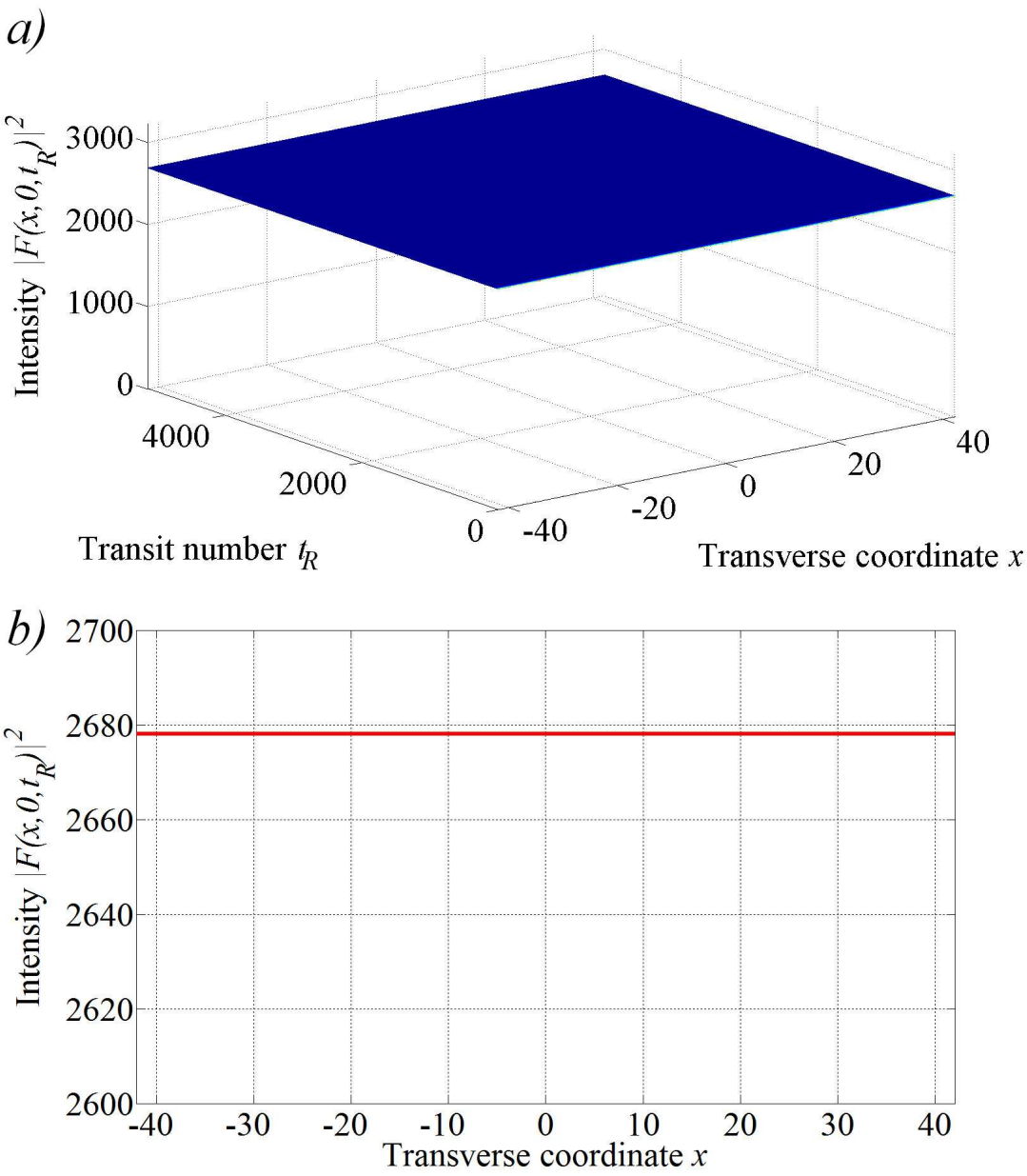

Figure 4.8: Simulations of the absorptive bulk ring cavity where $r_1^2 = 0.9$, $I_0 = 26.784 \times 10^2$, $K_0 = 0.5988$, $K_C = 0.9$, $T_1T_2 = 0.1$, $\delta = \pi/4$, $\alpha_0 L = 1$, $\Delta = 0$, and $d/k_0 = 1$.

4.3 Conclusion

We have analyzed a ring cavity that is completely filled with a host medium of the two-level saturable absorber type. The full complexity of the Maxwell-Bloch modelling, as considered by other authors [10], has been simplified by assuming the adiabatic elimination of both the material variables (population difference and polarization). A linearization technique has been deployed in the limit of weak absorption and the corresponding spectrum obtained for predicting the threshold for spontaneous Turing (i.e., static) patterns. This spectrum displays similar qualitative features of its thin-slice counterpart (when the latter neglects diffusion), such as multiple "tear-drop" islands sharing a common (global) minimum.

Given the multiple-comparable-minimum structure of the Turing spectrum, the expectation was to observe simple pattern formation (typically hexagons, squares, stripes, etc.) and, beyond that, the emergence of spontaneous fractality (subject to manipulation of a spatial filter and the presence of Helmholtz diffraction). However, such expectations have so far proven to be false. Even simple patterns have not been observed in the bulk model.

One possible explanation for the absence of patterns may be due to an oversimplification of the underlying Maxwell-Bloch equations (i.e., adoption of the adiabatic elimination procedure). Such an explanation would seem unlikely, given that spontaneous patterns have been observed in a very similar single-component model by Brambilla, Columbo, and Maggipinto [7]. A more likely source of the problem is some of the assumptions made in the linear analysis. The spectrum predicted by the method deployed in Sec. 4.2 does not, for example, describe the Ikeda-type instabilities expected in the plane-wave ($K = 0$) solution. Moreover, it clearly predicts the wrong threshold intensities (as evidenced by simulations).

An alternative iterpretation may be that spontaneous pattern formation may not be achievable in a system with purely-absorptive nonlinearity. Simulations in systems beyond the mean-field limit have tended to involve significant levels of dispersion, in addition to absorptive effects.

4.3.1 Matrix exponentiation

The standard formula for exponentiating a 2×2 matrix is:

$$\exp\begin{bmatrix} a & b \\ c & d \end{bmatrix} = \frac{1}{D}\exp\left(\frac{a+d}{2}\right)\begin{pmatrix} m_{11} & m_{12} \\ m_{21} & m_{22} \end{pmatrix},$$

where

$$\begin{aligned} m_{11} &\equiv D\cosh\left(\frac{D}{2}\right) + (a-d)\sinh\left(\frac{D}{2}\right), \\ m_{12} &\equiv 2b\sinh\left(\frac{D}{2}\right), \\ m_{21} &\equiv 2c\sinh\left(\frac{D}{2}\right), \\ m_{22} &\equiv D\cosh\left(\frac{D}{2}\right) + (d-a), \sinh\left(\frac{D}{2}\right) \end{aligned}$$

and

$$D \equiv \sqrt{(a-d)^2 + 4bc}.$$

References

[1] J. G. Huang and G. S. McDonald. Spontaneous optical fractal pattern formation. *Physical Review Letters*, 94(17):174101, 2005.

[2] A. S. Patrascu, C. Nath, M. Le Berre, E. Ressayre, and A Tallet. Multi-conical instability in the passive ring cavity: linear analysis. *Optics Communications*, 91(5):433–443, 1992.

[3] M. Le Berre, D. Leduc, E. Ressayre, and A. Tallet. Biconical emission of spatially mode-locked patterns with wave-number ratio $\sqrt{2}$ in a ring cavity device. *Physical Review A*, 54(4):3428, 1996.

[4] M. Le Berre, A. S. Patrascu, E. Ressayre, and A. Tallet. Daisy patterns in the passive ring cavity with diffusion effects. *Optics Communications*, 123(4):810–824, 1996.

[5] J. G. Huang, J. M. Christian, and G. S. McDonald. Spontaneous spatial fractal pattern formation in absorptive systems. *Journal of Nonlinear Optical Physics & Materials*, 21(02): art. no. 1250018, 2012.

[6] J. G. Huang. *Spontaneous optical fractals in linear & nonlinear systems*. Ph.D thesis, University of Salford, 2006.

[7] M. Brambilla, L. Columbo, and T. Maggipinto. Three-dimensional self-organized patterns in the field profile of a ring cavity resonator. *Journal of Optics B: Quantum and Semiclassical Optics*, 6(5):S197, 2004.

[8] D. W. McLaughlin, J. V. Moloney, and A. C. Newell. New class of instabilities in passive optical cavities. *Physical Review Letters*, 54(7):681, 1985.

[9] W. J. Firth and A. J. Scroggie. Spontaneous pattern formation in an absorptive system. *Europhysics Letters*, 26(7):521, 1994.

[10] L. A. Lugiato and C. Oldano. Stationary spatial patterns in passive optical systems: two-level atoms. *Physical Review A*, 37(10):3896, 1988.

Chapter 5

Conclusion

5.1 Summary of results

The primary objective of the research undertaken here was to consider the spontaneous fractal-generating properties of simple optical systems not previously analyzed in multi-scale pattern contexts. In so doing, the *comparable multiple Turing minima* signature proposed by Huang *et al.* [1–3] was to be tested in new feedback regimes with a view to confirming its true universal character. A central theme to be pursued was the generalization from thin-slice geometries to bulk-medium systems.

In-depth analysis of a diffusive thin-slice FP cavity (see Chapter 2) has uncovered a Turing spectrum with the desired multiple-minimum structure, and simulations have demonstrated conclusively that such a simple model is indeed capable of generating spontaneous spatial fractals. As in the case of the SFM system [3] the dimension of emergent multi-scale patterns can be quantified with the aid of specialist software [4] and parametrized by physical quantities such as the diffusion length, mirror reflectivity, and intracavity light intensity. In the limit of an instantaneous (non-diffusing) photoexcitation density, the fractal patterns tend to become area-filling (i.e., they have dimension 2).

There have, however, been some unexpected results encountered throughout our bulk-medium considerations. The first analysis (see Chapter 3) considered a fully-Helmholtz approach whereby light propagating inside a slab of Kerr-type material (that completely fills a ring cavity) is governed by a nonparaxial type of wave equation (this scenario is in stark con-

trast to the thin-slice approximation, where diffraction is neglected within the medium). Linear analysis was deployed (seemingly for the first time in the Helmholtz-type nonparaxial context) to predict the Turing instability spectrum, which turned out to have a multiple-island type of structure. While simulations were able to demonstrate simple pattern emergence close to threshold (and with both one and two transverse dimensions), operating in higher-intensity regimes tended to introduce numerical instabilities. This disappointing result is somewhat surprising, given that the difference-differential algorithm [5] routinely used for the integration of Helmholtz governing equations is extremely robust and reliable [6–8]. Thus, we have not yet been able to find evidence of fractal pattern formation in the dispersive bulk system.

A second disappointing result was also encountered for a bulk saturable-absorber ring cavity (see Chapter 4). The standard three-component Maxwell-Bloch model [9–11] was reduced to a single equation describing the intracavity field (with the population difference and polarization variables both eliminated adiabatically). While linear analysis predicted a multi-Turing instability spectrum with "tear drop"-shaped islands, the simplified model failed to generate any patterns (either simple or fractal) in purely-absorptive regimes with paraxial diffraction. While patterns have previously been observed using type of this model [12], it appears that only highly-dispersive regimes with a small level of absorption have been considered in simulations.

Results from the FP analysis undertaken here fully support the assertion that the fractal-generating signature proposed by Huang *et al.* [1–3] may be universal, at least within the context of thin-slice models. Indeed, the multi-Turing instability spectrum as an indicator of a system's innate capacity to generate complex (multi-scale) emergent behaviour has now been demonstrated fairly conclusively for a range of nonlinearities (both dispersive and absorptive) and boundary conditions (SFM, ring cavity, and FP), though some configurations remain to be explored.

The results from bulk-medium considerations merit further attention, particularly in the context of the multi-Turing signature [1–3, 13]. While bulk ring cavities (dispersive and absorptive) may indeed possess Turing instability spectra with a highly discrete structure (typical families of instability *islands*), it is unclear as to whether or not such a feature *by itself* is sufficient to act as an indicator for fractal patterns. While simulations have certainly not ruled out

the existence of such types of spatial structure, numerical instabilities (in the case of dispersive cavities) and sustained uniformity (in absorptive systems) add additional layers of complexity to the problem not really seen in thin-slice models. Such issues have, instead, prevented us from drawing any firm conclusions with regards fractal pattern formation in bulk systems.

It has been extensively documented that spontaneous pattern formation with Kerr-type media is possible, and that such media are well-placed to make comparisons between experimental results and the predictions of relatively simple analytical models [14, 15]. However, to be able to produce the fractal patterns studied in this thesis, one would require a high-power continuous-wave laser with a large beam area and a Kerr-type medium with a high nonlinear coefficient (in order to be able to generate sufficiently-large nonlinear phase shifts) [16].

Applications of the presented research involve utilizing the features of fractal light to improve the sensitivity of surface roughness measurements [17]. In addition, light patterns with multiple spatial scalelengths could play a important role within the fields of fractal antenna engineering and optical information encoding [18].

5.2 Future research directions

The most successful aspects of the research presented here has been in the context of the simple thin-slice FP cavity, suggesting that thin-slice models is where future investigations may be predominantly directed. The first immediately obvious generalization involves the classic SFM configuration [19, 20] but where the dispersive slice is replaced by a Maxwell-Bloch-type saturable absorber [9–11]. In the same way, a second generalization might consider the FP cavity with an absorptive component. While both SFM and FP geometries have already demonstrated their fractal-generating potential in purely dispersive contexts, their ability to generate similar patterns in the presence of medium-based losses remains unknown.

More interestingly, perhaps, is generalizing the ring cavity itself. Analyses to date have considered ring resonators as uni-directional devices [1, 12, 21–24]. However, they may also operate in bi-directional regimes [25] and this reconfiguration offers the potential for further study with a new class of boundary condition in combination with beam counterpropagation effects.

References

[1] J. G. Huang. *Spontaneous optical fractals in linear & nonlinear systems.* Ph.D thesis, University of Salford, 2006.

[2] J. G. Huang, J. M. Christian, and G. S. McDonald. Spontaneous spatial fractal pattern formation in absorptive systems. *Journal of Nonlinear Optical Physics & Materials*, 21(02): art. no. 1250018, 2012.

[3] J. G. Huang and G. S. McDonald. Spontaneous optical fractal pattern formation. *Physical Review Letters*, 94(17):174101, 2005.

[4] BENOIT 1.3, TruSoft International Inc., www.trusoft-international.com.

[5] P. Chamorro-Posada, G. S. McDonald, and G. H. C. New. Non-paraxial beam propagation methods. *Optics Communications*, 192(1):1–12, 2001.

[6] J. M. Christian, G. S. McDonald, T. F. Hodgkinson, and P. Chamorro-Posada. Wave envelopes with second-order spatiotemporal dispersion. I. Bright Kerr solitons and cnoidal waves. *Physical Review A*, 86(2):023838, 2012.

[7] J. M. Christian, E. A. McCoy, G. S. McDonald, J. Sánchez-Curto, and P. Chamorro-Posada. Helmholtz bright spatial solitons and surface waves at power-law optical interfaces. *Journal of Atomic, Molecular, and Optical Physics*, page art. no. 137967, 2012.

[8] J. M. Christian, G. S. McDonald, T. F. Hodgkinson, and P. Chamorro-Posada. Spatiotemporal dispersion and wave envelopes with relativistic and pseudorelativistic characteristics. *Physical Review Letters*, 108(3)(034101), 2012.

[9] L. A. Lugiato and R. Lefever. Spatial dissipative structures in passive optical systems. *Physical Review Letters*, 58(21):2209–2211, 1987.

[10] L. A. Lugiato and C. Oldano. Stationary spatial patterns in passive optical systems: two-level atoms. *Physical Review A*, 37(10):3896, 1988.

[11] P. Mandel, M. Georgiou, and T. Erneux. Transverse effects in coherently driven nonlinear cavities. *Physical Review A*, 47(5):4277, 1993.

[12] M. Brambilla, L. Columbo, and T. Maggipinto. Three-dimensional self-organized patterns in the field profile of a ring cavity resonator. *Journal of Optics B: Quantum and Semiclassical Optics*, 6(5):S197, 2004.

[13] J. G. Huang, J. M. Christian, C. Bostock, and G. S McDonald. Spontaneous spatial optical fractals in ring cavities. *Manuscript in preparation*, 2015.

[14] A. J. Scroggie, W. J. Firth, G. S. McDonald, M. Tlidi, R. Lefever, and L. A. Lugiato. Pattern formation in a passive Kerr cavity. *Chaos, Solitons & Fractals*, 4(8):1323–1354, 1994.

[15] F. T. Arecchi. Optical morphogenesis: pattern formation and competition in nonlinear optics. *Physica D: Nonlinear Phenomena*, 86(1)(297–322), 1995.

[16] G. D'Alessandro and W. J. Firth. Spontaneous hexagon formation in a nonlinear optical medium with feedback mirror. *Physical Review Letters*, 66(2):2597–2600, 1991.

[17] N. Wada, J. Uozumi, and T. Asakura. Optical evaluation of fractality of rough surfaces using fractal illumination. *Optics communications*, 166(1):163–171, 1999.

[18] D. H. Werner and P. L. Werner. On the synthesis of fractal radiation patterns. *Radio science*, 30(1):29–45, 1995.

[19] W. J. Firth. Spatial instabilities in a Kerr medium with single feedback mirror. *Journal of Modern Optics*, 37:151–153, 1990.

[20] G. D'Alessandro and W. J. Firth. Hexagonal spatial patterns for a Kerr slice with a feedback mirror. *Physical Review A*, 41(1):537–548, 1992.

[21] A. S. Patrascu, C. Nath, M. Le Berre, E. Ressayre, and A Tallet. Multi-conical instability in the passive ring cavity: linear analysis. *Optics Communications*, 91(5):433–443, 1992.

[22] D. W. McLaughlin, J. V. Moloney, and A. C. Newell. New class of instabilities in passive optical cavities. *Physical Review Letters*, 54(7):681, 1985.

[23] M. Le Berre, A. S. Patrascu, E. Ressayre, and A. Tallet. Daisy patterns in the passive ring cavity with diffusion effects. *Optics Communications*, 123(4):810–824, 1996.

[24] K. Ikeda, H. Daido, and O. Akimoto. Optical turbulence: chaotic behavior of transmitted light from a ring cavity. *Physical Review Letters*, 45(9):709, 1980.

[25] H. Zeghlache, P. Mandel, N. B. Abraham, L. M. Hoffer, G. L. Lippi, and T. Mello. Bidirectional ring laser: Stability analysis and time-dependent solutions. *Physical Review A*, 37(2):470, 1988.

Appendix A

Publications

A.1 List of conference contributions

1. Bostock, C & Christian, J M & McDonald, G S 2015, 'The thin-slice nonlinear Fabry-Pérot cavity: spatial optical patterns and fractal dimension calculations', College of Science & Technology "Research Showcase Day", University of Salford, Greater Manchester, UK, 28th May

2. Bostock, C & Christian, J M & McDonald, G 2015, 'Complexity in nonlinear Fabry-Pérot cavities: reaction-diffusion optical systems and spontaneous spatial patterns', Salford Postgraduate Annual Research Conference (SPARC 15), University of Salford, Greater Manchester, UK, 26th - 28th May

3. Bostock, C & Christian, J M & McDonald, G 2014, 'Spontaneous patterns in a Fabry-Pérot cavity: multi-Turing spectra & fractality', College of Science & Technology "Research Showcase Day", University of Salford, Greater Manchester, UK, 18th June.abstract

4. Bostock, C & Christian, J M & McDonald, G S 2013, 'Spontaneous spatial fractal patterns: towards nonparaxial nonlinear ring cavities', College of Science & Technology "Research Showcase Day", University of Salford, Greater Manchester, UK, 19th June

5. Readman, S L & Christian, J M & Bostock, C & McDonald, G S 2013, 'The absorptive ring cavity: dynamics & patterns beyond the mean-field limit', College of Science &

Technology “Research Showcase Day”, University of Salford, Greater Manchester, UK, 19th June

6. Patel, S & Christian, J M & Bostock, C & McDonald, G S 2013, ‘The nonlinear Fabry-Pérot cavity: complexity in a simple optical feedback system’, College of Science & Technology “Research Showcase Day”, University of Salford, Greater Manchester, UK, 19th June

7. Bostock, C & Christian, J M & McDonald, G S 2013, ‘Spontaneous spatial fractal light patterns in simple nonlinear cavities’, Salford Postgraduate Annual Research Conference (SPARC 13), University of Salford, Greater Manchester, UK, 5th - 6th June

A.2 List of published conference proceedings

1. Bostock, C & Christian, J M & Leite, A B & McDonald, G S & Huang, J G 2015, Multi-Turing instabilities & spontaneous patterns in discrete nonlinear systems: simplicity and complexity, cavities and counterpropagation, in: ‘WAVES 2015 - 12th International Conference on the Mathematics and Numerical Aspects of Wave propagation’, Institut National de Recherche en Informatique et en Automatique (INRIA), Karlsruhe, Germany

2. Bostock, C & Christian, J M & McDonald, G S & Leite, A B & Huang, J G 2014, Multi-Turing instabilities in Fabry-Pérot resonators and discrete microcavities, in: ‘EOSAM 2014’, European Optical Society, Berlin, Germany. Conference details: European Optical Society Annual Meeting

3. Christian, J M & Bostock, C & McDonald, G S & Huang, J G 2014, Multi-Turing instability spectra and spatial fractals in absorptive systems, in: ‘Photon 14’, Institute of Physics: Optics and Photonics Division, London, UK. Conference details: National Photonics Conference

4. Bostock, C & Christian, J M & McDonald, G 2013, Multi-Turing instabilities in nonlinear cavities: implications for pattern formation, in: ‘4th CSE Doctoral School Postgraduate Research Conference’, University of Salford, Greater Manchester, UK, 13th November

5. Bostock, C & Christian, J M & McDonald, G S 2013, Spontaneous symmetry-breaking & spatial fractal patterns in optical models, in: 'Warwick Centre for Complexity Science', Oxford Brookes University, Oxford, UK, 14th - 17th August. Conference details: Third Annual Student Conference on Complexity Sciences (SCCS 2013)

6. Bostock, C & Christian, J M & McDonald, G S & Heyes, A S & Huang, J G 2013, Multi-Turing instability and spontaneous spatial fractals in simple optical systems, in: 'Nonlinear Optics Topical Meeting', Optical Society of America, Kohala Coast, Hawaii, United States of America

7. Bostock, C & Christian, J M & McDonald, G S 2012, Spontaneous optical patterns: from simplicity to complexity in nonlinear cavities, in: '3rd CSE Doctoral School Postgraduate Research Conference', University of Salford, Greater Manchester, UK, pp.5-7

8. McDonald, G S & Christian, J M & Huang, J G & Walsh, T M & Bostock, C 2012, Spontaneous spatial fractal patterns in simple linear and nonlinear optical cavities, in: 'EOSAM 2012', European Optical Society, Aberdeen, UK. Conference details: European Optical Society Annual Meeting

Appendix B

Fabry-Pérot analysis

B.1 Governing equations

The boundary condition for the FP cavity are as follows:

$$F(\boldsymbol{X}, 0, t) = t_1 F_{in} + r_1 \exp(i\delta) B(\boldsymbol{X}, 0, t), \tag{B.1a}$$

$$B(\boldsymbol{X}, L, t) = r_2 \exp\left(i \frac{d}{k_0} \nabla_\perp^2\right) F(\boldsymbol{X}, L, t - t_R). \tag{B.1b}$$

The coupled field–medium dynamics in the slice are governed by the following:

$$\frac{\partial F}{\partial z} = i\chi n F, \tag{B.2a}$$

$$\frac{\partial B}{\partial z} = -i\chi n B, \tag{B.2b}$$

$$\tau \frac{\partial n}{\partial t} - l_D^2 n + n = |F|^2 + |B|^2. \tag{B.2c}$$

B.2 Stationary state

Obtain the stationary state solutions where $\partial/\partial t \to 0$ which are spatially uniform $\nabla_\perp^2 \to 0$. Additionally set F, B, and n to F^0, B^0, and n_0. This then gives the following:

$$\frac{\partial F^0}{\partial z} = i\chi n_0 F^0, \tag{B.3a}$$

$$\frac{\partial B}{\partial z} = -i\chi n_0 B^0, \tag{B.3b}$$

$$n_0 = |F^0|^2 + |B^0|^2. \tag{B.3c}$$

Look for the solutions of the following:

$$F^0(z) = A\exp(i\chi n_0 z), \tag{B.4a}$$

$$B^0(z) = C\exp(-i\chi n_0 z), \tag{B.4b}$$

$$n_0 = |A|^2 + |C|^2. \tag{B.4c}$$

To obtain constants A and C the above must be substituted into the boundary conditions:

$$C\exp(-i\chi n_0 z) = r_2 A\exp(i\chi n_0 L),$$

$$C = r_2 A\exp(i2\chi n_0 L), \tag{B.5}$$

and

$$\begin{aligned} A &= t_1 F_{in} + r_1\exp(i\delta)C, \\ &= t_1 F_{in} + r_1 r_2\exp(i\delta)A\exp(i2\chi n_0 L), \\ &= t_1 F_{in} + r_1 r_2\exp(i\Phi)A. \end{aligned} \tag{B.6}$$

Where $\Phi = 2\chi n_0 l$, this yields the following:

$$A = \frac{t_1 F_{in}}{1 - r_1 r_2\exp(i\Phi)}, \tag{B.7a}$$

$$C = r_2\frac{t_1 F_{in}}{1 - r_1 r_2\exp(i\Phi)}\exp(i2\chi n_0 L). \tag{B.7b}$$

However $n_0 = |A|^2 + |C|^2 = (1 + r_2^2)A$.

$$|A|^2 = \frac{t_1^2 |F_{in}^2}{1 + r_1^2 r_2^2 - 2r_1 r_2 \cos\phi}. \tag{B.8}$$

The stationary state solution can now be shown to be:

$$F^0(Z) = \frac{t_1 F_{in}}{1 - r_1 r_2 \exp(i\Phi)} \exp(i\chi n_0 L) \tag{B.9a}$$

$$B^0(z) = \frac{t_1 F_{in}}{1 - r_1 r_2 \exp(i\Phi)} \exp[i\chi n_0 (2L - z)] \tag{B.9b}$$

$$n_0 = (1 + r_2^2) \frac{t_1^2 |F_{in}^2}{1 + r_1^2 r_2^2 - 2r_1 r_2 \cos\phi}. \tag{B.9c}$$

B.3 Linear stability analysis

To proceed with the LSA the following perturbations need to be introduced:

$$F(\boldsymbol{X}, z, t) = F^0(z)[1 + f(\boldsymbol{X}, z, t)], \tag{B.10a}$$

$$B(\boldsymbol{X}, z, t) = B^0(z)[1 + b(\boldsymbol{X}, z, t)], \tag{B.10b}$$

$$n(\boldsymbol{X}, t) = n_0 + \Delta n(\boldsymbol{x}, t). \tag{B.10c}$$

Substitute these into the medium equations,

$$\left(-l_D^2 \nabla_\perp^2 + \tau \frac{\partial}{\partial t} + 1\right)(n_0 + \Delta n) = |F^0(Z)|^2 (1 + f)(1 + f^*) + |B^0(z)|^2 (1 + b)(1 + b^*). \tag{B.11a}$$

$\therefore$

$$\cancel{n_0} + \left(-l_D^2 \nabla_\perp^2 + \tau \frac{\partial}{\partial t} + 1\right) \Delta n(\boldsymbol{X}, t) = |A|^2 (\cancel{1} + f + f^* + |f|^2) + |C|^2 (\cancel{1} + b + b^* + |b|^2). \tag{B.11b}$$

$\therefore$

$$\left(-l_D^2 \nabla_\perp^2 + \tau \frac{\partial}{\partial t} + 1\right) \Delta n(\boldsymbol{X}, t) = |A|^2 (f + f^*) + r_2^2 |A|^2 (b + b^*), \tag{B.11c}$$

but $|A|^2 = t_1^2|F_{in}^2/(1 + r_1^2 r_2^2 - 2r_1 r_2 \cos\phi)$. The linearised master equation can now be shown to be:

$$\left(-l_D^2\nabla_\perp^2 + \tau\frac{\partial}{\partial t} + 1\right)\Delta n(\boldsymbol{X},t) = |F^0|^2[f(\boldsymbol{X},z,t)+f^*(\boldsymbol{X},z,t)]+r_2^2|F^0|^2[b(\boldsymbol{X},z,t)+b^*(\boldsymbol{X},z,t)]. \tag{B.12}$$

The z–dependence in f and b can be from:

$$\begin{aligned}\frac{\partial F}{\partial z} &= i\chi nF,\\ \frac{\partial}{\partial z}F^0(z)[1+f(\boldsymbol{X},z,t)] &= i\chi(n_0\Delta n)F^0(z)[1+f(\boldsymbol{X},z,t)],\end{aligned} \tag{B.13}$$

$\therefore$

$$[1+f(\boldsymbol{X},z,t)]\cancel{\frac{\partial F^0}{\partial z}} + F^0(z)\frac{\partial f}{\partial z} = \cancel{i\chi n_0 F^0(z)}\,[1+f(\boldsymbol{X},z,t)] + i\chi F^0(z)\Delta n, \tag{B.14}$$

$\therefore$

$$\frac{\partial}{\partial z}f(\boldsymbol{X},z,t) = i\chi\Delta n(\boldsymbol{X},t), \tag{B.15}$$

integrate the above with regards to z so that

$$f(\boldsymbol{X},z,t) = f(\boldsymbol{X},0,t) + i\chi\Delta n(\boldsymbol{X},t)z. \tag{B.16}$$

Now look for the b from:

$$\begin{aligned}\frac{\partial B}{\partial z} &= -i\chi nB\\ \frac{\partial}{\partial z}B^0(z)\,[1+b\,(\boldsymbol{X},z,t,)] &= -i\chi nB^0(z)\,[1+b\,(\boldsymbol{X},z,t,)]\\ &= -i\chi B^0(z)(n_0+\Delta n)\,[1+b\,(\boldsymbol{X},z,t,)]\end{aligned} \tag{B.17}$$

$\therefore$

$$[1+b(\boldsymbol{X},z,t)]\cancel{\frac{\partial B^0}{\partial z}} + B^{)}(z)\frac{\partial b}{\partial z} = -i\chi n_0\cancel{B^0(z)}[1+b(\boldsymbol{X},z,t) - i\chi B^0(z)\Delta n. \tag{B.18}$$

Cancel the stationary state so that:

$$\frac{\partial}{\partial z}b(\boldsymbol{X},z,t) = -i\chi\Delta n(\boldsymbol{X},t) \therefore b(\boldsymbol{X},z,t) = b(\boldsymbol{X},0,t) - i\chi\Delta n(\boldsymbol{X},t)z. \tag{B.19}$$

The field equation inside the slice provide the following relations:

$$f(\boldsymbol{X},z,t) = f(\boldsymbol{X},0,t) + i\chi\Delta n(\boldsymbol{X},t)z, \tag{B.20a}$$

$$b(\boldsymbol{X},z,t) = b(\boldsymbol{X},0,t) - i\chi\Delta n(\boldsymbol{X},t)z. \tag{B.20b}$$

N.B.

$$\begin{aligned} f(\boldsymbol{X},z,t) + f^*(\boldsymbol{X},z,t) &= f(\boldsymbol{X},0,t) + \cancel{i\chi\Delta n(\boldsymbol{X},t)z} + f^*(\boldsymbol{X},0,t) - \cancel{i\chi\Delta n(\boldsymbol{X},t)z}, \\ b(\boldsymbol{X},z,t) + b^*(\boldsymbol{X},z,t) &= b(\boldsymbol{X},0,t) - \cancel{i\chi\Delta n(\boldsymbol{X},t)z} + b^*(\boldsymbol{X},0,t) + \cancel{i\chi\Delta n(\boldsymbol{X},t)z}, \end{aligned} \tag{B.21}$$

$\therefore$ the medium equation can now be shown to be:

$$\left(-l_D^2\nabla_\perp^2 + \tau\frac{\partial}{\partial t} + 1\right)\Delta n(\boldsymbol{X},t) = |F^0|^2[f(\boldsymbol{X},0,t)+f^*(\boldsymbol{X},0,t)]+r_2^2|F^0|^2[b(\boldsymbol{X},0,t)+b^*(\boldsymbol{X},0,t)]. \tag{B.22}$$

Now substitute into the boundary condition,

$$\begin{aligned} F^0(0)[\cancel{1} + f(\boldsymbol{X},0,t)] &= \cancel{t_1 F_{in}} + r_1\exp(i\delta)B^0(0)[\cancel{1} + f(\boldsymbol{X},0,t)], \\ F^0(0)f(\boldsymbol{X},0,t) &= r_1\exp(i\delta)B^0(0)b(\boldsymbol{X},0,t), \\ &= r_1\exp(i\delta)r_2\exp(i2\chi n_0 L)F^0(0)b(\boldsymbol{X},0,t), \end{aligned} \tag{B.23}$$

$\therefore$

$$f(\boldsymbol{X},0,t) = r_1 r_2\exp(i\Phi)b(\boldsymbol{X},0,t). \tag{B.24}$$

$\Rightarrow$

$$B^0(L)[1+b(\boldsymbol{X},L,t)] = r_2 \exp\left(i\frac{d}{k_0}\nabla_\perp^2\right) F^0(l)[1+f(\boldsymbol{X},L,t-t_R)] \tag{B.25}$$

$\Rightarrow$

$$\cancel{B^0(L)}[1+b(\boldsymbol{X},L,t)] = \cancel{r_2 F^0(L)} \exp\left(i\frac{d}{k_0}\nabla_\perp^2\right)[1+f(\boldsymbol{X},L,t-t_R)]. \tag{B.26}$$

From here the FP cavity boundary conditions give rise to the following relations between f and b:

$$f(\boldsymbol{X},0,t) = r_1 r_2 \exp(i\Phi) b(\boldsymbol{X},0,t), \tag{B.27a}$$

$$b(\boldsymbol{X},L,t) = \exp\left(i\frac{d}{k_0}\nabla_\perp^2\right) f(\boldsymbol{X},L,t-t_R). \tag{B.27b}$$

This then gives rise to the following:

$$f(\boldsymbol{X},0,t) + f^*(\boldsymbol{X},0,t) = r_1 r_2[\exp(i\Phi) b(\boldsymbol{X},0,t) + \exp(-i\Phi) b^*(\boldsymbol{X},0,t)]. \tag{B.28}$$

Therefore the perturbation in n is driven by one quantity, namely $b(\boldsymbol{X},0,t)$, however

$$b(\boldsymbol{X},0,t) = b(\boldsymbol{X},L,t) + i\chi L \Delta n(\boldsymbol{X}),$$

$\therefore$

$$b(\boldsymbol{X},0,t) + b^*(\boldsymbol{X},0,t) = b^*(\boldsymbol{X},L,t) + b^*(\boldsymbol{X},L,t). \tag{B.29}$$

Also

$$\exp(i\Phi) b(\boldsymbol{X},0,t) + \exp(-i\Phi) b^*(\boldsymbol{X},0,t) = 2\Re\mathrm{e}[\exp(i\Phi) b(\boldsymbol{X},0,t)], \tag{B.30}$$

$\therefore$

$$\begin{aligned} \exp(i\Phi) b(\boldsymbol{X},0,t) &= \exp(i\Phi)[b(\boldsymbol{X},L,t) + i\chi L \Delta n(\boldsymbol{X},t)], \\ &= (\cos\Phi + i\sin\Phi)\{\Re\mathrm{e}(b_L) + i[\Im\mathrm{m}(b_L) + \chi L \Delta n(\boldsymbol{X},t)]\}, \end{aligned} \tag{B.31}$$

where $b_L = b(\boldsymbol{X}, L, t)$. From here the following can be obtained:

$$\Re\mathrm{e}[\exp(i\phi)b(\boldsymbol{X},0,t)] = \cos\Phi\Re\mathrm{e}(b_L) - \sin\phi[\Im\mathrm{m}(b_L) + i\chi L\Delta n(\boldsymbol{X},\boldsymbol{t}]. \tag{B.32}$$

N.B.

$$\Re\mathrm{e}(b_L) = \frac{b_L + b_L^*}{2},$$

$$\Im\mathrm{m}(b_L) = \frac{b_L - b_L^*}{2i}. \tag{B.33}$$

$\therefore$

$$\Re\mathrm{e}[\exp(i\Phi)b(\boldsymbol{X},0,t)] = \frac{\cos\Phi(b_L + b_L^*)}{2} - \frac{\sin\Phi(b_L - b_L^*)}{2i} - \chi L\sin\Phi\Delta(\boldsymbol{X},t) \tag{B.34}$$

$\therefore$

$$2\Re\mathrm{e}[\exp(i\Phi)b(\boldsymbol{X},0,t)] = \cos\Phi(b_L + b_L^*) + i\sin\Phi(b_L - b_L^*) - 2\chi L\sin\Phi\Delta(\boldsymbol{X},t), \tag{B.35}$$

$\therefore$

$$\left(-l_D^2\nabla_\perp^2 + \tau\frac{\partial}{\partial t} + 1\right)\Delta n(\boldsymbol{X},t) = \quad r_1r_2|F_0|^2\Big[\cos\Phi(b_L + b_L^*) + i\sin\Phi(b_L - b_L^*)$$

$$-2\chi L\sin\Phi\Delta(\boldsymbol{X},t)\Big] + r_2^2|F_0|^2(b_L + b_L^*), \tag{B.36}$$

$\therefore$

$$\left(-l_D^2\nabla_\perp^2 + \tau\frac{\partial}{\partial t} + 1\right)\Delta n(\boldsymbol{X},t) = \quad |F_0|^2(r_2^2 + r_1r_2\cos\Phi)(b_L + b_L^*) + i|F_0|^2r_1r_2\sin\Phi(b_L - b_L^*)$$

$$-2r_1r_2\chi L|F_0|^2\sin\phi\Delta n(\boldsymbol{X},t). \tag{B.37}$$

Finally, one needs to establish a way of including time delay, t_R, into the governing equation

$$\begin{aligned} b(\boldsymbol{X},L,t) &= \exp\left(i\frac{d}{k_0}\nabla_\perp^2\right) f(\boldsymbol{X},L,t-t_R), \\ &= \exp\left(i\frac{d}{k_0}\nabla_\perp^2\right)\Big[f(\boldsymbol{X},0,t)+i\chi L\Delta n(\boldsymbol{X},t-t_R)\Big], \\ &= \exp\left(i\frac{d}{k_0}\nabla_\perp^2\right)\Big\{r_1r_2\exp(i\Phi)b(\boldsymbol{X},0,t)+i\chi L\Delta n(\boldsymbol{X},t-t_R)\Big\}, \\ &= \exp\left(i\frac{d}{k_0}\nabla_\perp^2\right)\Big\{r_1r_2\exp(i\Phi)\Big[b(\boldsymbol{X},L,t-t_R)+i\chi L\Delta n(\boldsymbol{X},t-t_R)\Big] \\ &\quad +i\chi L\Delta n(\boldsymbol{X},t-t_R)\Big\}. \end{aligned}$$

The time-retarded contribution is thus locked up in:

$$\begin{aligned} b(\boldsymbol{X},L,t) &= \exp\left(i\frac{d}{k_0}\nabla_\perp^2\right)\Big\{r_1r_2\exp(i\Phi)b(\boldsymbol{X},L,t-t_R) \\ &\quad +i\chi L\Big[1+r_1r_2\exp(i\Phi)\Big]\Delta n(\boldsymbol{X},t-t_R)\Big\}. \end{aligned} \tag{B.38}$$

Now transform to the Fourier domain using $\nabla_\perp^2 \to K^2$, so that:

$$\begin{aligned} \left(1+l_D^2K^2+\tau\frac{\partial}{\partial t}\right)\Delta\tilde{n}(\boldsymbol{X},t) &= |F_0|^2(r_2^2+r_1r_2\cos\Phi)\Big[\tilde{b}(\boldsymbol{K},L,t)+\tilde{b^*}(\boldsymbol{K},L,t)\Big] \\ &\quad +i|F_0|^2r_1r_2\sin\Phi\Big[\tilde{b}(\boldsymbol{K},L,t)-\tilde{b}^*(\boldsymbol{K},L,t)\Big] \\ &\quad -2r_1r_2\chi L|F_0|^2\sin\phi\Delta\tilde{n}(\boldsymbol{K},t), \end{aligned} \tag{B.39a}$$

$$\begin{aligned} \tilde{b}(\boldsymbol{K},L,t) &= r_1r_2\exp\Big[i(\Phi-\theta)\Big]\tilde{b}(\boldsymbol{K},L,t-t_R) \\ &\quad +i\chi L\Big\{r_1r_2\exp\Big[i(\phi-\theta)\Big]+\exp(-i\theta)\Big\}\tilde{n}(\boldsymbol{K},t-t_R). \end{aligned} \tag{B.39b}$$

$$\begin{aligned}\tau\frac{\partial y(t)}{\partial t} &= A\left[\tilde{b_L}(t)+\tilde{b_L}(t)^*\right]+iB\left[\tilde{b_L}(t)-\tilde{b_L}(t)^*\right]-Cy(t),\\ \tilde{b_L}(t) &= D\tilde{b_L}(t-t_R)+Ey(t-t_R),\end{aligned} \tag{B.40}$$

where

$$y(t)=\eta\exp(\lambda t)+\eta^*\exp(\lambda^* t), \tag{B.41a}$$

$$\tilde{b_L}(t)=\epsilon\exp(\lambda t)+\mu^*\exp(\lambda^* t). \tag{B.41b}$$

and

$$A \equiv |F_0|^2(r_2^2+r_1r_2\cos\Phi), \tag{B.41c}$$

$$B \equiv |F_0|^2 r_1 r_2\sin\Phi, \tag{B.41d}$$

$$C \equiv 1+l_D^2K^2+2\chi LB, \tag{B.41e}$$

$$D \equiv r_1r_2\exp[i(\Phi-\theta)], \tag{B.41f}$$

$$E \equiv i\chi L\left[D+\exp(-i\theta)\right]. \tag{B.41g}$$

Now obtain the solutions for $\tilde{b_L}(t-t_R)$, and $t(t-t_R)\Rightarrow$

$$y(t-t_R)=\eta\exp\left[\lambda(t-t_R)\right]+\eta^*\exp\left[\lambda^*(t-t_R)\right], \tag{B.42a}$$

$$\tilde{b_L}(t-t_R)=\epsilon\exp\left[\lambda(t-t_R)\right]+\mu^*\exp\left[\lambda^*(t-t_R)\right]. \tag{B.42b}$$

$$\tilde{b_L}(t) = D\tilde{b_L}(t)(t-t_R) + Ey(t-t_R), \tag{B.43}$$

$$\begin{aligned}\epsilon\exp(\lambda t) + \mu\exp(\lambda t) &= D\left\{\epsilon\exp\left[\lambda(t-t_R)\right] + \mu^*\exp\left[\lambda^*(t-t_R)\right]\right\} \\ &\quad + E\left\{\eta\exp\left[\lambda(t-t_R)\right] + \eta^*\exp\left[\lambda^*(t-t_R)\right]\right\}.\end{aligned} \tag{B.44}$$

Collect the coefficients of $\exp(\lambda t)$, and $\exp(\lambda^* t)$:

$$\left[\exp(\lambda t)\right], \epsilon = D\epsilon\exp(-\lambda t_R) + E\eta\exp(-\lambda t_R) \tag{B.45a}$$

$$\epsilon = \frac{E\eta}{\exp(\lambda t_R) - D}, \tag{B.45b}$$

$$\left[\exp(\lambda^* t)\right], \mu^* = D\mu^*\exp(-\lambda t_R) + E\eta^*\exp(-\lambda^* t_R), \tag{B.45c}$$

$$\mu = \frac{E^*\eta}{\exp(\lambda t_R) - D^*}. \tag{B.45d}$$

This then yields:

$$\tilde{b_L}(t) = \epsilon\exp(\lambda t) + \mu^*\exp(\lambda^* t), \tag{B.46}$$

$$= \frac{E\eta}{\exp(\lambda t_R) - D}\exp(\lambda t) + \frac{E\eta^*}{\exp(\lambda^* t_R) - D}\exp(\lambda^* t). \tag{B.47}$$

Additionally,

$$y(t) = \eta\exp(\lambda t) + \eta^*\exp(\lambda^* t) \tag{B.48a}$$

$\therefore$

$$\frac{\partial y(t)}{\partial t} = \lambda\eta\exp(\lambda t) + \lambda^*\eta^*\exp(\lambda^* t). \tag{B.48b}$$

When combined this gives the following relation:

$$\tau\left[\lambda\eta e^{(\lambda t)}+\lambda^*\eta^* e^{(\lambda^* t)}\right]=$$

$$A\left[\frac{E\eta}{e^{(\lambda t_R)}-D}e^{(\lambda t)}+\frac{E\eta^*}{e^{(\lambda^* t_R)}-D}e^{(\lambda^* t)}+\frac{E^*\eta^*}{e^{(\lambda^* t_R)}-D^*}e^{(\lambda^* t)}+\frac{E^*\eta}{e^{(\lambda t_R)}-D^*}e^{(\lambda t)}\right]+$$

$$iB\left[\frac{E\eta}{e^{(\lambda t_R)}-D}e^{(\lambda t)}+\frac{E\eta^*}{e^{(\lambda^* t_R)}-D}e^{(\lambda^* t)}-\frac{E^*\eta^*}{e^{(\lambda^* t_R)}-D^*}e^{(\lambda^* t)}-\frac{E^*\eta}{e^{(\lambda t_R)}-D^*}e^{(\lambda t)}\right]-$$

$$C\left(\eta e^{(\lambda t)}+\eta^* e^{(\lambda^* t)}\right). \tag{B.49}$$

Collect the coefficients of the term $\exp(\lambda t)$:

$$\tau\lambda\eta=\frac{AE\eta}{e^{(\lambda t_R}-D}+\frac{AE^*\eta}{e^{(\lambda t_R)}-D^*}+\frac{iBE\eta}{e^{(\lambda t_R)}-D}-\frac{iBE^*\eta}{e^{(\lambda t_R)}-D^*}-C\eta \tag{B.50}$$

$\therefore$

$$\Big(\tau\lambda+C\Big)\eta=\frac{\Big(A+iB\Big)E\eta}{e^{(\lambda t_R)}-D}+\frac{\Big(A-iB\Big)E^*\eta}{e^{(\lambda t_R)}-D^*}, \tag{B.51}$$

$\therefore$

$$\Big(\tau\lambda+C\Big)\Big(e^{(\lambda t_R)}-D\Big)\Big(e^{(\lambda t_R)}-D^*\Big)\not{\eta}=$$

$$\Big(A+iB\Big)\Big(e^{(\lambda t_R)}-D^*\Big)E\not{\eta}+\Big(A-iB\Big)\Big(e^{(\lambda t_R)}-D\Big)E^*\not{\eta}. \tag{B.52}$$

Take $\lambda=0\therefore$

$$\begin{aligned}\Big(1-D\Big)\Big(1-D^*\Big) &= E\Big(A+iB\Big)\Big(1-D\Big)+E^*\Big(A-iB\Big)\Big(1-D\Big),\\ &= 2\Re\mathrm{e}\Big[E(A+iB)(1-D^*)\Big].\end{aligned} \tag{B.53}$$

Define Y to be:

$$Y=E(A+iB)(1+D^*), \tag{B.54}$$

where:

$$D \equiv \Re\mathrm{e}(D) + i\Im\mathrm{m}(D),$$

$$D^* \equiv \Re\mathrm{e}(D) - i\Im\mathrm{m}(D). \tag{B.55}$$

$$\begin{aligned} Y &= E(A+iB)(1-D^*), \\ &= \Big[\Re\mathrm{e}(E) + i\Im\mathrm{m}(E)\Big](A+iB)(1-D^*), \\ &= \Big\{A\Re\mathrm{e}(E) - B\Im\mathrm{m}(E) + i\Big[A\Im\mathrm{m} + B\Re\mathrm{e}(E)\Big]\Big\}\Big[1-\Re\mathrm{e}(D) + i\Im\mathrm{m}(E)\Big]. \end{aligned} \tag{B.56}$$

$\therefore$

$$\Re\mathrm{e} = \underbrace{\Big[A\Re\mathrm{e}(E) - B\Im\mathrm{m}(E)\Big]\Big[1-\Re\mathrm{e}(D)\Big]}_{Y_1} - \underbrace{\Big[A\Im\mathrm{m}(E) + B\Re\mathrm{e}(E)\Big]\Im\mathrm{m}(D)}_{Y_2}. \tag{B.57}$$

Also:

$$\Re\mathrm{e}(E) \equiv \chi L\Big[\sin\theta - r_1 r_2 \sin(\Phi-\theta)\Big],$$

$$\Im\mathrm{m}(E) \equiv \chi L\Big[\cos\theta - r_1 r_2 \cos(\Phi-\theta)\Big], \tag{B.58}$$

$$\begin{aligned} &2\Big(Y_1 - Y_2\Big) = \\ &\Big[1 + r_1^2 r_2^2 - 2r_1 r_2\cos(\Phi-\theta)\Big]\Big(1 + l_D^2 K^2\Big) + \\ &2\chi I L\Big\{r_1 r_2 \sin\Phi\Big[1 + r_1^2 r_2^2 - 2r_1 r_2\cos(\Phi-\theta)\Big]\Big\} \end{aligned} \tag{B.59}$$

Define:

$$Q \equiv r_1 r_2 \sin\Phi\Big[1 + r_1^2 r_2^2 - 2r_1 r_2\cos(\Phi-\theta)\Big] - \frac{Y_1 - Y_2}{\chi I L} \tag{B.60}$$

$\therefore$

$$
\begin{aligned}
Q \equiv\ & r_1 r_2 \sin\Phi\Big[1 + r_1^2 r_2^2 - 2 r_1 r_2 \cos(\Phi - \theta)\Big] - \\
& \Big[1 - r_1 r_2 \cos(\Phi - \theta)\Big]\Bigg\{(r_2^2 + r_1 r_2 \cos\Phi)\Big[\sin\theta - r_1 r_2 \sin(\Phi - \theta)\Big] - \\
& r_1 r_2 \sin\Phi\Big[\cos\theta + r_1 r_2 \cos(\Phi - \theta)\Big]\Bigg\} + \\
& r_1 r_2 \sin(\Phi - \theta)\Bigg\{(r_2^2 + r_1 r_2 \cos\Phi)\Big[\cos\theta - r_1 r_2 \cos(\Phi - \theta)\Big] - \\
& r_1 r_2 \sin\Phi\Big[\sin\theta + r_1 r_2 \sin(\Phi - \theta)\Big]\Bigg\}
\end{aligned}
\tag{B.61}
$$

Expand the $1 - r_1 r_2 \cos(\Phi - \theta)$ terms:

$$
\begin{aligned}
Q \equiv\ & r_1 r_2 \sin\Phi\Big[1 + r_1^2 r_2^2 - 2 r_1 r_2 \cos(\Phi - \theta)\Big] - \\
& \Big[1 - r_1 r_2 \cos(\Phi - \theta)\Big]\Bigg\{(r_2^2 + r_1 r_2 \cos\Phi)\Big[\sin\theta - r_1 r_2 \sin(\Phi - \theta)\Big] - \\
& r_1 r_2 \sin\Phi\Big[\cos\theta + r_1 r_2 \cos(\Phi - \theta)\Big]\Bigg\} + \\
& r_1 r_2\Bigg\{(r_2^2 + r_1 r_2 \cos\Phi)\Big[\sin\theta\cos(\Phi - \theta) - r_1 r_2 \sin(\Phi - \theta)\cos(\Phi - \theta)\Big] - \\
& r_1 r_2 \sin\Phi\Big[\cos\theta\cos(\Phi - \Theta) + r_1 r_2 \cos^2(\Phi\theta)\Big]\Bigg\} + \\
& r_1 r_2\Bigg\{(r_2^2 + r_1 r_2 \cos\Phi)\Big[\sin(\Phi - \theta)\cos\theta - r_1 r_2 \sin(\Phi - \theta)\cos(\Phi - \theta)\Big] + \\
& r_1 r_2 \sin\Phi\Big[\sin\theta\sin(\Phi - \Theta) + r_1 r_2 \sin^2(\Phi - \theta)\Big]\Bigg\}.
\end{aligned}
\tag{B.62}
$$

Where

$$r_1r_2X_1 \equiv r_1r_2\Big\{(r_2^2+r_1r_2\cos\Phi)\Big[\sin\theta\cos(\Phi-\theta)-r_1r_2\sin(\Phi-\theta)\cos(\Phi-\theta)\Big]-$$

$$r_1r_2\sin\Phi\Big[\cos\theta\cos(\Phi-\Theta)+r_1r_2\cos^2(\Phi\theta)\Big]\Big\}+$$

$$r_1r_2\Big\{(r_2^2+r_1r_2\cos\Phi)\Big[\sin(\Phi-\theta)\cos\theta-r_1r_2\sin(\Phi-\theta)\cos(\Phi-\theta)\Big]+$$

$$r_1r_2\sin\Phi\Big[\sin\theta\sin(\Phi-\Theta)+r_1r_2\sin^2(\Phi\theta)\Big]\Big\}. \tag{B.63}$$

Simply X_1:

$$\begin{aligned} X_1 &= (r_2^2+r_1r_2\cos\Phi)\Big[\sin\Phi\Big]-r_1r_2\sin\Phi\cos\Phi-(r_1r_2)^2\sin\Phi \\ X_1 &= r_2^2\sin\Phi+\cancel{r_1r_2\sin\Phi\cos\Phi}-\cancel{r_1r_2\sin\Phi\cos\Phi}-(r_1r_2)^2\sin\Phi \\ X_1 &= r_2^2(1-r_1^2)\sin\Phi. \end{aligned} \tag{B.64}$$

This now implies the following result:

$$Q \equiv r_1r_2\sin\Phi\Big[1+r_1^2r_2^2-2r_1r_2\cos(\Phi-\theta)\Big]+r_1r_2.r_2^2(1-r_1^2)\sin\Phi$$

$$\underbrace{-\Big\{(r_2^2+r_1r_2\cos\Phi)\Big[\sin\Phi-r_1r_2\sin(\Phi-\theta)\Big]-r_1r_2\sin\Phi\Big[\cos\theta+r_1r_2\cos(\Phi-\theta)\Big]\Big\}}_{-X_2} \tag{B.65}$$

From the relation simply X_2:

$$X_2 \equiv (r_2^2+r_1r_2\cos\Phi)\Big[\sin\Phi-r_1r_2\sin(\Phi-\theta)\Big]-r_1r_2\sin\Phi\Big[\cos\theta+r_1r_2\cos(\Phi-\theta)\Big] \tag{B.66}$$

$\therefore$

$$\begin{aligned} X_2 &= r_2^2 \sin\theta + r_1 r_2 \sin\theta \cos\Phi - r_2^2 r_1 r_2 \sin(\Phi-\theta) - (r_1 r_2)^2 \sin(\Phi-\theta)\cos\Phi - \\ & \quad r_1 r_2 \sin\Phi\cos\theta - (r_1 r_2)^2 \sin\Phi\cos(\Phi-\theta), \\ &= r_2 \sin\theta + r_1 r_2 \sin(\theta-\Phi) - r_1^2 r_2^2 \sin(2\Phi-\theta) - r_2^2 r_1 r_2 \sin(\Phi-\theta), \\ &= r_2^2 \sin\theta - r_1 r_2(1+r_2^2)\sin(\Phi-\theta) - r_1 r_2 \sin(2\Phi-\theta). \end{aligned} \tag{B.67}$$

From here Q can be shown to be:

$$\begin{aligned} Q &= r_1 r_2 \sin\Phi\Big[1 + r_1^2 r_2^2 - 2 r_1 r_2 \cos(\Phi-\theta)\Big] + r_1 r_2 . r_2^2 (1-r_1^2)\sin\Phi - \\ & \quad r_2^2 \sin\theta - r_1 r_2(1+r_2^2)\sin(\Phi-\theta) - r_1 r_2 \sin(2\Phi-\theta). \end{aligned} \tag{B.68}$$

From here expand and simplify the above solution,

$$
\begin{aligned}
Q &= r_1 r_2 \sin\Phi + \cancel{(r_1 r_2)^3} \sin\Phi - 2(r_1 r_2)^2 \sin\Phi\cos(\Phi-\theta) + (r_1 r_2) r_2^2 \sin\Phi - \\
&\quad \cancel{(r_1 r_2)^3} \sin\Phi - r_2 \sin\Phi + r - 1 r_2 (1 + r_2^2)\sin(\Phi-\theta) + r_1^2 r_2^2 \sin(2\Phi-\theta), \\
&= r_1 r_2 \sin\Phi + r_1^2 r_2^2 \Big[\sin(2\Phi-\theta) - 2\sin\Phi\cos(\Phi-\theta) \Big] + \\
&\quad + (r_1 r_2) r_2^2 \sin\theta - r_2^2 \sin\theta + r_1 r_2 (1 + r_2^2)\sin(\Phi-\theta), \\
&= r_1 r_2 (1 + r_2^2)\sin\Phi + r_1 r_2 (1 + r_2^2)\sin(\Phi-\theta) + \\
&\quad r_1^2 r_2^2 \Big\{ \sin\Big[\Phi + (\Phi-\theta)\Big] - 2\sin\Phi\cos(\Phi-\theta) \Big\} - r_2 \sin\theta, \\
&= r_1 r_2 (1 + r_2^2)\Big[\sin\Phi + \sin(\Phi-\theta) \Big] + \\
&\quad r_1 r_2 \Big[\sin\Phi\cos(\Phi-\theta) + \sin(\Phi-\Theta)\cos\Phi - \sin\Phi\cos(\Phi-\theta) \Big] - r_2 \sin\theta. \qquad \text{(B.69)}
\end{aligned}
$$

Collect the coefficients of $r_1^2 r_2^2$:

$$
\begin{aligned}
\Big[r_1^2 r_2^2 \Big] &= -\sin\Phi\cos(\Phi-\theta) + \sin(\Phi-\theta)\cos\Phi, \\
&= \sin(\Phi-\theta)\cos\Phi - \cos(\Phi-\theta)\sin\Phi, \\
&= \sin\Big[(\Phi-\theta) - \Phi\Big], \\
&= \sin(-\theta), \\
&= -\sin\theta. \qquad \text{(B.70)}
\end{aligned}
$$

$\Rightarrow$

$$Q = r_1 r_2 (1 + r_2^2)\Big[\sin\Phi + \sin(\Phi - \theta)\Big] - r_2^2(1 + r1^2)\sin\theta. \tag{B.71}$$

Which leads to the threshold condition:

$$\chi IL = \frac{\Big[1 + r_1^2 r_2^2 - 2r_1 r_2 \cos(\Phi - \theta)\Big]\Big(1 + l_D^2 K^2\Big)}{2\Bigg\{(1 + r_1^2) r_2^2 \sin\theta - r_1 r_2 (1 + r_2^2)\Big[\sin\Phi + \sin(\Phi - \theta)\Big]\Bigg\}} \tag{B.72}$$

Appendix C

Nonlinear Helmholtz bulk ring cavity analysis

C.1 Governing equation

$$\kappa\frac{\partial^2 F_n}{\partial\zeta^2} + i\frac{\partial F_n}{\partial\zeta} + \frac{\sigma}{2}\nabla_\perp^2 F_n + N(|F_n|^2)F_n = 0. \tag{C.1}$$

C.2 Steady state solution

Look for steady state solutions ($\nabla_\perp^2 \to 0$)

$$\kappa\frac{\partial^2 F_n}{\partial\zeta^2} + i2\frac{\partial F_n}{\partial\zeta} = -N(|F_n|^2)F_n = 0. \tag{C.2}$$

From here look for solutions of the form $G(z) = G(0)\exp(ik_\zeta\zeta)$

$$\begin{aligned} F(\zeta) &= F(0)\exp(ik_\zeta\zeta), \\ \partial F(\zeta)/\partial\zeta &= ik_\zeta F(0)\exp(ik_\zeta\zeta), \\ \partial^2 F(\zeta)/\partial\zeta^2 &= -k_\zeta^2 F(0)\exp(ik_\zeta\zeta). \end{aligned} \tag{C.3}$$

Insert the above equations into eq. (C.2).

$$-k_\zeta^2 \cancel{F(0)\exp(ik_\zeta\zeta)} - 2k_\zeta \cancel{F(0)\exp(ik_\zeta\zeta)} + N(I)\cancel{F(0)\exp(ik_\zeta\zeta)} = 0, \tag{C.4}$$

$\therefore$

$$-k_\zeta^2 - 2k_\zeta + N(I) = 0. \tag{C.5}$$

From here k_ζ can be obtained through the use of the quadratic formula to yield the following solution:

$$\begin{aligned} k_\zeta &= \frac{1}{2\kappa}\Big[-2 \pm \sqrt{4-4\kappa N(I)}\Big], \\ &= \frac{1}{\kappa}\Big[-1 \pm \sqrt{1-\kappa N(I)}\Big]. \end{aligned} \tag{C.6}$$

$\Rightarrow$

$$\begin{aligned} G(\zeta) &= G(0)\exp(i\beta\zeta), \\ \beta &\equiv \frac{1}{\kappa}\Big[-1 \pm \sqrt{1-\kappa N(I)}\Big]. \end{aligned} \tag{C.7}$$

C.3 Linear stability analysis

$\Rightarrow$

$$\kappa\frac{\partial^2 f_n}{\partial\zeta^2} + i\epsilon\frac{\partial}{f}_n\partial\zeta + \frac{\sigma}{2} + \nabla_\perp^2 f_n(\boldsymbol{\xi},\zeta) + \chi|F^0|^2\Big[f_n(\boldsymbol{\xi},\zeta) + f_n^*(\boldsymbol{\xi},\zeta)\Big] = 0, \tag{C.8}$$

where:

$$\begin{aligned} f_{n+1}(\boldsymbol{\xi},0) &= r_1\exp(i\Phi)f_n(\boldsymbol{\xi},L), \\ \epsilon &\equiv \sqrt{1+4\kappa\chi|F^0|^2}. \end{aligned} \tag{C.9}$$

The perturbation ansatz is defined to be:

$$\begin{aligned} f_n(\boldsymbol{\xi},\zeta) &= \exp(i\beta\zeta)\Big[a_n\exp(i\boldsymbol{K}.\boldsymbol{\xi})+b_n\exp(-i\boldsymbol{K}.\boldsymbol{\xi})\Big]+ \\ &\quad \exp(-i\beta\zeta)\Big[c_n\exp(i\boldsymbol{K}.\boldsymbol{\xi})+d_n\exp(-i\boldsymbol{K}.\boldsymbol{\xi})\Big] \end{aligned} \tag{C.10}$$

$\therefore$

$$\begin{aligned} \frac{\partial^2 f_n}{\partial\zeta^2} &= -\beta^2 f_n, \\ \nabla_\perp^2 f_n &= -\boldsymbol{K^2} f_n. \end{aligned} \tag{C.11}$$

Substitute these into eq. (C.8):

$$\begin{aligned} &-\kappa\beta^2 f_n + i\epsilon\Bigg\{i\beta\exp(i\beta\zeta)\Big[a_n\exp(i\boldsymbol{K}.\boldsymbol{\xi})+b_n\exp(-i\boldsymbol{K}.\boldsymbol{\xi})\Big]+ \\ &-i\beta\exp(-i\beta\zeta)\Big[c_n\exp(i\boldsymbol{K}.\boldsymbol{\xi})+d_n\exp(-i\boldsymbol{K}.\boldsymbol{\xi})\Big]\Bigg\}-\frac{\sigma\boldsymbol{K^2}}{2}f_n+ \\ &\chi|F^0|^2\Bigg\{z\exp(i\beta\zeta)\Big[a_n\exp(i\boldsymbol{K}.\boldsymbol{\xi})+b_n\exp(-i\boldsymbol{K}.\boldsymbol{\xi})+\Big] \\ &\exp(-i\beta\zeta)\Big[c_n\exp(i\boldsymbol{K}.\boldsymbol{\xi})+d_n\exp(-i\boldsymbol{K}.\boldsymbol{\xi})\Big]+ \\ &\exp(-i\beta\zeta)\Big[a_n^*\exp(-i\boldsymbol{K}.\boldsymbol{\xi})+b_n^*\exp(i\boldsymbol{K}.\boldsymbol{\xi})+\Big] \\ &\exp(i\beta\zeta)\Big[c_n^*\exp(-i\boldsymbol{K}.\boldsymbol{\xi})+d_n^*\exp(i\boldsymbol{K}.\boldsymbol{\xi})\Big]\Bigg\}=0. \end{aligned} \tag{C.12}$$

Collect together the coefficients of $\Big[\exp(i\beta\zeta\Big]$

$$\Big[\exp(i\beta\zeta)\Big], \quad -\kappa\beta^2\Big[a_n\exp(i\boldsymbol{K.\xi})+b_n\exp(-i\boldsymbol{K.\xi})\Big]-\epsilon\beta\Big[a_n\exp(i\boldsymbol{K.\xi})+b_n\exp(-i\boldsymbol{K.\xi})\Big]-$$

$$\frac{\sigma\boldsymbol{K^2}}{2}\Big[a_n\exp(i\boldsymbol{K.\xi})+b_n\exp(-i\boldsymbol{K.\xi})\Big]+\chi|F^0|^2\Big\{\Big[a_n\exp(i\boldsymbol{K.\xi})+b_n\exp(-i\boldsymbol{K.\xi})\Big]$$

$$+\Big[c_n^*\exp(-i\boldsymbol{K.\xi})+d_n^*\exp(i\boldsymbol{K.\xi})\Big]\Big\}=0. \tag{C.13}$$

From here now collect together the coefficients of the terms $\Big[\exp(i\boldsymbol{K}\xi)\Big]$ and $\Big[\exp(-i\boldsymbol{K}\xi)\Big]$:

$$\Big[\exp(i\boldsymbol{K.\xi})\Big], \quad -\kappa\beta^2a_n+\epsilon\beta a_n-\frac{\sigma\boldsymbol{K^2}}{2}a_n+\chi|F^0|^2a_n+\chi|F^0|^2d_n^*=0,$$

$$\Big[\exp(-i\boldsymbol{K.\xi})\Big], \quad -\kappa\beta^2b_n+\epsilon\beta b_n-\frac{\sigma\boldsymbol{K^2}}{2}b_n+\chi|F^0|^2b_n+\chi|F^0|^2c_n^*=0, \tag{C.14}$$

Similarly collect together the coefficients of $\Big[\exp(-i\beta\zeta\Big]$

$$\Big[\exp(-i\beta\zeta)\Big], \quad -\kappa\beta^2\Big[c_n\exp(i\boldsymbol{K.\xi})+d_n\exp(-i\boldsymbol{K.\xi})\Big]+\epsilon\beta\Big[c_n\exp(i\boldsymbol{K.\xi})+d_n\exp(-i\boldsymbol{K.\xi})\Big]-$$

$$\frac{\sigma\boldsymbol{K^2}}{2}\Big[c_n\exp(i\boldsymbol{K.\xi})+d_n\exp(-i\boldsymbol{K.\xi})\Big]+\chi|F^0|^2\Big\{\Big[c_n\exp(i\boldsymbol{K.\xi})+d_n\exp(-i\boldsymbol{K.\xi})\Big]$$

$$+\Big[a_n^*\exp(-i\boldsymbol{K.\xi})+b_n^*\exp(i\boldsymbol{K.\xi})\Big]\Big\}=0. \tag{C.15}$$

Additionally, collect together the coefficients of the terms $\Big[\exp(i\boldsymbol{K}\xi)\Big]$ and $\Big[\exp(-i\boldsymbol{K}\xi)\Big]$:

$$\Big[\exp(i\boldsymbol{K.\xi})\Big], \quad -\kappa\beta^2 c_n + \epsilon\beta c_n - \frac{\sigma\boldsymbol{K^2}}{2}c_n + \chi|F^0|^2 c_n + \chi|F^0|^2 b_n^* = 0,$$

$$\Big[\exp(-i\boldsymbol{K.\xi})\Big], \quad -\kappa\beta^2 d_n + \epsilon\beta d_n - \frac{\sigma\boldsymbol{K^2}}{2}d_n + \chi|F^0|^2 d_n + \chi|F^0|^2 a_n^* = 0, \tag{C.16}$$

$\Rightarrow$

$$-\chi|F^0|^2 d_n^* = \Big(-\kappa\beta^2 - \epsilon\beta - \frac{\sigma\boldsymbol{K^2}}{2} + \chi|F^0|^2 \Big) a_n, \tag{C.17a}$$

$$-\chi|F^0|^2 c_n^* = \Big(-\kappa\beta^2 - \epsilon\beta - \frac{\sigma\boldsymbol{K^2}}{2} + \chi|F^0|^2 \Big) b_n, \tag{C.17b}$$

$$-\chi|F^0|^2 b_n^* = \Big(-\kappa\beta^2 + \epsilon\beta - \frac{\sigma\boldsymbol{K^2}}{2} + \chi|F^0|^2 \Big) c_n, \tag{C.17c}$$

$$-\chi|F^0|^2 a_n^* = \Big(-\kappa\beta^2 + \epsilon\beta - \frac{\sigma\boldsymbol{K^2}}{2} + \chi|F^0|^2 \Big) d_n, \tag{C.17d}$$

Look for solutions for β by combining eqs. (C.17a) and (C.17d).

$$d_n^* = \frac{-\chi|F^0|^2 a_n}{\Big(-\kappa\beta^2 - \epsilon\beta - \frac{\sigma\boldsymbol{K^2}}{2} + \chi|F^0|^2 \Big)}, \tag{C.18}$$

$\therefore$

$$\cancel{\chi}|F^0|^2 \left[\frac{-\chi|F^0|^2 \cancel{a_n}}{-\kappa\beta^2 - \epsilon\beta - \frac{\sigma\boldsymbol{K^2}}{2} + \chi|F^0|^2} \right] = \Big(-\kappa\beta^2 - \epsilon\beta - \frac{\sigma\boldsymbol{K^2}}{2} + \chi|F^0|^2 \Big) \cancel{a_n}. \tag{C.19}$$

$\therefore$

$$\Big(\chi|F^0|^2\Big)^2 = \Big(-\kappa\beta^2 + \epsilon\beta - \frac{\sigma\boldsymbol{K^2}}{2} + \chi|F^0|^2 \Big) \Big(-\kappa\beta^2 - \epsilon\beta - \frac{\sigma\boldsymbol{K^2}}{2} + \chi|F^0|^2 \Big). \tag{C.20}$$

Let $\alpha = -\kappa\beta^2 - \sigma\boldsymbol{K^2}/2 + \chi|F^0|^2$, so that

$$\begin{aligned}\left(\chi|F^0|^2\right)^2 &= (\alpha+\epsilon\beta)(\alpha-\epsilon\beta),\\ &= \alpha^2-\epsilon^2\beta^2,\\ &= \left\{-\left[\kappa\beta^2+\frac{\sigma\boldsymbol{K^2}}{2}\right]+\chi|F^0|^2\right\}^2-(1+4\kappa\chi|F^0|^2)^2\beta^2, \qquad \text{(C.21)}\end{aligned}$$

$\therefore$

$$\begin{aligned}\cancel{\left(\chi|F^0|^2\right)^2} &= \left[\kappa\beta^2+\frac{\sigma\boldsymbol{K^2}}{2}\right]^2-2\chi|F^0|^2\left(\kappa\beta^2+\frac{\sigma\boldsymbol{K^2}}{2}\right)+\cancel{\left(\chi|F^0|^2\right)^2}-\\ &\quad (1+4\kappa\chi|F^0|^2)^2\beta^2\\ 0 &= \left[\kappa\beta^2+\frac{\sigma\boldsymbol{K^2}}{2}\right]^2-2\chi|F^0|^2\left(\kappa\beta^2+\frac{\sigma\boldsymbol{K^2}}{2}\right)-\\ &\quad (1+4\kappa\chi|F^0|^2)^2\beta^2 \qquad \text{(C.22)}\end{aligned}$$

Asymptote the solution to the paraxial soltion by setting $\kappa \to 0$:

$$\beta^2 = \left(\frac{\sigma\boldsymbol{K^2}}{2}\right)\left[\left(\frac{\sigma\boldsymbol{K^2}}{2}\right)-2\chi|F^0|^2\right] \qquad \text{(C.23)}$$

$\Rightarrow$

$$\begin{aligned} 0 &= \left(\kappa\beta^2 + \frac{\sigma\boldsymbol{K^2}}{2}\right)^2 - 2\chi|F^0|^2\left(\kappa\beta^2 + \frac{\sigma\boldsymbol{K^2}}{2}\right) - (1+4\kappa\chi|F^0|^2)^2\beta^2 \\ &= (\kappa\beta^2)^2 + \left(\frac{\sigma\boldsymbol{K^2}}{2}\right)^2 + 2\kappa\beta^2\left(\frac{\sigma\boldsymbol{K^2}}{2}\right) - 2\chi|F^0|^2\left(\kappa\beta^2 + \frac{\sigma\boldsymbol{K^2}}{2} -\right) \\ &\quad (1+4\kappa\chi|F^0|^2)^2\beta^2, \\ &= \kappa^2\beta^4 - \left[1 + 6\chi|F^0|^2\kappa - 2\kappa\left(\frac{\sigma\boldsymbol{K^2}}{2}\right)\right]\beta^2 + \left(\frac{\sigma\boldsymbol{K^2}}{2}\right)\left[\left(\frac{\sigma\boldsymbol{K^2}}{2}\right) - 2\chi|F^0|^2\right] \end{aligned} \quad \text{(C.24)}$$

From here β can be obtained through the use of the quadratic formula. Now consider the boundary condition:

$$\begin{aligned} f_n(\boldsymbol{\xi},\zeta) &= \exp(i\beta\zeta)\Big[a_n\exp(i\boldsymbol{K.\xi}) + b_n\exp(-i\boldsymbol{K.\xi})\Big] + \\ &\quad \exp(-i\beta\zeta)\Big[c_n\exp(i\boldsymbol{K.\xi}) + d_n\exp(-i\boldsymbol{K.\xi})\Big] \\ f_{n+1}(\boldsymbol{\xi},0) &= r_1\exp(i\beta\zeta)f_n(\boldsymbol{\xi},L). \end{aligned} \quad \text{(C.25)}$$

The result of substituting f_n into the boundary condition yields:

$$\begin{aligned} &\Big[a_{n+1}\exp(i\boldsymbol{K.\xi}) + b_{n+1}\exp(-i\boldsymbol{K.\xi}) + c_{n+1}\exp(i\boldsymbol{K.\xi}) + d_{n+1}\exp(-i\boldsymbol{K.\xi})\Big] = \\ &r_1\exp(i\Phi)\Big[a_n\exp(i\boldsymbol{K.\xi}) + b_n\exp(-i\boldsymbol{K.\xi}) + c_n\exp(i\boldsymbol{K.\xi}) + d_n\exp(-i\boldsymbol{K.\xi})\Big]. \end{aligned} \quad \text{(C.26)}$$

Collect together the coefficients of $\exp(i\boldsymbol{K.\xi})$ and $\exp(-i\boldsymbol{K.\xi})$:

$$\Big[\exp(i\boldsymbol{K.\xi})\Big], \quad a_{n+1} + c_{n+1} = r_1\exp(i\Phi)\Big[\exp(i\beta L)a_n + \exp(-i\beta L)c_n\Big], \quad \text{(C.27)}$$

$$\Big[\exp(-i\boldsymbol{K.\xi})\Big], \quad b_{n+1} + d_{n+1} = r_1\exp(i\Phi)\Big[\exp(i\beta L)b_n + \exp(-i\beta L)d_n\Big]. \quad \text{(C.28)}$$

From (C.17b):

$$b_n = \frac{-\chi|F^0|^2 c_n^*}{-\kappa\beta^2 - \epsilon\beta - \frac{\sigma \boldsymbol{K^2}}{2} + \chi|F^0|^2},$$

$$= -\frac{\chi|F^0|^2 c_n^*}{\alpha - \epsilon\beta}. \tag{C.29}$$

Similarly from (C.17c):

$$d_n = \frac{-\chi|F^0|^2 a_n^*}{-\kappa\beta^2 + \epsilon\beta - \frac{\sigma \boldsymbol{K^2}}{2} + \chi|F^0|^2},$$

$$= -\frac{\chi|F^0|^2 a_n^*}{\alpha + \epsilon\beta}. \tag{C.30}$$

Substitute these into (C.28)

$$\cancel{\frac{\chi|F^0|^2}{\alpha - \epsilon\beta}} c_{n+1}^* \cancel{\frac{\chi|F^0|^2}{\alpha + \epsilon\beta}} a_{n+1}^* = r_1 \exp(i\Phi) \times$$

$$\left\{ \exp(i\beta L) \left[\cancel{\frac{\chi|F^0|^2}{\alpha - \epsilon\beta}} c_n^* \right] + exp(-i\beta L) \left[\cancel{\frac{\chi|F^0|^2}{\alpha - \epsilon\beta}} a_n^* \right] \right\}. \tag{C.31}$$

$\Rightarrow$

$$\frac{c_{n+1}^*}{\alpha - \epsilon\beta} + \frac{a_{n+1}^*}{\alpha + \epsilon\beta} = r_1 \exp(i\Phi) \left[\exp(i\beta L) \frac{c_n^*}{\alpha - \epsilon\beta} + \exp(-i\beta L) \frac{a_n^*}{\alpha - \epsilon\beta} \right]. \tag{C.32}$$

$\therefore$

$$c_{n+1} = r_1 \exp(i\Phi) \left[\exp(i\beta L) c_n + \exp(-i\beta L) a_n \frac{\alpha - \epsilon\beta}{\alpha - \epsilon\beta} \right] - a_{n+1} \frac{\alpha - \epsilon\beta}{\alpha + \epsilon\beta}. \tag{C.33}$$

Eliminate c_{n+1} from eq (C.27)

$$a_{n+1} + r_1 \exp(i\Phi) \left[\exp(i\beta L) c_n + \exp(-i\beta L) a_n \frac{\alpha - \epsilon\beta}{\alpha - \epsilon\beta} \right] - a_{n+1} \frac{\alpha - \epsilon\beta}{\alpha + \epsilon\beta} =$$

$$r_1 \exp(i\Phi) \Big[\exp(i\beta L) a_n + \exp(-i\beta L) c_n \Big], \tag{C.34}$$

$\therefore$

$$\left(1-\frac{\alpha-\epsilon\beta}{\alpha+\epsilon\beta}\right)a_{n+1} = -r_1\exp(-i\Phi)\left[\exp(i\beta L)c_n+\exp(i\beta L)\left(\frac{\alpha-\epsilon\beta}{\alpha+\epsilon\beta}\right)a_n\right]+$$

$$r_1\exp(i\Phi)\Big[\exp(i\beta L)a_n+\exp(-i\beta L)c_n\Big], \tag{C.35}$$

$\therefore$

$$\left(1-\frac{\alpha-\epsilon\beta}{\alpha+\epsilon\beta}\right)a_{n+1} = r_1\exp(i\beta L)\left[\exp(i\Phi)a_n-\exp(-i\Phi)\left(\frac{\alpha-\epsilon\beta}{\alpha+\epsilon\beta}\right)a_n\right]+$$

$$r_1\exp(-i\beta L)\Big[\exp(i\Phi)c_n-\exp(-i\Phi)c_n\Big]. \tag{C.36}$$

Now expand the exponential functions using $\exp(i\theta)=\cos\theta+i\sin\theta$, and $\exp(-i\theta)=\cos\theta-i\sin\theta$:

$$\left(1-\frac{\alpha-\epsilon\beta}{\alpha+\epsilon\beta}\right)a_{n+1} = r_1\exp(i\beta L)\left[\cos\Phi+i\sin\Phi-\Big(\cos\Phi-i\sin\Phi\Big)\left(\frac{\alpha-\epsilon\beta}{\alpha+\epsilon\beta}\right)\right]a_n+$$

$$i2r_1\sin\Phi\exp(-i\beta L)c_n \tag{C.37}$$

$$= r_1\exp(i\beta L)\left[\left(1-\frac{\alpha-\epsilon\beta}{\alpha+\epsilon\beta}\right)\cos\Phi+i\left(1+\frac{\alpha-\epsilon\beta}{\alpha+\epsilon\beta}\right)\sin\Phi\right]a_n+$$

$$i2r_1\sin\Phi\exp(-i\beta L)c_n, \tag{C.38}$$

substitute the terms defined below into the above equation:

$$1-\frac{\alpha-\epsilon\beta}{\alpha+\epsilon\beta} = \frac{2\epsilon\beta}{\alpha+\epsilon\beta}, \tag{C.39}$$

$$1+\frac{\alpha-\epsilon\beta}{\alpha+\epsilon\beta} = \frac{2\alpha}{\alpha+\epsilon\beta}, \tag{C.40}$$

this the yields the following:

$$\frac{2\epsilon\beta}{\alpha+\epsilon\beta}a_{n+1} = r_1\exp(i\beta L)\left[\frac{2\epsilon\beta}{\alpha+\epsilon\beta}\cos\Phi + i\frac{2\alpha}{\alpha+\epsilon\beta}\sin\Phi\right]a_n +$$

$$i2r_1\sin\Phi\exp(-i\beta L)c_n. \tag{C.41}$$

$\Rightarrow$

$$a_{n+1} = r_1\exp(i\beta L)\left[\cancel{\left(\frac{\alpha+\epsilon\beta}{2\epsilon\beta}\right)}\cancel{\left(\frac{2\epsilon\beta}{\alpha+\epsilon\beta}\right)}\cos\Phi + i\left(\frac{\cancel{\alpha+\epsilon\beta}}{\cancel{2}\epsilon\beta}\right)\left(\frac{\cancel{2}\alpha}{\cancel{\alpha+\epsilon\beta}}\right)\sin\Phi\right]a_n +$$

$$i\frac{\alpha+\epsilon\beta}{\cancel{2}\epsilon\beta}\cancel{2}r_1\sin\Phi\exp(-i\beta L)c_n, \tag{C.42}$$

$$= r_1\exp(i\beta L)\left[\cos\Phi + i\frac{\alpha}{\epsilon\beta}\sin\Phi\right]a_n + i\frac{\alpha+\epsilon\beta}{\epsilon\beta}r_1\sin\Phi\exp(-i\beta L)c_n. \tag{C.43}$$

Refer back to eq. (C.32) and rearrange to obtain a_{n+1}

$$a^*_{n+1} = r_1\exp(i\Phi)\left[\exp(i\beta L)\left(\frac{c^*_n}{\alpha-\epsilon}\right) + \exp(-i\beta L)\left(\frac{a^*_n}{\alpha+\epsilon}\right)\right](\alpha+\epsilon\beta) - c^*_{n+1}\frac{\alpha+\epsilon\beta}{\alpha-\epsilon\beta},$$

$$a_{n+1} = r_1\exp(-i\Phi)\left[\exp(-i\beta L)\left(\frac{\alpha+\epsilon\beta}{\alpha-\epsilon\beta}\right)c_n + \exp(i\beta L)a_n\right] - c_{n+1}\frac{\alpha+\epsilon\beta}{\alpha-\epsilon\beta}. \tag{C.44}$$

Eliminate a_{n+1} from the boundary condition eq. (C.27)

$$a_{n+1} + c_{n+1} = r_1\exp(i\Phi)\left[\exp(-i\beta L)a_n + \exp(i\beta L)c_n\right], \tag{C.45}$$

$\Rightarrow$

$$c_{n+1} + r_1\exp(-i\Phi)\left[\exp(-i\beta L)\left(\frac{\alpha+\epsilon\beta}{\alpha-\epsilon\beta}\right)c_n + \exp(i\beta L)a_n\right] - c_{n+1}\frac{\alpha+\epsilon\beta}{\alpha-\epsilon\beta} =$$

$$r_1\exp(i\Phi)\left[\exp(-i\beta L)a_n + \exp(i\beta L)c_n\right]. \tag{C.46}$$

$\Rightarrow$

$$\left(1-\frac{\alpha+\epsilon\beta}{\alpha+\epsilon\beta}\right)c_{n+1} = r_1\exp(i\Phi)\left[\exp(i\beta L)a_n+\exp(-i\beta L)c_n\right]- r_1\exp(i\Phi)\left[\exp(i\beta L)c_n\frac{\alpha+\epsilon\beta}{\alpha-\epsilon\beta}+\exp(i\beta L)a_n\right], \quad (C.47)$$

$$= r_1\exp(i\beta L)\left[\exp(i\Phi)-\exp(-i\Phi)\right]a_n + r_1\exp(-i\beta L)\left[\exp(i\Phi)-\exp(-i\Phi)\frac{\alpha+\epsilon\beta}{\alpha-\epsilon\beta}\right]c_n, \quad (C.48)$$

$$= r_1\exp(i\beta L)\left[\cos\Phi+i\sin\Phi-\Big(\cos\Phi-i\sin\Phi\Big)\right]a_n,+ r_1\exp(i\beta L)\left[\cos\Phi+i\sin\Phi-\Big(\cos\Phi-i\sin\Phi\Big)\frac{\alpha+\epsilon\beta}{\alpha-\epsilon\beta}\right]c_n. \quad (C.49)$$

The following can now be shown:

$$\left(1-\frac{\alpha+\epsilon\beta}{\alpha-\epsilon\beta}\right)c_{n+1} = r_1\exp(i\beta L)\left[\left(1-\frac{\alpha+\epsilon\beta}{\alpha-\epsilon\beta}\right)\cos\Phi+i\left(1+\frac{\alpha+\epsilon\beta}{\alpha-\epsilon\beta}\right)\sin\Phi\right]c_n + i2r_1\sin\Phi\exp(i\beta L)a_n. \quad (C.50)$$

Substitute the terms defined below into the above equation:

$$1-\frac{\alpha+\epsilon\beta}{\alpha-\epsilon\beta} = \frac{-2\epsilon\beta}{\alpha-\epsilon\beta}, \quad (C.51)$$

$$1+\frac{\alpha+\epsilon\beta}{\alpha-\epsilon\beta} = \frac{2\alpha}{\alpha-\epsilon\beta}, \quad (C.52)$$

$\Rightarrow$

$$\frac{-2\epsilon\beta}{\alpha-\epsilon\beta}c_{n+1} = r_1\exp(i\beta L)\left[\frac{-2\epsilon\beta}{\alpha-\epsilon\beta}\cos\Phi+i\frac{2\alpha}{\alpha-\epsilon\beta}\sin\Phi\right]c_n + i2r_1\sin\Phi\exp(i\beta L)a_n, \quad (C.53)$$

$\Rightarrow$

$$c_{n+1} = r_1 \exp(-i\beta L)\left[\cos\Phi - i\frac{\alpha}{\epsilon\beta}\sin\Phi\right]c_n + i\left(1 - \frac{\alpha}{\epsilon\beta}\right)r_1 \sin\Phi \exp(i\beta L)a_n. \tag{C.54}$$

a_{n+1}, and c_{n+1} can now be shown to be:

$$a_{n+1} = r_1 \exp(i\beta L)\Big(\cos\Phi + iY\sin\Phi\Big)a_n + \Big(1+Y\Big)r_1\sin\Phi\exp(-i\beta L), \tag{C.55}$$

$$c_{n+1} = r_1 \exp(-i\beta L)\Big(\cos\Phi - iY\sin\Phi\Big)a_n + \Big(1-Y\Big)r_1\sin\Phi\exp(i\beta L), \tag{C.56}$$

$$\tag{C.57}$$

where $Y \equiv \alpha/(\epsilon\beta)$. The above equation can also be represented by the following matrix:

$$\begin{pmatrix} a_{n+1} \\ c_{n+1} \end{pmatrix} = M \begin{pmatrix} a_n \\ c_n \end{pmatrix}, \tag{C.58}$$

where

$$M = \begin{bmatrix} \exp(i\beta L)(\cos\Phi + iY\sin\Phi) & i(1+Y)r_1\sin\Phi\exp(-i\beta L) \\ i(1-Y)r_1\sin\Phi\exp(i\beta L) & \exp(-i\beta L)(\cos\Phi - iY\sin\Phi) \end{bmatrix}. \tag{C.59}$$

From here look for the eigenvalues of M, which can be achieved by solving the characteristic equation $\det(M-\lambda) = 0$, $\therefore$

$$\begin{vmatrix} M_{11}-\lambda & M_{12} \\ M_{21} & M_{22}-\lambda \end{vmatrix} = 0, \tag{C.60}$$

$\Rightarrow$

$$(M_{11}-\lambda)(M_{22}-\lambda) - M_{12}M_{21} = 0, \tag{C.61}$$

$\therefore$

$$M_{11}M_{22} - \lambda(M_{11}+M_{22}) + \lambda^2 - M_{12}M_{21} = 0, \tag{C.62}$$

$\therefore$

$$\lambda^2 - \lambda \mathrm{Tr}(M)\det(M) = 0. \tag{C.63}$$

Obtain the trace and the determinate of matrix M.

$$\begin{aligned}
\mathrm{Tr}(M) &\equiv M_{11} + M_{22}, \\
&= r_1 \exp(i\beta L)\Big[\cos\Phi + iY\sin\Phi\Big] + r_1\exp(-i\beta L)\Big[\cos\Phi - iY\sin\Phi\Big], \\
&= r_1\cos\Phi\Big[\exp(i\beta L) + \exp(-i\beta L)\Big] + ir_1 Y\sin\Phi\Big[\exp(i\beta L) - \exp(-i\beta L)\Big], \\
&= r_1\cos\Phi 2\cos(\beta L) + ir_1 Y\sin\Phi 2i\sin(\beta L), \\
&= r_1\cos\Phi 2\cos(\beta L) - r_1 Y\sin\Phi 2\sin(\beta L). \qquad \text{(C.64)}
\end{aligned}$$

$\Rightarrow \mathrm{Tr}(M) = 2r_2 b$ where

$$b \equiv \cos\Phi\cos(\beta L) - Y\sin\Phi\sin(\beta L). \qquad \text{(C.65)}$$

Obtain then solution of $\det(M)$:

$$\begin{aligned}
\det(M) &\equiv M_{11}M_{22} - M_{12}M_{21}, \\
&= r_1^2\Big[\cos\Phi + iY\sin\Phi\Big]\Big[\cos\Phi - iY\sin\Phi\Big], \\
&= r_1^2\Big[\cos^2\Phi - i^2Y^2\sin^2\Phi - i^2(1-Y^2)\sin^2\Big], \\
&= r_1^2\Big[\cos^2\Phi + \cancel{Y^2\sin^2\Phi} + (1-\cancel{Y^2})\sin^2\Big], \\
&= r_1^2. \qquad \text{(C.66)}
\end{aligned}$$

The characteristic equation now becomes:

$$\lambda^2 - 2r_1 b\lambda + r - 1^2 = 0. \qquad \text{(C.67)}$$

The stability threshold condition ($\lambda = 1$) is obtained when b takes the value of b_{th}, where

$1 - 2r_1 b_{th} + r_1 = 0, \therefore$

$$b_{th} = \frac{1}{2}\left(r_1 + \frac{1}{r_1}\right). \tag{C.68}$$

$\Rightarrow$

$$\cos\Phi_{th}\cos(\beta_{th}L) - Y_{th}\sin\Phi_{th}\sin(\beta_{th}L) = \frac{1}{2}\left(r_1 + \frac{1}{r_1}\right), \tag{C.69}$$

where:

$$\Phi_{th} = \delta + \chi L I_{th}, \tag{C.70}$$

$$\beta_{th}L = \sqrt{\left(\frac{\boldsymbol{K^2}L}{2k_0}\right)}\left[\left(\frac{\boldsymbol{K^2}L}{2k_0}\right) - 2\chi L I_{th}\right]^{1/2}, \tag{C.71}$$

$$Y_{th} = \frac{1}{\beta_{th}L}\left[\chi L I_{th} - \left(\frac{\boldsymbol{K^2}L}{2k_0}\right)\right]. \tag{C.72}$$

Appendix D

Absorptive bulk ring cavity analysis

D.1 Governing equations

Inside the slice, the coupled Field-medium dynamics are governed by:

$$i\frac{\partial F}{\partial z} + \frac{\sigma}{2}\bigtriangledown_{\perp}^{2} F + i\frac{\alpha_0 L}{2}\frac{1-i\Delta}{1+\Delta^2+T_1T_2|F|^2}F = 0, \tag{D.1}$$

and the boundary condition is defined to be:

$$F(\boldsymbol{x},0) = t_1 F_{in} + r_1 \exp(i\delta) F(\boldsymbol{x},1). \tag{D.2}$$

D.2 Steady state solutions

Look for steady state solutions ($\bigtriangledown_{\perp}^{2} \to 0$):

$$\frac{dF^0}{dz} = -\frac{\alpha_0 L}{2}\frac{1-i\Delta}{1+\Delta^2+T_1T_2|F^0|^2}F^0 \tag{D.3}$$

$\to$

$$F^0(z) = F_0 \exp\left[-\frac{\alpha_0 L}{2}\frac{1-i\Delta}{1+\Delta^2+T_1T_2|F^0|^2}z\right]. \tag{D.4}$$

From the boundary condition

$$F_0 = t_1 F_{in} + r_1 \exp(i\delta) F_0 \exp\left[-\frac{\alpha_0 L}{2}\frac{1-i\Delta}{1+\Delta^2+T_1T_2|F^0|^2}\right] \tag{D.5}$$

Simplify the above by parametrising:

$$\Phi \equiv \delta + \frac{\alpha_0 L}{2} \frac{1 - i\Delta}{1 + \Delta^2 + T_1 T_2 |F^0|^2}, \tag{D.6a}$$

and

$$R_1 \equiv r_1 \exp\left[-\frac{\alpha_0 L}{2} \frac{1 - i\Delta}{1 + \Delta^2 + T_1 T_2 |F^0|^2} \right] \tag{D.6b}$$

This gives the following:

$$F^0(z) = F_0 \exp\left[-\left(\frac{\alpha_0 L}{2}\right) \frac{1 - i\Delta}{1 + \Delta^2 + T_1 T_2 |F^0|^2} \right] \tag{D.7}$$

$$F_0 = \frac{t_1 F_{in}}{1 - R_1 \exp(i\Phi)}. \tag{D.8}$$

D.3 Linear stability analysis

Write the intra cavity field as:

$$F(\boldsymbol{x}, z) = F^0(z)[1 + f(\boldsymbol{x}, z)], \tag{D.9}$$

where $|f| \ll O(1)$.

$$i\left[(1 + f)\frac{dF^0}{dz} + F^0(z)\frac{\partial f}{\partial z} \right] + F^0(z)\frac{\sigma}{2} \bigtriangledown_\perp^2 f + g(|F|^2)F^0(z)(1 + f) = 0. \tag{D.10}$$

$$|F|^2 = |F^0(z)|^2(1 + f)(1 + f^*), \tag{D.11}$$

$$= |F^0(z)|^2[1 + f + f^*|f|^2, \tag{D.12}$$

$$\tag{D.13}$$

$\rightarrow$

$$|F| = I + \Delta I, \tag{D.14}$$

$$I \equiv |F^0|^2, \tag{D.15}$$

$$\Delta I \equiv |F^0|^2(f + f^*). \tag{D.16}$$

$\Rightarrow$

$$g(|F|^2) = g(I + \Delta I), \tag{D.17}$$

$$\approx g(I) + \left.\frac{\partial g}{\partial |F|^2}\right|_I \Delta I + \ldots, \tag{D.18}$$

$\Rightarrow$

$$g(|F|^2) \approx g(|F^0|^2) + g'(|F^0|^2)|F^0|^2(f + f^*), \tag{D.19}$$

where

$$g'(|F^0|^2) \equiv \left.\frac{\partial g}{\partial |F|^2}\right|_{|F^0|^2}. \tag{D.20}$$

$\therefore$

$$i\left[(1+f)\frac{dF^0}{dz} + F^0(z)\frac{\partial f}{\partial z}\right] + F^0(z)\frac{\sigma}{2}\bigtriangledown_\perp^2 f + \left[g(|F^0|^2) + g'(|F^0|^2)|F^0|^2(f+f^*)\right]F^0(1+f) \approx 0. \tag{D.21}$$

Cancel the stationary states:

$$(1+f)\left[i\frac{dF^0}{dz} + g(|F^0|^2)F^0\right] + F^0\left[i\frac{\partial f}{\partial z} + \frac{\sigma}{2}\bigtriangledown_\perp^2 f\right] + |F^0|^2 g'(|F^0|^2)(f+f^*)F^0(1+f) \approx 0, \tag{D.22}$$

$$i\frac{dF^0}{dz} + g(|F^0|^2)F^0 + 0, \tag{D.23}$$

$\therefore$

$$\frac{\partial f}{\partial z} + \frac{\sigma}{2} \bigtriangledown_{\perp}^{2} f + |F^0|^2 g'(|F^0|^2)(f + f^*)(1 + f). \tag{D.24}$$

An analytical expression for $g'(|F^0|^2)$ is required:

$$g(|F^0|^2) = i\frac{\alpha_0 L}{2} \frac{1 - i\Delta}{1 + \Delta^2 + T_1 T_2 |F|^2} \tag{D.25}$$

$\Rightarrow$

$$\frac{\partial g}{\partial |F|^2} = i\frac{\alpha_0 L}{2}(1 - i\Delta)(-1)(1 + \Delta^2 + T_1 T_2 |F|^2)^2 T_1 T_2, \tag{D.26}$$

$$= -i\frac{\alpha_0 L}{2} \frac{1 - i\Delta}{1 + \Delta^2 + T_1 T_2 |F^0|^2} T_1 T_2, \tag{D.27}$$

$\therefore$

$$g'(|F^0|^2) = -i\frac{\alpha_0 L}{2} \frac{1 - i\Delta}{1 + \Delta^2 + T_1 T_2 |F^0|^2} T_1 T_2, \tag{D.28}$$

$\Rightarrow$

$$|F^0|^2 g'(|F^0|^2) = -i\frac{\alpha_0 L}{2} \frac{1 - i\Delta}{1 + \Delta^2 + T_1 T_2 |F^0|^2} T_1 T_2 |F^0|^2 \tag{D.29}$$

$$= G(|F^0|^2). \tag{D.30}$$

The linearised equation for the perturbation $f(\boldsymbol{x}, z)$ is then given by

$$i\frac{\partial}{\partial z} f(\boldsymbol{x}, z) + \frac{\sigma}{2} \bigtriangledown_{\perp}^{2} + G(|F_0|^2)[f(\boldsymbol{x}, z) + f^*(\boldsymbol{x}, z)] \approx 0. \tag{D.31}$$

We now need additional information about the boundary condition:

$$F^0(0)[1+f(\boldsymbol{x},0)] = t_1F_{in} + r_1\exp(i\delta)F^0(1)[1+f(\boldsymbol{x},1)], \tag{D.32}$$

$$F_0[1+f(\boldsymbol{x},0)] = t_1F_{in} + r_1\exp(i\delta)F_0\exp\left[-i\frac{\alpha_0 L}{2}\frac{1-i\Delta}{1+\Delta^2+T_1T_2|F^0|^2}\right][1+f(\boldsymbol{x},1)], \tag{D.33}$$

$\Rightarrow$

$$F_0[\not{1}+f(\boldsymbol{x},0)] = \cancel{t_1F_{in}} + R_1\exp(i\Phi)F_0[\not{1}+f(\boldsymbol{x},1)] \tag{D.34}$$

$$\cancel{F_0}f(\boldsymbol{x},0) = R_1\exp(i\Phi)\cancel{F_0}f(\boldsymbol{x},1) \tag{D.35}$$

$$\Rightarrow f(\boldsymbol{x},0) = R_1\exp(i\Phi)f(\boldsymbol{x},1) \tag{D.36}$$

Look for solutions that have the following form

$$f(\boldsymbol{x},z) = \epsilon(z)\exp(i\boldsymbol{K}\cdot\boldsymbol{x}) + \mu^*(z)\exp(-i\boldsymbol{K}\cdot\boldsymbol{x}). \tag{D.37}$$

$\therefore$

$$\frac{\partial f}{\partial z} = \exp(i\boldsymbol{K}\cdot\boldsymbol{x})\frac{d\epsilon}{dz} + \exp(-i\boldsymbol{K}\cdot\boldsymbol{x})\frac{d\mu^*}{dz} \tag{D.38}$$

$$\bigtriangledown_\perp^2 f = -\boldsymbol{K}^2[\exp(i\boldsymbol{K}\cdot\boldsymbol{x})\epsilon(z) + \exp(-i\boldsymbol{K}\cdot\boldsymbol{x})\mu^*(z)] \tag{D.39}$$

$$f + f^* = \epsilon(z)\exp(i\boldsymbol{K}\cdot\boldsymbol{x}) + \mu^*(z)\exp(-i\boldsymbol{K}\cdot\boldsymbol{x}) \tag{D.40}$$

$$\epsilon^*(z)\exp(-i\boldsymbol{K}\cdot\boldsymbol{x}) + \mu(z)\exp(i\boldsymbol{K}\cdot\boldsymbol{x})$$

$$= [\epsilon(z)+\mu(z)]\exp(i\boldsymbol{K}\cdot\boldsymbol{x}) + [\epsilon^*(z)+\mu^*(z)]\exp(-i\boldsymbol{K}\cdot\boldsymbol{x}) \tag{D.41}$$

Substitute this into the linearised master equation.

$$\Big[\exp(i\boldsymbol{K}\cdot\boldsymbol{x})\Big]$$

$$i\frac{d\epsilon}{dz} - \frac{\sigma\boldsymbol{K}^2}{2}\epsilon + G(|F_0|^2)(\epsilon+\mu) = 0 \tag{D.42}$$

$$\rightarrow i\frac{d\epsilon}{dz} = \frac{\sigma\boldsymbol{K}^2}{2}\epsilon - G(|F_0|^2)(\epsilon+\mu) \tag{D.43}$$

$$\Big[\exp(-i\boldsymbol{K}\cdot\boldsymbol{x})\Big]$$

$$i\frac{d\mu^*}{dz} - \frac{\sigma\boldsymbol{K}^2}{2}\mu^* + G(|F_0|^2)(\mu^*+\epsilon^*) = 0 \tag{D.44}$$

$$\rightarrow i\frac{d\mu^*}{dz} = \frac{\sigma\boldsymbol{K}^2}{2}\mu^* - G(|F_0|^2)(\mu^*+\epsilon^*) \tag{D.45}$$

$\Rightarrow$

$$i\frac{d\epsilon}{dz} = i\left[G(|F_0|^2) - \frac{\sigma\boldsymbol{K^2}}{2}\right]\epsilon + iG(|F_0|^2)\mu \tag{D.46}$$

$$i\frac{d\mu}{dz} = -i\left[G^*(|F_0|^2) - \frac{\sigma\boldsymbol{K^2}}{2}\right]\mu + iG^*(|F_0|^2)\epsilon \tag{D.47}$$

$$\frac{d}{dz}\begin{pmatrix}\epsilon\\ \mu\end{pmatrix} = iM\begin{pmatrix}\epsilon\\ \mu\end{pmatrix}, \tag{D.48}$$

where:

$$M = \begin{bmatrix} G(|F_0|^2) - \frac{\sigma K^2}{2} & G(|F_0|^2) \\ -G^*(|F_0|^2) & -\left(G^*(|F_0|^2) - \frac{\sigma K^2}{2}\right)\end{bmatrix}. \tag{D.49}$$

The solution from this matrix can be obtain though a formal integration of the matrix which results in the following:

$$A(1) \equiv \exp(iM)\cdot A(0) \equiv E\cdot A(0), \tag{D.50}$$

where: $A \equiv (\epsilon\cdot\mu)^T$, T denotes the transpose, and $E = \exp(iM)$. Matrix M can be exponen-

tiated by using the formula:

$$\exp\begin{bmatrix} a & b \\ c & d \end{bmatrix} = \frac{1}{D}\exp\left(\frac{a+d}{2}\right)\begin{pmatrix} m_{11} & m_{12} \\ m_{21} & m_{22} \end{pmatrix}, \tag{D.51}$$

where:

$$\begin{aligned} m_{11} &\equiv D\cosh\left(\frac{D}{2}\right) + (a-d)\sinh\left(\frac{D}{2}\right), \\ m_{12} &\equiv 2b\sinh\left(\frac{D}{2}\right), \\ m_{21} &\equiv 2c\sinh\left(\frac{D}{2}\right), \\ m_{22} &\equiv D\cosh\left(\frac{D}{2}\right) + (d-a),\sinh\left(\frac{D}{2}\right) \end{aligned} \tag{D.52}$$

and

$$D \equiv \sqrt{(a-d)^2 + 4bc}. \tag{D.53}$$

$$a + b = i\left[G(|F_0|^2) - \frac{\sigma \cancel{\boldsymbol{K}^2}}{\cancel{2}}\right] - i\left[G^*(|F_0|) - \frac{\sigma \cancel{\boldsymbol{K}^2}}{\cancel{2}}\right] \tag{D.54}$$

$$= i[G(|F_0|^2) - G^*(|F_0|^2)] \tag{D.55}$$

$$= i\left\{2i\Im\mathrm{m}\left[G(|F_0|^2\right]\right\} \tag{D.56}$$

$$= -2\Im\mathrm{m}\left[G(|F_0|^2\right] \tag{D.57}$$

$\Rightarrow$

$$a - d = \left[G(|F_0|^2) + G^*(|F_0|^2)\right] - i\sigma \boldsymbol{K}^2. \tag{D.58}$$

$$= i2\Re\mathrm{e}\left[G(|F_0|^2)\right] - i\sigma \boldsymbol{K}^2. \tag{D.59}$$

$\Rightarrow$

$$a - d = i2\Re\mathrm{e}\left[G(|F_0|^2)\right], \tag{D.60}$$

where

$$\theta \equiv \frac{\sigma \boldsymbol{K}^2}{2} = \frac{\boldsymbol{K}^2 L}{2k_0 b^2}. \tag{D.61}$$

$\therefore$

$$(a-d)^2 + 4bc = \left\{i2\left[\Re\mathrm{e}\left[G(|F_0|^2)\right] - \theta\right]\right\} + 4[iG(|F_0|^2)][-iG^*(|F_0|^2)] \tag{D.62}$$

$$= -4\left\{\Re\mathrm{e}\left[G(|F_0|^2)\right] - \theta\right\}^2 + 4\left|G(|F_0|^2)\right|^2 \tag{D.63}$$

$$= -4\left\{\cancel{\Re\mathrm{e}\left[G(|F_0|^2)\right]^2} + \theta^2 - 2\theta\Re\mathrm{e}\left[G(|F_0|^2)\right]\right\} +$$

$$4\left\{\cancel{\Re\mathrm{e}\left[G(|F_0|^2)\right]^2} + \Im\mathrm{m}\left[G(|F_0|^2)\right]\right\} \tag{D.64}$$

$$= -4\left\{\theta^2 - 2\theta\Re\mathrm{e}\left[G(|F_0|^2)\right]\right\} + 4\Im\mathrm{m}\left[G(|F_0|^2)\right]^2 \tag{D.65}$$

$\Rightarrow$

$$D = 2\sqrt{\theta\left\{2\Re\mathrm{e}\left[G(|F_0|^2)\right] - \theta\right\} + \Im\mathrm{m}^2\left[G(|F_0|^2)\right]} \tag{D.66}$$

From here the exponentiation can now be summarised to be:

$$E = \begin{bmatrix} E_{11} & E_{12} \\ E_{21} & E_{22} \end{bmatrix} = \frac{1}{D}\exp\left\{-\Im\mathrm{m}\left[G(|F_0|^2)\right]\right\}\begin{pmatrix} m_{11} & m_{12} \\ m_{21} & m_{22} \end{pmatrix}, \tag{D.67}$$

where:

$$
\begin{aligned}
E_{11} &= \exp\left\{-\Im\mathrm{m}\left[G(|F_0|)^2\right]\right\}\left[\cosh\left(\frac{D}{2}\right)+i\frac{2}{D}\left\{\Re\mathrm{e}\left[G(|F_0|)^2-\theta\right]\right\}\sinh\left(\frac{D}{2}\right)\right],\\
E_{12} &= \exp\left\{-\Im\mathrm{m}\left[G(|F_0|)^2\right]\right\}i\frac{2G(|F_0|^2)}{d}\sinh\left(\frac{D}{2}\right),\\
E_{21} &= -\exp\left\{-\Im\mathrm{m}\left[G(|F_0|)^2\right]\right\}i\frac{2G^*(|F_0|^2)}{d}\sinh\left(\frac{D}{2}\right),\\
E_{22} &= \exp\left\{-\Im\mathrm{m}\left[G(|F_0|)^2\right]\right\}\left[\cosh\left(\frac{D}{2}\right)-i\frac{2}{D}\left\{\Re\mathrm{e}\left[G(|F_0|)^2-\theta\right]\right\}\sinh\left(\frac{D}{2}\right)\right],\\
D &= 2\sqrt{\theta\left\{2\Re\mathrm{e}\left[G(|F_0|^2-\theta\right]\right\}+\Im\mathrm{m}^2\left[G(|F_0|^2)\right]}.
\end{aligned}
\tag{D.68}
$$

$$
\begin{bmatrix}\epsilon(1)\\ \mu(1)\end{bmatrix}=\begin{pmatrix}E_{11} & E_{12}\\ E_{21} & E_{22}\end{pmatrix}\begin{bmatrix}\epsilon(0)\\ \mu(0)\end{bmatrix},
\tag{D.69}
$$

$\Rightarrow$

$$
\epsilon(1)=E_{11}+E_{12}\mu(0)
\tag{D.70}
$$

$$
\mu(1)=E_{11}+E_{12}\mu(0),
\tag{D.71}
$$

now apply this ti the ring cavity boundary condition, $f(\boldsymbol{x},0)=R_1\exp(i\Phi)f(\boldsymbol{x},1)\rightarrow$

$$
\epsilon(0)\exp(i\boldsymbol{K}\cdot\boldsymbol{x})+\mu^*\exp(-i\boldsymbol{K}\cdot\boldsymbol{x})=R_!\exp(i\Phi)\left[\epsilon(1)\exp(i\boldsymbol{K}\cdot\boldsymbol{x})+\mu^*(1)\exp(-i\boldsymbol{K}\cdot\boldsymbol{x})\right].
\tag{D.72}
$$

Now collect the terms at $\exp(\pm \boldsymbol{K} \cdot \boldsymbol{x})$, this gives the following:

$$\left[\exp(i\boldsymbol{K} \cdot \boldsymbol{x})\right]$$

$$\epsilon(0) = R_1 \exp(i\Phi)\epsilon(1), \tag{D.73}$$

$$\left[\exp(-i\boldsymbol{K} \cdot \boldsymbol{x})\right]$$

$$\mu(0) = R_1 \exp(-i\Phi)\mu(1), \tag{D.74}$$

now substitute into the component of the matrix equation

$$\begin{aligned} \epsilon(1) &= E_{11}\epsilon(0) + E_{12}\mu(0), & \text{(D.75)} \\ &= E_{11}R_1 \exp(i\Phi)\epsilon(1) + E_{12}R_1 \exp(-i\Phi)\mu, & \text{(D.76)} \\ \mu(1) &= E_{21}\epsilon(0) + E_{22}\mu(0), & \text{(D.77)} \\ &= E_{21}R_1 \exp(i\Phi)\epsilon(1) + E_{22}R_1 \exp(-i\Phi)\mu, & \text{(D.78)} \end{aligned}$$

$$\begin{bmatrix} 1 - R_1 \exp(i\phi)E_{11} & -R_1 \exp(i\phi)E_{12} \\ -R_1 \exp(i\phi)E_{21} & 1 - R_1 \exp(i\phi)E_{22} \end{bmatrix} \begin{bmatrix} \epsilon(1) \\ \mu(1) \end{bmatrix} = \begin{bmatrix} 0 \\ 0 \end{bmatrix}. \tag{D.79}$$

$\rightarrow$

$$\left[1 - R_1 \exp(i\phi)E_{11}\right]\left[1 - R_1 \exp(-i\phi)E_{22}\right] - R_1^2 E_{12}E_{21} \tag{D.80}$$

$\rightarrow$

$$1 - R_1\left[E_{11} \exp(i\phi) + E_{22} \exp(-i\phi)\right] + R_1^2(E_{11}E_{22} - E_{12}E_{21}) = 0, \tag{D.81}$$

$\therefore$

$$\exp\left\{2\Im\mathrm{m}\left[G(|F_0|^2)\right]\right\} + R_1^2(E_{11}E_{22} - E_{12}E_{21}) - R_1^2(E_{11}E_{22} - E_{12}E_{21}). \tag{D.82}$$

$$E_{11} = \cosh\left(\frac{D}{2}\right) + i\frac{D}{2}\left\{\Re\mathrm{e}\left[G(|F_0|^2)\right] - \theta\right\}\sinh\left(\frac{D}{2}\right) \tag{D.83}$$

$$E_{22} = \cosh\left(\frac{D}{2}\right) - i\frac{D}{2}\left\{\Re\mathrm{e}\left[G(|F_0|^2)\right] - \theta\right\}\sinh\left(\frac{D}{2}\right) \tag{D.84}$$

$$E_{12} = i\left(\frac{2}{D}\right)G(|F_0|^2)\sinh\left(\frac{D}{2}\right) \tag{D.85}$$

$$E_{21} = -i\left(\frac{2}{D}\right)G^*(|F_0|^2)\sinh\left(\frac{D}{2}\right) \tag{D.86}$$

$$\frac{D}{2} = \sqrt{\theta\left\{2\Re\mathrm{e}\left[G(|F_0|^2{-}\theta\right]\right\} + \Im\mathrm{m}^2\left[G(|F_0|^2)\right]}. \tag{D.87}$$

$\rightarrow$

$$\frac{D}{2} = \sqrt{\theta\left\{2\Re\mathrm{e}\left[G(|F_0|^2{-}\theta\right]\right\} + \Im\mathrm{m}^2\left[G(|F_0|^2)\right]} = i\beta L, \tag{D.88}$$

also:

$$\cosh\left(\frac{D}{2}\right) = \cosh(i\beta L) = i\cos(\beta L), \tag{D.89}$$

$$\sinh\left(\frac{D}{2}\right) = \sinh(i\beta L) = i\sin(\beta L), \tag{D.90}$$

now re-write the matrix entries E_{ij}:

$$E_{11} = \cos(\beta L) + \cancel{i}\frac{\Re\mathrm{e}\left[G(|F_0|^2)\right] - \theta}{\cancel{i}\beta L}i\sin(\beta L), \tag{D.91}$$

$$E_{22} = \cos(\beta L) - \cancel{i}\frac{\Re\mathrm{e}\left[G(|F_0|^2)\right] - \theta}{\cancel{i}\beta L}i\sin(\beta L), \tag{D.92}$$

$$E_{12} = \cancel{i}\frac{G(|F_0|^2)}{\cancel{i}\beta L}i\sin(\beta L), \tag{D.93}$$

$$E_{21} = -\cancel{i}\frac{G^*(|F_0|^2)}{\cancel{i}\beta L}i\sin(\beta L). \tag{D.94}$$

$\Rightarrow$

$$E_{11}\exp(i\Phi)+E_{22}\exp(-i\Phi) = \exp(i\Phi)\left[\cos(\beta L)+i\frac{\Re\mathrm{e}\left[G(|F_0|^2)\right]-\theta}{\beta L}\sin(\beta L)\right]+$$

$$\exp(i\Phi)\left[\cos(\beta L)-i\frac{\Re\mathrm{e}\left[G(|F_0|^2)\right]-\theta}{\beta L}\sin(\beta L)\right], \quad \text{(D.95)}$$

$$= \cos(\beta L)\left[\exp(i\phi)+\exp(-i\phi)\right]+$$

$$i\frac{\Re\mathrm{e}\left[G(|F_0|^2)\right]-\theta}{\beta L}\sin(\beta L)\left[\exp(i\phi)+\exp(-i\phi)\right], \quad \text{(D.96)}$$

$$= 2\cos(\beta L)\cos(\Phi)+$$

$$i\frac{\Re\mathrm{e}\left[G(|F_0|^2)\right]-\theta}{\beta L}\sin(\beta L)2i\sin(\Phi), \quad \text{(D.97)}$$

$$= 2\Big[\cos(\Phi)\cos(\beta L)-$$

$$\frac{\Re\mathrm{e}\left[G(|F_0|^2)\right]-\theta}{\beta L}\sin(\beta L)\sin(\Phi)\Big]. \quad \text{(D.98)}$$

Now we are require to calculate $E_{11}E_{22}-E_{12}E_{21}\equiv\det(E)$

$$E_{11}E_{22}-E_{12}E_{21} = \left[\cos(\beta L)+i\frac{\Re\mathrm{e}\left[G(|F_0|^2)\right]-\theta}{\beta L}\sin(\beta L)\right]\times$$

$$\left[\cos(\beta L)-i\frac{\Re\mathrm{e}\left[G(|F_0|^2)\right]-\theta}{\beta L}\sin(\beta L)\right]$$

$$-i\frac{G(|F_0|^2)}{\beta L}\sin(\beta L)\left[-fracG^*(|F_0|^2)\beta L\sin(\beta L)\right], \quad \text{(D.99)}$$

$$= \cos^2(\beta L)+\frac{\left\{\Re\mathrm{e}\left[G(|F_0|^2)\right]-\theta\right\}^2}{(\beta L)^2}\sin^2(\beta L)-$$

$$\frac{\left|G(|F_0|^2)\right|^2}{(\beta L)^2}\sin^2(\beta L). \quad \text{(D.100)}$$

It should be noted that:

$$\left|G(|F_0|^2)\right|^2 \equiv \Re\mathrm{e}^2\left[G(|F_0|^2)\right] + \Im\mathrm{m}^2\left[G(|F_0|^2)\right]. \tag{D.101}$$

$\Rightarrow$

$$\begin{aligned} E_{11}E_{22} - E_{12}E_{21} &= \cos^2(\beta L)\frac{1}{(\beta L)^2}\Big\{\cancel{\Re\mathrm{e}^2\left[G(|F_0|^2)\right]} + \theta^2 - 2\theta\Re\mathrm{e}^2\left[G(|F_0|^2)\right] - \\ &\quad \cancel{\Re\mathrm{e}^2\left[G(|F_0|^2)\right]} - \Im\mathrm{m}^2\left[G(|F_0|^2)\right]\Big\}\sin^2(\beta L), \qquad \text{(D.102)} \\ &= \cos^2(\beta L) + \\ &\quad \cancel{\frac{1}{(\beta L)^2}\Big\{\theta^2 - 2\theta\Re\mathrm{e}^2\left[G(|F_0|^2)\right] - \Im\mathrm{m}^2\left[G(|F_0|^2)\right]\Big\}} \times \\ &\quad \sin^2(\beta L). \qquad \text{(D.103)} \end{aligned}$$

$\therefore$

$$\begin{aligned} E_{11}\exp(i\Phi) + E_{22}\exp(-i\Phi) &= 2\Big[\cos(\Phi)\cos(\beta L) - \\ &\quad \frac{\Re\mathrm{e}\left[G(|F_0|^2)\right] - \theta}{\beta L}\sin(\beta L)\sin(\Phi)\Big], \qquad \text{(D.104)} \end{aligned}$$

and

$$E_{11}E_{22} - E_{12}E_{21} \equiv \det(E) = +1. \tag{D.105}$$

Assuming that $|F_0|^2 \equiv I_{th}$ the threshold condition for a ring cavity with a bulk host medium is:

$$cos\phi\cos(\beta L) - \frac{\Re\mathrm{e}[G(I_{th}) - \theta]}{\beta L}\sin\phi\sin(\beta L) = \frac{1}{R_{1_{th}}^2}\left\{\exp\left(2\Im\mathrm{m}G(I_{th}) + R_{1_{th}}^2\right)\right\} \tag{D.106}$$

Appendix E

Fabry-Pérot plane wave analysis

The following set of figures have the relevant r_1^2, r_2^2, and $|F_{in}|^2$ values located above the corresponding plots, in addition to having the following set of parameters: $\chi = +1$, $\delta = \pi/4$, $l_D = 0$, $\tau = 0$ and $L = 1$.

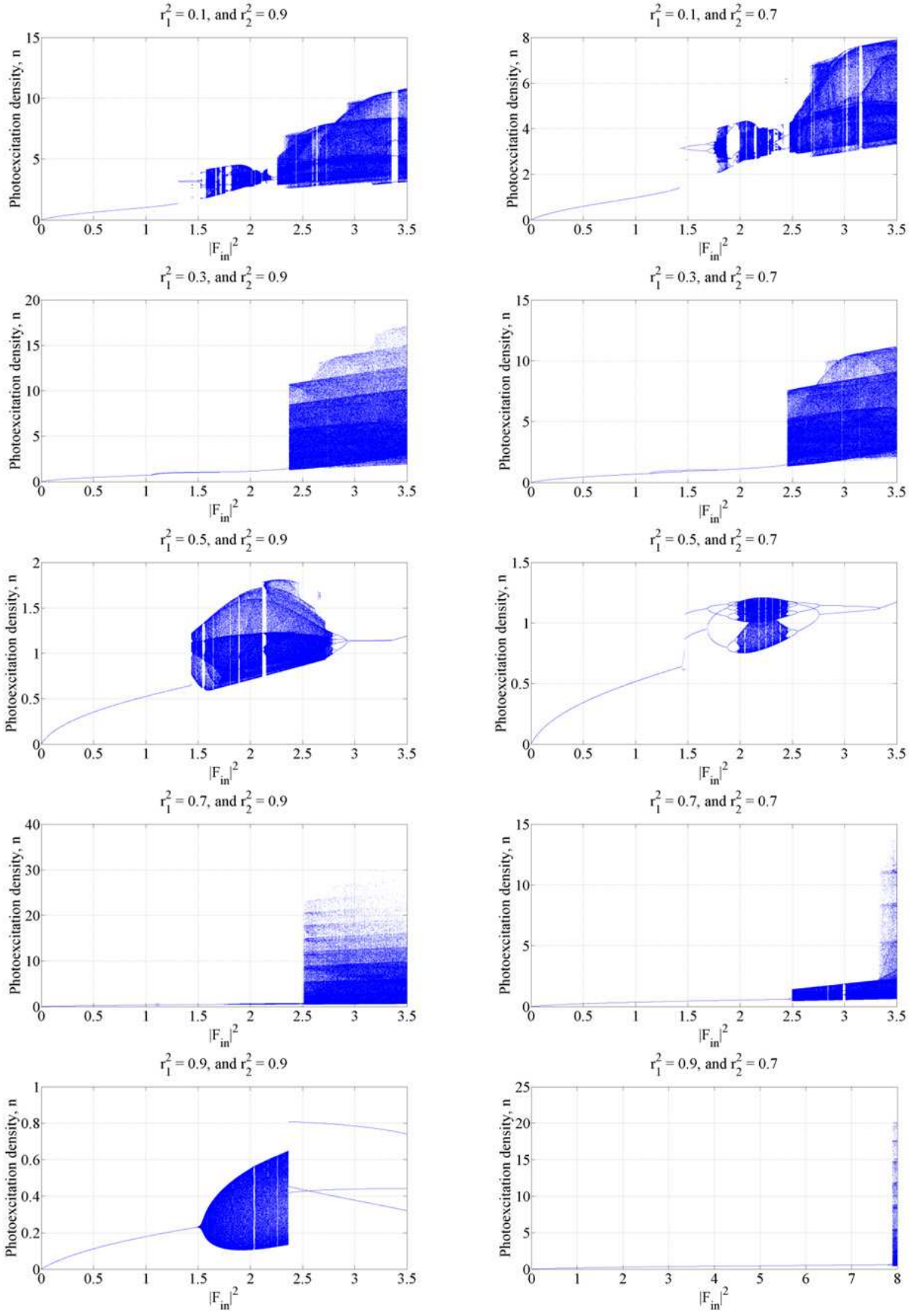

Figure E.1: Bifurcation diagrams of the Fabry-Pérot cavity

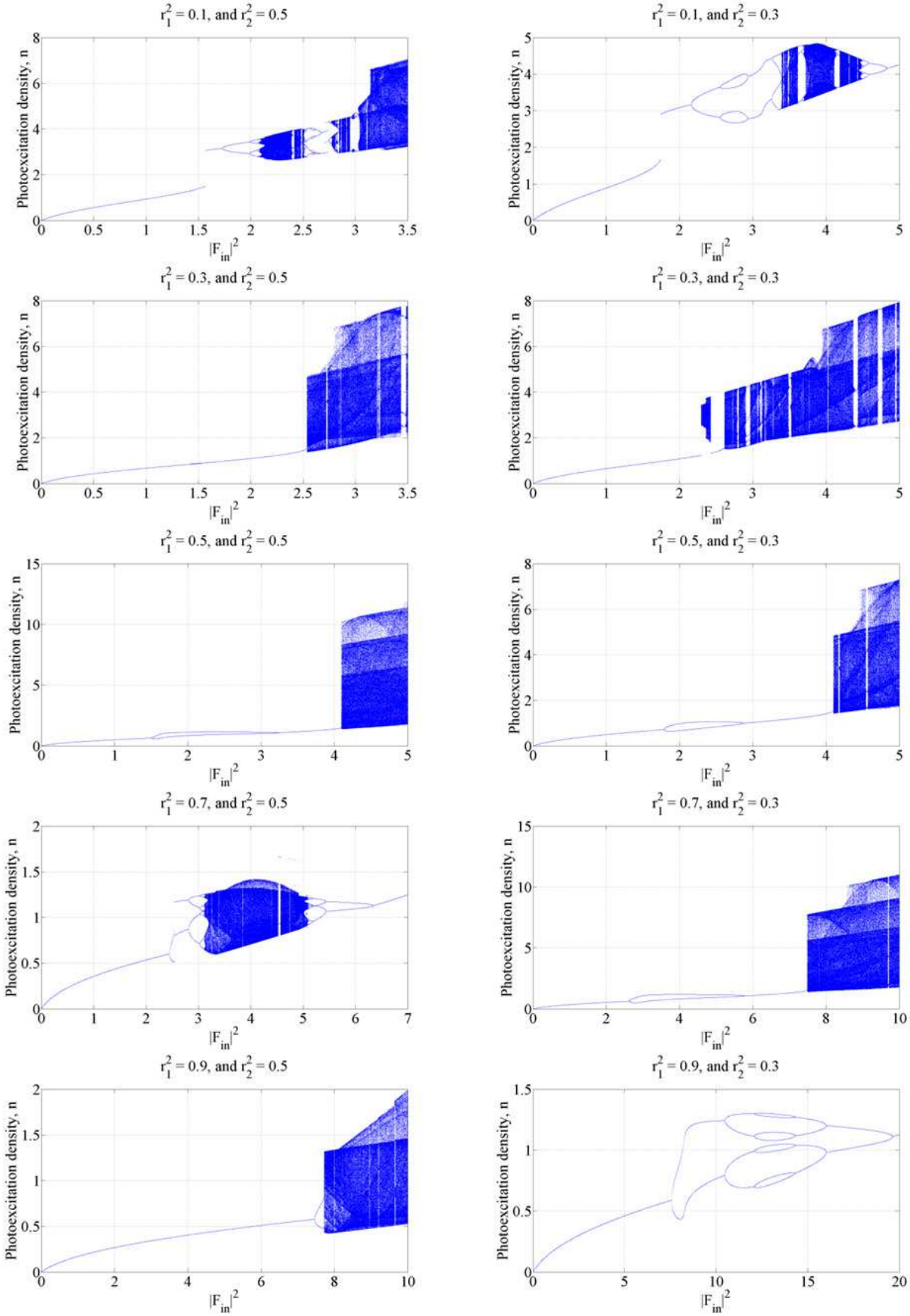

Figure E.2: Bifurcation diagrams of the Fabry-Pérot cavity

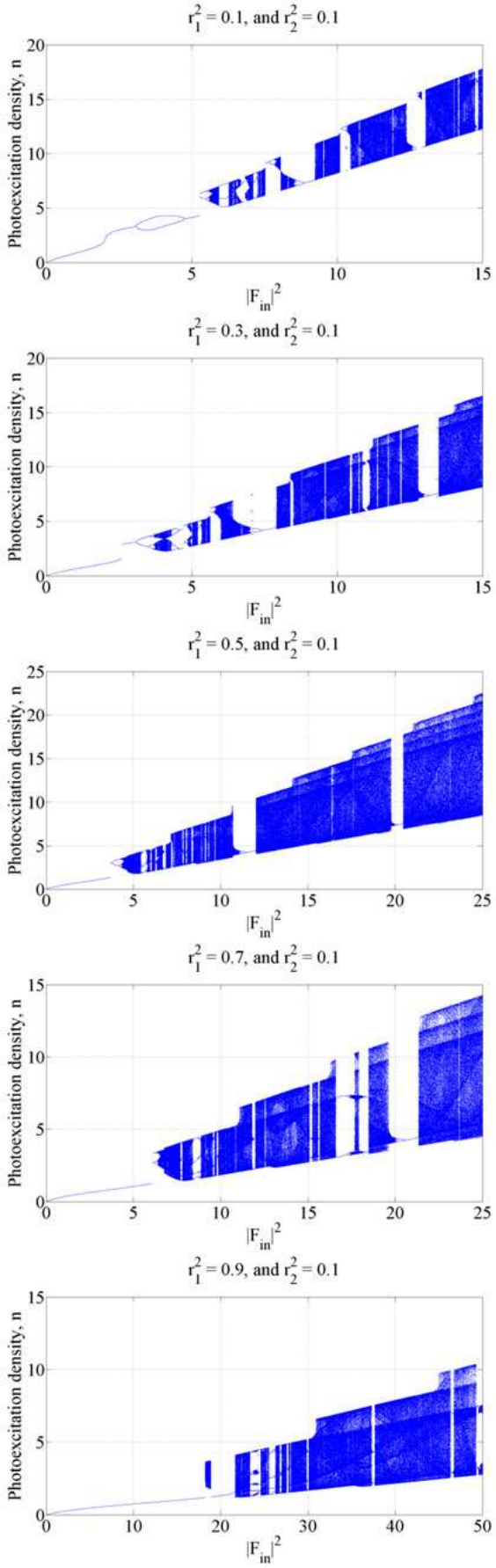

Figure E.3: Bifurcation diagrams of the Fabry-Pérot cavity

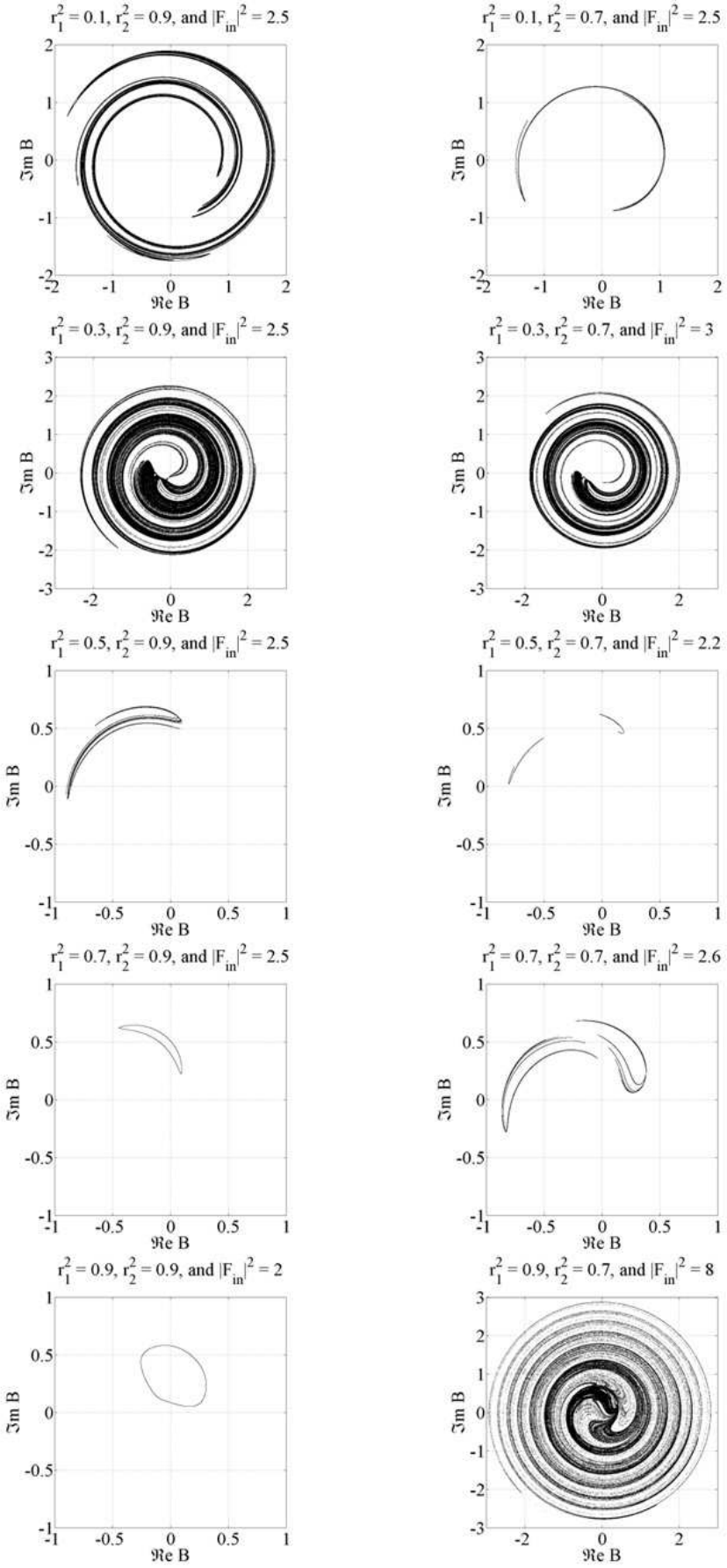

Figure E.4: Phase space portraits of the Fabry-Pérot cavity

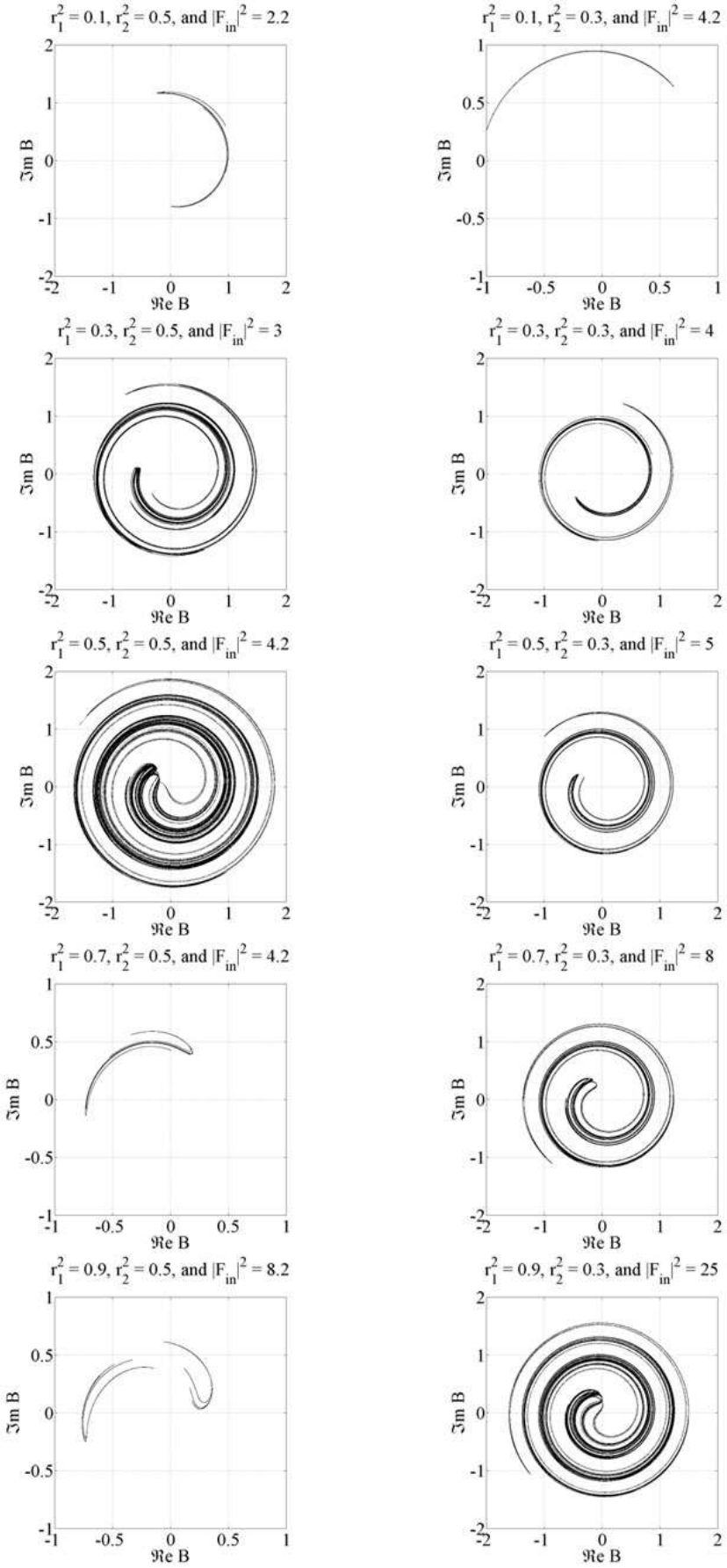

Figure E.5: Phase space portraits of the Fabry-Pérot cavity

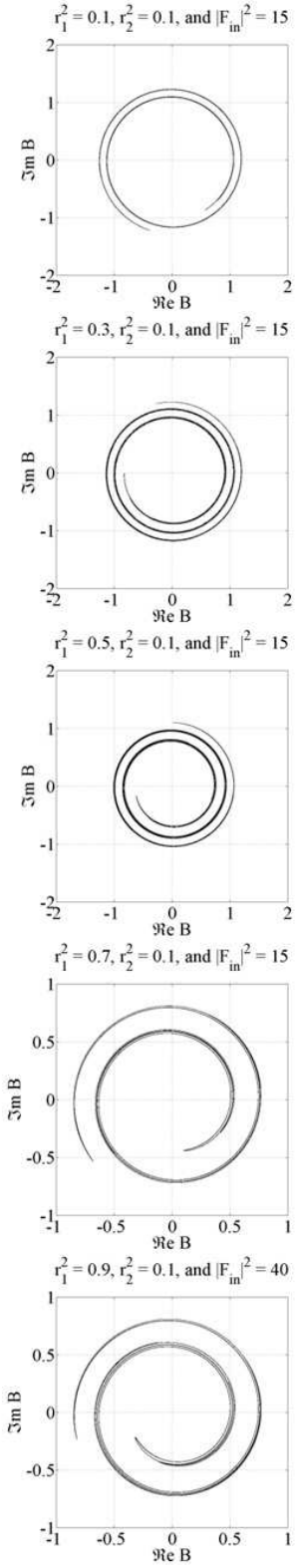

Figure E.6: Phase space portraits of the Fabry-Pérot cavity